Joint Institute for Nuclear Research

FUNDAMENTAL INTERACTIONS & NEUTRONS, NUCLEAR STRUCTURE, ULTRACOLD NEUTRONS, RELATED TOPICS

XXVIII International Seminar on Interaction of Neutrons with Nuclei

Dubna, Russia, May 24–28, 2021

Proceedings of the Seminar

Dubna • 2021

УДК 539.125.5(042)
ББК 22.383.2я431+22.383.5я431+22.383.25я431
F97

Organizing Committee

V. N. Shvetsov (*JINR*), *co-chairman*,
Hei Dongwei (*NINT, China*), *co-chairman*,
E. V. Lychagin (*JINR*), *scientific secretary*,
V. I. Furman, Yu. N. Kopatch, P. V. Sedyshev, L. V. Mitsyna,
M. V. Frontasyeva, I. I. Zinicovscaia

The contributions are reproduced directly from the originals presented
by the Organizing Committee.

Fundamental Interactions & Neutrons, Nuclear Structure, Ultracold Neutrons, Related
F97 Topics: Proceedings of the XXVIII International Seminar on Interaction of Neutrons with Nuclei (Dubna, Russia, May 24–28, 2021). — Dubna: JINR, 2021. — 277 p.
ISBN 978-5-9530-0565-4

This collection of papers reflects the present state of neutron-aided investigations of the properties of the nucleus, including fundamental symmetries, properties of the neutron itself, neutron-excited reactions, and the parameters of the nucleus that determine the reaction cross section, as well as the latest theoretical development of all these problems. The works on experimental investigations in the physics of fission by neutrons of various energies are presented in great detail. The present state of experiments on the physics of ultracold neutrons and facilities to obtain them is described at length. The status achieved by now of the latest (from the viewpoint of technique) experiments and environment studies is covered as well.

Фундаментальные взаимодействия и нейтроны, структура ядра, ультрахолодные нейтроны, связанные темы: Труды XXVIII Международного семинара по взаимодействию нейтронов с ядрами (Дубна, Россия, 24–28 мая 2021 г.). — Дубна: ОИЯИ, 2021. — 277 с.
ISBN 978-5-9530-0565-4

В сборнике представлено современное состояние исследований свойств ядра с помощью нейтронов: фундаментальных симметрий и свойств самого нейтрона, возбуждаемых им реакций и параметров ядра, определяющих их сечения, а также последние теоретические разработки всех этих вопросов. Очень детально представлены работы по всем аспектам, связанным с экспериментальными исследованиями физики деления ядра нейтронами различных энергий. Достаточно полно описано современное состояние экспериментов по физике ультрахолодных нейтронов и установок для их получения, а также достигнутый к настоящему времени статус методически новейших экспериментов и результаты экологических исследований.

УДК 539.125.5(042)
ББК 22.383.2я431+22.383.5я431+22.383.25я431

ISBN 978-5-9530-0565-4

CONTENTS

Neutron Facilities & Advanced Neutron Sources and Perspective Experiments

Neutron Detection & Methodical Aspects

Neutron Radiation Effects & Radiation Transportation and Simulation

Nuclear and Related Analytical Techniques in Environmental and Material Sciences

Nuclear Fission

Fundamental Properties of the Neutron & UCN

Reactions with Neutrons, Properties of Compound States, Nuclear Structure

ISINN-28 Preface

The annual International Seminar on Interaction of Neutrons with Nuclei, ISINN-28, was scheduled to be held in Beijing, China, in May 2020, but because of pandemic, after much debate with Chinese co-organizers, it was put off and took place on-line only on 24–28 May 2021. Preparation for the Seminar was realized by the Frank Laboratory of Neutron Physics, JINR in conjunction with colleagues from Chinese institutes and universities. It was one of the world's first conferences on nuclear physics since the pandemic began in 2019.

The Seminar Program traditionally included a wide range of problems of Neutron Physics: promising neutron sources, fundamental properties of a neutron, fundamental interactions in the reactions with neutrons, nuclear fission, ultracold neutrons, as well as application of analytical methods in archaeology, material science, ecology and life sciences.

The Conference was of interest to more than 120 participants from physical centers of Albania, Azerbaijan, Belarus, Bulgaria, China, Czechia, Egypt, France, India, Iran, Kazakhstan, Moldavia, Romania, Russia, Serbia, Spain, Sweden, USA and Vietnam. From Russia, the declared reports were presented by physicists from the Institute of Physics and Power Engineering (IPPE) and the Medical Radiological Research Center (MRRC), Obninsk, the Moscow National Research Center "Kurchatov Institute" (NRC KI) and the Institute of Theoretical and Experimental Physics (ITEP) of NRC KI, Petersburg Nuclear Physics Institute (PNPI) of NRC KI, Gatchina, Institute for Nuclear Research of RAS, Troitsk, and from the Frank Laboratory of Neutron Physics and Flerov Laboratory of Nuclear Reactions, JINR, Dubna (see the ISINN-28 program and the introduced presentations in http://isinn.jinr.ru/past-isinns/isinn-28/program.html).

We have the opportunity to publish in the Seminar Proceedings only the reports received from authors to the appointed dead-line.

V.N. Shvetsov,
Co-Chairman of ISINN-28

Neutron Facilities & Advanced Neutron Sources and Perspective Experiments

Development of Transportable Accelerator-Driven Neutron Source in XJTU

S. Wang *, H.P. Li, X.B. Li, B.L. Ma, S.H. Yang, Y.S. Lv, Z.P. Qiao, Y.C. Hu,
Q.X. Jiang, J.Q. Hu

School of Nuclear Science and Technology, Xi’an Jiaotong University, Xi'an, 710049, China

* *E-mail: shengwang@xjtu.edu.cn*

1. Introduction

Neutrons have been widely used in many applications, such as Boron Neutron Capture Therapy (BNCT), neutron imaging, neutron scattering research, and so on [1]. Due to the low cost, small size, short construction time, and acceptable neutron yield for many purposes, the development of Compact Accelerator-driven Neutron Source (CANS) technology has progressed worldwide in recent years. And outdoor neutron non-destructive testing is likely to be realized by developing a Transportable Accelerator-driven Neutron Source (TANS) based on existing CANS facilities for some specific situations, like bridge and road detection. The project of TANS in Xi’an Jiaotong University (XJTU) has been carried out. The progress about compact accelerator, target design, shielding structure and neutron backscattering radiography system is stated as follow. And the layout of every consistence is shown in Fig. 1.

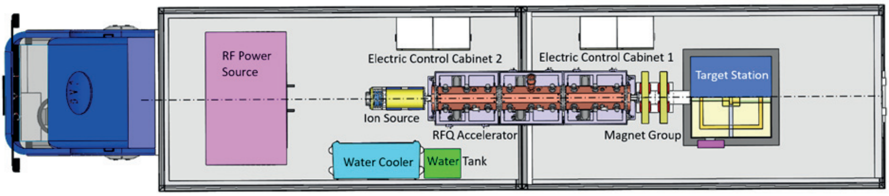

Fig. 1. Structure of the TANS.

2. RFQ accelerator

The four-vane RFQ accelerator has been adopted as its compact structure and high transmission efficiency. The whole accelerator system consists of RFQ cavity, RF power source, cooling machine, vacuum as well as generator. To reduce the costs and size of the accelerators system as much as possible, the working frequency of 325MHz has been selected with compromise between power consumption, cavity size and weight, as well as feasibility of construction. The RFQ was designed to accelerate the proton beam with peak current of 12mA to 2.5MeV in the acceleration efficiency above 93.2%. The RFQ length and weight were 2.6m and 1.5t, respectively. And the structure of RFQ accelerator for TANS is shown in Fig. 2.

3. Target design

We chose the ^{7}Li (p, n)^{7}Be reaction, in which lithium (Li) rather than beryllium (Be) was used as the target material due to its relatively higher neutron yield. Aiming at minimization on reduction in neutron attenuation and sufficient cooling, we proposed a new cooling configuration for a target featuring edge-cooling without flowing water in the back side to be applicable for TANS, which is shown in Fig.3. Based on the simulation by Monte Carle code and finite element method software, the effect on neutron attenuation and cooling effect have been evaluated, and the structure and size are optimized.

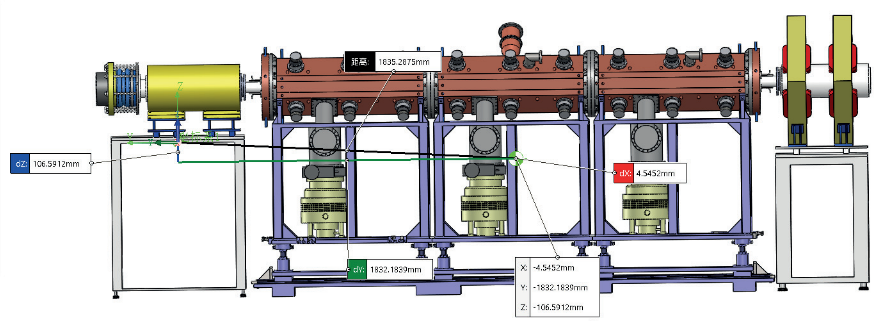

Fig. 2. Structure of RAQ accelerator for TANS.

Table.1. Parameter of RFQ accelerator for TANS

Frequency [MHz]	325
Beam current [mA]	12
W_{out} [MeV]	2.5
Input Nor. Rms emit. [mm·mrad]	0.10
Inter-vane voltage [kV]	65
Max. modulation	2.49
Max. phase [deg]	-19.0
Peak electric field [MV/m]	24.03
Kp factor	1.35
Electrode length [m]	
Average aperture [mm]	3.746
Minimal aperture [mm]	2.01
Trans. (PARMTEQM) [%]	98.1
Acc (PARMTEQM) [%]	93.2

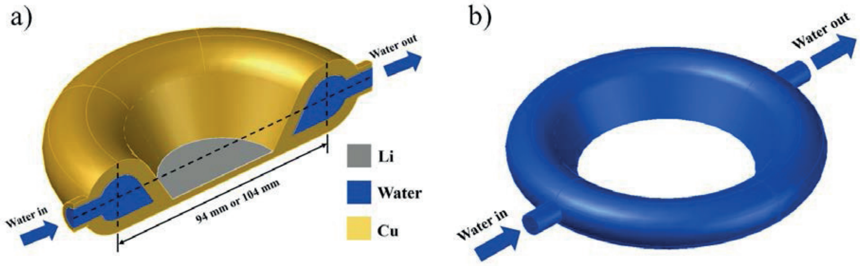

Fig. 3. Edge-cooling target: (a) vertical cross section; (b) perspective drawing to show the cooling water flowing.

4. Shielding structure

We optimized the reflector and the shielding design of the target station for TANS. A high-performance reflector material was selected by comparing a number of candidates, which aimed at enhancing the fast neutron intensity for the non-destructive testing. A compact and light-weight shielding design was optimized through a multi-objective optimization way based on NSGA-MC [2]. The target station of TANS is shown in Fig. 4.

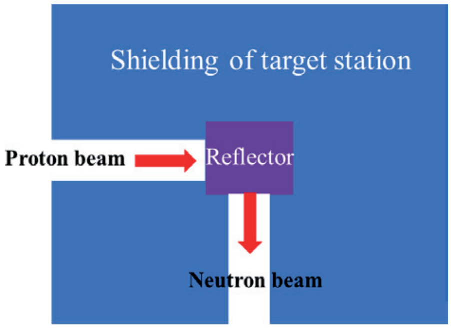

Fig. 4. Shielding structure of TANS

5. Neutron Backscattering Radiography System Based on TANS

TANS is a potential tool for infrastructure NDT, while the neutron backscattering radiography (NBR) is almost the only way to apply that. Our group has been committed to the development of TANS, and make important breakthroughs in key systems. Upper picture of Fig. 5 shows the structure of TANS backscattering radiography system. The source uses 2.5MeV proton and solid lithium target. Bottom picture of Fig. 5 shows energy spectrum of the neutron source.

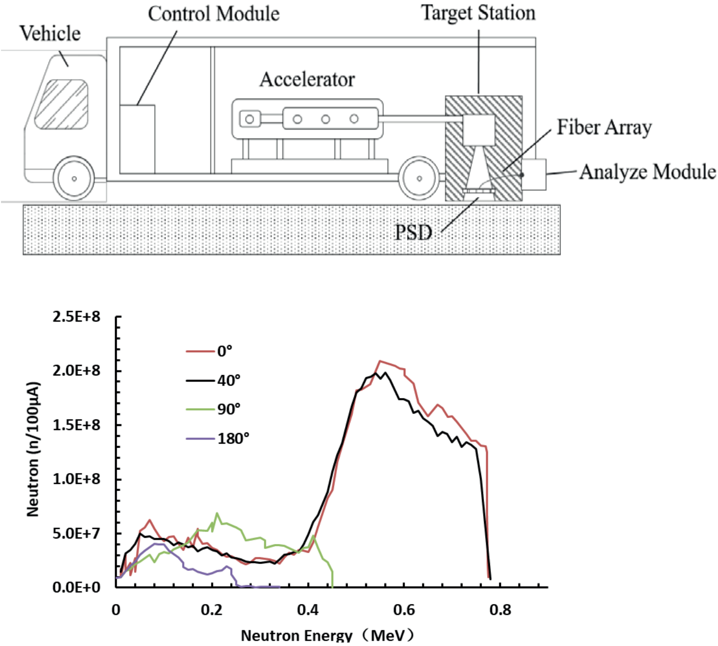

Fig. 5. Structure of TANS NBR system. Upper picture –system structure, bottom picture – energy spectrum.

NBR can effectively distinguish the defects, especially void and water gap. Fig. 6 shows the simulation results of defects detection. Defects depth is 10cm, size is 5×5×5cm. Detector size is 30px×30px, pixel size is 0.5cm. Water can reflect more thermal neutron than other material, while void can hardly reflect neutron, thus, NBR can distinguish void and water by means of backscattering neutron flux and energy.

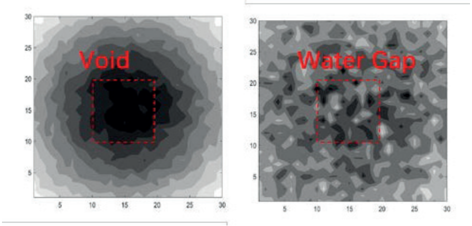

Fig. 6. NBR simulation of void and water defects.

References

[1] L. Xu, W. Schultz, C.Huiszoon, Petrophysics 51(3), 184 (2010).

[2] Ma B., Song L., Yan M., et al., Multi-objective Optimization Shielding Design for Compact Accelerator-driven Neutron Sources by Application of NSGA-II and MCNP[J].IEEE Transactions on Nuclear Science, 2020, PP(99):1-1.

Neutron Detection & Methodical Aspects

CHARACTERISTICS OF POSITION-SENSITIVE PLASTIC SCINTILLATION DETECTORS

S.B. Dabylova[1,2,3,*], N. Simbirtseva[1,3], D.N. Grozdanov[1,4], N.A. Fedorov[1.5], A. Yergashov[1,2,3], I.D. Dashkov[1,5], Yu.N. Kopatch[1], P.V. Sedyshev[1], I.N. Ruskov[4], V.R. Skoy[1], T.Yu. Tretyakova[1,5], and TANGRA collaboration

[1]*Joint Institute for Nuclear Research, Dubna, Russia*
[2]*L.N. Gumilyov Eurasian National University, Nur-Sultan, Kazakhstan*
[3]*Institute of Nuclear Physics, Almaty, Republic of Kazakhstan*
[4]*Institute for Nuclear Research and Nuclear Energy, Bulgarian Academy of Sciences, Sofia, Bulgaria*
[5] *Lomonosov Moscow State University, Moscow, Russia*

*dabylova_saltanat@mail.ru

Abstract

This work is devoted to the calibration of plastic scintillation detectors and comparison of their parameters. Long plastic detectors with photomultiplier tubes (PMT) at both ends were chosen for the study. The choice stems from the goal of obtaining position resolution using time information from both PMTs.

The measurements were carried out for two types of detectors with the same dimensions (5×10×100 cm). The first type is a plastic detector manufactured by EPIC CRYSTAL, Shanghai, China. It has a PMT model CR105 from HAMAMATSU. The second type is a plastic detector manufactured by ELJEN TECHNOLOGY, USA. It is equipped with a PMT model ETEL 9266KEB from ELECTRON TUBES.

The purpose of this study was to determine the main characteristics and optimal operating conditions of the detection system. The tests were carried out with ^{137}C and ^{60}Co gamma radiation sources. A digital signal recorder DSR-2/32, was used for data collection and preliminary analysis.

1. INTRODUCTION

At the Joint Institute for Nuclear Research (JINR, Dubna, Russia), within the framework of the TANGRA project (TAgged Neutrons and Gamma RAys) [1], experiments on the study of inelastic scattering of fast neutrons are continuing [2]. Various types of detectors are used to study reactions with neutrons, including plastic scintillators.

Plastic scintillators are often used in measurements with neutrons, most often using the time-of-flight technique [3,4]. This is due to a number of advantages that these detectors have: fast response, low cost, and the ability to manufacture a scintillator of almost any shape and volume.

Long plastic detectors with PMTs at both ends of the detector were chosen for the study. For the first time a detector with such characteristics was used by Charpak G. et al. [5]. The choice is due to the goal of obtaining positional resolution using time information from both PMTs.

The purpose of this study was to determine the detector characteristics (the time, position response, the attenuation length of light in the scintillator) and to select the PMT optimal voltage.

2. DESCRIPTION OF DETECTORS AND RESEARCH METHODS

The measurements were carried out for two types of detectors with the same overall dimensions (5×10×100 cm). The first type is a plastic detector manufactured by EPIC CRYSTAL, Shanghai, China [6]. It has a PMT, model CR105, from HAMAMATSU [7]. The second type is a plastic detector manufactured by ELJEN TECHNOLOGY, USA [8]. It is equipped with a PMT model ETEL 9266KEB, from ELECTRON TUBES [9]. A photo of the detectors and their schematic view are shown in Fig. 1 and 2, respectively.

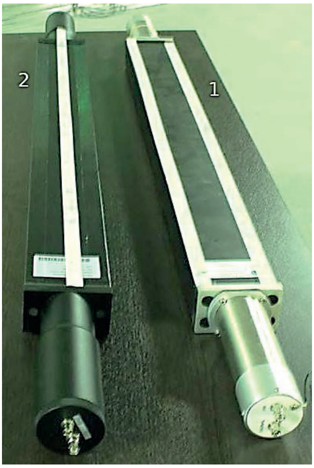

Fig. 1. Plastic scintillation detectors from ELJEN TECHNOLOGY (1), and EPIC CRYSTAL (2).

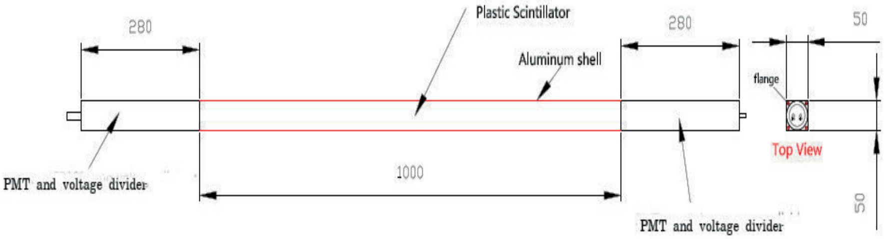

Fig. 2. The schematic view of the studied detectors [6].

The tests experiments were carried out with ^{137}Cs and ^{60}Co point-like gamma-ray sources. The digitizer DSR-2/32 was used for data collection and preliminary analysis.

The selection of the optimal voltage on the PMT was carried out using the point sources, which were alternately placed in the center (at the same distance from each PMT) in front of the detector. The spectra obtained in the experiment with a ^{60}Co source are shown in Fig. 3.

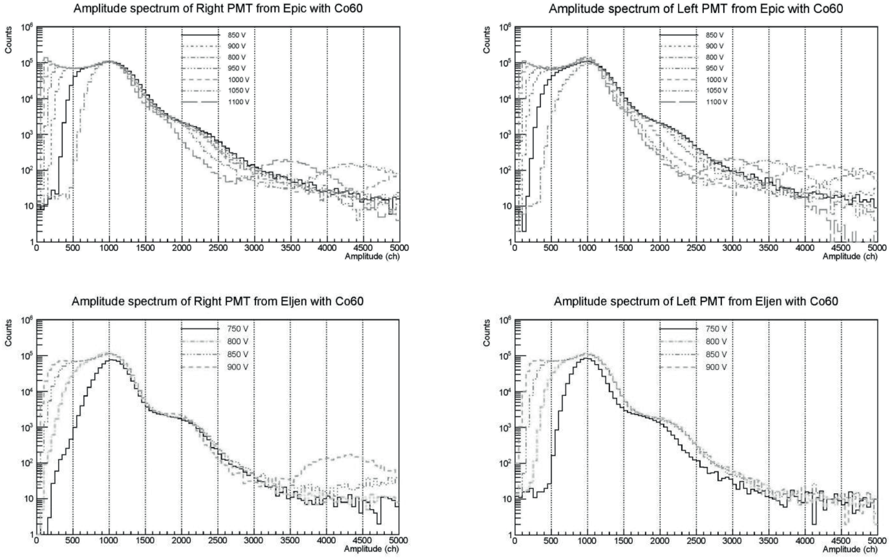

Fig. 3. Amplitude spectra of the right and left photomultipliers from the EPIC CRYSTAL and ELJEN TECHNOLOGY detectors.

Further, to study the characteristics of the detector, depending on the place of interaction of gamma radiation with the scintillator and select the optimal parameters of the system in the desired mode, the concept of "position coordinate" (or X coordinate) of the particle's passage through the detector is introduced. It can be obtained from the time difference between the signals received from the left (T_L) and right (T_R) PMT [3]:

$$X \sim (T_L - T_R). \tag{1}$$

In addition, the necessary input value is Q_{GM} – an integral charge, which is proportional to the energy of the incident particle. It is calculated as the geometric mean between two signals from the PMTs, practically does not depend on the hit position [10] and can be used as particle energy:

$$Q_{GM} = \sqrt{Q_L Q_R}, \tag{2}$$

where Q_L and Q_R are signals from the left and right photomultipliers, respectively.

The example of obtained amplitude spectra one can see on figure 4.

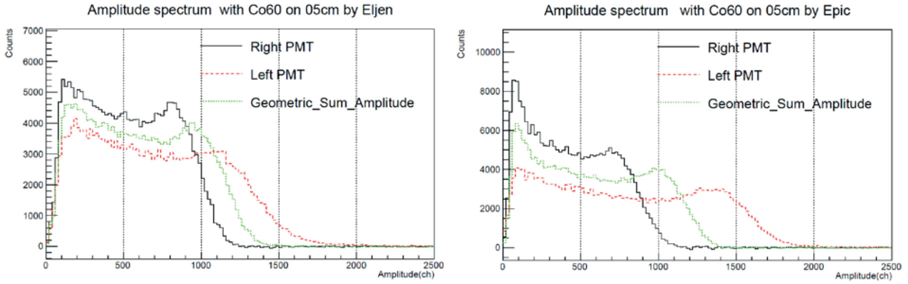

Fig. 4. Amplitude spectra of the right and left PMTs and their geometrical sum from the ELJEN TECHNOLOGY (left) and EPIC CRYSTAL (right) detectors.

Using the above expressions (1, 2), the time resolution was obtained. In figure 5, one can see examples of time spectra with EPIC detectors at a voltage of 950 V (with a threshold of 100 keV (a) and 700 keV (b)) and ELJEN detectors at a voltage of 850 V (with a threshold of 100 keV (c) and 700 keV (d)).

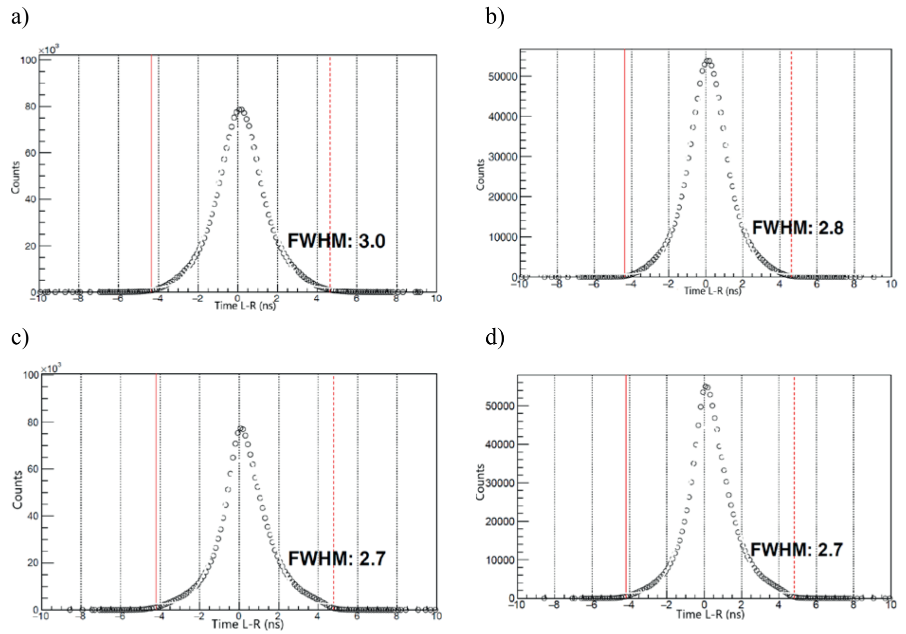

Fig. 5. Time spectra (T_L-T_R) for detectors: EPIC at a voltage of 950 V and an interaction threshold E_{thr} = 100 keV (a), E_{thr} = 700 keV (b) and ELJEN at a voltage of 850 V and an interaction threshold E_{thr} = 100 keV (c), E_{thr} = 700 keV (d).

The full width at half maximum (FWHM) was determined for each peak in the time spectrum at different voltages applied to the PMT. The obtained values include the contributions from the signal delay by the registering electronics and PMT. Figure 6 shows the FWHM dependence of the time peak on the PMT voltage for the EPIC and ELJEN detectors at the threshold of 100 and 700 keV. The data obtained were used to select the optimal voltage parameters for the detectors.

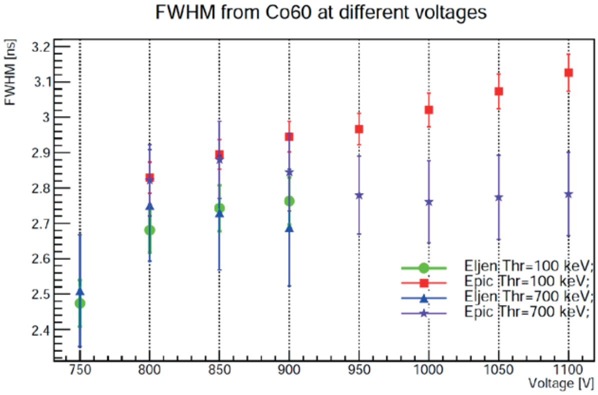

Fig. 6. FWHM of the time peak versus PMT voltage for the EPIC and ELJEN detectors with thresholds 100 and 700 keV.

Additional measurements were carried out with point radiation sources to obtain information about the interaction position or the X coordinate of the particle and other detector characteristics. During the experiment, γ-quanta from ^{137}Cs and ^{60}Co radioactive sources were collimated with lead bricks. The source and collimator assembly were moved along the length of the plastic detector with a step of ~ 14–15 cm (Fig.7).

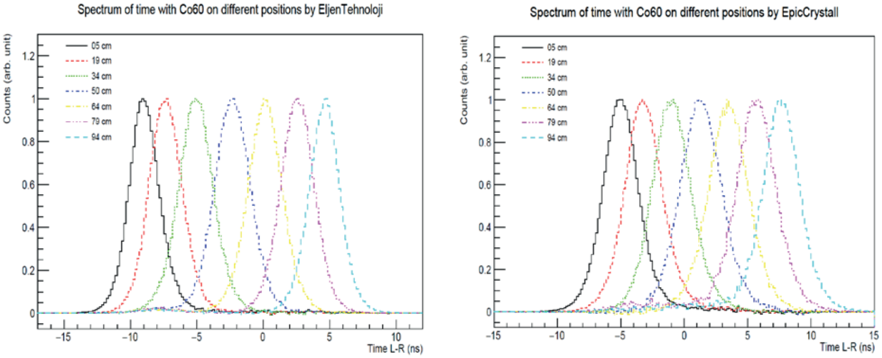

Fig. 7. The time difference spectra, obtained with ^{60}Co radioactive sources and collimator assembly for various distances of the exposed part from one end by the ELJEN (left) and EPIC (right) detectors.

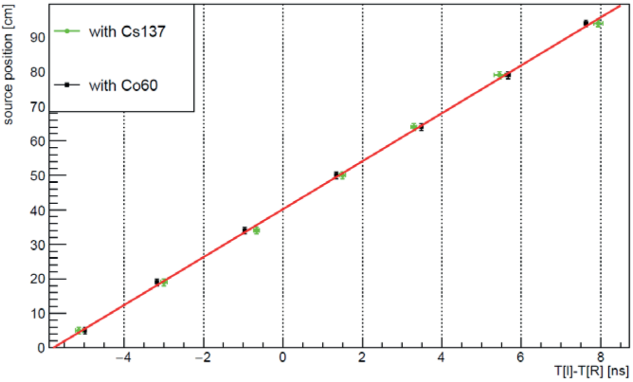

Fig. 8. Measured time difference versus the position of the radiation source for the EPIC detector. Experimental data were obtained with a ^{60}Co source (squares) and with a ^{137}Cs source (circles). The solid line is the fit of a linear function to the experimental data.

As can be seen from Fig. 8 (example of experimental data obtained with the EPIC detector), the dependence of $(T_L\text{-}T_R)$ on the source position is linear. The obtained dependence was used to determine the position resolution of the both detectors (Fig. 9).

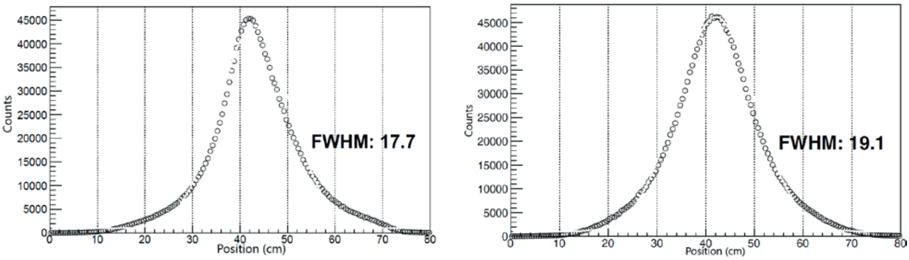

Fig. 9. Position resolution for ELJEN (left) and EPIC (right) detectors measured with a γ ray beam from a ^{60}Co point source collimated using appropriately placed lead bricks to illuminate a 0.5 cm wide portion of the plastic scintillator.

Another quantity characterizing the detector is the attenuation length of light in the scintillator (λ), determined from the exponential decay of the amplitude of the scintillation burst signal A with distance x [11]:

$$A(x) = Aexp\left(\frac{-x}{\lambda}\right). \tag{3}$$

Figure 10 shows the experimental amplitudes of the scintillation burst signals depending on the position of a ^{60}Co point source for ELJEN and EPIC detectors.

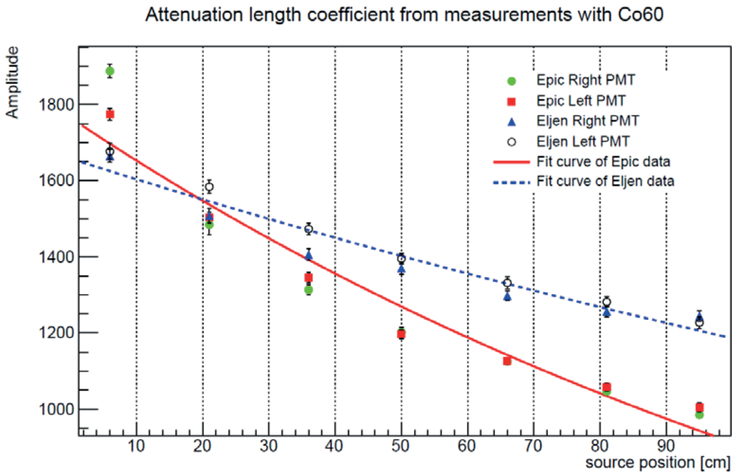

Fig. 10. Experimental amplitudes of scintillation burst signals as a function of the position of a ^{60}Co point source for ELJEN and EPIC detectors.

Then, using exponential approximation according to dependence (3), the values of the attenuation length of light in the scintillator for each of the detectors were obtained.

3. CONCLUSION

The article discusses the features of working with long plastic detectors from two different manufacturers – EPIC and ELJEN, their main characteristics are obtained. Calibration was carried out using ^{137}Cs and ^{60}Co point sources.

As a result of the study: the average time resolution obtained for EPIC detector was ~ 2.9 ns and for ELJEN ~ 2.5 ns. The uncertainty of the position coordinate (position resolution) was ~ 19.1 cm for EPIC and ~ 14.7 cm for ELJEN detectors. The obtained values of the light attenuation length in the scintillator were 151.5±2.1 cm for EPIC and 298.3±9.3 cm for ELJEN detectors.

In the future, it is planned to continue studies of the characteristics of detectors with a portable neutron generator ING-27.

REFERENCES

1. TANGRA Project, http://flnph.jinr.ru/en/facilities/tangra-project.
2. S.B. Dabylova, Yu.N. Kopatch, N.A. Fedorov, et al , Eurasian Journal of Physics and Functional Materials 5/1 (2021)15-23, https://doi.org/10.32523/ejpfm.2021050102.
3. P.C. Rout, D.R. Chakrabarty, V.M. Datar, Suresh Kumar, E.T. Mirgule, A. Mitra, V. Nanal, R. Kujur, A large area plastic scintillator detector array for fast neutron measurements, Nuclear Instruments and Methods in Physics Research Section A: Accelerators, Spectrometers, Detectors and Associated Equipment, Volume 598, Issue 2, 2009, Pages 526-533, ISSN 0168-9002, https://doi.org/10.1016/j.nima.2008.09.034.

4. Sukanya De, G. Mishra, R.G. Thomas, Ajay Kumar, A. Mitra, B.K. Nayak, Proc. of the DAE Symp. on Nucl. Phys. 64 (2019)451, http://www.sympnp.org/proceedings/64/B66.pdf
5. Charpak G., Dick L., Feuvrais L., Nucl. Instr. and Meth. 15 (1962) 323.
6. https://www.epic-crystal.com
7. https://www.hamamatsu.com
8. https://eljentechnology.com/
9. http://courses.washington.edu/phys433/equipment/electrontubes_9266B.pdf
10. L. Karsch, A. Böhm, K.-Th. Brinkmann, L. Demirörs, M. Pfuff, Design and test of a large-area scintillation detector for fast neutrons, Nuclear Instruments and Methods in Physics Research Section A: Accelerators, Spectrometers, Detectors and Associated Equipment, Volume 460, Issues 2–3, 2001, Pages 362-367, ISSN 0168-9002, https://doi.org/10.1016/S0168-9002(00)01072-X.
11. S.A. Bunyatov, A.V. Krasnoperov, Yu.A. Nefedov, B.A. Popov, V.V. Terechshenko, N.I. Bozhko, A.S. Vovenko, V.N. Goryachev, Yu.I. Salomatin, V.A. Senko, A.V. Sidorov, Calibration of Scintillation Counters in the Upgraded Calorimeter of the IHEP-JINR Neutrino Detector for Particle Identification by Time-of-Flight Measurements (in Russian).

Reconstruction of HPGe Detector Modeling for Efficiency Calibration

Zhang Changfan*, Hu Guangchun, Zeng Jun, Xiang Qingpei, Gong Jian

China Academy of Engineering Physics, Institute of Nuclear Physics and Chemistry, Mianyang city 621900, China

High purity germanium (HPGe) detector is a prior choice for determining the activity of the radioactive samples for nuclear diagnostics of Inertial Confinement Fusion (ICF) experiments. Efficiency calibration of gamma rays at a close distance from the surface of an HPGe detector is a crucial issue. So far as the detector structure is precisely clarified, a model of the detector can be well developed, based on which Gamma-ray detection efficiencies can be calculated accurately using Monte Carlo method. In this paper, internal geometry and structure except for dead layers of the HPGe detector is obtained by X-ray radiography and 3D reconstruction. The optimal dead layers of the germanium crystal are determined by tracing the minimal sum squared residual (SSR) of gamma-ray efficiencies between calculations and measurements for standard planar sources.

Keywords HPGe detector, Efficiency calibration, MC modeling, Nuclear diagnostics

1. Introduction

Nuclear diagnostics of inertial confinement fusion (ICF) experiments are critical to achieve ignition at a facility such as National Ignition Facility and Shenguang-III Laser Facility [1–4]. A key nuclear diagnostic is the detection of radiochemical samples following implosions [5–9]. The radiochemical samples can provide quantitative data on capsule performance parameters such as fuel areal density, neutron yield, neutron energy spectral information and so on [10–13]. The radiochemical samples, i.e. diagnostic indicators, come from materials which originally either present naturally in the capsule or doped specifically into the capsule. Iridium and Scandium are such essential indicators specifically doped into the capsule to diagnose ignition failures on National Ignition Campaign targets [14–15]. Reactions of ^{191}Ir(n,2n)^{190}Ir, ^{191}Ir(n,3n)^{189}Ir, ^{45}Sc(n,2n)^{44}Sc, and ^{45}Sc(n,2n)^{43}Sc provide radiochemical signatures over the high regime of incident neutron energy. The activity of the radioactive products can be determined by emitted gamma rays. However, this capability is limited by the amounts of the isotopes loaded inside the capsule without affecting performance and the collection efficiency of the capsule debris after implosion. High purity germanium (HPGe) detector is a prior choice for determining the activity of these radioactive samples because of its superior energy resolution. Anyway, the efficiency is quite limited for gamma-ray detection of HPGe detector compared with other kinds of detectors. Decreasing the distance between detector window and radioactive source is helpful to solve the dilemma. Therefore, efficiency calibration of gamma rays at a very close distance from the surface of an HPGe detector is a crucial issue. Considering the problem of the coincidence at a close distance, it is very important to construct a precise model of the HPGe detector. Therefore, gamma-ray efficiencies can be calculated accurately at an arbitrary distance from the surface of an HPGe detector using Monte Carlo method as long as the detector model is confirmed.

In recent years, radiography technologies such as CT scan or collimated gamma-ray scan are employed to reconstruct a very precise model for HPGe detectors [16–20]. Dead layers of the germanium crystal are also determined by standard radioactive sources [21,22].

In this paper, we focus on the precise modeling of an HPGe detector for efficiency calibration for the further diagnostics of ICF. Internal geometry and structure except for dead layers of the HPGe detector is obtained by X-ray radiography and 3D reconstruction. Several planar sources are utilized to calibrate the efficiencies at a certain distance from the surface of the HPGe detector window. Dead layers of the germanium crystal are determined by tracing the minimal sum squared residual of gamma-ray efficiencies between the calculations and the measurements. Nonuniform distribution of the dead layer is supposed and the corresponding model improves the accuracy of the calculated efficiencies.

2. Experiment and Methods

2.1 Apparatus

An HPGe detector is utilized to calibrate the efficiency. The detector is installed in a shielding chamber of lead. The nominal relative efficiency of this detector is 40% compared to a 3 inch × 3 inch NaI (Tl) crystal as measured at 1333 keV. The resolution of the detector is 1.88keV @ 1332keV of the ^{60}Co gamma-ray energy. The detector is connected to a Digi-multichannel analyzer, in which the pre-amplifier is integrated. The high voltage is set to positive 3050V and the rise-time is 8.00 μs. The course gain and fine gain are set as 20 and 1.18, respectively. Spectra are recorded over 16384 channels up to the energy level of 2 MeV. A Canberra Genie 2000 software (Version3.1.4) is used to acquire gamma-ray spectra.

2.2 Standard source

Several standard planar sources ^{241}Am, ^{60}Co, ^{133}Ba, ^{152}Eu and ^{166}Ho are utilized for the efficiency calibration. The sources are titrations of the radioactive solution on the filter paper, sealing within a PMMA container each. The radius of each filter paper is 18 mm. The uncertainty of the activity for each source is certified 2%.

2.3 Measurement

Each standard source is placed on a PMMA bracket which is set on the detector. The distance between the source and the detector window is 9.20 cm. The measurement layout is illustrated in Fig. 1.

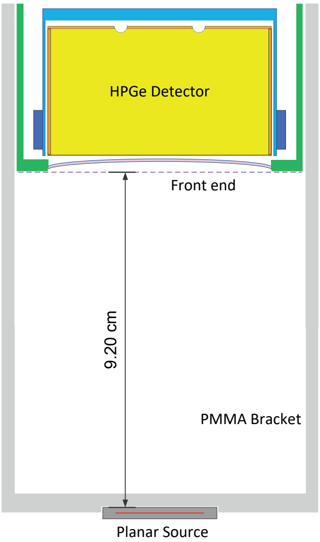

Fig. 1. Efficiency calibration for the planar sources at the distance of 9.20 cm between the source and the detector window.

The counting dead time ranges from 0.2% to 6.2%, depending on the activity of the source, which is consequently corrected during counting. The acquisition time, corresponding to at least 10^5 counts in the full energy peak, is sufficient to assure good counting statistics. The energy ranges from 59 keV to 1408 keV. The efficiency of the full energy peak $\varepsilon(E_i)$ is calculated by the following function:

$$\varepsilon(E_i) = \frac{S(E_i)}{A\eta(E_i)t_{live}}.$$

Here $S(E_i)$ is the full energy peak area of the peak E_i, A is the activity of the standard source, $\eta(E_i)$ is the intensity of the peak E_i, t_{live} is the live time of the measurement.

The measured efficiencies for gamma rays at a distance of 9.20 cm from the detector window is shown in Fig. 2.

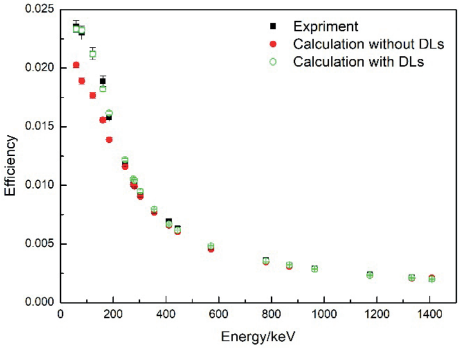

Fig. 2. The measured efficiencies (black squares) and calculated efficiencies (red circles and green hollow circles) for gamma rays at a distance of 9.20 cm from the detector window.

2.4 Radiography for MC modeling

Even though dimension of the detector is always provided by the manufacturer (not the case for this HPGe detector), the discrepancies between the nominal values and the actual values always exist. To obtain a reliable model, X-ray radiography and 3-D reconstruction illustrated in Fig. 3 were performed to determine the detector's precise dimensions. The geometrical structure and corresponding parameters of the detector, listed in Table1 and displayed in Fig. 3, are used for MC modeling.

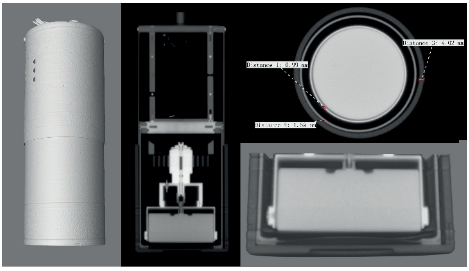

Fig. 3. X-ray radiography and the 3-D reconstruct of the detector.

Table 1 Parameters of the HPGe detector

Structure	Material	Density/g/cm^3
Crystal	high purity germanium	5.32
Beryllium window	beryllium	1.85
Inner lateral cap	copper	8.96
Fastening belt	copper	8.96
External lateral cap	aluminum	2.70

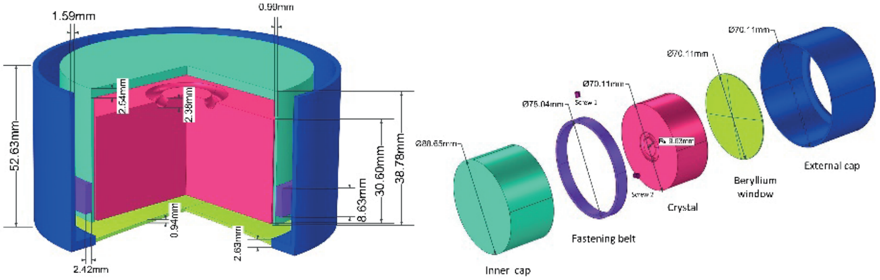

Fig. 4. Geometry parameters of the HPGe detector.

In the radiography, several geometrical subtle details are revealed. For instance, there is a circinate groove on the rear of the germanium crystal, the beryllium window is not flat, and the PMMA bracket is not homocentric with the crystal. All these details mentioned above, in Fig. 5, are considered in model reconstruction. However, it is worthy to note that the crystal dead layer (DL) thickness cannot be obtained by X-ray radiography. Determination for the DL thickness will be discussed in the latter section.

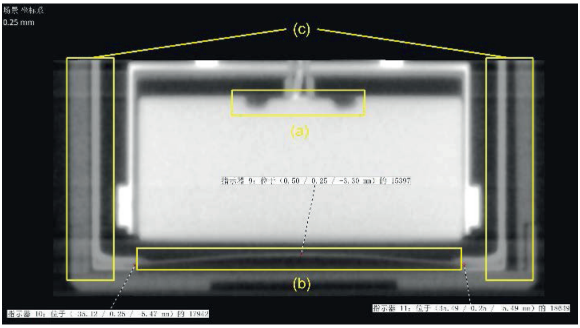

Fig. 5. Geometric subtle details are revealed in the X-ray radiography, such as (a) a groove on the rear crystal, (b) curving beryllium window, and (c) non-central symmetric PMMA bracket.

The gamma-ray measurement model, which contains the HPGe detector, the PMMA bracket and the standard source, was constructed by MCNP5 code [21]. The calculated efficiencies without DLs are shown as red dots in Fig. 2. The relative deviations between calculated efficiencies without DLs and measured ones are shown in Fig. 6(a). The results indicate that dead layers are needed to be considered.

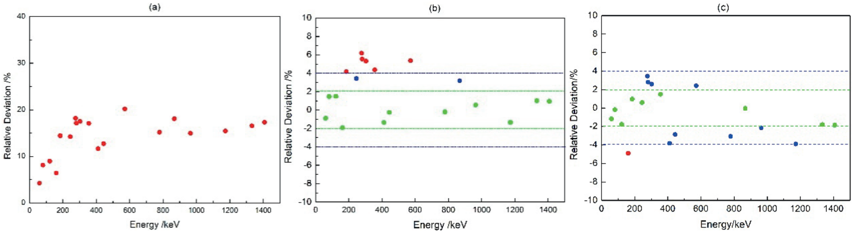

Fig. 6. Deviation of gamma-ray efficiencies between experiments and calculations (a) without DLs (b) with DLs and (c) with corrected DLs.

2.5 Determination for thicknesses of DLs

Here sum squared residual (SSR) of gamma-ray efficiencies is employed to calculate the optimal thicknesses of DLs:

$$SSR = \sum_{Ei<200keV} (\varepsilon_{cal,Ei} - \varepsilon_{\exp,Ei})^2 ,$$

where $\varepsilon_{cal,Ei}$ and $\varepsilon_{\exp,Ei}$ are the calculated efficiency and the measured efficiency at the energy E_i, respectively. The optimal DLs will minimize the SSR of gamma-ray efficiencies.

Because low-energy gamma rays are hard to penetrate the crystal and the efficiencies of them are sensitive to the thicknesses of the front-end and lateral DLs. Determination for the thicknesses of front-end and lateral DLs of the crystal can take advantage of the low-energy gamma rays. Likewise, determination for the thickness of the back-end DL can take advantage of high-energy gamma rays.

Determination for the optimal thicknesses of front-end and lateral DLs relies on 59 keV @ ^{241}Am, 81 keV @ ^{166}Ho, 121 keV@^{152}Eu and 160 keV@^{133}Ba. The *SSR* contour of low-energy gamma-ray efficiencies at different thicknesses of front-end and lateral DLs are shown in Fig. 7. Here the initial thicknesses of front-end and the lateral DLs are set as 0.001 cm and 0.04 cm, respectively. And the steps of front-end and the lateral DLs are set as 0.001 cm and 0.01 cm, respectively. Specially, the front-end DL is also set as 0.00001 cm and relevant calculations are shown in Fig. 7. The corresponding abscissa for the front-end Dl of 0.00001 cm is labeled as 0.000 cm.

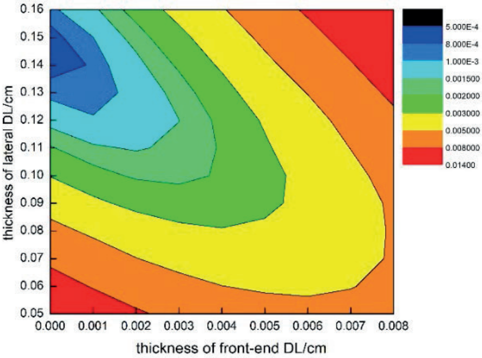

Fig. 7. *SSR* contour of low-energy and medium-energy gamma-ray efficiencies as thicknesses of front-end and lateral DLs varying.

The contour shows that the optimal DLs have a thicker lateral DL (ranges from 0.14 cm to 0.15 cm) and a very thin frontend DL (0.00001cm). Relative deviations of between measured efficiencies and calculated ones with the DLs mentioned above are listed in Table 2. These thicknesses of front-end and lateral DLs are both appropriate because the relative deviations are all within the uncertainties of the experiment results.

Table 2 Relative deviations of efficiencies between experiments and calculations

Energy/keV	Eff_{exp}	Thicknesses of the front-end/lateral DLs/cm	
		0.00001/0.14	0.00001/0.15
59.541	2.356E-02(2.1%)	-0.9%	-1.4%
80.586	2.301E-02(2.5%)	1.5%	1.0%
121.783	2.123E-02(2.4%)	1.6%	1.1%
160.613	1.889E-02(2.4%)	-1.2%	-1.8%

To pin the optimal thickness for the lateral DL, the backend DL is engaged and efficiencies of different gamma-ray regions are calculated. The contours (Fig. 8) are SSR of a) low-energy gamma-ray (<=160 keV), b) medium-energy gamma-ray (160 keV~1000 keV), and c) high-energy gamma-ray (>1000 keV) efficiencies as the lateral and back-end DLs change, respectively. The initial lateral and back-end DLs are set as 0.13 cm and 0.12 cm, respectively. The steps of the lateral and back-end DLs are set as 0.01 cm and 0.02 cm, respectively.

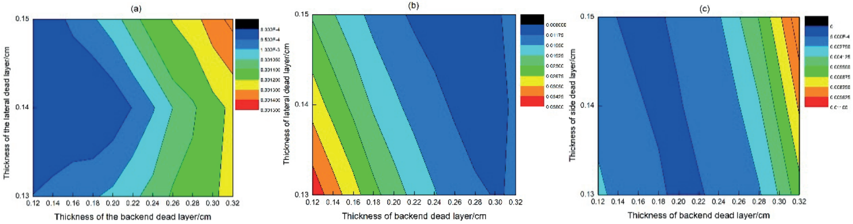

Fig. 8. SSR contours of a) low-energy gamma-ray, b) medium-energy gamma-ray and c) high-energy gamma-ray efficiencies as the lateral and backend DLs varying.

The low-lying overlap in SSR contours of low-energy (Fig. 8(a)) and high-energy (Fig. 8(c)) gamma-ray efficiencies locates at the lateral DL of 0.14 cm and the backend DL of 0.18 cm. While the optimal DLs for medium-energy gamma-ray efficiencies trend to be thicker (Fig. 8(b)). Relative deviations of gamma-ray efficiencies between experiments and calculations for the case of the lateral DL at 0.14 cm and the backend DL at 0.18 cm is illustrated in Fig. 6(b). It shows that points of calculated efficiencies are within 2% deviation compared with ones of the measurements for the low and high-energy rays, while most points of calculated efficiencies are beyond 4% than those of the measurements for medium-energy rays. It can be deduced that the lateral DL which affects the medium-energy gamma-ray efficiencies sensitively should be thicker than the current value.

However, increasing thickness for the whole lateral DL will decrease efficiencies for low-energy gamma rays. Since the optimal front-end DL is very thin (0.00001 cm) it is hard to be decreased again to fit a thicker lateral DL for the low-energy gamma rays.

To solve the problem, the lateral DL is modified to have a non-uniform thickness. Considering the locations of fastening belt and the screws, the vicinity electric field in the crystal will be changed. The position of a new-added lateral DL is fixed at the same height of the fastening belt and is adjacent to the original lateral DL (Fig. 9). The thickness (*d*) and the width (*L*) of the new-added DL are optimized by the minimal SSR of the medium-energy gamma-ray efficiencies. The initial values of *d* and *L* are set as 0.02 cm and 0.2 cm, respectively. The steps of *d* and *L* are set as 0.02 cm and 0.2 cm, respectively. The SSRs of low-energy and high-energy gamma-ray efficiencies are also calculated. The SSR contours for different energy range of gamma-rays are shown in Figure 10.

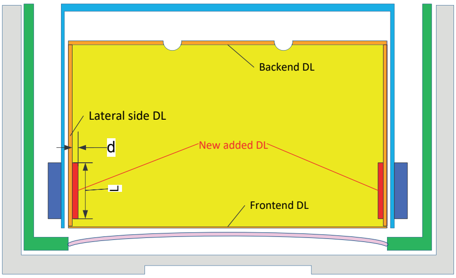

Fig. 9. Distribution of dead layers in the crystal.

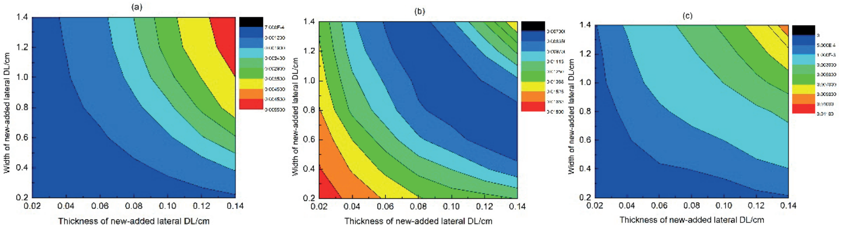

Fig. 10. SSR of a) low-energy gamma-ray, b) medium-energy gamma-ray and c) high-energy gamma-ray efficiencies as the thickness and the width of the new-added lateral DL varying.

The new-added lateral DL pined at *d* of 0.14 cm and *L* of 0.6 cm improves the minimal SSR of medium-energy gamma rays from less than 0.017(Fig.8(b)) to less than 0.00835 (Fig.10(b)). While this new-added DL increases the SSRs of low-energy and high-energy gamma rays. Relative deviations of efficiencies between calculations and experiments are shown in Fig. 6(c). The calculated efficiencies of MC model with corrected DLs are shown as green hollow circles in Fig. 1. Fig. 6(c) shows that almost all calculated efficiencies fall within 4% interval except one for 160 keV gamma ray. The reason of the exception may attribute to the weak SNR (signal to noise ratio) which is less than 0.18.

Compared with the MC model without any DLs (Fig. 6(a)), MC model with corrected DLs (Fig. 6(c)) improves the calculated efficiencies tremendously. Compared with the model with initial DLs (Fig. 6(b)), the model with corrected DLs eliminates offset of the calculated efficiencies, and makes the calculated efficiencies distribute equally around the measured ones within 4% interval.

3. Conclusion

A precise model of HPGe detector for efficiency calibration is constructed here. The geometric dimension and detailed subtle structures such as circinate groove on the rear end of the germanium crystal, the curving beryllium window, and the non-homocentric PMMA bracket are accurately determined by X-ray radiography. DLs of the germanium crystal is determined by tracing the minimal SSR of gamma-ray efficiencies. Nonuniform distribution of the lateral DL is supposed and the corresponding model improves the accuracy of the calculated efficiencies.

Acknowledgement

Special thanks to Li Shigeng of Institute of Applied electronics, China Academy of Engineering Physics for the X-ray radiography and 3-D model reconstruction.

Funding. This work was supported by the National Natural Science Foundation of China (No. 11905198).

References

1. E. Moses, The national ignition facility (NIF) and the National Ignition Campaign (NIC), LLNL-CONF-417770[R], Lawrence Livermore National Laboratory, 2009.
2. Jiang Shaoen, Ding Yongkun, Liu Shenye, et al. Recent inertial confinement fusion experiments and diagnostic techniques on the Shenguang laser facility [J]. Physics, 2010, 39(08).
3. T.J. Murphy, C.W. Barnes, R.R. Berggren, et al. Nuclear diagnostics for the National Ignition Facility[J]. Review of Scientific Instruments, 2001, 72(1): 773-779.
4. J. Kilkenny. NIF Diagnostics: now and in the future, LLNL-PRES-558191[R]. Lawrence Livermore National Laboratory, 2012.
5. M.A. Stoyer, C.J. Cerjan, K.J. Moody, et al. Radiochemistry: A versatile diagnostic for the NIF ignition campaign, LLNL-TR-405043[R]. Lawrence Livermore Laboratory, 2008.
6. R.D. Hoffman, C.J. Cerjan, D.A. Shaughnessy, et al. Radiochemistry diagnostics for the National Ignition Facility, LLNL-PROC-426088[R]. Lawrence Livermore Laboratory, 2010.
7. M.A. Stoyer, C.A. Velsko, B.K. Spears, D.G. Hicks, G.B. Hudson et al. Collection of solid and gaseous samples to diagnose inertial confinement fusion implosions [J]. Rev. Sci. Instrum. 83, 023505 (2012)
8. G.P. Grim, P.A. Bradley, T.A. Bredeweg, et al. Prompt radiochemistry at the National Ignition Facility[J]. Review of Scientific Instruments, 2008, 79(10): 10E503.
9. J.M. Gostic, D.A. Shaughnessy, P.M. Grant, et al. Development of solid collection diagnostics on NIF through blast shield analysis, LLNL-PROC-520621[R], Lawrence Livermore National Laboratory, 2011.
10. Song Zifeng, Tang Qi, Chen Jiabin et al. DT neutron yield diagnosis by copper activation on Shenguang-III laser facility [J]. High Power Laser and Particle Beams, 2015, 27(11): 101-105.
11. Song Zifeng, Chen Jiabin, Liu Zhongjie, et al. Evaluation of uncertainty in DD neutron yield diagnosis by indium activation. High Power Laser and Particle Beams, 2014, 26(3): 120-125.
12. A.C. Hayes. Diagnosing Mix in NIF Capsules with Charged-particle Reactions and RIF Neutrons, LA-UR-08-5693[R]. Los Alamos National Laboratory, 2008.
13. D.A. Shaughnessy, C. Cerjan, K.J. Moody, L. Bernstein, R. Hoffman, et al. Evaluation of the Radiochemical diagnostic as an assessment of fuel-ablator mix and fuel ρR, LLNL-TR-472595[R], Lawrence Livermore National Laboratory, 2011.
14. R. Fortner, L. Bernstein, C. Cerjan, et al. Ignition Failure Mode Radiochemical Diagnostics Initial Assessment, UCRL-TR-230178[R]. Lawrence Livermore National Laboratory, 2007.

15. Charles Cerjan, Radiochemistry for NIF Implosion Diagnostics, CRL PRES-235692[R], NIF Workshop on Nuclear Astrophysics, 2007.
16. Azbouche, A., Belgaid, M., Mazrou, H., Monte Carlo calculations of the HPGe detector efficiency for radioactivity measurement of large volume environmental samples[J], Journal of Environmental Radioactivity, 2015, 146: 119-124.
17. Azli, Tarek, Chaoui, Zine-El-Abidine. Performance revaluation of a N-type coaxial HPGe detector with front edges crystal using MCNPX[J], Applied Radiation and Isotopes, 2015,97: 106-112.
18. Chuong, Huynh Dinh, Thanh, Tran Thien, Ngoc Trang, Le Thi, et al. Estimating thickness of the inner dead-layer of n-type HPGe detector [J], Applied Radiation and Isotopes, 2016, 116: 174-177.
19. Dryak, Pavel, Kovar, Petr, Experimental and MC determination of HPGe detector efficiency in the 40–2754 keV energy range for measuring point source geometry with the source-to-detector distance of 25cm [J], Applied Radiation and Isotopes, 2006, 64: 1346-1349.
20. Maidana, Nora L. Vanin, Vito R. García-Alvarez, Juan A. et al. Experimental HPGe coaxial detector response and efficiency compared to Monte Carlo simulations[J], Applied Radiation and Isotopes, 2016, 108: 64-74.
21. M.T. Haj-Heidari, M.J. Safari, H. Afarideh, H. Rouhi, Method for developing HPGe detector model in Monte Carlo simulation codes, Radiation Measurements, 2016, 88: 1-6.
22. J. Eberth, J. Simpson, From Ge(Li) detectors to gamma-ray tracking arrays–50 years of gamma spectroscopy with germanium detectors, Progress in Particle and Nuclear Physics, 2008, 60: 283-337.
23. X-5 Monte Carlo Team, “MCNP – A General N-Particle Transport Code, Version 5” https://laws.lanl.gov/vhosts/mcnp.lanl.gov/mcnp5.shtml.

Neutron Radiation Effects & Radiation Transportation and Simulation

INVESTIGATION OF WASTE MANAGEMENT OF CONTROL ROD, IRRADIATION BOXES, AND STEEL LINING OF TEHRAN RESEARCH REACTOR AFTER DECOMMISSIONING

Gholamzadeh Z., Joz Vaziri A., Mirvakili S. M.

Reactor and Nuclear Safety Research School,
Nuclear Science and Technology Research Institute (NSTRI),
Tehran, Iran
Cadmium_109@yahoo.com, zgholamzadeh@aeoi.org.ir

ABSTRACT

Prediction of the radioactive behaviour of different components of a research reactor during the cooling time is important regarding their waste management and decommissioning. The present work investigate the radioactivity behaviour of control rod, aluminium irradiation box and steel lining of Tehran Research Reactor during the cooling times after the reactor shutdown. MCNPX and ORIGEN computational codes were used to estimate the behaviour. A benchmark study was done to evaluate the conformity of the experimental measurement with the simulation data. The carried out study showed the aluminium parts would be easily handled after at least 6 months after the reactor shutdown by means of the usual shield are used to transfer the radioactive components to the spent fuel pool or radioactive waste storage sites. In the case of the steel lining also after 6 months of cooling the gamma dose rate decreases noticeably. The gamma dose rate of control rods are very high and decreases slowly during the years after the reactor shutdown.

Keywords: *Gamma dose rate, decommissioning, waste components, Tehran Research Reactor*

1 INTRODUCTION

Decommissioning of a nuclear facility is an important process. When each part of a nuclear facility has a problem and the problem cannot be solved satisfactorily within a reasonable time, a decision may be made to discharge that part. The radioactive material decommissioning is a technical process and needs great attention to assure the minimization of the risks to both the public and the workers involved in the process. The IAEA has developed some guidance documents on decommissioning [1-3]

In this work, the future decommissioning of some core components of TRR has been investigated.

2 MATERIAL AND METHODS

2.1 Description of TRR

TRR is an open pool, MTR- type, light water moderated reactor. The core consists of fuel elements, graphite boxes as reflectors and irradiation boxes. TRR is a 5 MW reactor with 20% enriched fuels and 500 m3/h flow rate. There are two types of fuel elements, i.e. Standard Fuel Element (SFE) and Control Fuel Element (CFE). First of all the control rod of

TRR modelled using the MCNPX code and its radial neutron flux was calculate along its height then the flux was used in ORIGEN code to calculate the rod decay behaviour (Fig.1).

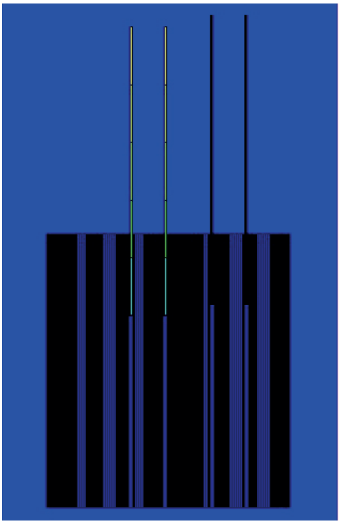

CR: 23%
RR: 29%

Figure 1: schematic view of TRR core and its control rods.

2.2 Simulation

In this study MCNPX 2.6.0 have been used as a powerful particle transport code with the ability to calculate deposited power and dose calculation [5]. In addition to MCNPX code, Origen 2.1 code [6] has been used to determine the photon spectrum. The TRR core with the control rods and its total containment has been modelled using the MCNPX.2.6 code. The spectrums of photons after 50 years of reactor operation time and in different cooling times have been determined on the surface of the control rod, central irradiation box and the hottest section of the steel lining of the research reactor using two ORIGEN and MCNPX codes. Dose calculations have been performed at the End Of Irradiation (EOI) using DE and DF cards and flux to dose conversion coefficients to the ICRP38 which is available in the MCNPX code appendix.

3 RESULTS AND DISCUSSION

The Ag-In-Cd control rods with precise dimensions and length of 65 cm were modelled according to Fig.2 using MCNPX code. An average of 23% of control rods and 29% of regulatory rods were assumed to be used inside the core in any operation. Consumption of rods from 2002 to 2015, is equivalent to 7300 MWD. The control rod decay behaviour on the cooling time is shown in Fig.2. As the figure shows the decay behaviour is tightly dependent to the neutron flux exposure the control rod and after 10 years of cooling its reduction is slow.

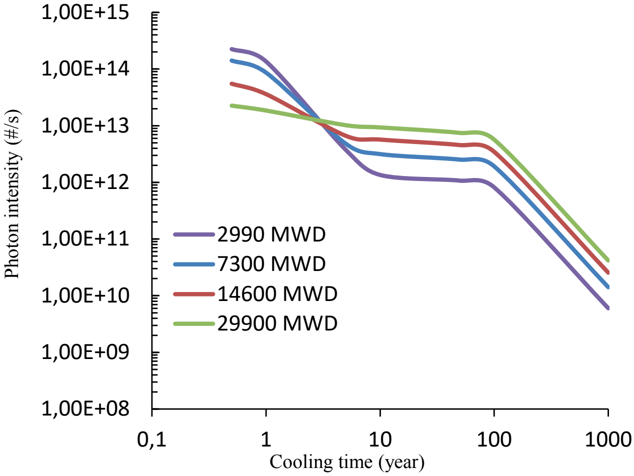

Figure 2: the gamma intensity variation of the activated control rod during the cooling time.

The gamma spectra variation of the radioactive control rod exposed to a neutron flux from a 7300 MWD TRR operation showed after the cooling times the gamma spectra shape does not change noticeably.

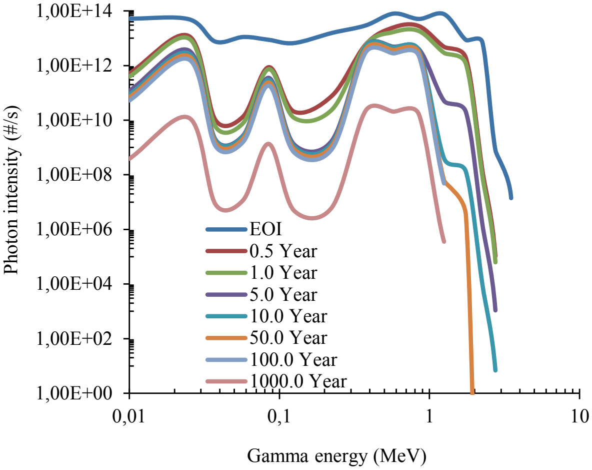

Figure 3: Comparison of Gamma spectra of the radioactive control rod at different cooling times and EOI.

To investigated the decay behaviour of one section of the control rod (13 cm) which is the internal ones in the TRR core during its operation, the received neutron flux by it was used in the ORIGEN code and the produced radioisotopes inside it was reported in Table 1.

Table 1: Investigation of radioactivity behaviour of the first part of the irradiated control rod at 7300 MWD at different cooling times

Radio-isotope	**End OF IRR**	**.5YR**	**10.0YR**	**50.0YR**	**100.0YR**	**1000.0YR**	**BR (%)**	**Particle**	**Energy (MeV)**
RH104	1.57E-02								
RH106	1.01E-02	2.64E-14	3.84E-17	4.35E-29					
PD107	8.10E-09	8.10E-09	8.10E-09	8.10E-09	8.10E-09	8.10E-09			
PD107M	1.87E-05								
PD109	5.98E+00								
PD109M	9.69E-02								
PD111	1.52E-01								
PD111M	2.12E-02								
AG106	3.13E-01	1.07E-07							
AG108	4.26E+03	7.17E-01	6.81E-01	5.47E-01	4.17E-01	3.07E-03	97.00	β	1.65
AG108M	8.08E+00	8.06E+00	7.65E+00	6.15E+00	4.68E+00	3.45E-02	92.00	γ	0.72
AG110	1.87E+04	8.31E+00	5.49E-04	1.38E-21					
AG110M	1.04E+03	6.25E+02	4.13E-02	1.04E-19					
AG111	2.50E+01	1.04E-06							
AG111M	1.25E+01								
AG112	4.07E-03								
CD107	9.93E-02								
CD109	5.57E+00	4.24E+00	2.38E-02	7.90E-12	1.12E-23		100.00	γ-β	0.088-0.125
CD111M	3.28E+00								
CD115	2.19E+01								
CD115M	1.88E+00	1.10E-01	4.16E-25						
CD117	6.53E-01								
CD117M	2.49E-02								
IN114	1.14E+02	3.67E+00	2.94E-21						
IN114M	4.95E+01	3.84E+00	3.08E-21						
IN115	5.13E-11	5.13E-11	5.13E-11	5.13E-11	5.13E-11	5.13E-11			
IN116	5.69E+03								
IN116M	4.48E+03								
IN117	3.50E-01								
IN117M	6.18E-01								
SN117M	4.72E+01	5.60E-03							
SN119M	1.28E-04	7.64E-05	4.17E-09	4.68E-27					
SUMTOT	3.45E+04	6.58E+02	8.42E+00	6.70E+00	5.10E+00	3.75E-02			

The mass of the control rod is approximately 455 grams, as the calculations of the ORIGEN code show that the activity of cadmium-109 after 10 years of cooling is about 0.19E+07 Bq/g. In general, cadmium-109, silver-108 and silver-108m are important radiobiological contaminants of the control rod. After 50 years of cooling of the rod, the amount of cadmium activity per unit mass of the rod reaches 0.0006 Bq/g, while the values of silver -108 dose not reach to the free release limit even after 1000 years (24×104 Bq/g >>0.02 Bq/g).

The measurements showed after 4 years of cooling the highest gamma dose rate of the control rod in 60 cm distance between the detector and the control rod in water is about 37 mSv/h. The simulation data showed the gamma dose rate value is about 480 mSv/h at 1 m of air after 6 months of cooling.

The irradiation boxes of TRR are made of Al6061. The 50-years irradiation was considered for the central Aluminium irradiation box, which is imposed in front of the highest neutron flux. The gamma source distribution on the irradiation box is shown in Fig.4.

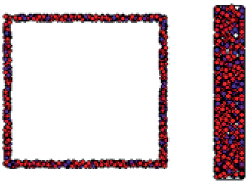

Figure 4: The gamma source distribution on the irradiation box using MCNPX code.

The gamma intensity variation of the radioactive irradiation box was determined by using the ORIGEN code. As Fig.5 shows after 0.5 year, the total gamma intensity reaches to 4.37E+08 #/s. the intensity was used to calculate the box dose rate.

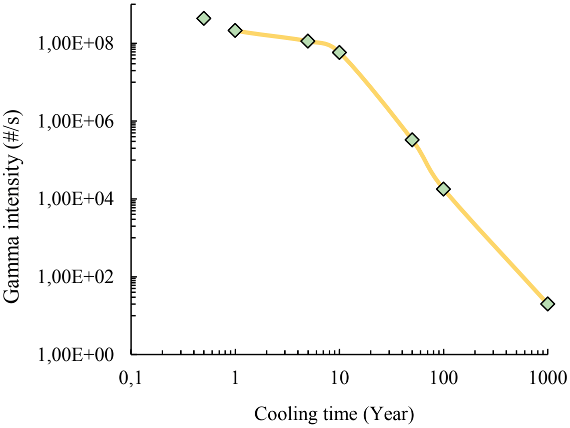

Figure 5: variation of Gamma intensity of the radioactive irradiation box on the cooling time.

In addition, the box gamma spectra of radioactive box were compared for the 6 months cooling time and EOI. As Fig.6 shows after 6 months of cooling the gamma spectra would be noticeable softer and high-energy gammas are not in the spectra so it is predictable the gamma dose rate decreases noticeably than EOI.

Clearly, the total intensity would decrease in order of 10000 after 6 months cooling. Calculations show that after 6 months of cooling, the maximum dose of the irradiated box at the box surface will be about 3.5 mSv/h. The dose at a distance of 1 m from the surface of the irradiated box in the air is about 35 µSv/h. Calculations show that nickel-63 is one of the most important problems of this box and its value will be about 20 Bq/g after 1000 years.

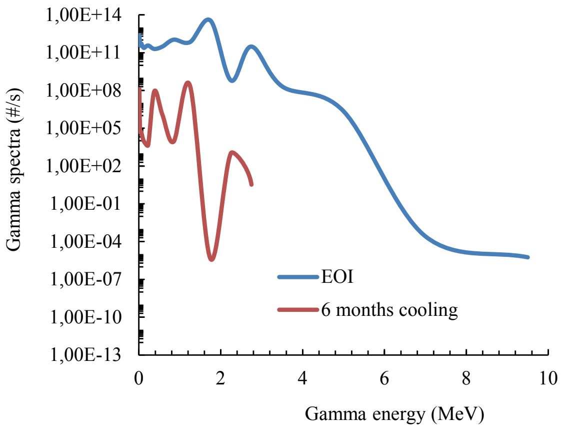

Figure 6: Comparison of Gamma spectra of the radioactive irradiation box at 6 months cooling time and EOI.

The highest radioactive section of the steel lining of the TRR pool wall was selected to calculate its radioactive behaviour. It's received neutron flux was calculated using MCNPX code and its mass and flux was used in the ORIGEN code to calculate its radioactive behaviour.

Calculations show that the gamma intensity emitted from the shutdown time to 6 months after the reactor shutdown decreases by about 55-fold and continues to decrease even up to 1000 years of cooling (Figure 7). At the time of 1 year after cooling, the gamma intensity of this piece of steel is in the order of 106 #/s, which its dose rate will be at a distance of 1 m in the order of nanosievert. It should be noted that in all these calculations, the share of the stabilized surface contamination on this calculation is not considered. Figure 8 shows that the gamma spectrum of this piece of steel which is severely softened after 6 months of cooling, and high-energy gammas are removed.

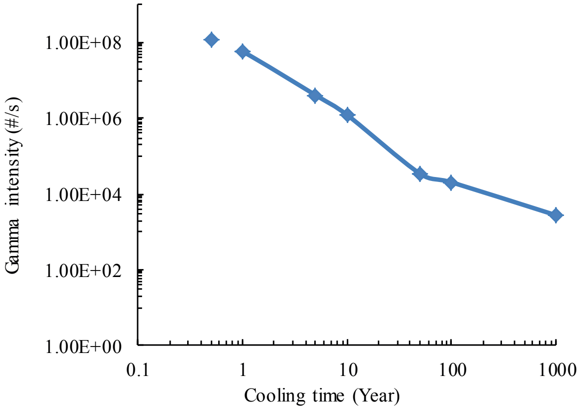

Figure 7: variation of Gamma intensity of the radioactive steel lining piece on the cooling time.

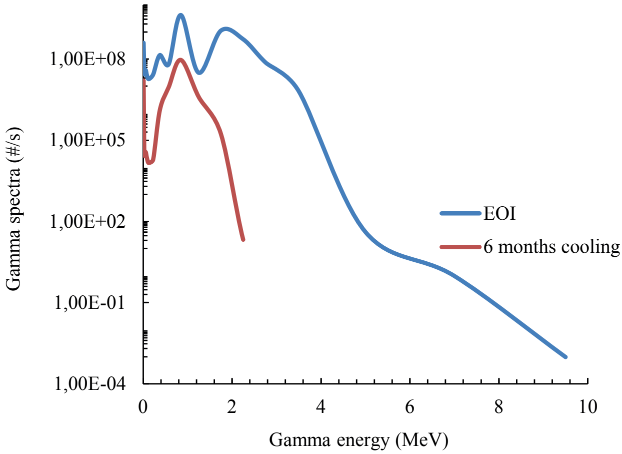

Figure 8: Comparison of Gamma spectra of the radioactive steel lining piece at 6 months cooling time and EOI.

Calculations show that the surface dose of this part after 6 months of cooling is 3.5 mSv/h. In the measurements that were done at the time of repairing the Tehran reactor in 2016, the dose of the steel piece in the most active parts was about 5 mSv/h and 3.7 mSv/h, which shows the consistency of the calculations with the experimental results (Figure 9). It should be noted that the lead shield hanging in front of the thermal column during repairs was not completely fixed to the wall and was slightly spaced from the right side of the wall, which led to a higher detected dose reading from this side. In addition, since the gamma dose readout belongs to all directions and this value was not only related to the steel layer of the pool wall, it was expected that the measurement value of Figure 8 would be higher than the computational value in this work.

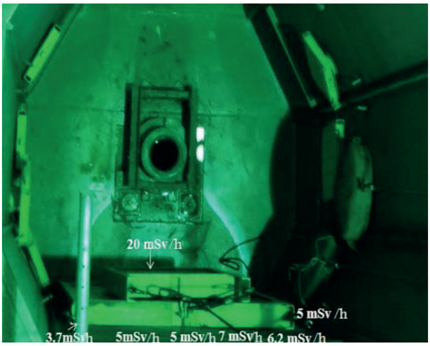

Figure 9: Measurement of gamma dose rate of the steel lining at 2016 year after 6 months of the reactor shutdown.

4 CONCLUSION

Waste management of the radioactive parts of a research reactor after its shutdown and during its decommissioning is very crucial concern. The decay behaviour of the activated components would be predicted using computational codes. This procedure could drastically help use to manage the waste components as easily as possible. In the present work, MCNPX and ORIGEN codes were used to estimate the decay behaviour of the Ag-In-Cd control rod, the aluminium irradiation box and the hottest section of the steel lining of the TRR. The calculation showed in the case of the aluminium parts at least 6 months transition time is needed to handle transportation of the radioactive components to storage sites or spent fuel pool. In the case of the steel lining, its gamma dose rate after 6 months of the reactor shutdown would not be noticeably high to impact on the personnel exposure when the reactor pool is empty of water. The calculation data suggests the gamma dose rate of control rods are very high in the first years after the reactor shutdown.

REFERENCES

[1] International atomic energy agency, Decommissioning Techniques for Research Reactors, Technical Reports Series No. 373, Vienna, 1994.

[2] International atomic energy agency, Safe Enclosure of Nuclear Facilities During Deferred Dismantling, Safety Reports Series No. 26, Vienna, 2002.

[3] International atomic energy agency, Decommissioning of Nuclear Power Plants and Research Reactors, Safety Standard Series No. WS-G-2.1, Vienna, 1999.

[4] Final Safety Analyses Report for Tehran Research Reactor (FSAR for TRR), Atomic Energy Organization of Iran, Tehran, 2009.

[5] A. G. Croff, A USER'S MANUAL FOR THE ORIGEN2 COMPUTER CODE, ORNL,1980

[6] D.B. Pelowitz, MCNPX: A General Monte Carlo N-Particle Transport Code.Version 2.6.0LA-CP-07-1473, 2008.

[7] RWMC Regulators' Forum (RWMC-RF), Removal of regularity controls for materials and sites, Sep. 2004.

[8] Radiation Safety Manual, Revised, Dalhousie University June. 2017.

INVESTIGATION OF HEAVY WATER LOADING IN NEUTRON BEAM CHANNEL OF TEHRAN RESEARCH REACTOR TO DECREASE FAST NEUTRON BACKGROUND AT DIFFRACTION TABLE

Gholamzadeh Z., Bavarnegin E., Joz Vaziri A., Safaei Arshi S., Mirvakili S. M.

Reactor and Nuclear Safety Research School,
Nuclear Science and Technology Research Institute (NSTRI),
Tehran, Iran
Cadmium_109@yahoo.com, zgholamzadeh@aeoi.org.ir

ABSTRACT

To obtain very sharp neutron diffraction pattern using the diffractometer facilities in research reactors, high-efficiency detectors, low fast neutron backgrounds, and high intensity neutron beam in the range of analysis are important factors. To improve the old diffraction system of Tehran Research Reactor, some reformations were investigated to decrease the fast neutron backgrounds at the diffraction table. However, crystalline neutron filters could obtain this aim easily, the homemade high-purity heavy water accessibility in TRR caused the cheap procedure is investigated in the present study. Hence, heavy water usage inside the horizontal channel of TRR was investigated using MCNPX code simulation. The obtained results showed about 10 litres heavy water loading inside the channel would reduce the fast neutrons with $E_n > 1$ MeV about 124 times but the thermal neutron in the range of analysis (0.02 eV< E_n <0.33 eV) would be reduced about 7.5 times. The calculations showed a donate-shaped (hollow cylinder) heavy water cylinder would allow the thermal neutron reduction is not noticeable (about 21%) while the fast neutron reduction is 1.83 times.

Keywords: *Heavy water, Fast neutron shielding, Neutron diffraction, Tehran Research Reactor*

1 INTRODUCTION

Epithermal and fast neutrons are often a major source of background in detectors. Neutron filters scatter out fast neutrons utilizing solid-state effects, while thermal neutrons pass the filter material. Thus, the neutron spectrum is modified massively however, their cost and stress-resistance of them in high neutron flux should be discussed [1,2].

Wu et al. (2015) illustrated that In recent decades, beam tube research reactors have become the largest community of users worldwide, and the number of neutron beam users continues to increase. They investigated a novel compact core design for beam tube reactors, in which a heavy water reflector was used between the core and light water shielding to maximize thermal flux in the beam channel [3].

The fast section of neutron spectra not only disturbs the diffraction pattern but causes noticeably higher dose rates at the experiment table and thereby the device operator. Figure 1 could clear importance of shielding or filtering of such neutrons.

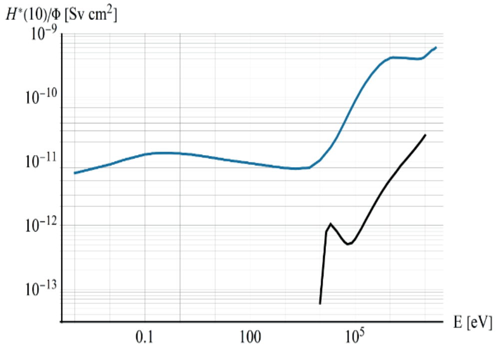

Figure 1: Plot of the energy dependency of the ambient dose equivalent H∗(10) from ICRP 74 [4].

From the above figure it is clear by shielding of neutron with E_n> 1 MeV, the neutron dose rate would be decreased drastically.

In the case of the Tehran Research Reactor (TRR), which is a pool-type reactor, the heavy water tank performance around the core is somehow difficult. Hence, in this work, loading of heavy water in the TRR horizontal channel has been investigated.

2 MATERIAL AND METHODS

TRR is an open pool, MTR- type, light water moderated reactor. The core consists of fuel elements, graphite boxes as reflectors and irradiation boxes. TRR is a 5 MW reactor with 20% enriched fuels and 500 m^3/h flow rate. There are two types of fuel elements, i.e. Standard Fuel Element (SFE) and Control Fuel Element (CFE). First of all the TRR core and beam channel of it was modelled using the MCNPX code (Fig.2). Effect of heavy water loading in the horizontal channel on thermal (E_n< 0.33 eV) and fast neutron (E_n> 1 MeV) spectra was investigated after the first soller-type collimator of the neutron channel. To reduce the calculation errors, the dxt capability of the computational code was used at the flux calculation position and F5 tally was used to determine the neutron flux at this position.

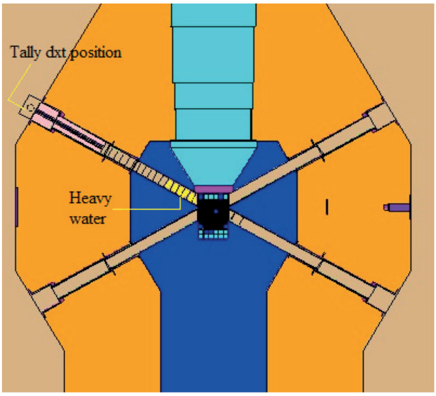

Figure 2: Schematic view of TRR core and its beam channel.

In this study MCNPX 2.6.0 have been used as a powerful particle transport code with the ability to calculate deposited power and dose calculation [5]. Application of a hollow cylinder, which allows the direct path of neutrons is open, was investigated at the second step of the present work. The deposited heat inside the heavy water was discussed in both configurations for loading of it in the horizontal channel. The heavy water temperature was determined at final step.

3 RESULTS AND DISCUSSION

For first step, heavy water thickness was optimized so that after that the fast shielding efficiency will not increase noticeably. For this purpose, inside the channel was divided to 11 cm sections as it is seen in figure 2. According to Fig.3, after 50 cm there is not noticeably reduction of fast neutrons at the flux monitoring position (after first collimator of the horizontal channel). The carried out calculations showed this thickness would result in the fast neutron reduction of 124 times than the empty channel. Nevertheless, this heavy water loading configuration decreases the thermal section of the neutron spectra about 7.5 times.

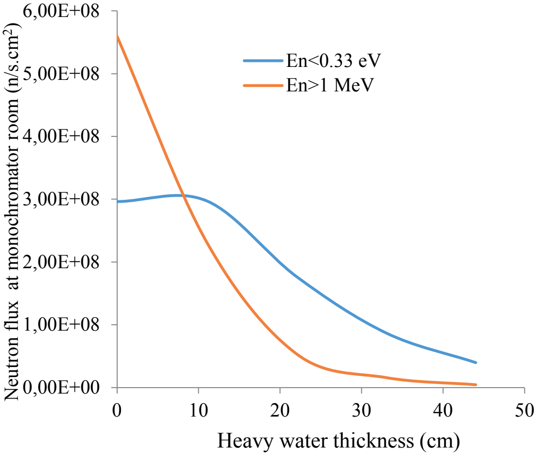

Figure 3: Thermal and fast neutron reduction as the heavy water thickness enhancement.

Next, the calculations were performed assuming that the path with the dimensions of the inlet of the first neutron collimator (radius of 7 cm) is open for neutrons and a hollow-shape heavy water cylinder according to Figure 4 is used to shield the fast neutrons. The results of these calculations showed that using a 50 cm hollow cylinder, the thermal neutron flux is reduced by 21% and the thermal neutron flux at the outlet of the first collimator will be 2.34×10^8 n/s.cm^2. In this case, the fast neutron flux decreases by 1.83 times and the fast neutron flux at the outlet of the first collimator will be 3.06×10^8 n/s.cm^2.

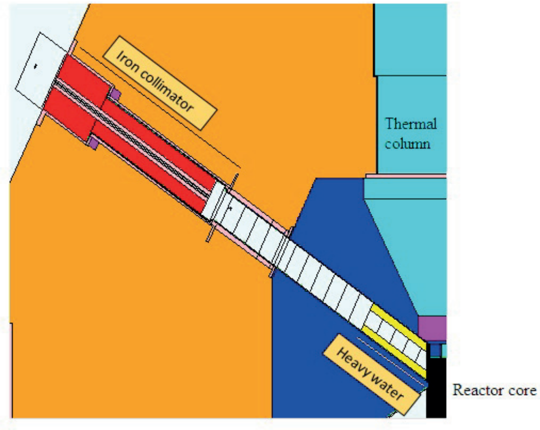

Figure 4: schematic view of TRR core and its beam tube with hallow-shape heavy water cylinder (yellow colour).

The above figure shows by using about 15 cm of solid cylindrical-shape heavy water inside the channel, fast section of the neutron spectra at the first collimator exit would decrease to half of its first value (the value without heavy water loading). In addition, the thermal section of the spectra remains approximately constant.

It should be noted that the use of heavy water in the channel should be checked for residual heat and heavy water temperature because its evaporation can cause problems due to the accumulation of steam in the monochromatic room. Therefore, in Table 1, the heat caused by neutrons and gamma in heavy water is presented in two states, solid and hollow cylinders. The table shows if 50 cm of heavy water solid cylinder is used, the total residual heat reaches to about 450 watts.

Table 1: Investigation of gamma and neutron heat deposition in heavy water

Heavy water thickness	Neutron deposited heat（W）	Gamma deposited heat（W）	Solid cylinder
0	0.107	0.182	
11	82.3	149	
22	117	277	
33	127	352	
44	129	393	
44	111	333	Hollow cylinder

At the next step, temperature of the hollow-shape cylindrical heavy water was calculated. The liquid heavy water could be loaded inside a hollow-shape aluminum box with thickness of 2 mm that avoids any evaporation formation inside the monochromatic room. The calculations showed the hollow cylinder temperature would reach to the order of 138 °C while the boiling point of heavy water is 104 °C.

However, heavy water decreases the fast neutron section of the neutron spectra inside the horizontal beam channels, but its application than neutron filter should be investigated in more details.

Stamatelatos et al. reported that sapphire of 15 cm thickness gives 62% transmission of neutrons with 0.11 nm wavelength (at the range of the interest wavelength in TRR) and 76% transmission for 0.25 nm (at the range of the interest wavelength in TRR) neutrons. The transmission of fast neutrons is 3% [7].

Also Adib et al investigated transition sapphire at different temperatures which their experimental measurements shows for 0.015–0.06 eV there are the highest transition of neutrons and the crystal temperature enhancement of 150 K to 300 K will result in about 6% reduction of the exited thermal neutrons from the crystal (Fig.5).

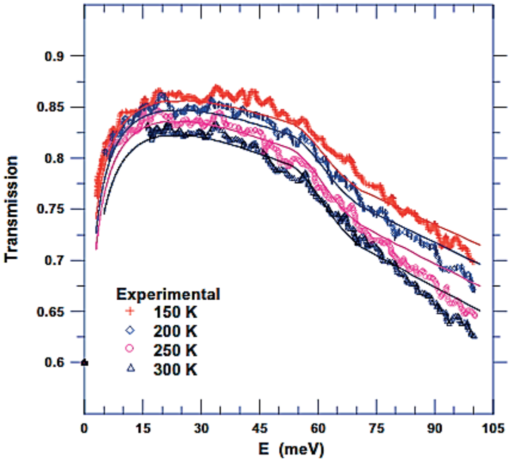

Figure 5: Neutron transmission of sapphire in the a-axis direction at various temperatures [8].

However, another experimental work published by Rantsiou et al. showed that transmission through sapphire crystals of various thicknesses for wavelengths between 0.7–10Å decreases by the crystal thickness enhancement: the minimum transmission for a 12 cm sapphire crystal is around ~30%. This goes up to ~50% when considering wavelengths between 1.5–6Å (at the range of the interest wavelength in TRR). Their report showed that by application of 12 cm of the sapphire filter the fast section of neutron beam decreases about 10 times; figure 6 [2].

In addition, we investigated our 111 homemade sapphire crystal in E radiography channel of TRR. The thermal and fast neutron flux was measured using gold foils and cadmium-covered gold foils respectively. The foils were placed on the front and back surfaces of the crystal. Fig. 7 shows the crystal and experiment setups. 5.5 cm 111 crystal decreases the thermal neutrons about 1.93 times. With cadmium ratio consideration, the fast neutron flux reduction is about 4 times using 5.5 cm 111 sapphire. The results showed good conformity with pervious reported experimental data by Rantsiou et al.

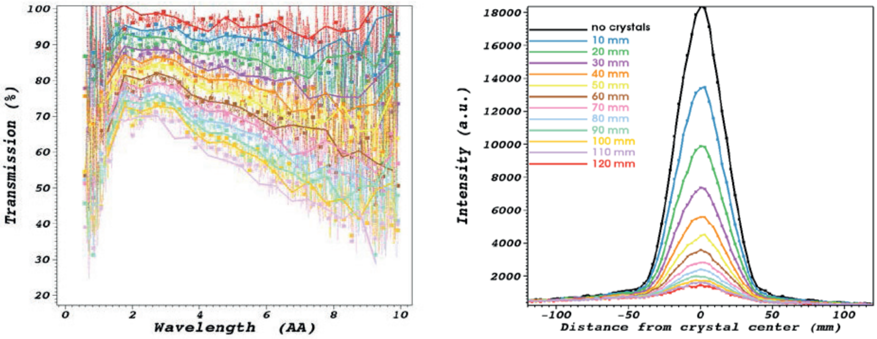

Figure 6: Neutron transmission of sapphire with different thicknesses, left) thermal, right) fast [2].

Figure 7: Neutron transmission measurement of sapphire with 5.5 cm thickness, right: experiment setup in front of radiography channel of TRR.

4 CONCLUSION

Fast neutron shielding at the analysis neutron devices position of research reactors is very important regard to both personnel received dose rates as well as achievement of sharper diffraction patterns with the least possible backgrounds. The present study investigated heavy water loading possibility inside the horizontal neutron channels of TRR in view of shielding power of fast neutrons. The obtained results showed however, the reflector would decrease the fast neutron section of the neutron spectra but in comparison with sapphire neutron filters, its application is less preferable for achieving a sharp diffraction pattern. However 15 cm heavy water solid cylindrical box (about 3.3 litter) decreases the fast neutrons about 50% and the thermal neutron intensity would be approximately constant but the deposited heat of about 230 W is a serious problem for avoiding vapour formation. 50 cm solid heavy water cylinder could compete with the sapphire crystal if the heat transmutation of the solid cylinder is solved. The sapphire crystals may decrease the fast neutron to one per tenth while the thermal neutron intensity may decrease about 50%.

REFERENCES

[1] W. Mach, Installation of a neutron beam instrument at the TRIGA reactor in Vienna. September 2018.

[2] E. Rantsiou, U. Filges, T. Panzner, E. Klinkby, Neutron Transmission through Sapphire Crystals: Experiments and Simulations, 2013.

[3] K Boning and P. Von Der Hardt, “Physics and Safety of Advanced Research Reactors,” Nuclear Instruments and Methods in Physics Research A **260**, 239–246 (1987).

[4] H. Smith, Conversion Coefficients for Use in Radiological Protection against External Radiation, ICRP publication 74, Annals of the ICRP 26 (1996) 3–4, Oxford: Pergamon press (1997), ISBN 0080427391.

[5] A. G. Croff, A User's manual for the ORIGEN2 computer code, ORNL,1980

[6] D.B. Pelowitz, MCNPX: A General Monte Carlo N-Particle Transport Code. Version 2.6.0LA-CP-07-1473, 2008.

[7] I. E. Stamatelatos and S. Messoloras, Sapphire filter thickness optimization in neutron scattering instruments, Rev. Sci. Instrum., Vol. **71**, No. 1, January (2000) 70–73.

[8] M. Adib, M. Kilany, N. Habib, M. Fathallah, Neutron transmission of single-crystal sapphire filters, Czech. J. Phys. **55** (2005) 563–578.

Nuclear and Related Analytical Techniques in Environmental and Material Sciences

IMPORTANT TOOLS IN AIR QUALITY STUDY: MOSS BIOMONITORING, ATMOSPHERIC DEPOSITION, TRACE ELEMENTS CONTENT AND DATA ANALYSIS

Shaniko Allajbeu[1], Flora Qarri[2], Lirim Bekteshi[3], Trajce Stafilov[4],
Marina Frontasyeva[5], Pranvera Lazo[1*]

[1] Department of Chemistry, Faculty of Natural Sciences, University of Tirana, Tirana, Albania
[2] Department of Chemistry, University of Vlora, Vlora, Albania
[3] Department of Chemistry, Faculty of Natural Sciences, University of Elbasan, Elbasan, Albania
[4] Institute of Chemistry, Faculty of Science, Ss. Cyril and Methodius University,
Skopje, North Macedonia
[5] Joint Institute for Nuclear Research, Dubna

* Corresponding author: pranveralazo@gmail.com

Abstract

This study examines the spatial distribution patterns of toxic metals (As, Cd, Cr, Co, Cu, Fe, Hg, Pb, Ni, and Zn) in atmospheric deposition by using Hypnum cupressiforme (Hedv.) moss as biomonitor. Moss samples were collected from 47 sampling sites distributed over the whole territory of Albania. Moss biomonitoring made it possible to evaluate the distribution pattern of metals at national scale. High concentration levels, higher than the most European countries, were found for Cr, Ni, and Fe.

The concentrations data were statistically processed to understand their variability, the relationship between the elements, and to estimate the most likely pollution sources of the elements. The spatial distribution analysis identified the local enrichments of Cr, Ni, and Co stretched in the north-southeastern direction of Albania and affected by the soils geochemistry, mining and metal high temperature processing, and mineral deposits of the area.

Keywords: air quality, moss biomonitoring, trace metals, statistical analysis, emission inventory, ICP-AES, Albania.

1. Introduction

The increased content of different pollutants in the environment is associated with natural and anthropogenic sources. Anthropogenic emission is an important factor of environmental pollution from various pollutants, particularly from toxic metals which have adverse effects on the health of the human beings and different plants. The requirement to live in a clean air environment is fundamental to the human health and the well-being (WHO, 2000). Environmental pollution from metals is an inorganic chemical hazard, associated mainly with the increased levels of lead, chromium, arsenic, cadmium, mercury, zinc, copper, cobalt and nickel (Järup, 2003). High concentration level of metals in the air we breathe may cause adverse and undesirable effects on human beings. Metals are generally found in the air in a variety of physicochemical forms, such as solid, liquid, gaseous, or very fine particles (Richards, 2020; EPA/600/P-99/002aF, 2004).

Different monitoring methods are available to assess the level of air pollution by using traditional classic methods or different plant organisms as bioindicators of certain contaminants. The conventional technique requires expensive equipment that may cover a small area of interest. For decades, the use of mosses as bioindicator to assess air pollution, particularly the metals' pollution, was developed and widely applied in European countries

(Schröder et al. 2016; Harmens et al. 2015, 2013; Gjengedal and Steinnes, 1990; Rühling, 1994) and after in Asia, Brazil and North America (Harmens et al. 2011). The use of mosses as biomonitors is a known technique implemented as an alternative method to define and characterize the pollution sources of metals in atmospheric deposition (Stanković et al. 2018; Steiness, 1989). Due to the widespread distribution of mosses around the world, the growth in a wide-spread population group, the ability to accumulate great amounts of metals (Tremper et al. 2004; Blagnytė and Paliulis, 2010), made them widely used as bioindicators of metals atmospheric deposition.

This paper deals with 2010 moss biomonitoring survey in Albania that were conducted under the framework of the European Cooperative Program on Effects of Air Pollution on Natural Vegetation and Crops. Only the most toxic elements (As, Cd, Cr, Co, Cu, Fe, Hg, Pb, Ni, and Zn) that show negative health impact and environmental risk are included in this study. The aim of this study is the harmonization and the combination of the concepts of biomonitoring - statistical analysis – emission inventory to produce detailed information on trace metals atmospheric deposition, to assess their local emission sources and long-range atmospheric transport and to differentiate their natural and anthropogenic sources.

2. Material and methods

2.1. Sampling

Sampling process significantly affects the uncertainty of the analytical results. Thus, to guarantee the representative samples relatively free from the interferences of external factors, sampling was carried out in accordance with the LRTAP Convention-ICP Vegetation protocol and sampling strategy of the European Program on Biomonitoring Heavy Metal Atmospheric Deposition (Harmens et al. 2010).

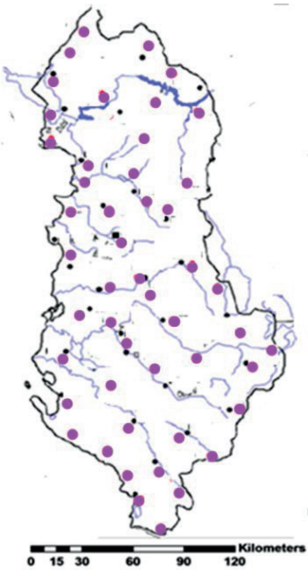

Fig. 1. The location of the sampling sites on the map of Albania position.

Moss samples (*Hypnum cupressiforme (Hedv.)* that are widely spread in Albania are collected from 47 sampling sites at relatively dry periods during October-November 2010 and June-July 2011. A systematic sampling scheme was applied using a homogeneous distribution of more or less equal densities (≈1.5 moss samples/1000 km^2). The locations of samples were situated at least 300 m away from main roads or buildings and 100 m from small roads and single houses. The distribution of the sampling sites is shown on the map of Albania (centered at the latitude 41°00′ north of the equator and the longitude 20°00′ east of Greenwich) (Fig. 1).

2.2. Moss analysis

Moss samples were cleaned from the adhering materials and the brown parts of the plant tissues were removed as died material. Only the green and green-brown parts of moss tissues that represent, at last, three years of moss growth, were selected for chemical analysis. Samples were dried at room temperature for about 72 hours.

The concentration of metals in moss was determined by instrumental neutron activation (INAA) and inductively coupled plasma-atomic emission spectrometry (ICP-AES). INAA is a non-destructive method of multi-elements analysis. It could achieve good detection limits, high accuracy and low systematic error in trace elements quantitative analysis. INAA measure the total amount of elements present in the samples of different matrixes without any pre-treatment of the sample (Salbu and Steinnes 1992). ENAA analyses were performed at the Frank Laboratory of Neutron Physics Joint Institute for Nuclear Research, Dubna, Russian Federation.

The dried samples were digested with a Microwave digestion system (Mars, CEM, USA) (Stafilov et al. 2018). The concentration of metals in moss was determined by inductively coupled plasma atomic emission spectrometry (ICP-AES) (Varian, 715ES) and, the electrothermal atomic absorption spectrometry (ETAAS-Varian, SpectrAA 640Z, only for Cd and As). The analysis was conducted at the Institute of Chemistry, Faculty of Science, St. Cyril and Methodius University, Skopje, Northern Macedonia. Three replications for moss samples were digested, and three replicate measurements for dissolution were made during analysis. Concentrations of metals (including mercury) are expressed in mg kg-1 dry weight.

2.3. Quality control

The quality control of ENAA results was examined by the analysis of reference materials SRMs 2710 Montana Soil (NIST), 1632b Trace Elements in Coal (NIST) and BCR 667 Estuarine Sediment (IRMM). INAA is relatively free from matrix effects and interferences that allows using standards of different compositions and physical state from the sample (Filby 1995), Frontasyeva 2011). The mean content of the elements under investigation are in good agreement with the certified data [29].

The quality assurance of ICP-AES was checked by two moss reference materials, M2 and M3, prepared firstly for the 1995/6 European moss survey (Steiness et al. 1997). Blank samples were measured simultaneously to the analysis of the moss samples. The recovery of the investigated elements was checked by standard addition method. It ranged between 98.5% and 101.2% for ICP-AES, 96.9% to 103.2% for AAS.

2.4. Data processing and statistical analysis

The variability and spatial distribution of the elements was investigated by using the statistical analysis, descriptive statistic and spatial analysis. The relationship between the elements in moss was tested by Pearson correlation analysis, confirmed by the statistical significance level, $P < 0.005$. Factor analysis (FA) was used to assess the most probable pollution sources of the elements under investigation. FA may explore the hidden multivariate structures of the data (Astel et al. 2008; Reimann et al. 2002) and may clarify the link between the elements that tend to have similar origins or to subsequently develop similar associations on the data matrix. The associations of the elements extracted from the Pearson correlation matrix may explain the role of the factors to the group of the associated elements. Statistical analysis was performed using the MINITAB 19 software package. The spatial distribution of the elements was visualized from the distribution maps, plotted with Arc-GIS 10.2 system by applying the local deterministic methods and the inverse distance weighting. The concentration data of the elements was divided by the respective median values to standardize the data at the same digit numbers. To compensate the natural variability and to distinguish the anthropogenic variability of concentration data, the data were normalized by using Li as normalizer element (Loring and Rantala, 1992).

3. Results and discussion

3.1. Trace metal concentrations in moss samples

The most important statistical parameters, such as mean, median, minimum, maximum, coefficient of variation (CV%), skewness, kurtosis and frequency distribution, are shown in Table 1. The mean, median and the concentration range are shown in mg kg^{-1}.

Table 1. Descriptive statistic analysis of trace metal data (N=47)

Elements	Mean	Median	Range	CV %	Sk	K^{N}
As	0.452	0.21	0.05–2.86	133	2.6	6.8
Cd	0.146	0.11	0.038–0.090	90	4.5	24.7
Cu	6.035	5.62	2.14–15.55	39	1.52	4.89
Hg	0.206	0.136	0.036–2.23	93	5.7	35.6
Pb	3.11	2.29	1.34–19.7	93	4.6	24.4
Zn	14.49	13.9	1.0–46.9	64	1.16	2.6
Ni	13.2	5.89	1.56–131	162	4.2	20.4
Cr	26	10.9	1.47–262	164	4.1	20.8
Co	1.84	1.2	0.389–7.47	87	2	3.3
Fe	1845	1540	469–5488	60	1.84	3.5

CV - coefficient of variation, Sk - skewness; K – kurtosis; CV - coefficient of variation; in brackets: statistical parameters of the normalized data

The distribution of concentration data (except Pb and Zn) and the normalized data of As, Cd, Hg, and Ni follow the lognormal distribution model, and are positively skewed with high variability (CV>75%). It indicates a high asymmetry of the concentration data affected by mixed factors. The sequences of the content of elements in moss samples were Fe > Zn > Cr > Ni > Cu > Pb > Co > As > Hg > Cd. The sequence of the variability of the normalized concentrations was Ni ≈ Cr > As > Hg ≈ Pb ≈ Cd> Co > Zn > Fe > Cu. It looks likely different from the sequence of the variation in concentration data, by indicating the presence of the anthropogenic effects. The median concentrations of Cr and Ni in current moss samples is about 6 and 20 times higher than the median concentration of the European moss survey (Allajbeu et al. 2017; Harmens et al. 2015) that may indicate high anthropogenic inputs of these elements in current moss samples. High variability of the elements and wide range of the concentration revealed heterogeneous spatial distributions of the metals in moss samples by indicating high effects of the anthropogenic sources. The concentration data onto Cu, Fe and Zn are characterized by moderate variation (CV<75%) and looks likely more stable in their distribution over the territory of the country. High metal concentrations on different locations and the disparity in the distribution of the concentration data indicates that the data are affected by mixed local factors may be associated with geochemical factors and local anthropogenic sources. The skewness and kurtosis of As, Pb, Cr, Fe and Zn are higher than the respective values of concentration data The situation is similar with the variability of Cu, Pb, Ni, Cr, Co and Zn normalized data that show higher variability than the respective values of the concentration data. This behavior of the normalized and the concentration data of the elements probably indicate high anthropogenic sources of these elements in moss samples.

3.2. Multivariate analysis

Pearson correlation analysis was carried out to investigate the linear relationship and the association between the elements.

Very strong and significant correlations ($r>0.8$, $p=0$) were found between the pairs of the concentration data of As, Pb, Cr, Ni and Co, and their respective normalized data by indicating strong anthropogenic sources of these elements. Strong ($0.6<r<0.8$, $p<0.005$) and/or moderate ($r = 0.4 – 0.6$, $p < 0.01$) and significant correlations were found between the pairs of the concentration data of the group of elements Cu, Cd, Zn, Pb, Hg, as well as with their normalized data.

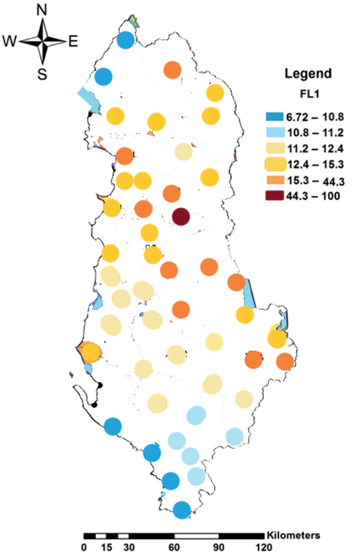

Fig. 2. Distribution pattern of factor loading FL1 linked with Cr(N), Ni(N), Ni, Co, Co(N), Fe(N) and Cr.

Moderate and significant correlations ($r = 0.4 – 0.6$, $p < 0.01$) between Cd, Cu, Pb, Hg, and Zn elements indicate their similar natural and anthropogenic origin in moss samples. The presence of these elements in atmospheric deposition is mostly derived by long-range atmospheric transport of pollutants from other parts of Europe (LRTP) and from local emitting sources such as high temperature of metal processing, traffic emission, and windblown dust that represents historical waste deposition and the geochemical properties of the area (Harmens et al. 2015).

For better explaining the association of the elements and to evaluate the probable sources of the elements in moss samples, Factor analysis (FA) was carried out.
Five main factors with 76.6% of the total variance were extracted from FA. The associations of metals within the same factor could be explained as follows:

Factor 1 (F1) is the strongest factor representing 22.2% of the total variance. It is followed by high loads of Ni(N), Cr(N), Ni, Cr, Fe(N), Co, and Co(N). These elements are anthropogenic elements mostly derived by different emission sources such as the geogenic contribution of Cr and Fe-Ni deposits, historical waste deposition, mining industry, iron, and steel and ferro-chromium metallurgy in Albania (Allajbeu et al. 2017; Qarri et al. 2014). The association of the anthropogenic fraction of Fe (represented by the Fe(N)) is highly supports the discussion above. Strong associations of the concentration data of Cr, Ni and Co with their respective normalized data indicate strong anthropogenic sources of these elements.

Factor 2 (F2) is the next strong factor representing 19.4 % of the total variance. It is linked with high loads of Cd(N), Zn(N), Cu(N) and Hg(N). The normalized concentration data of the elements come after the compensation of natural variations and indicate their anthropogenic fractions (Loring and Rantala, 1992) in moss samples. Geogenic factors, mining and nonferrous metallurgy should be important sources of these elements. Although the copper mining, smelting and processing industry in Albania had stopped since the beginning of years 1990 and emissions of metals such as copper, lead, cadmium, zinc, selenium etc., are decreased significantly, their concentrations in some parts of the country are still very high due to the historical deposition and the effects of mineral damps in vicinity of ex-copper industry particularly in the North part of the *Factor 2 (F2)* is the next strong factor representing 19.4 % of the total variance. It is linked with high loads of Cd(N), Zn(N), Cu(N) and Hg(N). The normalized concentration data of the elements come after the compensation of natural variations and indicate their anthropogenic fractions (Loring and Rantala, 1992) in moss samples. Geogenic factors, mining and nonferrous metallurgy should be important sources of these elements. Although the copper mining, smelting and processing industry in Albania had stopped since the beginning of years 1990 and emissions of metals such as copper, lead, cadmium, zinc, selenium etc., are decreased significantly, their concentrations in some parts of the country are still very high due to the historical deposition and the effects of mineral damps in vicinity of ex-copper industry particularly in the North part of the country (Lazo et al. 2019). GIS map is created to show the distribution pattern of high loads parameters of F2 (Cd(N), Zn(N), Cu(N) and Hg(N)) (Fig. 3).

Factor 3 (F3) is the next factor representing 13.8 % of the total variance. It is followed by high loads of Fe, Hg, Zn, Cd, and Cu. This group of elements is probably derived by geogenic factors that are linked with the sulfide minerals located in the North part of Albania, and other anthropogenic factors. Hg, Zn, Cd, and Cu are also typical elements for long-range transport of the chemicals, traffic emission. They may originate from oil-gas industry, shipping activity, and long-range transport of the pollutants. Hg and Cd point also the sources of fire industrial activities, waste incineration, while the association of these elements with Cu and Zn indicates the traffic emission and atmospheric deposition sources. Hg and Cd are typical anthropogenic elements probably entrapped to soil dust fine particles. It is also verified by the presence of Fe together with these elements under the same factor. Fe is naturally distributed as a typical soil element (Rudnick and Gao, 2003) that may indicate its soil dust origin. GIS map of Fig. 4 shows the distribution pattern of high loading parameters of F3 (Fe, Hg, Zn, Cd and Cu).

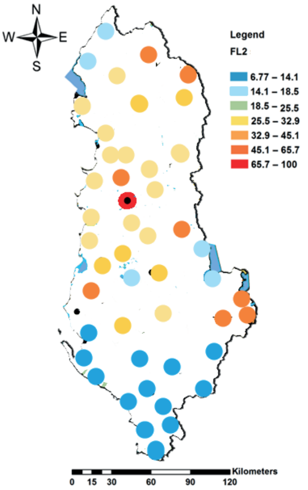

Fig. 3. Distribution pattern of factor loading FL2 linked with Cd(N), Zn(N), Cu(N) and Hg(N).

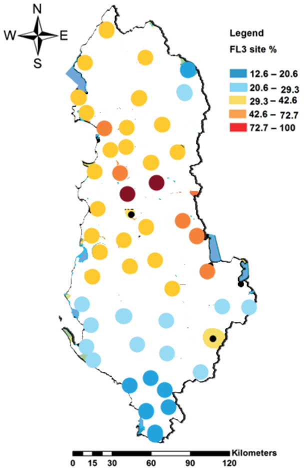

Fig. 4. Distribution pattern of factor loading FL3 linked with Fe, Hg, Zn, Cd and Cu.

Factor 4 (F4) and *Factor 5* (F5) respectively represent 11 % and 10% of the total variance. They are associated by high loads of the concentration and the normalized data of the same element, Pb and Pb(N) (F4), and As and As(N) (F5). The main sources of Pb are counted to be the vehicle exhaust and coal combustion, industrial emission sources, metallurgy of Elbasan, and geogenic factors. The strong Pb anomaly in Shkodra area is probably affected from the trans-boundary pollution of metals (Al and Fe) processing industry in Montenegro (Peck, 2004).

Arsenic is used in agriculture activity as inorganic fertilizers and herbicides. It may lead to the enrichment of As in the local soils which may enter in atmosphere as fine soil dust particles and then re-suspended as atmospheric deposition in different distances controlled by the size of dust particles. The next area with relatively high loads of As and As(N) belong to the mineralized belt in the Eastern part of the country that is probably linked with geogenic factors and soil geochemistry of the area. The distribution pattern maps of factor loads FL4 and FL5 linked with Pb and Pb(N) (FL4), and As and As(N) (FL5) are shown in Fig. 5.

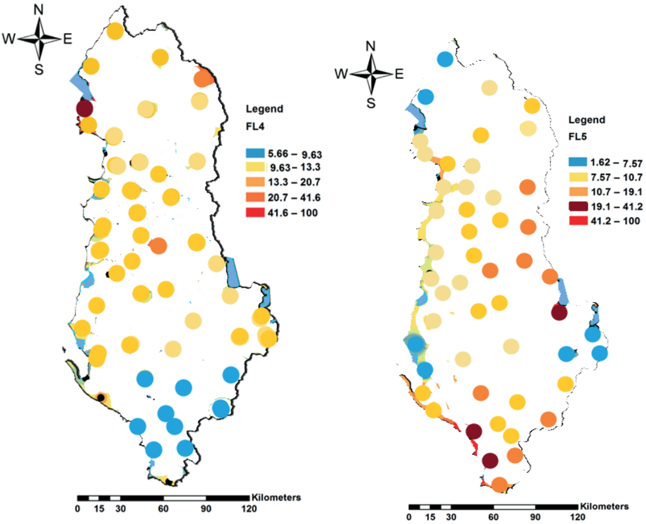

Fig. 5. Distribution pattern maps of factor loads FL4 and FL5 linked with Pb and Pb(N) (FL4), and As and As(N) (FL5).

4. Conclusions

Through this study it is clear that the biomonitoring technique by using mosses as bioindicators of metals in atmospheric deposits, combined with statistical analysis of concentration data and emission inventory gives a promising view for proper conclusions about air quality regarding the level and the presence of metals in the air.

Differentiation and the variation of metal concentrations in moss samples show strong influence of local emission sources compared to long-range atmospheric transport of the pollutants.

Higher anthropogenic level were found for Cr, Ni, Co the elements compared to the anthropogenic elements that pose high risk to human health (As, Cd, and Pb).

The results of this study represent the need for more rigorous measures regarding the emission of atmospheric pollutants originating from the mining industry, high temperature processing and smelting of metals, vehicle emissions, fertilization, pesticide spraying, waste incineration etc.

Acknowledgments

The authors express the gratitude to the staff of the NAA and Applied Research of Division of Nuclear Physics of FLNP JINR and the Institute of Chemistry, Faculty of Science, Sts. Cyril and Methodius University, Skopje, Macedonia for analyzing the Albanian moss samples.

References

1. Allajbeu, Sh., Qarri, F., Marku, E., Bekteshi, L., Ibro,V., Frontasyeva, V.M., Stafilov, T., Lazo, P., 2017. Contamination scale of atmospheric deposition for assessing air quality in Albania evaluated from most toxic heavy metal and moss biomonitoring. Air. Qual. Atmos. Health. **10**, 587–599, doi: 10.1007/s11869-016-0453-9.
2. Astel, A., Astel, K., Biziuk, A., 2008. PCA and multidimensional visualization techniques united to aid in the bioindication of elements from transplanted Sphagnum palustremoss exposed in Gdansk city area. Environ. Sci. Pollut. Res. **15** (1), 41–50.
3. Blagnytė, R., Paliulis, D., 2010. Research into Heavy Metals Pollution of Atmosphere Applying Moss as Bioindicator: a Literature Review. E. R. E. M. **4** (54), 26–33.
4. EPA/600/P-99/002aF, U.S., Final Report, 2004. Air Quality Criteria for Particulate Matter. U.S. Environmental Protection Agency, Washington, DC. Vol. **I**, p. 2–11.
5. Fernandez, J.A., Rey, A., Carballeira, A., 2000. An extended study of heavy metal deposition in Galicia (NW Spain) based on moss analysis. Sci. Total. Environ. 254, 31–44.
6. Filby, R. H. Isotopic and nuclear analytical techniques in biological systems: a critical study. Pure & Appl Chem.1995, **67**, 1929–1941.
7. Frontasyeva, M. V. Neutron activation analysis in the life sciences. Phys Part Nuclei. 2011, **42**, 332–378, doi:10.1134/S1063779611020043.
8. Gjengedal, E., Steinnes, E., 1990. Uptake of Metal Ions in Moss from Artificial Precipitation. Environ. Monit. Assess. **14**, 77–87, doi. 10.1007/BF00394359
9. Harmens, H., Norris, D.A., Sharps, K., Mills, G., Alber, R., Aleksiayenak, Y., Blum, O., Cucu-Man, S.M., Dam, M., De Temmerman, L., Ene, A., Fernandez, J.A., Martinez-Abaigar, J., Frontasyeva, M., Godzik, B., Jeran, Z., Lazo, P., Leblond, S., Liiv, S., Magnússon, S.H., Mankovska, B., Pihl Karlsson, G., Piispanen, J., Poikolainen, J., Santamaria, J.M., Skudnik, M., Spiric, Z., Stafilov, T., Steinnes, E., Stihi, C., Suchara, I., Thoni, L., Todoran, R., Yurukova, L., Zechmeister, H.G., 2015. Heavy metal and nitrogen concentrations in mosses are declining across Europe whilst some "hotspots" remain in 2010. Environ. Pollut. **200**, 93–104, doi: 10.1016/j.envpol.2015.01.036.
10. Harmens, H., Norris, D., Mills, G., and the participants of the ICP Vegetation moss survey, 2013. Heavy metals and nitrogen in mosses: spatial patterns in 2010/2011 and long-term temporal trends in Europe. ICP Vegetation Programme Coordination Centre, Centre for Ecology and Hydrology, Bangor, UK, p. 63. https://icpvegetation.ceh.ac.uk/
11. Harmens, H., Mills, G., Hayes F., Norris, D., and the participants of the ICP Vegetation moss survey, 2011. Air Pollution and Vegetation ICP Vegetation Annual Report 2010/2011. ISBN: 978-1-906698-26-3. https://icpvegetation.ceh.ac.uk/
12. Harmens, H., Norris, D. A., Steinnes, E., Kubin, E., Piispanen, J., Alber, R., Aleksiayenak, Y., Blum, O., Coşkun, M., Dam, M., De Temmerman, L., Fernández, J.A., Frolova, M., Frontasyeva, M., González-Miqueo, L., Grodzińska, K., Jeran, Z., Korzekwa, S., Krmar, M., Kvietkus, K., Leblond, S., Liiv, S., Magnússon, S.H., Maňkovská, B., Pesch, R., Rühling, Å., Santamaria, J.M., Schröder, W., Spiric, Z., Suchara, I., Thöni, L., Urumov, V., Yurukova, L., Zechmeister, H.G., 2010. Mosses as biomonitors of atmospheric heavy metal deposition: spatial and temporal trends in Europe. Environ. Pollut. **158**, 3144–3156.
13. Harmens, H., Buse, A., Büker, P., Norris, D., Mills, G., Williams, B., Reynolds, B., Ashenden T. W., Ruhling, A., Steinnes, E., 2004. Heavy Metal Concentrations in European Mosses: 2000/2001 Survey. J. Atmos. Chem. **49**, 425–436. doi. 10.1007/s10874-004-1257-0.

14. Järup, L., 2003. Hazards of heavy metal contamination. British Medical Bulletin. 68(1), 167–182, doi.10.1093/bmb/ldg032.
15. Lazo, P., Stafilov, T., Qarri, F., Allajbeu, Sh., Bekteshi, L., Fronasyeva, M., Harmens, H., 2019. Spatial and temporal trend of airborne metal deposition in Albania studied by moss biomonitoring. Ecol. Indic. **101**, 1007–1017, doi. 10.1016/j.ecolind.2018.11.053.
16. Loring, H.D., Rantala, R., 1992. Manual for the Geochemical Analyses of Marine Sediments and Suspended Particulate Matter. Earth-Science Review 32, 235–283, doi. 10.1016/0012-8252(92)90001-A.
17. Pacyna, J.M., Pacyna, E.G., 2001. An assessment of global and regional emissions of trace metals to the atmosphere from anthropogenic sources worldwide. Environ. Rev. **9**(4), 269–298, doi:10.1139/a01-012.
18. Peck, P., 2004. Reducing Environment and Security Risks from Mining in South Eastern Europe: Desk-assessment study for the Environment and Security Initiative Project. UNEP Division of Technology.
19. Qarri, F., Lazo, P., Stafilov, T., Bekteshi, L., Baceva, K., Marka, J., 2014. Survey of atmospheric deposition of Al, Cr, Fe, Ni, V and Zn in Albania by using Moss biomonitoring and ICP-AES. Air. Qual. Atmos. Health. **7**, 297–307, doi: 10.1007/s11869-014-0237-z.
20. Reimann, C., Filzmoser, P., Garrett, R., 2002. Factor Analysis applied to regional geochemical data: problems and possibilities. Appl. Geochem. **17** (3), 185–206, doi. /10.1016/S0883-2927(01)00066-X.
21. Richards, J.R., 2020. Control of Particulate Matter Emissions. APTI Course 413 Third Edition. ICES Ltd.EPA Contract No. 68D99022.
22. Rudnick, R.L., Gao, S., 2003. Composition of the continental crust. Treatise. Geochem. **3**, 1–64.
23. Rühling, A., 1994. Atmospheric Heavy Metal Deposition in Europe-Estimations Based on Moss Analysis. Nordic Council of Ministers, (ed.) AKA Print, A/S Arhus, p. 9.
24. Salbu, B., Steinnes, E. Applications of Nuclear Analytical Techniques in Environmental Research. Analyst. 1992, 117, 243–249.
25. Saxena, D.K., Singh, Sh., Srivastava, K., 2008. Atmospheric Heavy Metal Deposition in Garhwal Hill Area (India): Estimation Based on Native Moss Analysis. Aerosol Air Qual. Res. **8**(1), 94–111.
26. Schröder, W., Nickel, S., Schönrock, S., Meyer, M., Wosniok, W., Harmens, H., Frontasyeva, V.M., Alber, R., Aleksiayena, J., Barandovski, L., Carballeira, A., Danielsson, H., de Temmermann, L., Godzik, B., Jeran, Z., Karlsson, G.P., Lazo, P., Leblond, S., Lindroos, A.J., Liiv, S., Magnússon, S.H., Mankovska, B., Martínez-Abaigar, J., Piispanen, J., Poikolainen, J., Popescu, I.V., Qarri, F., Santamaria, J.M., Skudnik, M., Špirić, Z., Stafilov, T., Steinnes, E., Stihi, C., Thöni, L., Uggerud, H.T., Zechmeister , H.G., 2016. Spatially valid data of atmospheric deposition of heavy metals and nitrogen derived by MS for pollution risk assessments of ecosystems. Environ. Sci. Pollut. Res. **23** (11), 10457–10476, doi. 10.1007/s11356-016-6577-5.
27. Stafilov, T., Šajn, R., Barandovski, L., Bačeva, A.K., Malinovska. S., 2018. Moss biomonitoring of atmospheric deposition study of minor and trace elements in Macedonia. Air Qual. Atmos. Health. **11** (2), 137–152, doi.10.1007/s11869-017- 0529-1.
28. Stanković, J. D., Sabovljević, A. D., Sabovljević, M. S., 2018. Bryophytes and heavy metals: a review. Acta. Botanica. Croat. **77** (2), 109–118.
29. Steiness, E., 1989. Biomonitors of Air Pollution by Heavy Metals. In: Pacyna, J.M., Ottar, B., (eds) Control and Fate of Atmospheric Trace Metals. NATO ASI Series (Series C: Mathematical and Physical Sciences), Springer. Vol. **268**, p. 321–338, doi. 10.1007/978-94-009-2315-7-15.
30. Steiness, E., Rühling, Å.,Lippo, H., Makinen, H., 1997. Reference materials for large-scale metal deposition survey. Accred. Qual. Assur. **2**, 243–249.
31. Tremper, A. H., Agneta, M., Burton, S., Higgs, D. E. B., 2004. Field and laboratory exposures of two moss species to low level metal pollution. J. Atmos. Chem. **49**, 111–120.
32. UNDP-Albania, 2010. Ferrochrome smelter in Elbasan; Fwienv contract n_1-BH0381. In: Consultancy Services to Conduct Environmental Impact Assessment of Ten High Priority

Environmental Hotspots to Form the Basis for a Major Remediation Programme, for the Project: “Identification and Prioritization of Environmental Hot Spots in Albania” EIA Report Final.

33. UNEP, 2013. Environmental Risks and Challenges of Anthropogenic Metals Flows and Cycles, A Report of the Working Group on the Global Metal Flows to the International Resource Panel. Van Der Voet, E., Salminen, R., Eckelman, M., Mudd, G., Norgate, T., Hischier, R. Copyright © United Nations Environment Programme, 2013.
34. WHO, 2000. Air quality guidelines for Europe, second ed. 91, Ed. Theakston, F., WHO Regional Publications, Copenhagen. https://apps.who.int/iris/handle/10665/107335.

APPLICATION OF NEUTRON RESONANCE CAPTURE ANALYSIS FOR THE INVESTIGATION OF THE ELEMENT COMPOSITION OF THE PANEL FROM THE TRIPTYCH (PRESUMABLY 17TH CENTURY)

N.V. Simbirtseva[1,2], P.V. Sedyshev[1], S.T. Mazhen[1,2], A. Yergashov[1,2,3], A.Yu. Dmitriev[1], V.L. Ivchenkov[4]

[1]Frank Laboratory of Neutron Physics, Joint Institute for Nuclear Research, Dubna, Russia
[2]Institute of Nuclear Physics, Almaty, 050032, the Republic of Kazakhstan
[3] L.N. Gumilyov Eurasian National University, 010008 Nur-Sultan, Kazakhstan
[4]Museum and Exhibition Complex (MVK) "Volokolamsk Kremlin", Volokolamsk, Russia

The method of Neutron Resonance Capture Analysis (NRCA) is currently being developed at the Frank Laboratory of Neutron Physics (FLNP). The method is fully non-destructive it can be used to determine the bulk composition of objects without preparation or sample taking. The NRCA is based on the registration of neutron resonances and the measurement of the yield of reaction products in the resonances.

In this paper, we describe the application of NRCA for the investigation of an archeological object transferred to the FLNP by the Museum and Exhibition Complex (MVK) "Volokolamsk Kremlin". The object was the panel from the triptych (presumably 17th century) which was found in the Moscow region, Volokolamsk district, Chubarovo village.

1. INTRODUCTION

Neutron Resonance Capture Analysis (NRCA) is applied to determine the elemental composition of objects [1]. The method is non-destructive, doesn't require special preparation of samples, and allows measuring the bulk composition of objects. All these analysis characteristics listed are useful for the investigation of archeological samples. The method of NRCA is currently being developed at the Frank Laboratory of Neutron Physics (FLNP) [2,3]. It is based on the registration of neutron resonances and the measurement of reaction products yield in these resonances.

In this paper, we describe the application of NRCA for the investigation of an archeological object transferred to the FLNP by the Museum and Exhibition Complex (MVK) "Volokolamsk Kremlin" under terms of a concluded cooperation agreement. In total, 28 fragments of pottery and 25 metal finds were transferred for research.

One of the provided artifacts is the panel of the triptych (Fig.1). The object presumably dates back to the 17th century. The panel was found in the Moscow region, Volokolamsk district, Chubarovo village. Only one panel of the triptych was found in the excavation that is probably due to the Old Believers tradition. According to the tradition, during the wedding ceremony, the girl disassembled the triptych (the three-panel icon) and took one panel with her to her husband's house as a keepsake of her family. The artifacts investigations by various methods and the scientific analysis will reveal the handicraft production centers; clarify the finds dating and their technological schemes.

Fig. 1. The panel of the triptych (presumably 17th century).

2. EXPERIMENT

The sample was irradiated with neutrons by resonance neutron source (IREN) facility and reactions time-of-flight spectrum (n,γ) was registered. The main part of the IREN facility is a linear electron accelerator LUE-200 with a non-multiplying neutron-producing target of the VNZH-90 alloy [4, 5]. The facility parameters were: the average energy of electrons ~ 60 MeV, the peak current ~ 1.5 A, the width of electron pulse ~ 100 ns, and the repetition rate 25 Hz. The total neutron yield was about $3 \cdot 10^{11}$ s^{-1}. The measurements were carried out at 58.6 meters flight path of the IREN 3rd channel. A big liquid scintillator detector was used for the registration of γ-quanta [6]. The sample was placed inside the detector. The neutron flux was permanently monitored by the SNM-17 neutron counter. The signals from the detector and the monitor counter were simultaneously fed to two independent inputs of the time-to-digital converter (TDC). The time-of-flight spectra were stored on a computer disk for later offline processing.

The sample measurements lasted about 98 hours. The resonance energies were determined according to the following formula:

$$E = \frac{5227 L^2}{t^2}, \tag{1}$$

where, t – time of flight in microseconds, L – flight path in meters, E – kinetic energy of a neutron in eV.

The resonances of copper and zinc were identified on the time-of-flight spectrum (Fig.2) [7, 8].

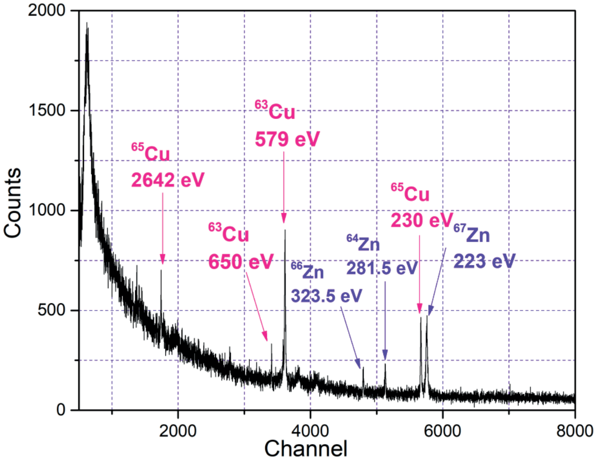

Fig. 2. The part of reactions time-of-flight spectrum (n,γ) obtained in measurements on the panel of the triptych material. The time channel width is 50 ns.

The measurements with standard samples of copper and zinc were made in addition to themeasurement with the investigated sample (Fig. 3, 4).

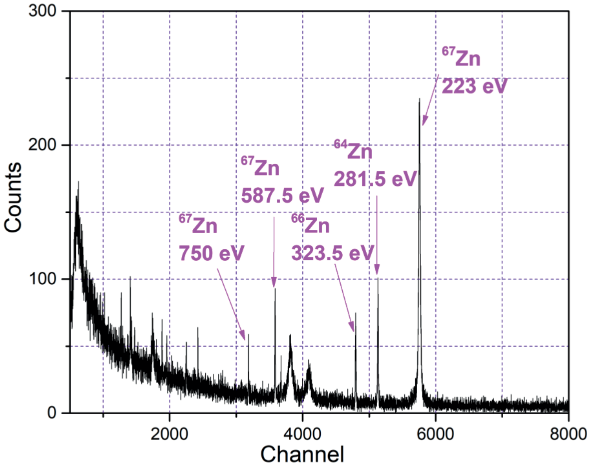

Fig. 3. The part of reactions time-of-flight spectrum (n,γ) of zinc standard sample. The time channel width is 50 ns.

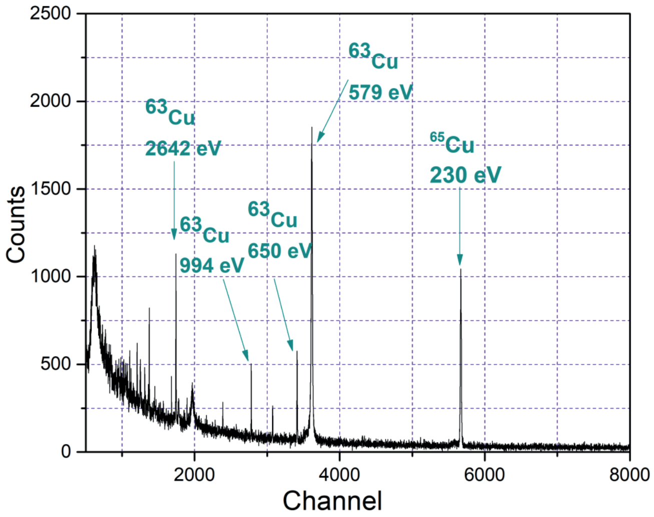

Fig. 4. The part of reactions time-of-flight spectrum (n,γ) of copper standard sample. The time channel width is 50 ns.

3. DATA ANALYSIS AND RESULTS

The number of the element nuclei in the sample was determined by gamma-quanta yield measurement in the resonances. Two resonances of zinc and two resonances of copper were selected during the experimental data analysis. The detector sum of counts in resonance is expressed by the following formula:

$$\sum N = f(E_0)\cdot S\cdot t\cdot \varepsilon_\gamma \cdot \frac{\Gamma_\gamma}{\Gamma} A\,. \tag{2}$$

Here, $f\,(E_0)$ is the neutron flux density at the resonance energy E_0, S – the sample area, t – measuring time, ε_γ – the detection efficiency of the detector radiative capture, $\Gamma\gamma$, Γ – the radiative and total resonance widths.

$$A = \int_{E1}^{E2} [1 - T(E)]dE \tag{3}$$

is a resonance area on the transmission curve, where $E1$, $E2$ – initial and final values of energy range near resonance.

$$T(E) = e^{-n\sigma(E)} \tag{4}$$

the energy dependence of the neutron transmission by the sample; σ(E) – the total cross section at this energy with Doppler broadening, n – the number of isotope nuclei per unit area. The value A was determined from experimental data for investigated sample by the next formula:

$$A_x = \frac{\sum N_x \cdot M_s \cdot S_s}{\sum N_s \cdot M_x \cdot S_x} \cdot A_s \quad (5)$$

Here, $\sum N_x$, $\sum N_s$ – counts under the resonance peak of the investigated and standard samples, S_x, S_s – the area of the investigated and standard samples. M_x, M_s – the number of monitor counts during the measurement of the investigated and standard samples.

The A_S value was calculated by means of known resonances and n_S parameters for the standard sample. The n_X value was determined from the investigated sample A_X value. The values of $\sigma(E)$ and A were numerically determined, by using the algorithm which was described in [9]. This procedure is schematically shown in (Fig.5). The analysis results are presented in the Table1.

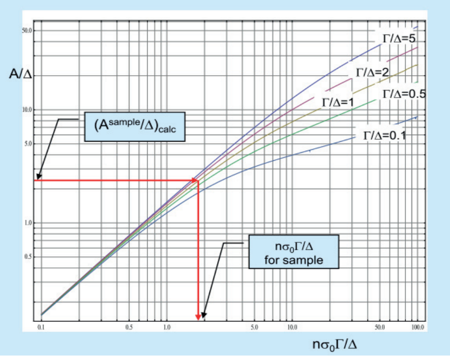

Fig**.** 5**.** Dependence of value *A* on a number of nuclei and resonance parameters [9].

Table 1. Measurements results of the panel of the triptych (presumably 17th century).

№	Element	Mass, g	Weight, %
1	Cu	10.6±2.1	57±11
2	Zn	7.71±0.39	41.5±2.1

4. CONCLUSION

The elemental and isotopic composition of the panel from the triptych was determined by NRCA. The mass of the artifact is 17.22 g. According to the result of the analysis, the value of determining total elements mass coincides with the triptych panel mass within the margin of error.

The elemental composition may help to identify the place of manufacture and the origin of the object. More likely it should be compared to both the local and the Pomor casting (Vygovsky Monastery), the Transfiguration Monastery casting in Moscow, the casting of Vychegda Old Believers.

Acknowledgements. The authors express their gratitude to the staff of the IREN facility and A.P. Sumbaev, the head of the facility development, to V.V. Kobets, the head of sector No.5 of the Scientific and Experimental Injection and Ring Division of the Nuclotron

(Veksler and Baldin Laboratory of High Energy Physics), for the supporting with uninterrupted operation of the facility in the process of measurements. We are also grateful to D. Borisov, a laboratory assistant of the Neutron-Nuclear Interactions Research sector, for useful discussion.

REFERENCES

[1] Postma H. and Schillebeeckx P., 2017, *Ed. by N. Kardjilov and G. Festa* Springer, Cham., pp.235–283.
[2] Sedyshev P.V., Simbirtseva N.V., Yergashov A.M., Mazhen S.T., Mareev Yu.D., Shvetsov V.N., Abramzon M.G., and Saprykina I.A., 2020, *Physics of Particles and Nuclei Letters*, vol.**17**, No.3, pp.389–400.
[3] Bazhazhina N.V., Mareev Yu.D., Pikelner L.B., Sedyshev P.V., Shvetsov V.N., 2015, *Physics of Particles and Nuclei Letters*, vol. **12**, pp. 578–583.
[4] Belikov O., Belozerov A., Becher Yu., Bulycheva Yu., Fateev A., Galt A., Kayukov A., Krylov A., Kobetz V., Logachev P., Medvedko A., Meshkov I., Minashkin V., Pavlov V., Petrov V., Pyataev V., Rogov A., Sedyshev P., Shabratov V., Shvec V., Shvetsov V., Skrypnik A., Sumbaev A., Ufimtsev V., and Zamrij V., 2010, *Journal of Physics: Conf.* Ser. **205**, 012053.
[5] Sumbaev A., Kobets V., Shvetsov V., Dikansky N., and Logatchov P., 2020, *https://iopscienchttps://doi.org/10.1088/1748- 0221/15/11/T11006*
[6] Maletsky H.,.Pikelner L.B.,.Rodionov K.G., Salamatin I.M., and Sharapov E.I., 1972, *Communication of JINR13-6609* Dubna, JINR, 1–15 (in Russian).
[7] Sukhoruchkin S.I., Soroko Z.N., and Deriglazov V.V., 1998, *Low Energy Neutron Physics. Landolt Bornstein. V.* **I/16B**, Berlin: Springer Verlag.
[8] Mughabghab S.F., 1984, Neutron Gross Sections, Neutron Resonance Parameters and Thermal Gross Sections. *Academic Press*, New York.
[9] Efimov V.N. and Shelontsev I.I., 1961, “Calculation for graphs of determining the parameters of neutron resonances by the transmission method”, *Communications of the JINR P-641,* Dubna, 1–19 (in Russian).

LITHIUM LEVEL IN THE PROSTATE OF THE NORMAL HUMAN: A SYSTEMATIC REVIEW

V. Zaichick

Medical Radiological Research Centre, Korolyev St., 4, Obninsk, 249036, Russia

e-mail: vzaichick@gmail.com

Introduction

The prostate gland is subject to various disorders and of them chronic prostatitis, benign prostatic hyperplasia (BPH), and prostate cancer (PCa) are extremely common diseases of ageing men [1–3]. The etiology and pathogenesis of these diseases remain not well understood. A better understanding of the etiology and causative risk factors are essential for the primary prevention of these diseases.

In our previous studies the significant involvement of trace elements (TEs) in the function of the prostate was found. [4–15]. It was also shown that levels of TEs in prostatic tissue can play a significant role in etiology of PCa [16–19]. Moreover, it was demonstrated that the changes of some TE levels and TE content ratios in prostate tissue can be used as biomarkers [20–26].

The effects of TEs, including Li (lithium), are related to their concentration. Recorded observations range from a deficiency state, through normal function as biologically essential components, to an imbalance, when excess of one element interferes with the function of another, to pharmacologically active concentrations, and finally to toxic and even life-threatening concentrations [27,28].

By now, an exceedingly scant literature exists on quantitative Li content in tissue of "normal" and affected glands. The analyses reported are few in number, incomplete and difficult to interpret. Moreover, the findings of various studies indicate some discrepancies.

The present study addresses the significance of Li levels in prostatic tissue as a biomarker of the gland's condition. Therefore, we systematically reviewed all the available relevant literature and performed a statistical analysis of Li content in tissue of "normal" glands, which may provide valuable insight into the etiology and diagnosis of prostate disorders.

Materials and Methods

Data sources and search strategy

Aiming at finding the most relevant articles for this review, a thorough comprehensive web search was conducted by consulting the Web of Science, Scopus, PubMed, MEDLINE, ELSEVIER-EMBASE, and Cochrane Library databases, as well as from the personal archive of the author collected between May 1966 to September 2021, using the key words: prostatic trace elements, prostatic Li content, prostatic tissue, and their combinations. For example, the search terms for Li content were: "Li mass fraction", "Li content", "Li level", "prostatic tissue Li" and "Li of prostatic tissue". The language of the article was not restricted. The titles from the search results were evaluated closely and determined to be acceptable for potential inclusion criteria. Also, references from the selected articles were examined as further search tools. Relevant studies noted for the each selected article were also evaluated for inclusion.

Eligibility criteria

Inclusion criteria

Only papers with quantitative data of Li prostatic content were accepted for further evaluation. Studies were included if the control groups were healthy human males with no history or evidence of urological or other andrological disease and Li levels were measured in samples of prostatic tissue.

Exclusion criteria

Studies were excluded if they were case reports. Studies involving persons from Li contaminated area and subjects that were Li therapeutic or occupational exposed were also excluded.

Data extraction

A standard extraction of data was applied, and the following available variables were extracted from each paper: method of Li determination, number and ages of healthy persons, sample preparation, mean and median of Li levels, standard deviations of mean, and range of Li levels. Abstracts and complete articles were reviewed independently, and if the results were different, the texts were checked once again until the differences were resolved.

Statistical analysis

Studies were combined based on means of Li levels in prostatic tissue. The articles were analyzed and "Median of Means" and "Range of Means" were used to examine heterogeneity of Li contents. The objective analysis was performed on data from the 23 studies, with 1190 healthy subjects.

Results

Information about Li levels in prostatic tissue in different prostatic diseases is of obvious interest, not only to understand the etiology and pathogenesis of prostatic diseases more profoundly, but also for their diagnosis, particularly for PCa diagnosis and PCa risk prognosis [27]. Thus, it dictates a need for reliable values of the Li levels in the prostatic tissue of apparently healthy subjects, ranging from young adult males to elderly persons.

Possible publications relevant to the keywords were retrieved and screened. A total of 2312 publications were primarily obtained, of which 2289 irrelevant papers were excluded. Thus, 23 studies were ultimately selected according to eligibility criteria that investigated Li levels in tissue of "normal" prostates (Table 1) and these 23 papers [8, 9, 12, 14, 25, 29–46] comprised the material on which the review was based. A number of values for Li mass fractions were not expressed on a wet mass basis by the authors of the cited references. However, we calculated these values using the medians of published data for water – 83% [47–50] and ash – 1% (on a wet mass basis) contents in "normal" prostates of adult men [49,51–53].

Table 1 summarizes general data from the 23 studies. The retrieved studies involved 1190 subjects. The ages of subjects were available for 22 studies and ranged from 0–87 years. Information about the analytical method and sample preparation used was available for 23 studies. All studies determined Li levels by destructive (require acid digestion of tissue samples) analytical methods (Table 1): eight using inductively coupled plasma atomic emission spectrometry (ICP-AES) and nine – inductively coupled plasma mass spectrometry (ICPMS). In five studies a combination of ICP-AES and ICP-MS methods was used and results were summarized.

Table 1. Reference data of Li mass fractions (mg/kg wet tissue) in "normal" human prostatic tissue

Reference	Method	n	Age, years Range	Li M±SD	 Range
Zakutinsky et al. 1962 [29]	–	–	–	0.013	–
Zaichick et al. 2011 [30]	ICP-MS	10	0–10	0.0182±0.0088	0.0053–0.0289
		10	1–20	0.0053±0.0037	0.0026–0.0112
		28	21–40	0.0066±0.0046	0. 0026–0.0165
		27	41–60	0.0070±0.0041	0.0029–0.0170
		8	61–72	0.0075±0.0060	0.0026–0.0172
		83	0–72	0.0088±0.0070	0. 0026–0.0289
Zaichick et al. 2012 [31]	ICP-AES	64	13–60	0.0068±0.0041	0.0026–0.0170
Zaichick et al. 2012 [32[	ICP-MS	64	13–60	0.0068±0.0041	0.0026–0.0170
Zaichick et al. 2013 [8]	ICPAES	16	20–30	0.0068±0.0046	–
Zaichick et al. 2013 [9]	ICPMS	16	20–30	0.0109±0.0083	–
Zaichick et al. 2014b [33]	ICPAES	28	21–40	0.0068±0.0046	0.0026–0.0165
		27	41–60	0.0070±0.0039	0.0029–0.0170
		10	61–87	0.0075±0.0060	0.0026–0.0172
Zaichick et al. 2014 [34]	ICPMS	28	21–40	0.0068±0.0046	0.0026–0.0165
		27	41–60	0.0070±0.0039	0.0029–0.0170
		10	61–87	0.0075±0.0060	0.0026–0.0172
Zaichick et al. 2014 [12]	ICPAES	50	0–30	0.014±0.012	–
		29	0–13	0.020±0.014	–
		21	14–30	0.0088±0.0056	–
Zaichick et al. 2014 [35]	ICPMS	50	0–30	0.014±0.012	–
		29	0–13	0.020±0.014	–
		21	14–30	0.0084±0.0058	–
Zaichick et al. 2014 [14]	2 Methods	16	20–30	0.0068±0.0046	–
Zaichick 2015 [36]	2 Methods	65	21–87	0.0070±0.0044	–
Zaichick et al. 2016 [37]	ICPAES	28	21–40	0.0080±0.0079	–
		27	41–60	0.0086±0.0062	–
		10	61–87	0.0087±0.0076	–
Zaichick et al. 2016 [38]	ICPMS	28	21–40	0.0080±0.0079	–
		27	41–60	0.0086±0.0062	–
		10	61–87	0.0087±0.0076	–
Zaichick et al. 2016 [39]	ICPAES	37	41–87	0.0071±0.0044	0.0026–0.0172
Zaichick et al. 2016 [40]	ICPAES	32	44–87	0.0073±0.0046	0.0026–0.0172
Zaichick et al. 2016 [41]	ICPAES	37	41–87	0.0071±0.0044	0.0026–0.0172
Zaichick et al. 2016 [42]	ICPMS	32	44–87	0.0072±0.0055	–
Zaichick et al. 2016 [43]	ICPMS	37	41–87	0.0071±0.0056	–
Zaichick et al. 2017 [25]	ICPMS	37	41–87	0.0071±0.0056	–
Zaichick et al. 2017 [44]	2 Methods	37	41–87	0.0082±0.0049	0.00284–0.0190
Zaichick 2017 [45]	2 Methods	37	41–87	0.0071±0.0045	0.0026–0.0172
Zaichick et al. 2019 [46]	2 Methods	37	41–87	0.0071±0.0045	0.0026–0.0172
Median of means				0.0074	
Range of means (M_{min} - M_{max}),				0.0068–0.0200	
Ratio M_{max}/M_{min}				(0.0200/0.0068)=2.94	
All references				23	

Discussion

The range of means of Li mass fractions reported in the literature for "normal" prostatic tissue varies from 0.0068 mg/kg [33] to 0.020 mg/kg [35] with median of means 0.0074 mg/kg of wet tissue (Table 1). The maximal value of mean Li mass fraction reported [35] was 2.94 times higher the minimal published Li mass fraction (Table 1).

This variability of reported mean values can be explained by a dependence of Li content on many factors, including analytical method imperfections, differences in "normal" prostate definitions, possible non-homogeneous distribution of Li levels throughout the prostate gland volume, diet, smoking, alcohol intake and others. Not all these factors were strictly controlled in the cited studies.

In our opinion, the leading cause of inter-observer Li content variability was the need for sample destruction. In 22 of 23 reported papers such destructive analytical methods as ICP-AES and ICPMS were used. These methods require acid digestion of the samples at a high temperature. There is evidence that use of this treatment causes some quantities of TEs to be lost [24,54,55]. On the other hand, the Li content of chemicals used for acid digestion can contaminate the prostate samples. Thus, when using destructive analytical methods it is necessary to allow for the losses of TEs, for example when there is complete acid digestion of the sample. Then there are contaminations by TEs during sample decomposition, which require addition of some chemicals. It is possible to avoid these problems by using non-destructive methods, but up to now there are no analytical methods which allow to quantify Li content in "normal" prostate without acid digestion of the samples at a high temperature. It is, therefore, reasonable to conclude that the quality control of results is very important factor for using the Li content in prostatic tissue as biomarkers.

All natural chemical elements of the Periodic System, including Li, present in all subjects of biosphere [27,56,57]. During the long evolutional period intakes of Li in organisms were more or less stable and organisms were adopted for such environmental conditions. Moreover, organisms, including human body, involved low doses of this element in their functions. The situation began to change after the industrial revolution, particularly, over the last 100 years. The primary use of Li is in industry and medicine. Thus, inorganic Li is ubiquitously distributed in environment and food, water, and air everywhere contain this element. In addition to the abundant natural sources of Li, there are a large number of industrial and pharmaceutical sources of Li to the soil, water, and air (through atmospheric industrial emissions) contamination. From the polluted environment Li is subsequently introduced into the food chain and food is the major source of human exposure to Li.

There are some limitations in our study, which need to be taken into consideration when interpreting the results of this review. The sample size of each study was sometimes relatively small (from 10 to 65), and 22 of 23 studies were done one team. As such, it is hard to draw definite conclusions about the reference value of the Li content in "normal" prostate as well as about the clinical value of the Li levels in "normal" prostates as a biomarker.

References

1. Nickel J.C. (2011) Prostatitis. Can. Urol. Assoc. J. **5**:306–315.
2. Lim K.B. (2017) Epidemiology of clinical benign prostatic hyperplasia. Asian J. Urol. **4**:148–151.
3. Rawla P. (2019) Epidemiology of prostate cancer. World J. Oncol. **10**(2):63–89.

4. Avisyn A.P., Dunchik V.N., Zhavoronkov A.A., Zaichick V.E., Sviridova T.V. (1981) Histological structure of the prostate and content of zinc in it during various age period. Archiv Anatomy, Gistology, and Ebriology (Leningrad) **81**(11):76–83.
5. Zaichick V. (2004) INAA and EDXRF applications in the age dynamics assessment of Zn content and distribution in the normal human prostate. J. Radioanal Nucl. Chem. **262**:229–234.
6. Zaichick V., Zaichick S. (2013) The effect of age on Br, Ca, Cl, K, Mg, Mn, and Na mass fraction in pediatric and young adult prostate glands investigated by neutron activation analysis. Appl. Radiat. Isot. **82**:145–151.
7. Zaichick V., Zaichick S. (2013) INAA application in the assessment of Ag, Co, Cr, Fe, Hg, Rb, Sb, Sc, Se, and Zn mass fraction in pediatric and young adult prostate glands. J. Radioanal Nucl. Chem. **298**:1559–1566.
8. Zaichick V., Zaichick S. (2013) NAA-SLR and ICP-AES application in the assessment of mass fraction of 19 chemical elements in pediatric and young adult prostate glands. Biol. Trace Elem. Res. **156**:357–366.
9. Zaichick V., Zaichick S. (2013) Use of neutron activation analysis and inductively coupled plasma mass spectrometry for the determination of trace elements in pediatric and young adult prostate. Am. J. Analyt. Chem. **4**:696–706.
10. Zaichick V., Zaichick S. (2014) Relations of bromine, iron, rubidium, strontium, and zinc content to morphometric parameters in pediatric and nonhyperplastic young adult prostate glands. Biol. Trace Elem. Res. **157**:195–204.
11. Zaichick V., Zaichick S.(2014) Relations of the neutron activation analysis data to morphometric parameters in pediatric and nonhyperplastic young adult prostate glands. Advances in Biomedical Science and Engineering **1**:26–42.
12. Zaichick V., Zaichick S. (2014) Relations of the Al, B, Ba, Br, Ca, Cl, Cu, Fe, K, Li, Mg, Mn, Na, P, S, Si, Sr, and Zn mass fractions to morphometric parameters in pediatric and nonhyperplastic young adult prostate glands. BioMetals **27**:333–348.
13. Zaichick V., Zaichick S. (2014) The distribution of 54 trace elements including zinc in pediatric and nonhyperplastic young adult prostate gland tissues. Journal of Clinical and Laboratory Investigation Updates **2**(1):1–15.
14. Zaichick V., Zaichick S. (2014) Androgen-dependent chemical elements of prostate gland. Androl. Gynecol.: Curr. Res. 2:2.
15. Zaichick V., Zaichick S. (2015) Differences and relationships between morphometric parameters and zinc content in nonhyperplastic and hyperplastic prostate glands. Br. J. Med. & Med. Res. **8**:692–706.
16. Schwartz M.K. (1975) Role of trace elements in cancer. Cancer Res. **35**:3481–3487.
17. Zaichick V., Zaichick S. (1999) Role of zinc in prostate cancerogenesis. In: Mengen und Spurenelemente. 19. Arbeitstagung. Friedrich-Schiller-Universitat, Jena, pp 104–115.
18. Zaichick V., Zaichick S. Wynchank S. (2016) Intracellular zinc excess as one of the main factors in the etiology of prostate cancer. J. Anal. Oncol. **5**:124–131.
19. Zaichick V., Zaichick S., Rossmann M. (2016) Intracellular calcium excess as one of the main factors in the etiology of prostate cancer. AIMS Mol. Sci. **3**:635–647.
20. Dunchik V., Zherbin E., Zaichick V., Leonov A., Sviridova T. (1980) Method for differential diagnostics of prostate malignant and benign tumours. Russian patent (Author's Certificate No 764660, priority of invention 27.10.1977). Discoveries, Inventions, Commercial Models, Trade Marks 35:13.
21. Zaichick V., Sviridova T., Zaichick S. (1997) Zinc in the human prostate gland: normal, hyperplastic and cancerous. Int. Urol. Nephrol. **29**:565–574.
22. Zaichick V., Sviridova T., Zaichick S. (1997) Zinc in human prostate gland: normal, hyperplastic and cancerous. J. Radioanal. Nucl. Chem. **217**:157–161.

23. Zaichick S., Zaichick V. (2012) Trace elements of normal, benign hypertrophic and cancerous tissues of the human prostate gland investigated by neutron activation analysis. J. Appl. Radiat. Isot. **70**:81–87.
24. Zaichick V., Zaichick S. (2016) Ratios of selected chemical element contents in prostatic tissue as markers of malignancy. Hematol. Med. Oncol. **1**(2):1–8.
25. Zaichick V., Zaichick S. (2017) Trace element levels in prostate gland as carcinoma's markers. J. Cancer Ther. **8**:131–145.
26. Zaichick V., Zaichick S. (2017) Ratios of Zn/trace element contents in prostate gland as carcinoma's markers. Cancer Rep. Rev. **1**(1):1–7.
27. Zaichick V. (2006) Medical elementology as a new scientific discipline. J. Radioanal. Nucl. Chem. **269**:303–309.
28. Enderle J., Klink U., di Giuseppe R., Koch M., Seidel U., Weber K., Birringer M., Ratjen I., Rimbach G., Lieb W. (2020) Plasma lithium levels in a general population: a cross-sectional analysis of metabolic and dietary correlates. Nutrients **12**(8):2489.
29. Zakutinsky D.I., Parfyenov Yu.D., Selivanova L.N. (1962) Data book on the radioactive isotopes toxicology. State Publishing House of Medical Literature, Moscow.
30. Zaichick S., Zaichick V., Karandashev V., Nosenko C., Ermidou-Pollet S., Pollet S. (2011) The effect of age on the lithium content in prostate of healthy men. In: Interaction of Neutrons with Nuclei. Joint Institute for Nuclear Research, Dubna, Moscow Region, Russia, pp. 337–341.
31. Zaichick V., Nosenko S., Moskvina I. (2012) The effect of age on 12 chemical element contents in intact prostate of adult men investigated by inductively coupled plasma atomic emission spectrometry. Biol. Trace Elem. Res. **147**:49–58.
32. Zaichick S., Zaichick V., Nosenko S., Moskvina I. (2012) Mass fractions of 52 trace elements and zinc trace element content ratios in intact human prostates investigated by inductively coupled plasma mass spectrometry. Biol. Trace Elem. Res. **149**:171–183.
33. Zaichick V., Zaichick S. (2014) Determination of trace elements in adults and geriatric prostate combining neutron activation with inductively coupled plasma atomic emission spectrometry. Open Journal of Biochemistry **1**(2):16–33.
34. Zaichick V., Zaichick S. (2014) Use of INAA and ICP-MS for the assessment of trace element mass fractions in adult and geriatric prostate. J. Radioanal. Nucl. Chem .**301**(2):383–397.
35. Zaichick V., Zaichick S. (2014) The distribution of 54 trace elements including zinc in pediatric and nonhyperplastic young adult prostate gland tissues. Journal of Clinical and Laboratory Investigation Updates **2**(1):1–15.
36. Zaichick V. (2015) The variation with age of 67 macro- and microelement contents in nonhyperplastic prostate glands of adult and elderly males Investigated by nuclear analytical and related methods. Biol. Trace Elem. Res. **168**:44–60.
37. Zaichick V., Zaichick S. (2016) Age-related changes in concentration and histological distribution of 18 chemical elements in nonhyperplastic prostate of adults. World Journal of Pharmaceutical and Medical Research **2**(4):5–18.
38. Zaichick V., Zaichick S.(2016) Age-related changes in concentration and histological distribution of 54 trace elements in nonhyperplastic prostate of adults. Int. Arch. Urol. Complic. **2**(2):019.
39. Zaichick V., Zaichick S. (2016) The comparison between the contents and interrelationships of 17 chemical elements in normal and cancerous prostate gland. JPS Open Access 1(1):1–10.
40. Zaichick V., Zaichick S. (2016) Prostatic tissue level of some major and trace elements in patients with BPH. J.J. Nephro. Urol. **3**(1):1–10.
41. Zaichick V., Zaichick S. (2016) Distinguishing malignant from benign prostate using content of 17 chemical elements in prostatic tissue. Integr. Cancer Sci. Therap. **3**(5):579–587.
42. Zaichick S., Zaichick V. (2016) Prostatic tissue levels of 43 trace elements in patients with BPH. British Journal of Medicine & Medical Research **15**(2):1–12.
43. Zaichick V., Zaichick S. (2016) Prostatic tissue levels of 43 trace elements in patients with prostate adenocarcinoma. Cancer and Clinical Oncology **5**(1):79–94.

44. Zaichick V., Zaichick S. (2017) Chemical element contents in normal and benign hyperplastic prostate. Ann. Men Health Wellness **1**(2):1006.
45. Zaichick V. (2017) Differences between 66 Chemical Element Contents in Normal and Cancerous Prostate. Journal of Analytical Oncology **6**:37–56.
46. Zaichick V., Zaichick S. (2019) Comparison of 66 chemical element contents in normal and benign hyperplastic prostate. Asian Journal of Urology **6**:275–289.
47. Isaacs J.T. (1983) Prostatic structure and function in relation to the etiology of prostatic cancer. The Prostate **4**(4):351–366.
48. Leissner K.M., Fielkegard B., Tisell L.E. (1980) Concentration and content of zinc in human prostate. Invest. Urol. **18**:32–35.
49. Woodard H.Q., White D.R. (1986) The composition of body tissues. Br.J. Radiol. **59**:1209–1218.
50. Arnold W.N., Thrasher J.B. (2003) Selenium concentration in the prostate. Biol. Trace Elem. Res. **91**(3):277–280.
51. Tipton I.H., Cook M.J. (1963) Trace elements in human tissue. Part II. Adult subjects from the United States. Health Phys. **9**:103–145.
52. Schroeder H.A., Nason A.P., Tipton I.H., Balassa J.J. (1967) Essential trace metals in man: Zinc. Relation to environmental cadmium. J. Chron. Dis. **20**:179–210.
53. Saltzman B.E., Gross S.B., Yeager D.W., Meiners B.G., Gartside P.S. (1990) Total body burdens and tissue concentrations of lead, cadmium, copper, zinc, and ash in 55 human cadavers. Environ. Res. **52**:126–145.
54. Zaichick V. (1997) Sampling, sample storage and preparation of biomaterials for INAA in clinical medicine, occupational and environmental health. In: Harmonization of Health-Related Environmental Measurements Using Nuclear and Isotopic Techniques. IAEA, Vienna, pp 123–133.
55. Zaichick V. (2004) Losses of chemical elements in biological samples under the dry ashing process. Trace Elements in Medicine (Moscow) **5**(3):17–22.
56. Vernadsky V.I .(1978) Living Matter, Nauka, Moscow.
57. Zaichick V., Ermidou-Pollet S., Pollet S. (2007) Medical elementology: a new scientific discipline. Trace Elements and Electrolytes **24**(2):69–74.

MEASUREMENT OF Ca, Cl, K, Mg, Mn, Na, P, Sr CONTENTS AND Ca/P RATIO IN THE ENAMEL OF PERMANENT TEETH OF TEENAGERS USING NEUTRON ACTIVATION ANALYSIS

V. Zaichick

Medical Radiological Research Centre, Korolyev St., 4, Obninsk, 249036, Russia,
e-mail: vzaichick@gmail.com

Introduction

An examination of teeth condition requires exact knowledge of the nature and variation of the mineral matrix including the contents of some apatite and related bulk chemical elements such as Ca, P, Mg, Na, K, and Cl [1]. Data of Ca and P content allow calculate Ca/P ratio with is a very important parameter of teeth apatite. It is known also that apatite phases can apparently be affected by trace element incorporation into teeth with effects on the physicochemical properties [2]. This is why deficiency or excess of some trace elements, for example, such as Sr is one of the factors which determine the degree of susceptibility to caries and other dental diseases. So, chemical element analysis of teeth expands the knowledge of etiology of dental diseases and may be used for diagnostic, therapeutic and preventive purposes [3–10]. Furthermore, teeth have been suggested as monitors for human exposure to elements which concentrate in calcified tissues [11].

There are several reviews and texts regarding chemical element analysis of teeth, using chemical techniques and instrumental methods. However, the majority of these data are based upon non-intact teeth i.e. using separated tissues such as enamel, dentine or cement. It was shown that samples are contaminated by some trace elements from stainless steel tools during the separation [12]. In most cases, tooth samples are treated with solvents in order to remove the organic matrix, and are then ashed and acid digested. There is evidence that some chemical elements are lost by these methods, their quantitative relations also being affected [13,14]

In present study chemical element contents in intact enamel of permanent teeth of apparently healthy teenagers 11–13 year old was investigated. Mass fractions of Ca, Cl, K, Mg, Mn, Na, P, and Sr in tooth enamel samples were determined by instrumental neutron activation analysis and Ca/P ratio was calculated for each sample. Furthermore, effect of gender on chemical element contents in intact enamel of permanent teeth was investigated.

The Ethic Committee of the Medical Radiological Research Centre (MRRC) approved this research.

Experimental

Ten permanent teeth (incisors, canines and molars) from 10 teenagers (6 girls and 4 boys, age range 11–13 years), living in Kaluga region were collected by dentists from MRRC. All teeth were extracted by reason of chronic periodontitis. All teeth were caries free or without visual defects.

A horizontal channel in the pneumatic rabbit system of the WWR-c research nuclear reactor was used to determine Ca, Cl, K, Mg, Mn, Na, P, and Sr by instrumental neutron activation analysis using short-lived radionuclides (INAA-SLR). Samples of the standard reference material, NIST SRM1486 bone meal and certified reference material IAEA H-5 animal bone, were analyzed under the same conditions as enamel samples to estimate the precision and accuracy of results. Details of sample preparation, nuclear reactions, radionuclides, gamma-energies, methods of analysis and the results of quality control were presented in our earlier publications concerning the chemical elements of human bones and tooth enamel samples [15,16].

For all investigated chemical elements and Ca/P ratio some basic statistical parameters such as arithmetic mean, standard deviation, standard error of mean, minimal and maximal values, median, percentiles with 0.025 and 0.975 levels were estimated for tooth enamel in group of males and females separately and combined.

Results and Discussion

Table 1 represents certain statistical parameters (arithmetic mean, standard deviation, standard error of mean, minimal and maximal values, median, percentiles with 0.025 and 0.975 levels) of Ca, Cl, K, Mg, Mn, Na, P, and Sr contents and Ca/P ratio in intact enamel of permanent teeth of teenagers.

Table 1. Basic statistical parameters of Ca, Cl, K, Mg, Mn, Na, P, Sr mass fraction (mg kg^{-1}, dry mass basis) and Ca/P mass fraction ratio in the enamel of intact permanent teeth of teenagers (males and females combined)

El/R	Mean	SD	SEM	Min	Max	Med.	P0.025	P0.975
Ca	409557	49963	15800	333166	471172	416806	333480	469917
Cl	966	245	78	570	1370	934	611	1366
K	596	182	58	370	889	520	378	866
Mg	3131	813	257	1900	4430	2935	2035	4423
Mn	0.510	0.190	0.060	0.275	0.865	0.442	0.292	0.827
Na	5017	618	195	4370	5820	4865	4372	5813
P	209005	27792	8789	155830	254898	208309	161613	250079
Sr	155	66	21	80	308	138	86	281
Ca/P	1.97	0.22	0.07	1.60	2.27	2.03	1.61	2.24

El/R – chemical element or Ca/P ratio, M – arithmetic mean, SD – standard deviation, SEM – standard error of mean, Min – minimum value, Max – maximum value, Med. – median, P0.025 – percentile with 0.025 level, P0.975 – percentile with 0.975 level.

Table 2 and Table 3 give some statistical parameters of 8 chemical element contents and Ca/P ratio in the enamel of intact permanent teeth of males and females, respectively.

Gender-related comparison using the Student’s *t*-test did not show any statistically significant differences in Ca, Cl, K, Mg, Mn, Na, P, and Sr contents in tooth enamel, however the significant difference was found for Ca/P ratio. Obtained results were in good agreement with most reported data for tooth enamel.

Table 2. Basic statistical parameters of Ca, Cl, K, Mg, Mn, Na, P, Sr mass fraction (mg kg^{-1}, dry mass basis) and Ca/P mass fraction ratio in the tooth enamel of males

El/R	Mean	SD	SEM	Min	Max	Med.	P0.025	P0.975
Ca	409836	63484	31742	333166	471172	417503	336930	469708
Cl	833	212	106	570	1010	877	584	1009
K	603	178	89	407	761	622	414	760
Mg	3115	867	434	2500	4400	2780	2518	4282
Mn	0.503	0.24`1	0.121	0.368	0.865	0.390	0.369	0.830
Na	5130	781	391	4390	5820	5155	4400	5818
P	193449	31754	15877	155830	229194	194386	157758	227547
Sr	159	39	20	106	190	170	110	190
Ca/P	2.12	0.12	0.06	1.97	2.27	2.13	1.98	2.26

El/R – chemical element or Ca/P ratio, M – arithmetic mean, SD – standard deviation, SEM – standard error of mean, Min – minimum value, Max – maximum value, Med. – median, P0.025 – percentile with 0.025 level, P0.975 – percentile with 0.975 level.

Table 3. Basic statistical parameters of Ca, Cl, K, Mg, Mn, Na, P, Sr mass fraction (mg kg^{-1}, dry mass basis) and Ca/P mass fraction ratio in the tooth enamel of females

El/R	Mean	SD	SEM	Min	Max	Med.	P0.025	P0.975
Ca	409371	45553	18597	334560	465596	416806	340833	462111
Cl	1055	240	98	868	1370	934	869	1368
K	591	202	83	370	889	520	381	876
Mg	3142	859	351	1900	4430	3075	2000	4335
Mn	0.515	0.174	0.071	0.275	0.696	0.562	0.284	0.690
Na	4942	551	225	4370	5670	4865	4371	5649
P	219376	21510	8781	195457	254898	213129	196796	252221
Sr	152	82	34	80	308	119	84	291
Ca/P	1.87	0.22	0.09	1.60	2.12	1.89	1.60	2.12

El/R – chemical element or Ca/P ratio, M – arithmetic mean, SD – standard deviation, SEM – standard error of mean, Min – minimum value, Max – maximum value, Med. – median, P0.025 – percentile with 0.025 level, P0.975 – percentile with 0.975 level.

Table 4. Comparison of mean ((M± SEM) values of chemical element contents (mg kg^{-1}, dry mass basis) and Ca/P ratio in enamel of permanent teeth of males and females (teenagers)

Age, Element, Ca/P ratio	Males	Females	$p\leq$ (Student's *t*-test)
Age (year)	12.0±0.4	12.2±0.4	0.78
Ca	409836±31742	409371±18597	0.99
Cl	833±106	1055±98	0.17
K	603±89	591±83	0.93
Mg	3115±434	3142±351	0.96
Mn	0.503±0.121	0.515±0.071	0.94
Na	5130±391	4942±225	0.69
P	193449±15877	219376±8781	0.21
Sr	159±20	152±34	0.86
Ca/P	2.12±0.06	1.87±0.09	**0.05**

M –arithmetical mean, SEM – standard error of mean.

Conclusions

INAA using short-lived radionuclides is an efficient technique for the determination of many important chemical elements in tooth enamel. The method is simple, fast, multielemental, and non-destructive.

No statistically significant gender-related differences were found between element contents in enamel of permanent teeth of teenagers, whereas Ca/P ratio in tooth enamel of males was higher than in females.

Our data for Ca, Cl, K, Mg, Mn, Na, P, Sr mass fractions and Ca/P ratio in enamel of permanent teeth of teenagers may serve as indicative normal values for residents of the Russian Central European region.

References

1. Liu H., Chao J., Chuang C., Chiu H., Yang C., Sun Y., Study of P, Ca, Sr, Ba and Pb levels in enamel and dentine of human third molars for environmental and archaeological research. Advances in Anthropology 2013; **3**: 71–77.
2. Qamar Z., Rahim Z.H.A., Chew H.P., Fatima T., Influence of trace elements on dental enamel properties: A review. J. Pak. Med. Assoc. 2017; **67**(1):116–120.
3. Zaichick V., Ovchjarenko N.N., *In vivo* X-ray fluorescent analysis of Ca, Zn, Sr, and Pb in frontal tooth enamel. J, Trace and Microprobe Techniques 1996; **14**(1):143–152.
4. Zaichick V,, Ovchjarenko N,, Zaichick S., *In vivo* energy dispersive x-ray fluorescence for measuring the content of essential and toxic trace elements in teeth. Appl. Radiat. Isot. 1999; **50**(2):283–293.
5. Zaichick V., Neutron activation analysis of trace element contents in the crowns of human permanent teeth. In: Neutron Spectroscopy, Nuclear Structure, Related Topics. Joint Institute for Nuclear Research, Dubna, Moscow Region, Russia, 2009, pp.288–295.
6. Zaichick V., Neutron activation analysis of Ca, Cl, K, Mg, Mn, Na, P, and Sr contents in the crowns of human permanent teeth. J. Radioanal. Nucl. Chem. 2009, **281**(1): 41–45.
7. Zaichick V., Zaichick S., The effect of age and gender on calcium, phosphorus, and calcium-phosphorus ratio in the roots of permanent teeth. The Journal of Dentist 2014; **2**(2): 78–89.
8. Zaichick V., Zaichick S., Relationship between Ca, Cl, K, Mg, Mn, Na, P, and Sr contents in the intact crowns of human permanent teeth investigated by neutron activation analysis. In: Neutron Spectroscopy, Nuclear Structure, Related Topics. Joint Institute for Nuclear Research, Dubna, Moscow Region, Russia, 2016, pp. 429–436.
9. Zaichick V., Zaichick S., The effect of age on Ca, Cl, K, Mg, Mn, Na, P, and Sr contents in the roots of female permanent teeth. J. Radioanal. Nucl. Chem. 2016, 309(1): 295–301.
10. Zaichick V., Zaichick S., The effect of age and gender on calcium, phosphorus, and calcium-phosphorus ratio in the crowns of permanent teeth. EC Dental Science 2016, **5**(2): 1030–1046.
11. Sharon I.M., The significance of teeth in pollution detection. Perspect. Biol. Med. 1988, **32**: 124–131.
12. Zaichick V., Zaichick S., Instrumental effect on the contamination of biomedical samples in the course of sampling. J. Anal. Chem.1996, **51**(2): 1200–1205.

13. Zaichick V., Sampling, sample storage and preparation of biomaterials for INAA in clinical medicine, occupational and environmental health. In: Harmonization of Health-Related Environmental Measurements Using Nuclear and Isotopic Techniques. IAEA, Vienna, 1997, pp. 123–133.
14. Zaichick V., Losses of chemical elements in biological samples under the dry ashing process. Trace Elements in Medicine 2004, **5**: 17–22.
15. Zaichick V., NAA of Ca, Cl, K, Mg, Mn, Na, P, and Sr contents in the human cortical and trabecular bone. J. Radioanal. Nucl. Chem. 2006, **269**: 653–659.
16. Zaichick S., Zaichick V., Neutron activation analysis of Ca, Cl, Mg, Mn, Na, P, and Sr contents in the enamel of primary teeth. In: Interaction of Neutrons with Nuclei. Joint Institute for Nuclear Research, Dubna, Moscow Region, Russia, 2011, pp. 342–349.

AGE-RELATED CHANGES OF IODINE/TRACE ELEMENT CONTENT RATIOS IN INTACT THYROID OF MALES INVESTIGATED BY ENERGY DISPERSIVE X-RAY FLUORESCENT ANALYSIS

Zaichick V.

Medical Radiological Research Centre, Korolyev St., 4, Obninsk, 249036, Russia

e-mail: vzaichick@gmail.com

Introduction

The endocrine organs, including the thyroid gland, undergo important functional changes during aging and a prevalence of thyroid dysfunction is higher in the elderly as compared to the younger population [1,2]. Advancing age is known to influence the formation of adenomatous goiter and thyroid cancer [3]. The prevalence of thyroid nodules is increased in the elderly, reaching a frequency of nearly 50% by the age of 65 [4]. Both prevalence and aggressiveness of thyroid cancer increase with age. Women are affected by thyroid nodule and cancer two to five times more often than men, but in age over 65 years a prevalence of thyroid cancer is higher in men [2–4,5].

In our previous studies the high mass fraction of iodine (I) and some other trace element (TE) were observed in intact human thyroid gland when compared with their levels in non-thyroid soft tissues of the human body [6–14]. However, some questions about the age-dependence of TE mass fraction and their relationships in thyroid of adult and, particularly, elderly males still remain unanswered. The findings of the excess or deficiency of TE contents in thyroid and the perturbations of their relative proportions in glands of adult and elderly males, may give an indication of their role in a higher prevalence of thyroid cancer in the elderly males.

The reliable data on TE mass fractions in normal geriatric thyroid is apparently extremely limited. There are many studies regarding TE content in human thyroid, using chemical techniques and instrumental methods [15–20]. However, the majority of these data are based on measurements of processed tissue and in many studies tissue samples are ashed before analysis. In other cases, thyroid samples are treated with solvents (distilled water, ethanol etc.) and then are dried at a high temperature for many hours. There is evidence that certain quantities of TE are lost as a result of such treatment [21–23]. Moreover, only a few of these studies employed quality control using certified/standard reference materials (CRM/SRM) for determination of the TE mass fractions.

In present study TE contents and the effect of age on TE contents in intact thyroid of apparently healthy male 2–80 year old was investigated. Mass fractions of Br, Fe, Cu, I, Rb, Sr, and Zn in thyroid tissue samples were determined using two methods of non-destructive energy-dispersive X-ray fluorescence analysis (EDXRF). In these methods X-ray fluorescence were induced by radionuclide ^{241}Am for I measurement and by radionuclide ^{109}Cd for Br, Fe, Cu, Rb, Sr, and Zn measurement.

All studies were approved by the Ethical Committee of the Medical Radiological Research Center, Obninsk.

Experimental

Samples of the human thyroid were obtained from randomly selected autopsy specimens of 71 males (European-Caucasian) aged 2.0 to 80 years. All the deceased were citizens of Obninsk and had undergone routine autopsy at the Forensic Medicine Department of City Hospital, Obninsk. Age ranges for subjects were divided into two age groups, with group 1, 2.0-35 years (22.5±1.4 years, M±SEM, n=36) and group 2, 36–80 years (52.4±2.4 years, M±SEM, n=36). These groups were selected to reflect the condition of thyroid tissue in the children, teenagers, young adults and first period of adult life (group 1) and in the second period of adult life as well as in old age (group 2). The available clinical data were reviewed for each subject. None of the subjects had a history of an intersex condition, endocrine disorder, or other chronic disease that could affect the normal development of the thyroid. None of the subjects were receiving medications or used any supplements known to affect thyroid trace element contents. The typical causes of sudden death of most of these subjects included trauma or suicide and also acute illness (cardiac insufficiency, stroke, embolism of pulmonary artery, alcohol poisoning). All right lobes of thyroid glands were divided into two portions using a titanium scalpel [24]. One tissue portion was reviewed by an anatomical pathologist while the other was used for the TE content determination. A histological examination was used to control the age norm conformity as well as the unavailability of microadenomatosis and latent cancer.

After the samples intended for TE analysis were weighed, they were transferred to -20°C and stored until the day of transportation in the Medical Radiological Research Center, Obninsk, where all samples were freeze-dried and homogenized [25]. The pounded sample was applied to the piece of Scotch tape serving as an adhesive fixing backing [26,27].

To determine the contents of the TE by comparison with a known standard, aliquots of commercial, chemically pure compounds were used [28]. The microliter standards were placed on disks made of thin, ash-free filter papers fixed on the Scotch tape pieces and dried in a vacuum. Ten subsamples of the Certified Reference Material (CRM) produced by the International Atomic Energy Agency (IAEA) CRM IAEA H-4 (animal muscle) were analyzed to estimate the precision and accuracy of results. The CRM IAEA H-4 subsamples were prepared in the same way as the samples of dry homogenized thyroid tissue.

Details of the sample preparation, the facility and method of analysis were presented in our previous publication on TE content investigation in human thyroid and prostate [12,26,27].

All thyroid samples were prepared in duplicate, and mean values of TE contents were used in final calculation. Using Microsoft Office Excel, a summary of the statistics, including, arithmetic mean, standard deviation, standard error of mean, minimum and maximum values, median, percentiles with 0.025 and 0.975 levels was calculated for TE contents. The reliability of difference in the results between two age groups was evaluated by the parametric Student's *t*-test and non-parametric Wilcoxon-Mann-Whitney *U*-test. For the estimation of the Pearson correlation coefficient between age and different TE content the Microsoft Office Excel programs were also used.

Results and Discussion

Table 1 depicts our data for seven TE in ten sub- samples of CRM IAEA H-4 (animal muscle) and the certified values of this material. Of 4 (Br, Fe, Rb, and Zn) TE with certified values for the CRM IAEA H-4 (animal muscle) we determined contents of all certified elements (Table 1). Mean values (M±SD) for Br, Fe, Rb, and Zn were in the range of 95% confidence interval. Good agreement of the TE contents analyzed by ^{109}Cd radionuclide-induced EDXRF with the certified data of CRM IAEA H-4 (Table 1) indicate an acceptable accuracy of the results obtained in the study and presented in Tables 2-4

Table 1. EDXRF data Br, Cu, Fe, I, Rb, Sr, and Zn contents in the IAEA H-4 (animal muscle) reference material compared to certified values (mg/kg, dry mass basis)

Element	Certified values			This work results
	Mean	95% confidence interval	Type	Mean±SD
Br	4.1	3.5 – 4.7	C	5.0±1.2
Cu	4.0	3.6 – 4.3	C	3.9±1.1
Fe	49	47 – 51	C	48±9
I	0.08	–	N	<5.0
Rb	18	17 – 20	C	22±4
Sr	0.1	–	N	<1.0
Zn	86	83 – 90	C	90±5

Mean – arithmetical mean, SD – standard deviation, C- certified values, N – non-certified values

Table 2 represents certain statistical parameters of the Br, Cu, Fe, I, Rb, Sr, and Zn mass fraction (mg/kg, dry mass basis) as well as I/Br, I/Cu, I/Fe, I/Rb, I/Sr, and I/Zn mass fraction ratios in intact (normal) thyroid of males.

Table 2. Some statistical parameters of Br, Cu, Fe, I, Rb, Sr, and Zn mass fraction (mg/kg, dry mass basis) as well as I/Br, I/Cu, I/Fe, I/Rb, I/Sr, and I/Zn mass fraction ratios in normal thyroid of male

Gender	Element	Mean	SD	SEM	Min	Max	Median	P 0.025	P 0.975
Males n=72	Br	10.8	10.0	1.3	1.90	54.4	8.05	2.33	42.0
	Cu	4.25	1.48	0.20	1.10	7.50	4.15	1.78	1.39
	Fe	221	102	13	47.1	502	224	58.4	419
	I	1574	974	123	112	4829	1582	220	3542
	Rb	10.1	6.96	0.89	1.80	42.9	8.60	2.65	27.5
	Sr	4.52	3.27	0.43	0.100	13.7	3.55	0.443	12.4
	Zn	122	41	5.2	35.4	221	115	57.2	201
	I/Br	226	183	24	4.26	902	191	13.1	645
	I/Cu	425	393	57	30.9	2055	312	34.8	1363
	I/Fe	11.0	12.5	1.7	0.223	59.4	5.97	0.749	41.3
	I/Rb	221	229	31	11.1	1036	162	19.1	839
	I/Sr	1046	2484	351	13.2	16570	390	49.8	5353
	I/Zn	14.0	9.0	1.2	0.679	36.7	12.0	1.43	27.3

M – arithmetic mean, SD – standard deviation, SEM – standard error of mean, Min – minimum value, Max – maximum value, P 0.025 – percentile with 0.025 level, P 0.975 – percentile with 0.975 level.

The obtained means for Br, Cu, Fe, I, Rb, Sr, and Zn mass fraction agree well with the medians of mean values cited by other researches for the human thyroid, including samples received from persons who died from different non-thyroid diseases [15–20].

To estimate the effect of age on the TE contents two age groups were examined (Table 3) and values of r – coefficient of correlation between age and all TE identified by us were calculated (Table 4) .

Table 3. Differences between mean values (M±SEM) of I/Br, I/Cu, I/Fe, I/Rb, I/Sr, and I/Zn mass fraction ratios in normal male thyroid of two age groups (AG)

Ratio	Male thyroid tissue				Ratio
	AG1 2.0-35 years n=36	AG2 36-80 years n=36	t-test $p\leq$	U-test p	AG2 to AG1
I/Br	246±40	208±30	0.447	>0.05	0.85
I/Cu	413±72	437±88	0.829	>0.05	1.06
I/Fe	10.1±1.9	12.1±3.0	0.587	>0.05	1.20
I/Rb	201±39	244±50	0.503	>0.05	1.21
I/Sr	820±246	1291±686	0.524	>0.05	1.57
I/Zn	15.2±1.8	12.7±1.6	0.317	>0.05	0.84

M – arithmetic mean, SEM – standard error of mean, *t*-test - Student's *t*-test, U-test - Wilcoxon-Mann-Whitney *U*-test.

Table 4. Correlations between age and I/Br, I/Cu, I/Fe, I/Rb, I/Sr, and I/Zn mass fraction ratios in the normal thyroid of male (r – coefficient of correlation)

Ratio	I/Br	I/Cu	I/Fe	I/Rb	I/Sr	I/Zn
r	0.130	0.206	0.315[a]	0.183	0.076	0.091

Statistically significant values: [a] $p\leq0.05$.

A significant direct correlation between age and I/Fe ratio was found in male thyroid (Table 4).

Conclusions

The developed methods of radionuclide-induced EDXRF are an efficient technique for the determination of many important TE in thyroid tissue. The methods are simple, fast, multielemental, and non-destructive. Our results for Fe, Cu, I, Rb, Sr, and Zn mass fractions in intact thyroid tissue may serve as indicative normal values for males of the Russian Central European region.

Acknowledgements

We are grateful to Dr. Yu. Choporov, former Head of the Forensic Medicine Department of City Hospital, Obninsk, for supplying thyroid samples.

References

1. Gesing A. (2015) The thyroid gland and the process of aging. Thyroid Research 8 (Suppl. 1): A8.
2. Mitrou P., Raptis S.A., Dimitriadis G., (2011) Thyroid disease in older people. Maturitas **70**: 5−9.
3. Kwong N., Medici M., Angell T.E., Liu X., Marqusee E., et al. (2015) The influence of patient age on thyroid nodule formation, multinodularity, and thyroid cancer risk. J. Clin. Endocrinol. Metab. **100** (12):434−440.
4. Mazzaferri E. (1993) Management of a solitary thyroid nodule. NEJM 328: 553−559.
5. Smailyte G., Miseikyte-Kaubriene E., Kurtinaitis J. (2006) Increasing thyroid cancer incidence in Lithuania in 1978−2003. BMC Cancer **11**(6): 284.
6. Zaichick V., Tsyb A., Vtyurin B.M. (1995) Trace elements and thyroid cancer. Analyst. **120**: 817−821.
7. Zaichick V., Choporov Yu. (1996) Determination of the natural level of human intra-thyroid iodine by instrumental neutron activation analysis. J. Radioanal. Nucl. Chem. **207**(1): 153−161.
8. Zaichick V., Zaichick S. (1997) Normal human intrathyroidal iodine. Sci. Total Environ. **206**(1): 39−56.
9. Zaichick V. (1998) Iodine excess and thyroid cancer. J. Trace Elements in Experimental Medicine **11**(4): 508−509.
10. Zaichick V. (1998) In vivo and in vitro application of energy-dispersive XRF in clinical investigations: experience and the future. J. Trace Elements in Experimental Medicine **11**(4): 509−510.
11. Zaichick V., Iljina T. (1998) Dietary iodine supplementation effect on the rat thyroid ^{131}I blastomogenic action. In: Die Bedentung der Mengen- und Spurenelemente. 18. Arbeitstangung. Anke M, et al., editors. Friedrich-Schiller-Universität, Jena, 294−306.
12. Zaichick V., Zaichick S. (1999) Energy-dispersive X-ray fluorescence of iodine in thyroid puncture biopsy specimens. J. Trace and Microprobe Techniques **17**(2): 219−232.
13. Zaichick V. (1999) Human intrathyroidal iodine in health and non-thyroidal disease. In: New aspects of trace element research. Abdulla M, et al., editors. Smith-Gordon and Nishimura London and Tokyo, 114−119.
14. Zaichick V. (2000) Relevance of and potentiality for in vivo intrathyroidal iodine determination. In: In Vivo Body Composition Studies. Yasumura S., et al., editors. Annals of the New York Academy of Sciences **904**: 630−632.
15. Zhu H., Wang N., Zhang Y., Wu Q., Chen R., et al. (2010) Element contents in organs and tissues of Chinese adult men. Health Phys **98**(1): 61−73.
16. Salimi J., Moosavi K., Vatankhah S., Yaghoobi A. (2004) Investigation of heavy trace elements in neoplastic and non-neoplastic human thyroid tissue: A study by proton – induced X-ray emissions. Iran J. Radiat. Res. **1**(4): 211−216.
17. Ataulchanov I.A. (1969) Age-related changes of manganese, cobalt, coper, zinc, and iron contents in the endocrine glands of females. Problemy Endocrinologii **15**(2): 98−102.
18. Reddy S.B., Charles M.J., Kumar M.R., Reddy B.S., Anjaneyulu Ch., et al. (2002) Trace elemental analysis of adenoma and carcinoma thyroid by PIXE method. Nucl. Instr. Meth. Phys. Res. B **196**(3–4): 333−339.

19. Boulyga S.F., Zhuk I.V., Lomonosova E.M., Kanash N., Bazhanova N.N. (1997) Determination of microelements in thyroids of the inhabitants of Belarus by neutron activation analysis using the k0-method. J. Radioanal. Nucl. Chem. **222**(1−2): 11−14.
20. Tipton I.H., Cook M.J. (1963) Trace elements in human tissue. Part II. Adult subjects from the United States. Health Phys. **9**(2): 103−145.
21. Zaichick V. (1997) Sampling, sample storage and preparation of biomaterials for INAA in clinical medicine, occupational and environmental health. In: Harmonization of Health-Related Environmental Measurements Using Nuclear and Isotopic Techniques. IAEA, Vienna, 123−133.
22. Zaichick V. (2004) Losses of chemical elements in biological samples under the dry ashing process. Trace Elements in Medicine **5**: 17−22.
23. Zaichick V., Zaichick S. (2000) INAA applied to halogen (Br and I) stability in long-term storage of lyophilized biological materials. J. Radioanal. Nucl. Chem. **244**(2): 279−281.
24. Zaichick V., Zaichick S. (1996) Instrumental effect on the contamination of biomedical samples in the course of sampling. The Journal of Analytical Chemistry **51**(12): 1200−1205.
25. Zaichick V., Zaichick S. (1997) A search for losses of chemical elements during freeze-drying of biological materials. J. Radioanal. Nucl. Chem. **218**(2): 249−253.
26. Zaichick S., Zaichick V. (2010) Method and portable facility for energy-dispersive X-ray fluorescent analysis of zinc content in needle-biopsy specimens of prostate. X-Ray Spectrom. **39**: 83−89.
27. Zaichick S., Zaichick V. (2011) The Br, Fe, Rb, Sr, and Zn content and interrelation in intact and morphologic normal prostate tissue of adult men investigated by energy dispersive X-ray fluorescent analysis. X-Ray Spectrom. **40**(6): 464−469.
28. Zaichick V. (1995) Applications of synthetic reference materials in the medical Radiological Research Centre. Fresenius J. Anal. Chem. **352**: 219−223.

Nuclear Fission

IMPROVEMENT OF THE EXPERIMENTAL CAPABILITY IN STUDIES OF THE CLUSTER EFFECTS IN HEAVY NUCLEI

D.V. Kamanin[1], Yu.V. Pyatkov[2,1], S. Pospíšil[3], M.O. Rudenko[1], A.A. Alexandrov[1],
I.A. Alexandrova[1], P. Burian[3], Z.I. Goryainova[1], M. Holík[3], E.A. Kuznetsova[1], R. Korsten[4],
L. Meduna[3], G.A. Ososkov[1], A.N. Solodov[1], A.O. Strekalovsky[1], O.V. Strekalovsky[5,2],
V.E. Zhuchko[1], O.V. Falomkina[6,1], Yu.P. Pyt'ev [6]

[1]Joint Institute for Nuclear Research, 141980 Dubna, Russia
[2]National Nuclear Research University "MEPhI", 115409 Moscow, Russia
[3]IEAP CTU (Prague, Czech Republic)
[4]University of Stellenbosch, South Africa
[5]Dubna State University, 141980 Dubna, Russia
[6]Lomonosov Moscow State University, Physics Faculty, Computer Methods in Physics Division, Moscow, Russia

INTRODUCTION

In accordance with our previous experiments [1–3], at least some of the fragments of binary fission of low excited actinides are born in the shape isomers states. A strongly deformed fragment is a weakly bound binary system (shape isomer) which in a solid foil, in the case of inelastic scattering, breaks up with a certain probability, even in tangential collisions with a large impact parameter. One of the breakup products is a magic core, for example $^{68,\ 72}$Ni. To label the totality of the observed manifestations of such a process, especially high collinearity of the partners, we have proposed the term "collinear cluster tripartition" (CCT).

In less excited fragments, the population of the state of the shape isomer is also possible, but the system turns out to be more strongly coupled than in the previous case, and its breakup in the solid foil is observed at lower impact parameters. And in this case, at least one of the decay products turns out to be a magic nucleus, for example, $^{128,\ 132}$Sn, ^{144}Ba, etc. Both decay products fly in the same direction, with a very small angle between them, in the range of 0.3^0–2^0 (experimental estimate). Moreover, one of them has energy of several MeV, which makes it extremely difficult to separately detect them with the measurement of the mass of each of the products.

Thus, the population of previously unknown states of shape isomers in fragments of binary fission of actinide nuclei occurs, in fact, in the process of binary fission, and the interaction of the fragment with a solid-state foil serves as a specific detector of the presence of such a state.

Most of the data concerning the manifestations of clustering in fissile actinides and fragments of their fission were obtained by us within the framework of the "missing mass" method. To construct an adequate model of the observed effects, *a kinematically complete experiment* with the measurement of masses, energies, and velocity vectors of all nuclei involved in the process is required. Such experiment was not performed so far, and improvement of our experimental capabilities in studies of the cluster effects currently continues.

EXPERIMENTAL FACILITIES USED IN OUR STUDIES OF THE MULTIBODY DECAYS

We investigate rather rare multibody decay modes of low excited heavy nuclei with yields in the range of 10^{-3} and lower per binary fission. These peculiarities define the general requirements for spectrometers to be used, namely of high efficiency and mosaic structure of the detector. Among known methods of ion mass-spectrometry only time of flight-energy (TOF–E) method is suitable for study of the multibody decays. The 4–π FOBOS spectrometer [4] installed in FLNR (JINR) met all of the listed requirements, and first CCT dedicated experiments [1] were performed using this facility. FOBOS spectrometer was based on the gas-filled detectors that demand complicated gas-supply system. The spectrometer consisted of 32 big modules provided relatively low granularity of the detection system (figures 1(a), (b)). In order to overcome these shortcomings, we switched to the semiconductor detectors. The whole series of experiments were performed then using different modifications of the COMETA spectrometer (COrrelation Mosaic E-T Array) [2] setup (figures 1(c), (d)).

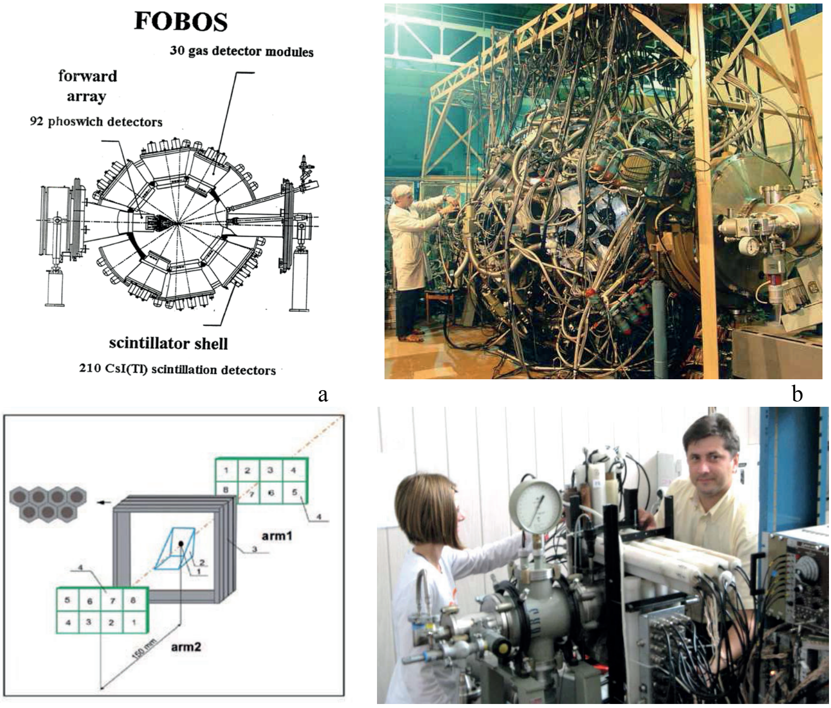

a b c d

FIGURE 1. Design of the 4-π FOBOS spectrometer (a) and its overall view (b). Design of the COMETA setup (b). In the presented version it consists of two mosaics of eight PIN diodes each (4), microchannel-plates-based start-detector (2) with the ^{252}Cf source inside (1) and neutron belt consisting of 32 ^{3}He filled neutron counters (3). The overall view of the setup is shown in figure 1(d).

NEW IMPROVED VERSION OF THE COMETA SETUP

Accumulated experience of using the COMETA setup and new experimental tasks followed from the analysis of already obtained data initiated the development of the improved version of this facility.

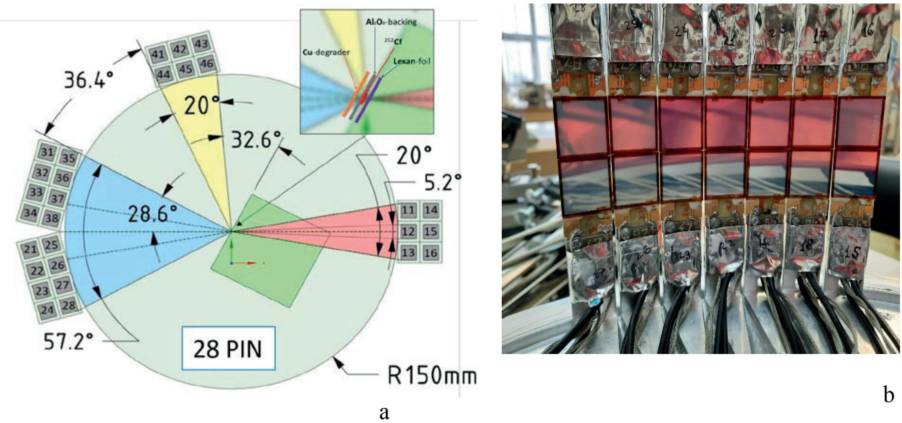

a

b

FIGURE 2. Location of the detectors in the COMETA-m setup. 28 PIN-diodes united in three mosaics are planned to use for measuring of the angular distribution of the CCT partners. Microchannel-plates-based start detector is located in the center of the design (a). Photo of the forward mosaic (b).

The following features are realized in the COMETA-m setup:

1. Measurement of the angular correlations of the ternary decay partners in a wide range of angles.
2. Strips between the adjacent PIN dioses do not exceed 2 mm which is twice as small when compared to an actual version of the spectrometer.
3. New frame bounds an active surface of PIN diode in order to suppress fission fragments (FF) scattering.
4. Rigid geometry of the detector arrangement provides better reproducibility of the results.

USING OF THE TIMEPIX3 PIXEL DETECTORS IN STUDIES OF THE MULTIBODY DECAYS

While it is necessary to create an adequate model of the observed effects, the angular distribution of the CCT partners moving in a small open angle up to 0.3^0 has not been measured so far. For this purpose, joint work with a group from the Institute of Experimental and Applied Physics, Czech Technical University in Prague, Czech Republic has begun on the use of Timepix3 two-coordinate pixel detector [5] (figure 3(a)), with a spatial resolution of 55μ, in studies of the multibody decays. Heavy ion mass spectrometry using this detector is an original and non-trivial methodological problem. Initially the device was designed for detection of the soft photons, while in the present task we require to register heavy ions with the energies up to tens of MeV.

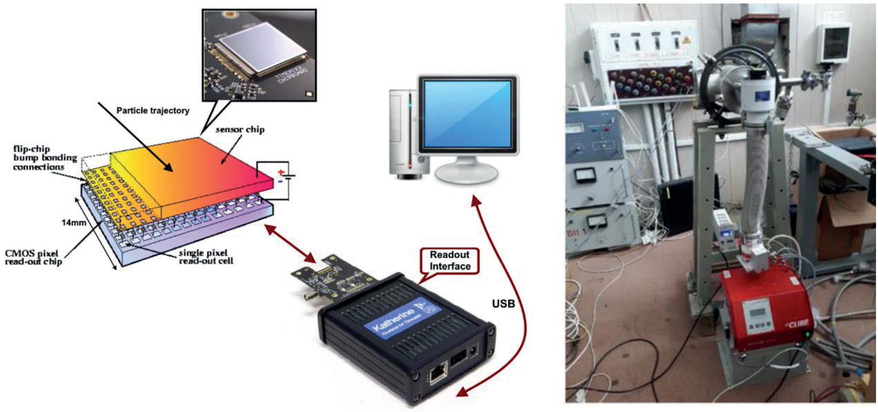

b

a

FIGURE 3. Schematical view of the Timepix3 detector with Katerine readout (a), photo of the TDS-1 (**T**ernary **D**ecays **S**pectrometer) experimental setup (b).

As the first step in the study of rare ternary decays using Timepix detectors, the following first-day experiment was performed. Detection of the “fork” of two CCT partners (for instance, the Ni/Ca pair, figure 4(a)) which hit the Timepix3 detector in a short time interval and substantially differ in their energies, gives evidence of the CCT event. Kinematical scheme of one of the CCT mode is shown in figure 4(a). Similar ternary decays were searched for in the experiment. An example of the data processing is presented in figure 4(b).

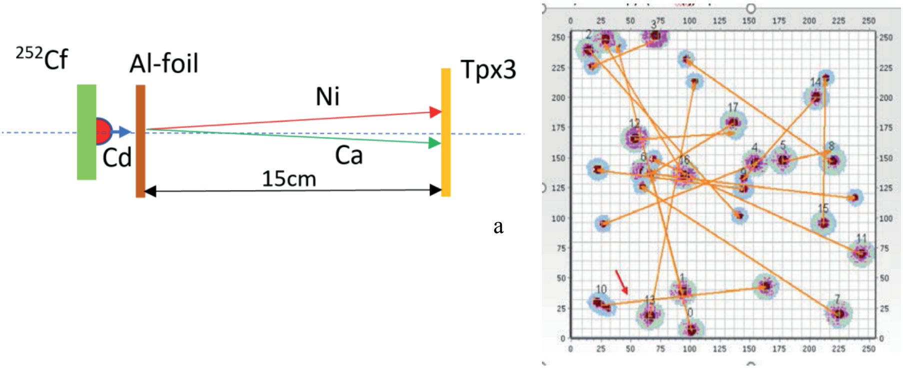

a

b

FIGURE 4. Schematical presentation of the tri-partition of the mother nucleus ^{252}Cf → Sn+Cd → Ni+Ca chosen as an example of the CCT and kinematics of the decay partners in the TDS-1 setup (a). Typical result of the data processing (b). The cluster 10 marked by the red arrow is presumably due to the CCT event, while the orange arrow connects this cluster with another one produced most likely by the Al ion knocked out from the foil by Cd-like fragment.

DEVELOPMENT OF THE TIME PICK-OFF ALGORITHMS

To correctly measure heavy ion's TOF with PIN diodes, it is necessary to account for the so-called plasma delay effect (PDE) which is due to generation of plasma in a heavy ion track in the PIN diode. Because of the PDE, the initial relatively long part of the signal lies inside the "noise track", and the time stamp turns out to be shifted in relation to the true signal's start. It is possible to account for plasma delay by using its parameterization proposed in Ref. [6], excluding the region of small masses and energies.

Thanks to using fast digitizer and having digital images of the signals, we have developed an alternative approach aimed at finding an actual beginning of the signal. It is done by approximating its initial part that lies partially inside the noise track with parabolic curve which vertex lies on the average of the noise and serves as the "true" signal's start. The first realization of this idea was Parab-algorithm [7] which used only parabolic function for interpolation of the signal's noisy region. To increase a robustness of the algorithm against a choice of region for parabola interpolation, Parab-algorithm was followed by Parablin-algorithm [8] which seamlessly sewed parabola with a linear function that approximated points of the rising edge of the signal lying above the noisy region. Its main drawback was the need to manually choose points for linear function approximation. To further increase robustness of the method, we propose Paraspline-algorithm which describes the initial part of the signal by parabola seamlessly sewed with a spline that automatically approximates points above the noisy region, without user interference.

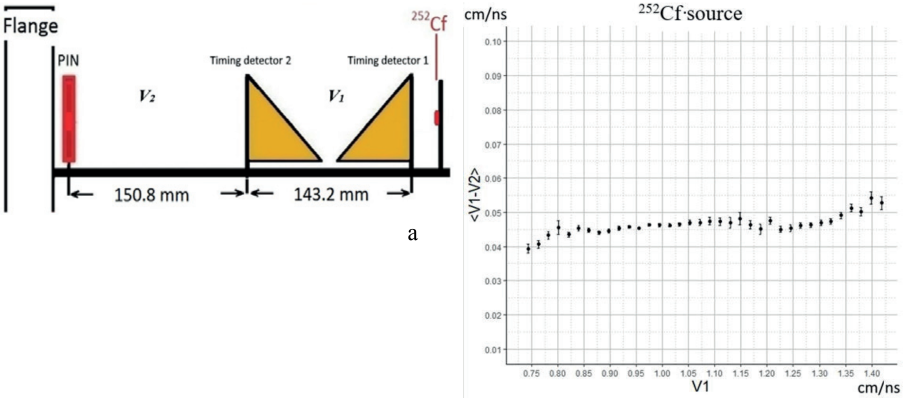

a

b

FIGURE 5. Layout of LIS spectrometer (a). Mean difference $<V_1-V_2>$ as a function of V_1 for the fission fragments from the ^{252}Cf source (b).

In order to verify Paraspline-algorithm in experiment, LIS setup was used (figure 5(a)). The FF velocity is measured sequentially on two flight-passes by means of using the timing detectors based on the microchannel plates (V_1 value) and PIN diode as a "stop" detector when V_2 value is obtained (figure 5(a)). Event by event comparison of "true" velocity V_1 and V_2 is presented in figure 5(b). Good agreement between the compared values is observed.

MATHEMATICAL TESTING OF THE STATISTICAL RELIABILITY OF LINEAR STRUCTURES IN THE FF MASS-MASS DISTRIBUTIONS

A theoretical description of nuclear reactions, such as fission and quasi-fission, presents the evolution of a nuclear system in the form of trajectories in a multidimensional deformation space. Finding images of such trajectories in the space of experimentally observable variables was proposed in Refs. [9–12] as a new approach to data analysis. The trajectories look like “fine structures” in two-dimensional distributions, for example, in mass correlation distributions. By definition, *fine structure* means local regions (peaks) in a two-dimensional distribution with the yield higher than on a smooth substrate, which is the background to the sought-after effect. For finding fine structures with the given level of reliability, methods of image morphological analysis were applied in Ref. [13].

New specific fine structure which looks like a rhombic meander (figure 6(a)) has been revealed in the mass correlation distribution of the FFs from ^{252}Cf(sf) obtained at the COMETA setup. To test the hypothesis that the structure actually exists and is not a noise artifact, it was proposed to use a deep convolution network as a binary classifier trained on a large model sample and noise images [14]. The results of the testing the neuro classifier prove high statistical reliability of fine structure revealed.

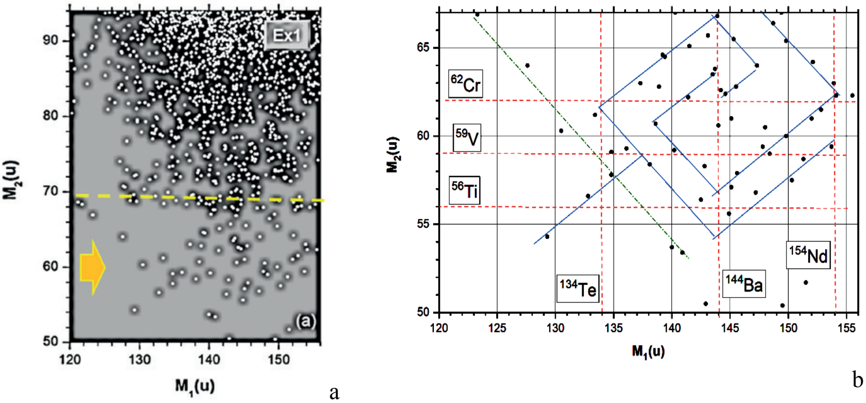

FIGURE 6. Correlation mass distribution of the FFs from ^{252}Cf(sf) obtained at the COMETA setup. Specific rhombic meander structure is marked by the arrow (a). The same structure in the larger scale (b). The meander vertexes coincide with known magic isotopes listed in boxes.

CONCLUSION

In the previous year, we have paid our attention to upgrade of the spectrometers used, mastering Tpx3 pixel detectors, and development of the data processing procedures. Our efforts aim to perform kinematically complete experiments dedicated to previously unknown ternary decays of low excited heavy nuclei.

REFERENCES

1. Yu.V. Pyatkov et al., Eur. Phys. J. A **45** (2010) 29.
2. Yu.V. Pyatkov et al., Eur. Phys. J. A **48** (2012) 94.
3. Yu.V. Pyatkov et al., Phys. Rev. C **96** (2017) 064606.
4. H.G. Ortlepp et al., Nucl. Instrum. Methods Phys. Res. A. **403** (1998) 65–97.
5. T. Poikela et al., JINST. **9** (2014) C05013.
6. H.O. Neidel et al. // Nucl. Instrum. Meth. 1980. V. **178**. P. 137.
7. A.O. Strekalovsky et al., Nucl. Phys. Engin. 2015, Vol. **6**, No, 5–6, p. 290–296 (in Russian).
8. Yu.V. Pyatkov, D.V. Kamanin, A.O. Strekalovsky et al. // Bull. Russ. Acad. Sci.: Phys, 2018, Vol. **82**, No. 6, p. 804–807.
9. Yu.V. Pyatkov et al., Nucl. Phys. A **611**, 355–369 (1996).
10. Yu.V. Pyatkov et al., Nucl. Phys. A **624**, 140 (1997).
11. Yu.V. Pyatkov et al., Nucl. Instrum. Methods Phys., Res., Sect. A **488**, 381 (2002).
12. Yu.V. Pyatkov et al., Phys. At. Nucl. **67**, 1726 (2004).
13. Yu.V. Pyatkov et al., Pattern Recogn. Image Anal. **21**, 82–87 (2011).
14. G.A. Ososkov, Yu.V. Pyatkov, and M.O. Rudenko, Physics of Particles and Nuclei Letters, 2021, Vol. **18**, No. 5, pp. 559–569.

Hidden Variables in Angular Correlations of the Particles Emitted in Fission

F.F. Karpeshin
D.I.Mendeleev All-Russian Research Institute for Metrology, 19005 Saint-Petersburg, Russia
fkarpeshin@gmail.com

A comparative analysis of experiments on studying the (n, f), on one hand, and (n, n), on the other hand, angular correlations in fission is carried out, based on the model proposed by muonic conversion in fragments of prompt fission of ^{238}U with negative muons. Their fundamental difference is shown in the sense of the information that can be inferred from them. Historically, the situation resembles the EPR paradox. An experimental check of the empirical relation between the alignment and polarization parameters $A_{n,J} = 2A_{n,f}$ is proposed.

1 Introduction

Probably, the most revolutionary moment in the development of quantum mechanics (QM) was the Heisenberg uncertainty relation. It showed that far not each of the parameters one uses in the everyday life can be also measured in microcosm with an arbitrary precision. This seemed paradoxical from the point of view of everyday consciousness. The famous Einstein's expression "God does not play dice" and the EPR paradox, the interest in which continues to this day, date back to this time. To test and understand the principles of QM, the theory of "hidden parameters" was put forward. It runs that there may be additional parameters, for example, spin projection. If we knew them before measurement, we could predict the result unambiguously. Indeed, classical spin naturally has three projections. In quantum mechanics, there is only one left — that on the quantization axis. The other two remain quite objective parameters, but pass into the area of those hidden from observation. If someone wants, nevertheless, to deal with them explicitly, then he will receive the wrong answer.

The HV-theory is rejected by the community. However, examples can be noted of how variations on the theme of HV suddenly interplay, for example, in modern simulations of the angular distributions of gamma quanta or neutrons emitted from fission fragments. Consider the angular distribution of the neutrons from fission with respect to the direction of the light fragment. It is well known that the spins of fragments are mainly aligned in a plane perpendicular to the fission axis. In order to take this circumstance into account, one may consider the spin of each fragment to have a definite direction in the plane perpendicular to the fission axis, and then average over the directions in the plane. Nevertheless, such a way that might seem evident at first glance, turns out to be certainly erroneous. In such an approach, the supposed direction of the fragment's spin appears as a HV, additional to the projection on the quantization axis z which is in the fission direction. Contrary, in a consecutive QM approach, the state of the fragment is characterized by two quantum numbers: the spin and its projection onto the quantization axis z. Then the alignment of the fragments merely means that the projection of their spins onto this axis is close to zero. And in the general case of incomplete alignment, it is necessary to use the density matrix.

Therebefore, the angular correlations provide a useful guide to experimental studying the interrelation of hidden variables with QM. An explicit consideration of the additional spin projection, which is treated as a non-observable one in a consistent QM approach, leads to an obvious contradiction with QM, which can be observed experimentally. Let us consider this interplay in more detail. We use angular correlations of the conversion muons, emitted from the fission fragments in prompt fission of actinide nuclei in muonic atoms of ^{233}U, occurring as a result of radiationless excitation in a muonic transition. This process was discovered in JINR [1]. We remind the process in the next section. Formulas necessary for analysis of the angular correlations in the c. m. of the fragments are derived in section 3. The account of the translation of the muon on the fragment is performed in section 4. There is also a fraction of the muons emitted as a result of shake-off at the neck rupture. They can be compared to the scission neutrons emitted in fission. Their contribution is taken into account in the same section, together with comparing to experiment. In the concluding section 5, we sum up the results obtained, draw conclusions, outline prospects for future investigation.

2 Physical premises

This unique process gives a direct information on the fission dynamics. Beams of negative muons are slowed down in matter, then the process of the muon capture into high orbits of the muonic atoms starts. The muons are captured into the orbits with the main quantum number $n \approx 14$. After this, they cascade down by means of the radiative and Auger transitions. When the muons jump between the lowest inner orbits, there is a chance that the transition energy is transferred to the nucleus, which undergoes fission. This kind of fission is called prompt fission, contrary to the delayed fission, induced by the nuclear capture of the muon. As a result of prompt fission, the muons are entrained on a fragment, and then can be emitted due to internal conversion during the cascade deexcitation of the fragments.

Experimentally the angular distribution of the muons from prompt fission of ^{233}U was undertaken in Refs. [2] in nuclear photoemulsions. Theoretical calculations were performed in [3]. Calculated spectrum of the conversion muons is up to 1–2 MeV. Furthermore, experiment shows a significant focusing of the muons along the fission axis. This can be understood in terms of the alignment of the fragments in the plane perpendicular to the direction of fission [6] (Fig. 1). Correspondingly, two ways of analysis can be put forward. One looks very natural: consider that the spin of the fragment is directed somewhere in the (x, y) plane, so that the spins of the muons are assumed $M = J$ in the internal system. After recalculation to the labsystem, one has to average over the directions of the spin in the azimuthal (x, y) plane. Such would be a HV way. Another way, consecutively QM one, is that the quantization axis is chosen along the fission direction, in correspondence with the experimental conditions of observation. Then the spin projections of the muons are assumed $M = 0$.

3 Formulas

The actual angular distribution depends on the multipolarity of the transition. Consider first $E1$ transitions. In the HV model, the angular distribution of the emitted

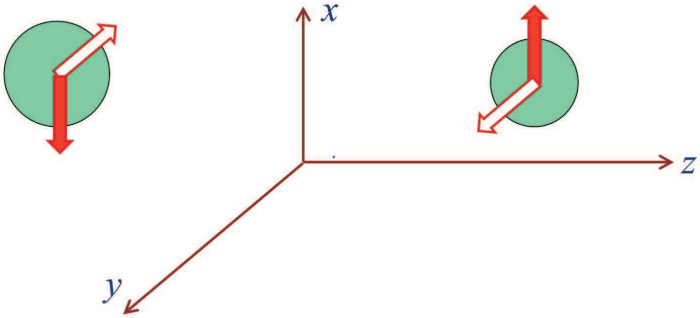

Figure 1: Scheme of the fragment spin alignment in the plane perpendicular to the fission axis. The spins are oriented in the (x, y) plane arbitrarily, but necessarily in opposite directions to each other.

neutrons in the internal coordinate system will be

$$\mathrm{X}'(\theta', \phi') = |Y_{11}(\theta', \phi')|^2 \sim \sin^2\theta' \,. \tag{1}$$

After transformation to the angle α relative to the fission axis z in the c. m. system of the fragment and averaging over the azimuthal angle ϕ of the spin in the (x, y) plane, one arrives at the angular distributions in this system, calculated within the HV-theory:

$$\mathrm{X}_{h.v.}(\alpha) = \frac{1}{2}(1 + \cos^2\alpha) \,. \tag{2}$$

Factor of $\frac{1}{2}$ takes into account the normalization of the full number of the emitted particles. Contrary, within the framework of the QM approach one obtains

$$\mathrm{X}_{\mathrm{QM}}(\alpha) = |Y_{10}(\alpha, \phi)|^2 \sim \cos^2\alpha \,. \tag{3}$$

In the case of the $E2$ transitions, one has the angular distribution in the c.m. system $\Phi'(\theta', \phi') = |Y_{22}(\theta', \phi')|^2 \sim \sin^4\theta$. Correspondingly, one obtains in the c. m. system expressions

$$\Phi_{h.v.}(\alpha) = \frac{3\pi}{4}(1 + \frac{2}{3}\cos^2\alpha + \cos^4\alpha) \tag{4}$$

$$\Phi_{\mathrm{QM}}(\alpha) = |Y_{20}(\alpha, \phi)|^2 = 1 - 6\cos^2\alpha + 9\cos^4\alpha \,. \tag{5}$$

Comparison of Eqs. (2) and (3) shows that the HV polarization turns out to be twice less than the QM one (see next section in more detail). This conflict shows inconsistence of HV with quiantum mechanics. Furthermore, in the case of the $E2$ emission, the form itself of the angular dependence becomes different. Experiment can test which approach is true. The difference speaks for itself.

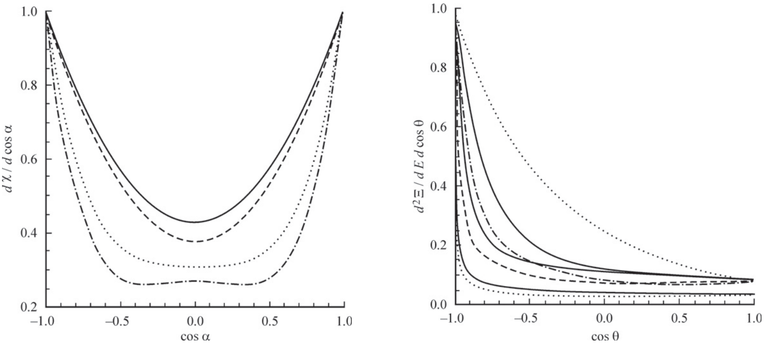

Figure 2: Left: calculated angular distribution of the conversion muons in the center-of-mass system for the $E1$ transitions in the case of the initial spin of the nucleus $I = 7$ and 4 (solid and dashed lines) and for the $E2$ transitions (dashed and dash-dotted lines, respectively). In the case of isotropic emission, $\frac{d\chi}{d\cos\alpha} = const$. Right: that of the conversion muons for light fragments with the atomic number $Z = 40$ in the laboratory system, for the $E1$- and $E2$-transitions with the kinetic energy of the muons $E_\mu = 1$, 0.25 and 0.1 MeV, respectively (in the order of approach to the origin). Upper dotted line corresponds to isotropic emission in the c. m. system.

4 Comparison to experiment

For comparison with experiment, it should be taken into account that the alignment of the fragments is not 100%. Therefore, the general expression for the (n,n) correlations instead of (1) will be written as

$$\chi'(\theta',\phi') = 1 + A_{nJ}\sin^2\theta'\,, \tag{6}$$

and for the (n,f) correlation — in the form

$$\chi_{QM}(\alpha) = 1 + A_{nf}\cos^2\alpha \tag{7}$$

instead of (3). Experience shows that $A_{nf} \ll 1$ is a parameter within 10 % [7]. Then in the labsystem, Eq. (2) goes over

$$\chi_{h.v.}(\alpha) = 1 + \frac{1}{2}A_{nJ}\cos^2\alpha\,. \tag{8}$$

Comparing (8) with (7), in the case of the $E1$ transitions one arrives at the relation [7]

$$A_{nJ} \simeq 2A_{nf}\,. \tag{9}$$

The results are presented in Fig. 2, left for the both $E1$ and $E2$ transitions in the c.m. of a fragment. It is symmetric for the angles between 0 and π, and has a distinctive 0—$\frac{\pi}{2}$ anisotropy. In the labsystem, the distribution concentrates along the velocity of the fragment, as shown in Fig. 2, right.

Shake-off muons come from a sudden change of the potential due to snapping-back the remnants of the neck. They can be compared to the scission neutrons. As distinct from the latter, emission of the shake muons is sharply anisotropic (Fig. 3, left).

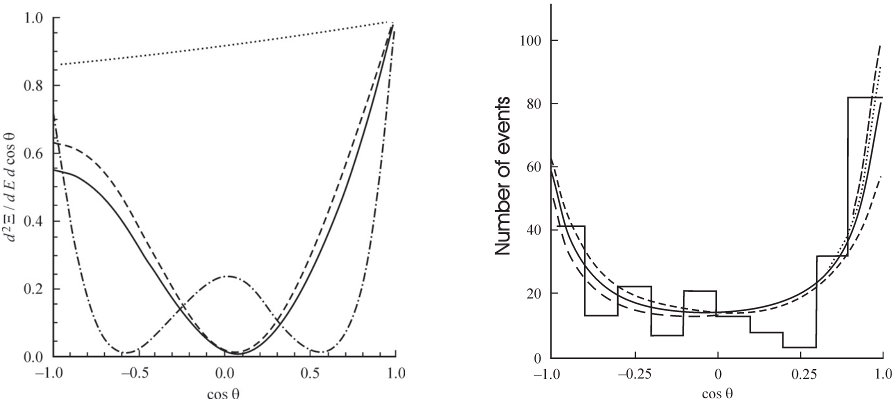

Figure 3: Left: angular distribution of shake muons. Solid and dashed lines: the $E1$ transitions with the kinetic energy of the conversion muons $E_\mu = 1$ and 0.5 MeV, respectively. Dotted and dash-dotted lines: the $E2$ and $E0$ transitions with $E_\mu = 1$ MeV, respectively. Right: comparison of the calculated angular distribution with experiment [2]. The solid curve corresponds to a mixture of the multipoles $90\%E1 + 10\%E2$, dotted line — $50\%E1 + 15\%E2 + 35\%M1$. For comparison, short and long strokes show the angular distribution for pure $E1$ and $E2$ transitions, respectively.

In Fig. 3, right the theoretical angular distributions, averaged over the fragment distributions and the energies of the muons are presented in comparison with the experimental histogram from Ref. [2]. Two characteristics of the fission fragments can be inferred from this comparison.

1)There is a fraction of the $E2$ component at the level of 15% in the radiation spectrum of the fission fragments.

2) There is also a share of the shake muons within 5%.

Of course, these values are obtained within the QM approach, without HV. Shake muons are similar to the scission neutrons.

5 Conclusion

(μ, f) as well as (n, f) angular correlations appear as a convenient example for experimental investigation of the difference between the HV theory and QM approach. Alignment and polarization are two manifestations of the spin state. They should be considered in different experiments. Projection $M = J$ in the internal system of fragments does not mean that detection of another projection of the spin — on the perpendicular axis of fission — will result in $M = 0$. Degree of polarization of such states can be measured in (n, n) angular correlations. The state $M = 0$ is a different vector of state. It should be measured simultaneously with detection of the fission direction. This result shows that if we knew the hidden spin projection, we could calculate of course the angular distribution, also with respect to any direction, *e.g.* fission direction. But in order to know, one should first make a measurement of it. And this is a different experiment. Therefore, one should chose the quantization axis in accordance with what is observed experimentally, and consider the corresponding magnetic quantum number of the spin.

Simultaneous consideration of another projection turns out to be unobservable — that is hidden variable, whose involving into calculation leads to a wrong result.

At the same time, note that the two distributions, given by Eqs. (2) and (3), are presently under CORA experimental investigation [7] of the (n, n) and (n, n, f) correlations. Thus, the ratio of the parameters turns out to be a measurable quantity. The equality of this ratio to two is justified above only for the case of 100% polarization or alignment. Moreover, it is different in the case of the $E2$ transitions. In general case, the angular distribution also depends on the initial and final spins of the fragments, as one can see from Fig. 2. Therefore, the resulting form (8) or (7) instead of (4) or (5) of the emission spectra can be due to averaging over all the fragments with their spins and multipole mixtures of the transitions.

Furthermore, in the internal coordinate system, the fragments are 100% polarized. Therefore, one could expect, that in the case of (n, n) angular correlations, the right form should be just (1), not (6), under supposition of mostly $E1$ transitions, though. And the choice of A_{nJ} has nothing to do with A_{nf} as taken from the (n, f) experiment. The CORA experiment, performed at IPHC Strasbourg, aims at elucidating neutron emission mechanisms in the fission. Experimental check of the relations obtained above, and Eq. (9) first of all, looks very significant for the progress to this end.

The author would like to express his gratitude to I. Guseva for detailed and fruitful discussions.

References

[1] Balatz M Y., Kondratiev L. N., Lansberg L.G. et al. Zh. Exp. Teor. Fiz. **38**, 1715 (1960); **39**, 1168 (1961).

[2] Belovitskii G. Y., Baranov V. N. and Steingrad O. M. Yad. Fiz. **57**, 2140 (1994).

[3] F. F. Karpeshin, Yad. Fiz., **40**, 643, 1984 *Engl. transl.* Sov. J. Nucl. Phys., *40*, 412, 1984.

[4] F. F. Karpeshin, *Angular asymmetries in emission of muons from prompt fission fragments.* Nucl. Phys. **A617**, 211 (1997).

[5] F. F. Karpeshin, *Nuclear Fission in Muonic Atoms and Resonance Conversion*, Saint Petersburg: "Nauka", 2006.

[6] Skarsvag K. Phys. Rev. **C 22**, 638 (1980).

[7] A. Chietera, L. Stuttg, F. Goennenwein *et al.* EPJ A 54, 98 (2018).

[8] I.S. Guseva, in Proceedings of ISINN-23, Dubna, May 25–29, 2015, JINR, E3-2016-12 (Dubna, 2016), p. 80.

POST SCISSION NEUTRON EMISSION AND TRANSFORMATION OF FISSION FRAGMENTS YIELD: ARE THE REGULARITIES?

V.T. Maslyuk, O.O. Parlag, M.I. Romanyuk, O.I. Lengyel, O.M. Pop, N.I. Svatyuk

Institute of Electron Physics, Universitetska str., 21, 88017 Uzhhorod, Ukraine

volodymyr.maslyuk@gmail.com

1. Introduction

Studying the peculiarities of the formation of fission fragments and the processes of nuclear transformations of atomic nuclei is an important and urgent task of modern physics [1]. The success of its solution demonstrates the depth of our understanding of the fundamental issues of the stability of nuclear matter, the nature of nuclear forces, and nuclear transformations, for example, after the emission of post fission neutrons or beta particles. Applied aspects of this problem are:

- nuclear energy use;
- nuclear geophysics;
- radioecology;
- medicine with its advances in isotope and radiation therapies;
- a number of other applications.

Neutron activity is a permanent attribute of the fission of atomic nuclei and the related relaxation processes of the nuclear fragments' system with the emission of elementary nuclear particles [2]. Neutron emission spectra have their regularities connected to the topology of mass-charge spectra of fission fragments (MCSFF) with two or three humped yields curves. Thus, we are talking about "tooth-like" dependences of emitted neutrons $n(A)$ on the mass (A) or charge (Z) of fission fragments, which follow the topology of the MCSFF nucleus [3]. To determine $n(A)$ or $n(Z)$ we need a qualitative experiment.

Investigation of the nature of the temporal evolution of MCSFF, for example, taking into account the post-fissile emission of elementary particles, is also a difficult task for theoretical research. The basis of modern theoretical approaches to describe the processes of nuclear fission and yields of fission fragments are various modifications of the liquid drop model. Within this model, it is possible to consider its spatial and deformation parameters and take into account the dynamics of atomic nuclei fission [4, 5]. The post-fission state of the nucleus is considered a bi-nuclide system in which nuclear transformations are neglected. Despite the significant progress made by these methods for nuclear physics, they all need some fitting parameters as the viscosity of nucleus, surface tension data on the density of states energy levels, etc.

The theoretical approach proposed in studied the post-scission ensemble of nuclei, created by all fission fragments with the thermodynamic parameters as temperature T and pressure P, are determined from the state of a fissile nucleus. This approach did not require fitting parameters and can study the fission characteristics both as light (pre actinides) and super-heavy nuclei. In this work, we present the results of the study of the influence of the emission of nuclear particles, mainly neutrons of fission, on the post-fission state of MCSFF, their isotopic and isobaric characteristics. These calculations are essential for understanding the nature of neutron activity and explaining the features of the dependences $n(A)/n(Z)$ as, for example, their "tooth-like" behavior. The calculation was performed on the example of actinide nuclei, the isotope ^{235}U, for which there are sufficiently complete bases of nuclear physical constants.

2. Theory: the many ensambles model

The basics of the post-scission approach and the proposed statistical method for the systematization of fission fragments are described earlier [2, 6–9]. The study's subject is the post scission configurations or the ensemble of fission fragments of the fissioning nucleus with atomic mass A_0 and the charge Z_0 obtained due to thermodynamic ordering. This ensemble's single nuclear cluster, denoted by i, comprises two fission fragments j=1, 2 with $N^i_{p,j}$ protons and $N^i_{n,j}$ neutrons when nuclear particles are emitted. Each cluster satisfies the following conservation conditions:

$$\sum_{j=1,2}(N^i_{p,j} + N^i_{n,j} + n^i_j) = A_0,$$
$$\sum_{j=1,2}(N^i_{p,j} + m^i_j) = Z_0; \qquad (1)$$

The positive sign m^i_j has the meaning of the number of emitted $^+\beta$ and a negative one, respectively, the number of $^-\beta$ particles. There are several options for constructing ensembles of fission fragments, taking into account post scission emission of nuclear particles. In the first one, such an ensemble can be built for fixed values of n, m in (1), i.e. $n^i_1 = n^i_2 = n$, $m^i_1 = m^i_2 = m$. In this paper, considering the statistical nature of the emission of nuclear particles, we used an extended version, when $\{n, m\}$ only sets the limits within which the emission of nuclear particles can occur. In other words, the ensemble will contain all the fission fragments obtained, taking into account both the neutron emission in the range $(0 – n)$ and for beta particles, respectively, in the range $(0 – m)$. Only the conservation conditions (1) must be hold. By changing the sets {n, m}, it is possible to realize a different number of ensembles, each of which contains all the fission fragments obtained after emission of the nuclear particles within the range of values (0, 1,… n) and (0, 1,… m). Further calculation in the case of many ensembles based on the following assumptions [10]:

- Nucleons with different binding energy for different nuclei fragments must be considered as statistically non-equivalents. This requires the introduction of new color statistics for systems whose energy is not additive in the number of particles;
- The most probable characteristics post fission ensembles of nucleus nucleons such as MCSFF, isotopic, isobaric outputs, characteristics of neutron activity are the observed values.

The proposed thermodynamic method contains no time variables and cannot consider the kinetics of the fission process. It is focused on investigating only the final state of the fission fragments ensemble realized after the complex radioactive-decay processes of neutron/beta particle emission both as prompt and delayed. However, the time evolution of MCSFF can be considered indirectly by constructing many nuclei ensembles resulting after the emission of chains of nuclear particles of different lengths. Increasing the size of the chains of emitted particles allows one to realize the state of the system of fission fragments after a long time since the scission of the initial nucleus. Such a procedure can simulate the conditions for post-fission experiments when measurements are carried out after a long "cooling" time of an irradiated sample [10]. The parameters that determine the equilibrium condition for each of the investigated ensembles of nuclear fragments are subsequently deduced from the state of the minimum thermodynamic potential of constant pressure [11], which for *i*th nuclear cluster has the form:

$$G_i = \varepsilon_i - TS_i + PV_i \tag{2}$$

For *i*th cluster here ε_i is the internal energy, and V_i, respectively, the volume of a two fragments cluster, $V_i = V_1^i + V_2^i$. The ε_i values can be determined by the binding energy of the two-fragment cluster and have the negative values corresponding to the bound states of the nucleons. For different nuclear clusters, its spectrum $\{\varepsilon_i\}$ is an additive quantity in the binding energy, $B(N_{p,i}^j, N_{n,i}^j)$, of the *j*th nucleus fragment from the *i*th cluster:

$$\varepsilon_i = \sum_{j=1,2} B(N_{p,i}^j, N_{n,i}^j). \tag{3}$$

Here according to (1), $N_{n,1}^i + N_{n,2}^i = A_0 - n_1^i - n_2^i$, $N_{p,1}^i + N_{p,2}^i = A_0 - m_1^i - m_2^i$. Binding energies, $B(N_{p,i}^j, N_{n,i}^j)$, used in (3) are tabulated in [12,13], and their extrapolation is given, for example, in [14,15]. The term PV_i can be written as $PN^i\Delta\text{v}$, where N^i – number of fission-fragments nucleons, $N^i = N_{n,1}^i + N_{n,2}^i + N_{p,1}^i + N_{p,2}^i$, and Δv is the elementary volume of the nucleus per nucleon, which is 40–50 times larger than the size of the nucleon [1]. The constant $P\Delta$v is a parameter of the theory. It can be roughly evaluated through the ideal gas law: $P\Delta V = \Delta N \cdot T$, and $\Delta N \sim 1$, and the value of $P\Delta$v must be in the same order as T. More detailed value based on neutron emission spectra gives for $P\Delta$v range 3–5 MeV [2]. The configurational entropy S_i in (2):

$$S_i = \ln(\omega_i) \tag{4}$$

is calculated through the degeneracy factor ω_i with the account of the statistical nonequivalence of nucleons with different specific binding energy:

$$\omega_i = A_0!/(\prod_{j=1,2} K(n_j^i)(N_{p,j}^i!(N_{n,j}^i - n_j^i)!), \tag{5}$$

where n_j^i – number of fission neurons of *j*th fission fragment from *i*th cluster, $K(n_j^i) = 1/n_j^i!$, $\prod_{j=1,2} x_j! = x_1!x_2!$. From the (5), one can see that with increasing the nuclear temperature T entropy term in eq. (2) is responsible for the increase the symmetry of fission fragments yields. This is since the maximum ω_i is achieved at $N_{p,1}^i = N_{p,2}^i, N_{n,1}^i = N_{n,2}^i$. Formulas (1) – (4) allow one to find the probability of realization or yield of two-fragments nuclear clusters of the *i*- sort. In the isothermal-isobaric ensemble, the probability of a microstate, here two-fragments cluster i, is defined by the term $\exp(-G_i/T)$ [31] and has the form:

$$Y(N_{p,1}^{i}, N_{p,2}^{i}, N_{n,1}^{i}, N_{n,2}^{i}) = \omega_i \exp\{-(\varepsilon_i + PV_i)/T\}/z, \tag{6}$$

where ε_i is the spectrum values (3) of the two-fragments cluster, ω_i determines its degeneration by the formula (5), the partition function of the system z is written as:

$$z = \sum_i \omega_i \exp\{-(\varepsilon_i + PV_i)/T\}. \tag{7}$$

The expression (6) refers to the probability of realization only of two-fragment clusters. The next step is calculating the distribution function $F(A_1)/F(Z_1)$ for the single fission fragment with mass A_1, or charge Z_1. To construct them from the array of values, (6), one must select all the functions whose arguments satisfy the condition $N_{p,1}^{i} + N_{n,1}^{i} = N_{p,2}^{i} + N_{n,2}^{i} = A_1$. The summing of such functions and to spread this procedure for all A_1 values is the next stage for mass spectrum finding. The same method is valid to build the charge spectra, only with selection for the argument $N_{p,1}^{i} = N_{p,2}^{i} = Z_1$ from all the functions (6). The final stage is to apply the normalization procedure for the sums obtained and determine the normalized values of $F(A_1)$ and $F(Z_1)$. These functions must satisfy the following equations:

$$\sum_{<A_1>} F(A_1) = \sum_{<Z_1>} F(Z_1) = 200\% \tag{8}$$

where the symbols $<A_1>$, $<Z_1>$ mean that the summation is over all masses/charges of heavy and light fission fragments.

3. The post fission emission of nuclear particles and the nuclear fission fragments yields: ^{235}U

The studies were performed on the example of odd-even isotope ^{235}U, whose MCSFF has been well established [16,17]. All possible schemes of post-fission emission of nuclear particles and construction of an array of many ensembles for them are considered. Each ensemble contains the ^{235}U isotope fission fragments after the nuclear particles' emission within their length chains. For the j-th nucleus from the i-th cluster, the result of the emission of m_j^i beta particles leads to the transformation $N_{p,j}^{i} \Rightarrow (N_{p,j}^{i} - m_j^i)$, where the positive sign m_j^i is for $^{+}\beta$ and the negative for $^{-}\beta$ particles, respectively. After the emission of the neutrons n_j^i: $N_{p,j}^{i} + N_{n,i}^{i} \Rightarrow N_{p,j}^{i} + N_{n,j}^{i} - n_1^i - n_2^i$. The calculation carried out for the ^{235}U shows that both the beta particles and the neutron's emission may change the most probable pairs of fission fragments' nucleon composition. It also favors the formation of most probable clusters with closed-shell fragments, having a greater specific binding energy. The neutrons emission leads to an increase in the configuration entropy (5) of the nuclear fission cluster. The most probable are two fragments fission clusters obtained from the minimum of the thermodynamic potentials of Gibbs (2) for a constant pressure ensemble. The results of calculations are given in Table 1 containing from M=1 to five of the most probable two fragments clusters, both without and when taking into account the emission of nuclear particles.

The calculation was given in the "cold", T=0.5 MeV and “hot” T=1.0 MeV assumptions for the ^{235}U fission temperature; the $P\Delta v$=3 MeV. The sign in front of n is always positive, while the sign in front of m indicates the sort of beta particles emitted: minus suggests that there is the chain of $^{-}\beta$ particles from the (-*m*, 0) range; positive m values relate to $^{+}\beta$ particles with their emission range (0, *m*).

Table 1. The evolution of five the most probable two-fragment clusters after the ^{235}U fission, *M*=1–5, after emission the neutrons of different chains’ lengths: n defines all their sets from the ranges (0, *n*) and similar for beta-particles: the ranges (-*m*, 0) for -β particles (0, *m*) for +β, respectively.

	n=0; *m*=0		*n*=2; *m*=0		*n*=2; *m*=-2	
M	T=0.5 MeV	T=1 MeV	T=0.5 MeV	T=1 MeV	T=0.5 MeV	T=1 MeV
1	$\{^{105}_{42}Mo,{}^{130}_{50}Sn\}$	$\{^{105}_{42}Mo,{}^{130}_{50}Sn\}$	$\{^{106}_{42}Mo,{}^{128}_{50}Sn\}$	$\{^{103}_{42}Mo,{}^{128}_{50}Sn\}$	$\{^{106}_{44}Ru,{}^{128}_{50}Sn\}$	$\{^{107}_{44}Ru,{}^{124}_{50}Sn\}$
2	$\{^{104}_{42}Mo,{}^{131}_{50}Sn\}$	$\{^{104}_{42}Mo,{}^{130}_{50}Sn\}$	$\{^{104}_{42}Mo,{}^{128}_{50}Sn\}$	$\{^{101}_{42}Mo,{}^{130}_{50}Sn\}$	$\{^{107}_{44}Ru,{}^{128}_{50}Sn\}$	$\{^{106}_{44}Ru,{}^{125}_{50}Sn\}$
3	$\{^{107}_{42}Mo,{}^{128}_{50}Sn\}$	$\{^{107}_{42}Mo,{}^{128}_{50}Sn\}$	$\{^{104}_{42}Mo,{}^{130}_{50}Sn\}$	$\{^{97}_{40}Zr,{}^{134}_{52}Te\}$	$\{^{106}_{44}Ru,{}^{126}_{50}Sn\}$	$\{^{105}_{44}Ru,{}^{126}_{50}Sn\}$
4	$\{^{103}_{41}Nb,{}^{132}_{51}Sb\}$	$\{^{103}_{41}Nb,{}^{132}_{50}Sn\}$	$\{^{102}_{42}Mo,{}^{130}_{50}Sn\}$	$\{^{104}_{42}Mo,{}^{130}_{50}Sn\}$	$\{^{105}_{44}Ru,{}^{127}_{50}Sn\}$	$\{^{108}_{44}Ru,{}^{124}_{50}Sn\}$
5	$\{^{102}_{40}Zr,{}^{133}_{52}Te\}$	$\{^{112}_{44}Ru,{}^{123}_{48}Cd\}$	$\{^{105}_{42}Mo,{}^{130}_{50}Sn\}$	$\{^{102}_{40}Mo,{}^{129}_{50}Sn\}$	$\{^{107}_{44}Ru,{}^{126}_{50}Sn\}$	$\{^{114}_{46}Pd,{}^{118}_{48}Cd\}$

M	*n*=3; *m*=0	*n*=3; *m*=-1	*n*=3; *m*=-2	*n*=3; *m*=-3	*n*=3; *m*=-4
1	$\{^{96}_{40}Zr,{}^{130}_{50}Sn\}$	$\{^{105}_{43}Te,{}^{128}_{50}Sn\}$	$\{^{106}_{44}Ru,{}^{128}_{50}Sn\}$	$\{^{109}_{45}Rh,{}^{126}_{50}Sn\}$	$\{^{112}_{46}Pd,{}^{122}_{50}Sn\}$
2	$\{^{106}_{42}Mo,{}^{128}_{50}Sn\}$	$\{^{103}_{43}Te,{}^{130}_{50}Sn\}$	$\{^{108}_{44}Ru,{}^{126}_{50}Sn\}$	$\{^{106}_{44}Ru,{}^{129}_{51}Sb\}$	$\{^{110}_{46}Pd,{}^{124}_{50}Sn\}$
3	$\{^{104}_{42}Mo,{}^{128}_{50}Sn\}$	$\{^{102}_{42}Mo,{}^{131}_{51}Sb\}$	$\{^{106}_{42}Mo,{}^{126}_{50}Sn\}$	$\{^{112}_{46}Pd,{}^{121}_{49}In\}$	$\{^{112}_{46}Pd,{}^{123}_{50}Sn\}$
4	$\{^{104}_{42}Mo,{}^{130}_{50}Sn\}$	$\{^{96}_{40}Zr,{}^{135}_{53}J\}$	$\{^{109}_{44}Ru,{}^{126}_{50}Sn\}$	$\{^{109}_{45}Rh,{}^{124}_{50}Sn\}$	$\{^{111}_{46}Pd,{}^{124}_{50}Sn\}$
5	$\{^{103}_{42}Mo,{}^{130}_{50}Sn\}$	$\{^{106}_{43}Te,{}^{128}_{50}Sn\}$	$\{^{106}_{44}Ru,{}^{126}_{50}Sn\}$	$\{^{114}_{44}Ru,{}^{121}_{49}In\}$	$\{^{118}_{48}Cd,{}^{118}_{48}Cd\}$

Figure 1 shows the results of the MCSFF calculations for the above cases. As one can see, the emission of $^{+}\beta$ particles has almost no effect on their MCSFF compared to $^{-}\beta$ particles' emission. As mentioned above, it is because the asymmetric fission fragments of ^{235}U are neutron-proficient nuclei. The emission of $^{+}\beta$ particles only increases the neutron excess in the nucleus. The corresponding nuclear clusters don’t increase the probability of realization than before the emission of $^{+}\beta$ particles. Therefore, the effect of the emission of $^{+}\beta$ particles on the formation of MCSFF is insignificant. When we consider the emission of $^{-}\beta$particles, another nature of the MCSFF change will occur. In this case, there are significant changes in the MCSFF and the redistribution among the most probable fission fragments, see Tables 1. All this causes a change in the topology of the MCSFF. At $n = 0$, the peak of the light distribution fragments is formed by Mo isotopes. If one considers nuclear particles' emission, this peak mainly became would be created by the isotopes Mo, Nb, Zr, Ru, Pd and Cd. All these isotopes result from the influence of both the filled neutron shells $N = 50$ and the entropy term (4), which stimulates the symmetry effects of the fission fragments.

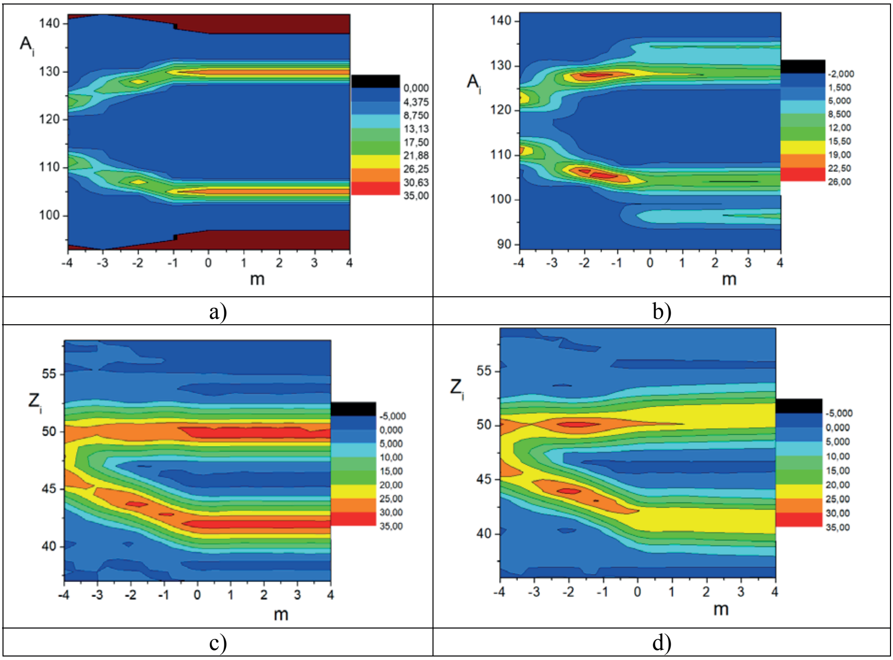

a) b)

c) d)

Fig. 1. The mass a), b) and charge c), d) fission fragments yields spectra of the ^{235}U obtained with consideration the beta particles and the neutrons emission with different chains length. Here a) and c) were built for *n*=0; b), d) with account the neutron emission chains with a capacity of *n* = 3. Minus in front of *m* suggests that there is the chain of $^{-}\beta$ particles from the (-*m*, 0) range; positive m values relate to $^{+}\beta$ particles with their emission range (0, *m*).

For the peak of the heavy fission fragments, if we consider the neutron's emission, only the isotopes of Sn can be changing on the isotopes Sb, Te, Cd, J, In. These all neutron emissions lead to growing the configuration entropy of the nuclear clusters, affecting MCSFF symmetrization. Fig. 1 shows that nuclear particles' emission intensifies the convergence of the asymmetric peaks, which looks like enhanced the symmetry mode of the MCSFF yields. Herewith, the proportionality of two peaks shape for the light and heavy nuclei-fragments can be violated. This state is because the peak of heavy fission fragments within the magic number 50 is formed by the most massive amount of two fission fragment clusters than the corresponding light ones with *Z* from the range (41, 43). For mass spectra, the peak of heavy fission fragments near *A* = 132 is the dominant one and formed by also the most massive sets of fragments closer to the doubly magic nuclei Sn. Genetically related light fission fragments sets have an *A* range (96 – 100).

It is very useful to investigate how the MCSFF transformation after the post-fission emission of nuclear particles affects the isotopic spectra and values of the probable value of Z_{prob} for a given A_{i}, or $Z_{\text{prob}} = Z_{\text{prob}}(A_{\text{i}})$. In this work, the Z_{prob} calculations were performed using isotope spectra for each chemical element with a fixed *Z*. They have shown that all such spectra are substantially varied, taking into account the post-fission emission of nuclear particles. Figure 2 (a) presents the results of such calculations for the Rb, Rh and Cs isotope spectra, all are a reliable markers of the fission of actinide nuclei. The sum of Y of the Rb, Rh, Cs isotopes yields were 100% normalized, and all data were fitted using B-spline procedure. This distribution was used to find value for Z_{prob}, considering the probable characteristics of the isotope spectra of these isotopes. The parameters for the beta particle and neutron chains were selected from Table 1. Fig. 2 b) demonstrates the dependence of Z_{prob} on the masses of the fission fragments A_i obtained with the same emission parameters as in Fig. 3 a). As one can see, the most significant changes of Z_{prob} from curve 1 to 2 occur for isotopes that do not contain magic numbers $Z = 50, 82$.

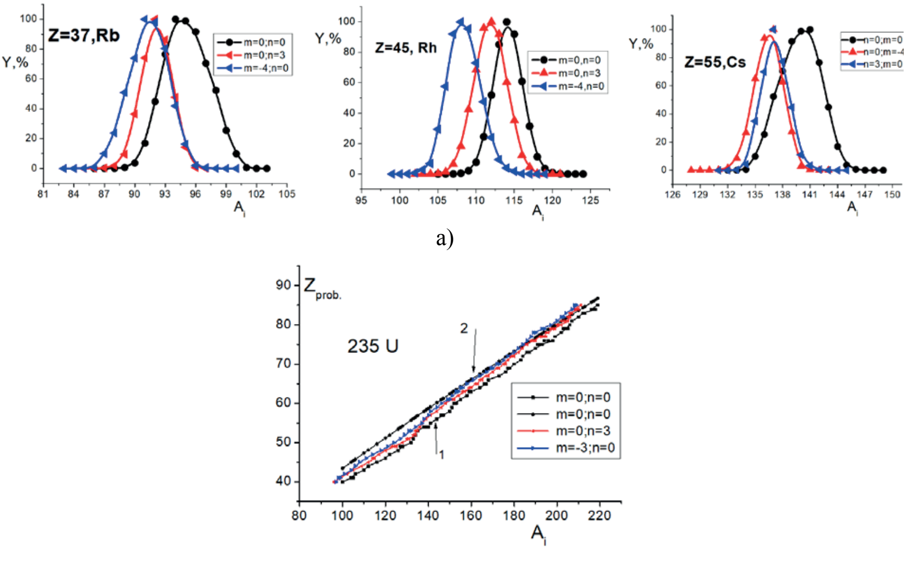

a)

b)

Fig. 2 (Color online) a) isotope spectra of Rb, Rh and Cs nuclides obtained without and accounting the post-scission emission of nuclear particles; b) dependencies between the masses A_i of fission fragments and their probable charges value Z_{prob}. Curve 1 is constructed for the pre-emission (m=n=0) state of nuclear fragments, 2, respectively, is obtained from formula (9) as for beta-stable isobars. The curves for m = -3, n = 0 and m = 0, n = 3 illustrate how the emission of nuclear particles approaching $Z_{prob}(A_i)$ curves to the beta-stable dependencies (9) .

The emission of nuclear particles shifts the dependences of $Z_{prob}= Z_{prob}(A_i)$ from the values realized in the pre-emission case, (n=0, m=0) and highlighted as 1, to dependence 2, determined from the liquid drop model for beta-stable isobars [1]:

$$Z_{ld} = \frac{A}{1.98 + 0.015A^{2/3}} \tag{9}$$

Moreover, such trends, Fig.2 b) are more pronounced, taking into account the emission of beta particles than neutrons or in the presence of neutrons and beta-particles.

4. Method of many ensembles and function of neutron activity of nuclei: ^{236}U

The proposed theoretical approach allows for the calculation of some observable neutron parameters: the total number of emitted neutrons as a function of the initial fragment mass (neutron emission function) ν*(A)* and total neutron emission number $\bar{n}$. These functions are very important for neutron physics and numerous applications of neutron fluxes. Among the factors that determine ν*(A)* and $\bar{n}$, the isotopic composition of the initial nucleus and its excitation energy or temperature *T* are the most important. The method of the ν*(A)* function calculation is based on the probability determining of the two-fragment cluster's realization (yield) that contains a pre-neutron emission fragment with mass *A* and the equilibrium number of neutrons *n*. Considering that cumulative yield of the fission fragments, $\bar{\nu}(A_i)$ is equal to value for all clusters containing the fragment with mass A_i from the cumulative chain:

$$\bar{\nu}(A_i) = 1/m\sum_{j=1}^{m}\nu_j(A_i)\,, \tag{10}$$

where *m* is the length of the cumulative chain that forms the yields of the fragments with the mass A_i. The total number of neutrons emitted in the act of nucleus fission $\bar{n}$ is calculated in a following way (normalization to 200% is used):

$$\bar{n} = 1/200\sum_{A_i=1}^{A_i=A_0}\nu(A_i)F(A_i)\,. \tag{11}$$

In Figure 3 the calculated and experimental [18] neutron emission functions for fission fragments of ^{236}U are shown. The cumulative chain length was *m*=10. The values of T, $P\nu_0$, their fluctuation varies and the number of statistical events were the same as in the previous calculations described above. We obtained that the average value $\bar{n}$ for such number of statistical events is 2.69 particles.

As one can see, the theoretical data agree well with the experiment. Moreover, the 9th order polynomial fit of obtained data (solid red line in Figure 3) reproduces the known experimental "saw-tooth"-curve of the neutron multiplicity, namely the peak about 115, minimum in vicinity of 128, the further growth in the range of 145 and decrease to 160. In addition, the proposed statistical method allows one to obtain the fine structure of ν*(A)*, like local minima at 98, 104, 117, 121, 128, 134, 158 and local maxima at 92, 101, 109, 114, 119, 124, 133, 144, 154.

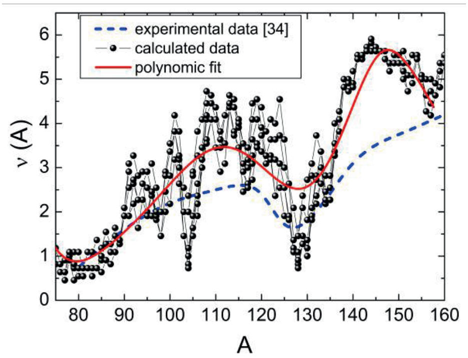

Figure 3. The fission neutron yield is given as a function of the fusion fragment mass of ^{236}U: dashed line corresponds to the experimental data [18], circles with line present the calculated data and the solid line is the polynomial fit of our data (see more detail in the text).

It should be noted that the experimental dependences $\nu(A_i)$ provide no data on such fine structure [3, 18, 20]. The fine structure might be caused by many factors such as presence of light and heavy fragments with the magic and near-magic numbers in the cluster; the optimal proton/neutron ratio in the fragments or influence of the odd/even effects, etc.

Conclusions

Thus, the “many ensembles method” shows the possibility to investigate how the post-scission emission of the nuclear particles influences the MCSFF and establish the nature of the “saw-tooth” behavior curve of the neutron multiplicity. Note that the proposed theory assumes the same “saw-tooth” dependence for beta particles multiplicity. It is shown that the fission emission of nuclear particles of beta and neutrons is focused on the achievement of the state of beta-stable isobars by fragments of fission of the nuclear cluster (9). The calculation indicates that the neutron emission function $n(A)$ must have a fine structure that is not obtained in the experiment. Note that it would be interesting to establish a similar experimental dependence of the beta particles emission function. Like neutrons, these particles contribute to the relaxation of fission fragments to the state of beta-stable isobars, described by the formula (9). The thermodynamic approach used in the paper allows us to establish the most probable two fragment clusters after the emission of nuclear particles and investigate their stability parameters. Such calculations help develop recommendations for processing nuclear experiments to study the fission fragments of atomic nuclei.

References

1. V.Yu. Denisov, V.A. Plyuyko. Problems of nuclear physics and nuclear reactions: https://inis.iaea.org/collection/NCLCollectionStore/_Public/45/091/45091761.pdf.
2. V.T. Maslyuk et al, J. Mod. Phys., 1555–1562 (2013), 4. http://dx.doi.org/10.4236/jmp.2013.412191.
3. U. Brosa, Phys. Rev. C32 (1985) 1438–1441.

4. F.O. Ivanyuk et al., Phys. Rev. C. 054331, 1–10 (2018) 97.
5. M.D. Usang et al., Sci. Rep. 1525 1–9 (2019) 9.
6. V.T. Maslyuk et al., Phys. Part. Nucl. Lett. 4 (2007) 78.
7. V.T. Maslyuk et al., Nuclear Physics 955 (2016) 79.
8. V.T. Maslyuk et al., EPL, 112 (2015) 52001
9. V.T. Maslyuk et al., Phys. Rev. C 98 (2018) 064608.
10. V.T. Maslyuk et al. arXiv:1907.04922v1 [nucl-th] .2019. 9 p.; Canad. J. Phys. (2021). https://doi.org/10.1139/cjp-2020-356
11. Zhirifalko. Statistical Physics of Materials (1973) 382 p. (in Russian).
12. Wang et al., Phys. Rev. C 84 (2011) 051303 (2011).
13. Wang et al., Chin. Phys. C36 (2012) 1603–2014.
14. G. Audi et al., Chin. Phys. C 41 (2017) 030001.
15. G. Audi et al., Chin. Phys. C 36 (2012) 1287.
16. R. Howell et al., Phys. Rev. C 100 (2019) 014608
17. M.E. Gooden et al., Nuclear Data Sheets 131, 319 (2016)
18. D.R. Nethaway et al., Phys. Rev. 139 (1965) 1505–1513.
19. Al-Adilia et al., Physics Procedia 47 (2013) 131–136.
20. M. Montoya, A. Rivera, Results in Physics 11 (2018) 449–451.

Parameterization of Neutron Yields for the First Chance Photofission Fragments

E.V. Oleynikov, A.I. Lengyel, V.T. Maslyuk, O.O. Parlag, I.V. Pylypchynec

Institute of Electron Physics, Universitetska str., 21, 88017 Uzhhorod, Ukraine

1. INTRODUCTION

The number of prompt neutrons is important nuclear-physical parameters necessary for practical calculations. This value is determined in detail and accurately for neutron-induced reactions for the most nuclides. At the same time, the experimental data and evaluation of prompt neutron yield in the case of photofission are much scarcer. With the increasing interest in the methods of nuclear fuel burning and long-lived actinide decontamination the need in precise values of nuclear constants. This is especially true for photonuclear constants. Therefore, the search was focused on a search the methods that can be used to estimate the value of averaged number $\bar{\nu}(A_F)$ and number of neutrons $\nu(A)$, emitted by corresponding fission fragments of atomic mass for photofission of arbitrary actinide.

The same data are also used to obtain the mass and charge distribution of actinide nuclei fission products and to convert the secondary fragments (products) yields into the primary ones. Typically, to estimate the number of neutrons $\nu(A)$, emitted by corresponding fission fragments of atomic mass A the phenomenological Wahl method [1] is applied, which is widely used till present for estimation of $\nu(A)$ during neutron- and gamma-induced fission. However, this method does not reflect the complex structure of sawtooth-like $\nu(A)$ dependence due to nuclear shells effect.

So far there is only information about the average number of neutrons emitted by two conjugated fragments and there is no information on photofission neutron emission curves. Primarily, this is due to experimental difficulties of time-span or direct neutron measurements in photofission experiments. However, in principle, neutron emission curves can be obtained combining the measurement of fragments mass distribution and post-fission neutrons.

The question is whether it is possible to identify some of the basic laws using the results of calculations depending on such parameters of actinides photofission as charge, mass, photon energy, shell characteristics. According to the results, one can parameterize neutron yields depending on the mass of actinide photofission fragments and other parameters that would reproduce the complex structure of saw-tooth behavior and allow to predict the dependence of $\nu(A)$ for the photofission of a wide class of actinide nuclei. This is the task of extreme interest.

2. PARAMETERIZATION OF ν(A) AND RESULT OF CALCULATION

A recent analysis of experimental data on neutron yields from fragments of thermal neutron fission of ^{233}U, ^{235}U, ^{239}Pu and spontaneous fission of ^{252}Cf showed that for a detailed account of “saw-tooth” particularity of dependence of fission neutron yield from a mass, an efficient tool is the value of model function $R(A)$, introduced by Wahl [1], which is defined as

$$R(A) = {\nu_{L,H}(A)}\Big/{\bar{\nu}(A)}, \qquad (1)$$

where $\nu_{L,H}(A)$ – prompt neutron yield of light and heavy fragment mass respectively, $\bar{\nu}(A)$ – total neutron yield, A – fragment mass and consists of several segments to reflect the observed features, depending on the complexity of the experimental behavior of $R(A)$. Therefore, the whole range of fragments mass was divided for more than 2×4 segments. "Experimental" values of $R(A)$ (with errors) can be determined using formula (1) from experimental values of $\nu_{L,H}(A)$ and $\bar{\nu}(A)$.

Model function $R(A)$ is chosen as a linear function for each segment:

$$R_i^L(A) = a_i^L + b_i^L(A - A_L), \tag{2}$$

$$R_i^H(A) = 1 - R_i^L(A - A_H) \tag{3}$$

for light and heavy fragments, respectively, i - number of the segment, a_i^L, b_i^L A_L – parameters, $A_H = A_f - A_L$, A_f – mass of compound nucleus.

To parameterize neutron emission and identify general prediction patterns we will use the results of $\nu(A)$ calculation for the photofission ^{235}U and ^{238}U at bremsstrahlung boundary energies of 12 ÷ 30 MeV (E* = 9.7–14.1 MeV) [2]. Here we simulate the behavior of neutrons from photofission of ^{235}U and ^{238}U actinides depending on the energy and nucleon composition in the giant dipole resonance energy range. As a result, we get the following picture (Fig. 1).

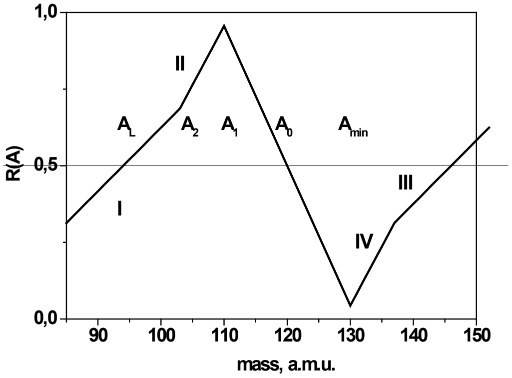

Fig. 1. An example of $R(A)$ function. The segments I-II and III-IV correspond to our parameterization.

Let us consider some features of $R(A)$ function. At the point of symmetric fission $A_0 = A_F/2$; $R(A_0) = 0.5$ and $R(A_L) = 0.5$, where A_L is determined from fitting. Kink points A_{min}, A_1 and A_2 are chosen from physical considerations and experiment: $A_{\min} = 130$ corresponds to the mass of nearly magic nucleus fragment associated with spherical shells $Z = 50$ and $N = 82$, where fission neutron yield is minimal. Then maximum neutron fission yield for light fragments will match point A_1, which is symmetrical to $A_{\min}$ relative to A_0,

$$A_1 = 2A_0 - A_{min}. \quad (4)$$

The kink point A_2 corresponds to the average fragment mass of light fragments,

$$A_2 = \langle A_L \rangle = A_F - \langle A_H \rangle \quad (5)$$

and related to the intermediate deformation of the fissioning nuclide.

The parameters a_i, b_i and A_L are determined by calculating the function $R(A)$ for 4 segments I – IV (see Fig.1). The number of free parameters can be reduced using the conditions.

$$a_1 = R(A_L) = 0{,}5 \quad (6)$$

$$a_2 = a_1 + (b_1 - b_2)(A_2 - A_L) \quad (7)$$

The dependence of b_i slopes on excitation energy is noticed on the Fig. 1 for $R(A)$, so we have chosen $b_i = x_i + yE_\gamma$. The value of A_L varies significantly with changes of actinide mass, at least for neutron-induced actinide fission. Therefore, we chose a similar parameterization [3]:

$$A_L = 90 + B * A_0 \quad (8)$$

B=1.45. To take even-even and even-odd effect into account we introduce the factor

$$P(N_F) = 2 - c[(-1)^{N_F} - (-1)^{Z_F}], \quad (9)$$

$$N_F = A_F - Z_F.$$

As a result b_i slopes will look as

$$b_i = (x_i + yE_\gamma)P(N_F), \qquad i = 1{,}2 \quad (10)$$

We calculate the function $R(A)$ for the photofission of actinides ^{235}U and ^{238}U according to (1) – (10) by fitting of 356 "experimental" values of $R(A)$.

Using the least squares method the five parameters x_1, x_2, c, B and y were defined to satisfactorily describe the characteristic "saw-tooth" behavior of prompt neutrons from the photofission of actinides with A = 235 a.m.u. and A=238 a.m.u.

Table 1. Calculated parameters of $R(A)$ function.

Parameter	Value	Error
x_1	$1.66 \cdot 10^{-2}$	$0.35 \cdot 10^{-2}$
x_2	$1.08 \cdot 10^{-2}$	$0.29 \cdot 10^{-2}$
y	$-0.384 \cdot 10^{-3}$	$0.212 \cdot 10^{-3}$
c	-0.282	0.159
B	$1.26 \cdot 10^{-2}$	$0.52 \cdot 10^{-2}$

The results of $R(A)$ calculation at the bremsstrahlung maximum energy 12 MeV are shown in Fig. 2.

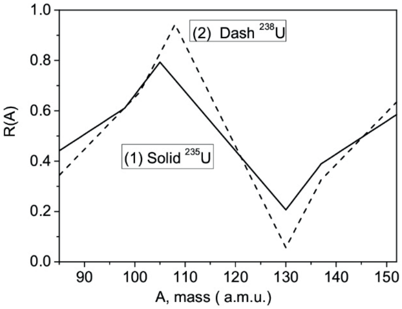

Fig. 2. The result of $R(A)$ functions calculation for ^{235}U ((1), solid line), ^{238}U ((2), dashed line) photofission at the bremsstrahlung maximum energy 12 MeV.

The curves for prompt neutrons yield $\nu_{L,H}(A)$ can be calculated with help (1), if the value of the prompt neutrons averaged number for photofission of the actinides is known. Otherwise instead the experimental values of $\bar{\nu}(A)$ in (1) one may use the results of empirical calculations of $\bar{\nu}(A_F)$, presented in [4] and described below.

The initial formula has been chosen:

$$\bar{\nu}(A_F,Z_F,E_\gamma) = \bar{\nu}_0(A_F,Z_F) + a(A_F,Z_F) * (E_\gamma - E_S) \tag{11}$$

where the slope $\bar{\nu}_0(A_F,Z_F)$ and the intercept $\alpha(A_F,Z_F)$ are :

$$\bar{\nu}_0(A_F,Z_F) = C_1 + C_2(Z_F - Z_0) + C_3(A_F - A_0) + C_4P(A_F,Z_F), \tag{12}$$

$$a(A_F,Z_F) = C_5 + C_6(Z_F - Z_0) + C_7(A_F - A_0) + C_8P(A_F,Z_F), \tag{13}$$

where $P(A, Z)$ – parity factor, E_S – nucleon separation.

Coefficients C_i were calculated by the least-square method. The final formula for calculating the averaged number of prompt neutrons for photofission of actinides was:

$$\begin{gathered}\bar{\nu}_0(A_F,Z_F) = (1{,}97 \pm 0{,}05) + (0{,}165 \pm 0{,}028)(Z_F - 90) + \\ +(0{,}0341 \pm 0{,}0093)(A_F - 232) - (0{,}0853 \pm 0{,}0094) * P(A_F,Z_F)\end{gathered} \tag{14}$$

$$\begin{gathered}a(A_F,Z_F) = (0{,}0963 \pm 0{,}75 * 10^{-2}) + (0{,}0371 \pm 0{,}43 * 10^{-2})(Z_F - 90) - \\ -(0{,}566 \pm 0{,}138) * 10^{-2} * (A_F - 232)\end{gathered} \tag{15}$$

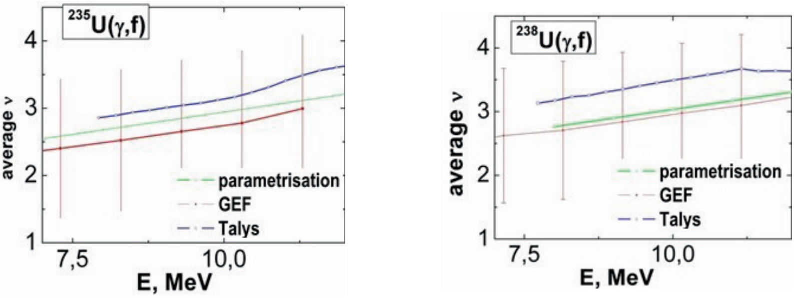

Fig.3. Energy dependence of the average number of prompt neutrons in photofission of ^{235}U and ^{238}U actinides.

The Fig. 3 shows the results of calculations of the energy dependence of the average number of prompt neutrons in the photofission of actinides ^{235}U and ^{238}U. Simulation results using the "GEF" [5] and "Talys" [6] codes are also presented, which are consistent with our data.

The results of the $\nu_{L,H}(A)$ calculation using (1) – (11), (14), (15) and Table 1 are shown in Fig. 2 and Fig. 4 (solid curve). As can be seen from the figures the calculated values for prompt neutrons yield are everywhere within the errors. For comparison we repeated our calculations, confining ourselves to two 2×1 segments in Fig. 4. Both calculations are indistinguishable from the x^2 criterion, but we prefer the first variant of the approximation $\nu(A)$, as such, in which physical considerations are taken into account. These observations allow to estimate the possible values of fission neutrons yield from light and heavy fragments with known total yields just through the mass distributions of fission fragments using the modified Terrell method [7].

The obtained results of the estimation of the dependence of the prompt neutron yields from light and heavy fragments for the first chance of actinide photofission are compared with the results of calculations (modeling) by the program codes "GEF" [5] and "Talys1.9" [6] (Fig. 5, 6).

With $R(A)$ function parameterization, which fairly well reproduces the characteristic features of its behavior and parameterization of average number of prompt neutrons, we can calculate the expected values of prompt neutrons yield for another actinides. Thus, to determine the photofission yield for neutron yield on fragment mass $\nu(A)$ of arbitrary actinides we need to know the value $\nu_F(A)$, which is determined by the general empirical formulas (11), (14–15). The resulting formulas of prompt neutron yield on fragment mass $\nu(A)$ of photofission of actinide nuclei can be used as initial (seed) for solving the integral equations [7] in these processes. The calculations are in qualitative agreement with the results of modeling by "GEF" [5] and "Talys1.9" [6].

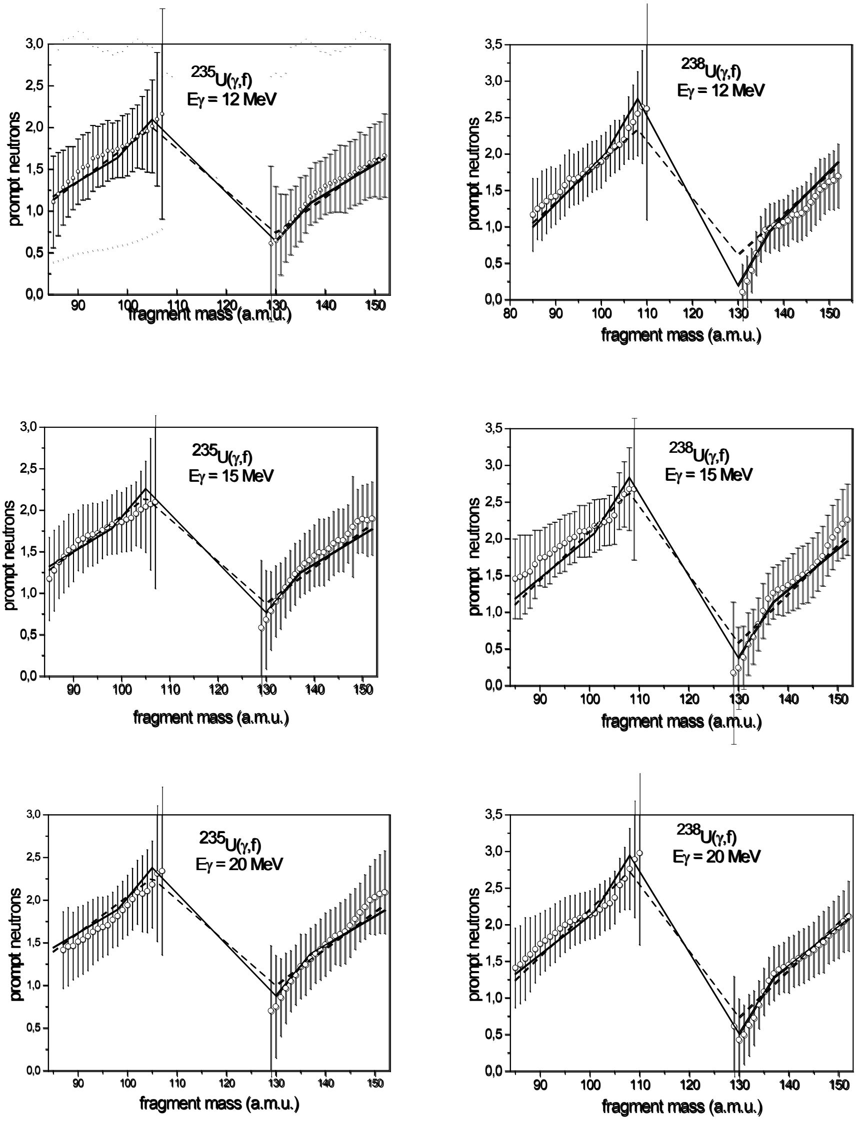

Fig. 4. Results of 2×2-segments calculation of $\nu_{L,H}(A)$ (solid lines) of ^{235}U (left) and ^{238}U (right) photofission with bremsstrahlung maximum energy of 12, 15, 20 MeV. Dashed lines correspond to 2×1-segment variant. Circles – experimental points of $\nu_{L,H}(A)$.

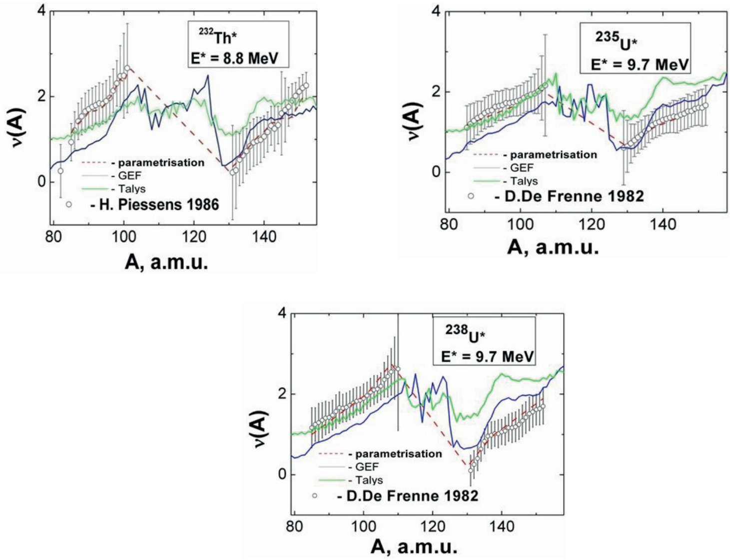

Fig. 5. Dependence $\nu_{L,H}(A)$ at close excitation energies for fissile nuclei ^{232}Th, ^{235}U, and ^{238}U.

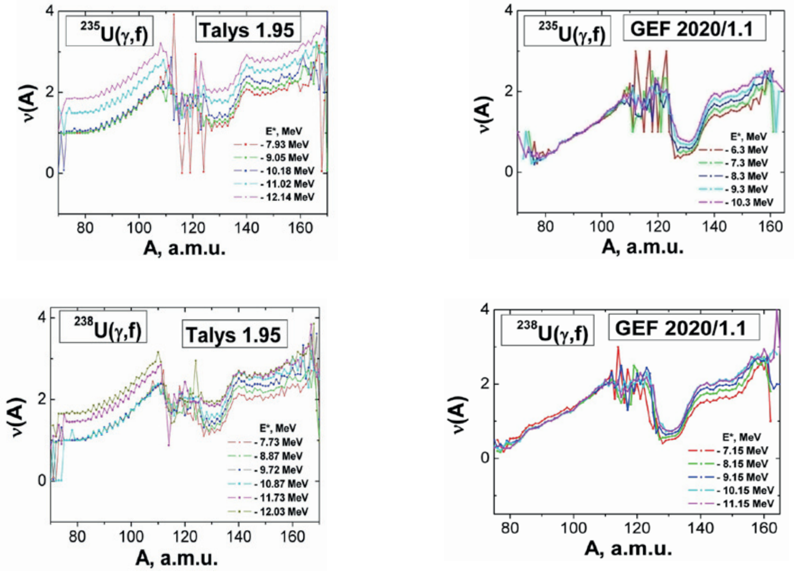

Fig. 6. Dependence of ν(A) on the excitation energy for fissile ^{235}U and ^{238}U nuclei.

3. CONCLUSIONS

The dependence of the averaged number of prompt neutrons emitted from fission products for each mass number (*A*) of photofission of actinide nuclei ^{232}Th, ^{235}U, and ^{238}U in the giant dipole resonance energy range have been parameterized. This approach allowed to describe the observed changes of "saw-tooth" behavior of neutron yield from the light and heavy fragments using few energy and nucleon composition-dependent free parameters and to predict (*A*) for other actinide isotopes. To estimate the number of neutrons emitted by corresponding fission fragments of atomic mass, *A*, the phenomenological Wahl method was applied. The total averaged number of prompt neutrons needs to construct the parametrizing function, which reasonably reproduces the characteristic features of its behavior and parameterization of averaged number of prompt neutrons. This method can calculate the expected values of prompt neutrons yield for arbitrary neighboring actinides, such as ^{237}Np or ^{239}Pu. It allows estimating the possible values of fission neutrons yield from light and heavy fragments with known total yields just through the mass distributions of fission fragments using the modified Terrell method. The obtained results of estimating the dependence of the prompt neutron yields from light and heavy fragments for the first chance of actinide photofission are compared with the results of calculations (modeling) by the program codes “GEF” and “Talys1.9”. Both approaches give the results qualitatively consistent. The energy dependence of neutron multiplicity is the same in both cases. Quite another, so called “Many Ensembles Method” to estimate the neutron multiplicity on bases the mass-charge spectra of fission fragments was used [8] with the same conclusion.

REFERENCES

1. *A.C. Wahl,* Systematics of fission product yields, Fission product yield data for the transmutation of minor actinide nuclear waste, IAEA 2008, 117–148.
2. *D. De Frenne et al.,* Charge distribution for photofission of ^{235}U and ^{238}U with 12–30 MeV bremsstrahlung, Phys. Rev. C., V. **26**, 4 (1982) 1356–1368.
3. *A.I. Lengyel et al.,* Parametrisation of prompt neutron yields from photofission fragments of actinide nuclei for the giant dipole resonance energy range, Problems of atomic science and technology, 2014, №5 (95), Series Nuclear Physics Investigations (63), p. 12–17.
4. *A.I. Lengyel et al.,* Calculation of average numbers of prompt neutrons for actinide photofission, Journal of Nuclear and Particle Physics, 2016, **6**(2), p. 43–46.
5. GEF 2020/1.1 http://www.khschmidts-nuclear-web.eu/GEF-2020-1-1.html
6. Talys 1.95 https://tendl.web.psi.ch/tendl_2019/talys.html
7. *J. Terrell,* Neutron yields from individual fission fragments, Phys. Rev., **127** (1962) p. 880–904.
8. *V.T. Maslyuk et al.* Post - scission neutron emission and transformation of fission fragments yield: are there regularities? (in present conference proceedings).

Fundamental Properties of the Neutron & UCN

A Possible Neutron-Antineutron Oscillation Experiment at PF1B at the Institut Laue-Langevin

V. Gudkov[1], E. Klinby[2], B. Meirose[3,4], D. Milstead[3], V.V. Nesvizhevsky[5],
K.V. Protasov[6], N. Rizzi[2], V. Santoro[7], W.M. Snow[8], R. Wagner[5], S.-C. Yiu[3]

[1] Department of Physics and Astronomy, University of South Carolina, South Carolina, USA-29208
[2] Technical University of Denmark, Anker Engelunds Vej 1, Lyngby, Denmark-2800
[3] Fysikum, Stockholm University, Stockholm, Sweden
[4] Fysiska institutionen, Lunds universitet, Lund, Sweden
[5] Institut Max von Laue – Paul Langevin, 71 avenue des Martyrs, Grenoble, France-38042
[6] Laboratoire de Physique Subatomique et de Cosmologie, UGA-CNRS/IN2P3, Grenoble, France-38026
[7] European Spallation Source, ERIC, Lund, Sweden
[8] Department of Physics, Indiana University, 727 E. Third St., Bloomington, Indiana, USA-47405;
wsnow@indiana.edu

Abstract: We consider a possible neutron-antineutron ($n-\bar{n}$) oscillation experiment at the PF1B instrument at Institut Laue Langevin. It can improve the best existing constraint on the transition rate and also allow the testing of the methods and instrumentation which would be needed for a later larger-scale experiment at ESS. The main gain factors over the most competitive experiment, performed earlier at PF1 instrument at ILL, are: a more intense neutron beam and a new operating mode based on coherent n and $\bar{n}$ mirror reflections. The installation of such an experiment would need a temporary replacement of the existing ballistic neutron guide by a specially designed $n/\bar{n}$ guide with a gradually increasing cross section and a specially selected coating as well as the development and construction of an advanced $\bar{n}$ annihilation detector with a high efficiency and low background. The overall gain factor could reach up to an order of magnitude and depends on the chosen experiment configuration.

1. Introduction

An observation of neutron-antineutron oscillations ($n-\bar{n}$) would be a major scientific discovery with fundamental implications for particle physics and cosmology. This process would violate baryon number (B) by 2 units. Although baryon number violation has not yet been seen in any laboratory experiment, it is the most obvious necessary ingredient in any attempt to explain the matter-antimatter asymmetry of the universe in terms of the Big Bang theory, as Sakharov explained long ago [1]. Unlike electric charge, the conservation of which is intimately associated with its role within the Abelian gauge theory of electromagnetism, there is no experimental evidence for any similar gauge interaction associated with baryon number which would automatically lead to baryon number conservation. If present, the long range that any such weakly-interacting "baryphoton" should possess would ruin the stringent experimental tests of the equivalence principle [2,3]. The spectacular observation of gravitational waves with properties as predicted by general relativity, the theory founded in part on this principle, arguably leaves even less room to expect baryphotons than before.

Given the above, we therefore expect that baryon number is violated based on our present understanding of both particle physics and cosmology [4]. If this is the case then it is "only" a matter of finding it. One should of course look in any system that supports a sensitive search which is consistent with all other known constraints. Baryon number violation by three units or more in a pointlike process involving fundamental fields is strongly ruled out by particle physics experiments and cosmological arguments. The present Standard Model of particles and interactions can exhibit baryon number and lepton number violation through nonperturbative electroweak gauge field configurations with a nontrivial topological winding number [5]. The finite action of these field configurations leads to the exponential suppression of these amplitudes in our vacuum today. However, thermally-activated tunneling in the hot early universe can activate them [6], and serious discussions about the possibility of finding these "sphalerons" in next-generation high energy colliders have begun. The other alternatives are baryon number violation by one or two units.

From the cosmological point of view there is an important distinction to be made among all cosmological baryogenesis models, namely, does the baryogenesis occur at an energy scale above, at, or below the electroweak crossover/phase transition, which is one of the most natural candidates for the out-of-equilibrium dynamics required by another one of Sakharov's baryogenesis conditions. If the sphaleron dynamics expected from the Standard Model are a feature of Nature, they can erase any baryon number violation from high energy scale processes of the type expected by dimensional analysis from the $\Delta B = 1$ operators responsible for proton decay. It can also convert high-scale lepton number violation into baryon number violation, as suggested in leptogenesis models. By contrast the scales associated with $\Delta B = 2$ operators can be slightly below the electroweak scale and still be consistent with present experiments, leading to the idea of "post-sphaeleron" baryogenesis [7–11] (PSB), so it is still possible to assert that sphaleron dynamics need not influence the cosmological baryon to photon ratio, which a successful theory of baryogenesis must explain. The long-term reach of the experiment to search for free neutron-antineutron oscillations described below has a potential for either a discovery of fundamental significance or the ability to narrow the phase space for PSB models so much that this option becomes very unlikely if the result is null, in which case it would be possible to conclude from experiment that sphaleron dynamics must (not merely could) be relevant for baryogenesis within the Sakharov paradigm. Opportunities for one laboratory experiment to close a loophole and make a qualitatively nontrivial statement of this nature through a null result about a process as difficult to access and as fascinating as baryogenesis are few and far between and should be seized. Neither searches for proton decay nor for CP violation in neutrino oscillations with foreseeable sensitivity can make a comparably crisp claim about the nature of baryogenesis even if one or both of these processes are discovered.

In this note, we explore the feasibility of an experiment at the PF1B instrument at the ILL to search for n–$\bar{n}$ oscillations, which has a potential to explore beyond the existing constraint. The main gain factors over the best experiment performed earlier at PF1 are: a more intense neutron beam and a new operating mode based on coherent n and $\bar{n}$ mirror reflections. In Section II, we present a general concept of this experiment. In Section III, we analyze the interaction of $\bar{n}$ with the n/ $\bar{n}$ guide walls and provide parameters for the design of the guide. In Section IV, we present a design of the n/ $\bar{n}$ guide. In Section V, we describe an advanced $\bar{n}$ annihilation detector. Such an experiment could take place before and would be complementary to the proposed HIBEAM/NNBAR program of neutron conversion searches at the European Spallation Source [12] at which an ultimate improvement of sensitivity to neutron-antineutron oscillations of three orders of magnitude compared to the last search with free neutrons [13] is expected.

2. A general concept of the proposed experiment

In Section II.A, we estimate a possible statistical sensitivity gain due to the move of the $n{-}\bar{n}$ experiment from PF1 to PF1B neutron facility. In Section II.B, we describe its new operating mode based on coherent n and $\bar{n}$ mirror reflections, estimate systematic uncertainties associated with the interaction of $\bar{n}$ with the guide walls, and introduce a concept of the $n/\bar{n}$ guide.

2.1. Comparison of statistical sensitivity on neutron beams PF1 and PF1B at ILL

The best constraint on the $n{-}\bar{n}$ oscillation time in experiments with free neutrons is equal $\tau_{n\to\bar{n}} > 0.86\cdot10^8$ s [13]. It was obtained using the PF1 neutron facility at ILL.

We start from comparing characteristic parameters of PF1 and PF1B neutron beams and their effect on the statistical sensitivity of this experiment; here, we still assume the experimental configurations to be the same.

The total neutron flux at PF1 at the entrance to the experiment was

$$F_{\mathrm{PF1}} \sim 1.7\cdot10^{11}\ \mathrm{n/s}, \tag{1}$$

the mean flight time was

$$t_{\mathrm{PF1}} \sim 0.11\ \mathrm{s}, \tag{2}$$

and the total experiment duration was

$$T_{\mathrm{PF1}} \sim 2.4\cdot10^{7}\ \mathrm{s}. \tag{3}$$

Since the last experiment, a more intense neutron beam has been built and the PF1 instrument was moved to a new position called PF1B. Its parameters at the exit of the guide have been measured [14]; the guide modernization mentioned in this paper has been done. The beam parameters at any intermediate point of the guide have not been directly measured but could be calculated to reasonable accuracy. The total neutron particle flux at the exit of the PF1B neutron guide is

$$F_{\mathrm{PF1B}} \sim 1.0\cdot10^{12}\ \mathrm{n/s}. \tag{4}$$

It is higher than that at positions upstream of the beam where a considered experiment can start. Not all $n/\bar{n}$ could reach the $\bar{n}$ annihilation detector. This is estimated below.

The mean flight time can be roughly calculated using the total experiment length and the mean neutron wavelength:

$$t(1)_{\mathrm{PF1B}} \sim 0.06\mathrm{s}, \tag{5}$$

$$t(2)_{\mathrm{PF1B}} \sim 0.085\mathrm{s}. \tag{6}$$

For the length estimation, we consider here a possibility to temporarily replace the downstream sections of the ballistic PF1B neutron guide by the $n{-}\bar{n}$ oscillations experiment.

There are two options for doing this: 1) replacing all sections starting from section 6 (see fig.1) ($t(1)_{\mathrm{PF1B}}$), with the guide length of 55 m guide plus the size of the annihilation detector, 2) replacing all sections starting from section 4 (see fig. 1) ($t(2)_{\mathrm{PF1B}}$), with the guide length of 75 m plus the size of the annihilation detector. Although technically possible, the second option is more difficult and expensive to realize. We do not consider further continuation of the experiment downstream the PF1B experimental zone because this modification would affect or even exclude the operation of some other ILL instruments. The mean neutron wavelength at the PF1B neutron guide exit is ~ 4.5A. However, it depends on the procedure of measurement and is different at the location upstream of the beam where $n-\bar{n}$ experiment can take place. It is simulated below.

A typical duration of major particle physics experiments at PF1B is 4 reactor cycles; there are 50 days per reactor cycle. This results in the experiment duration:

$$T_{\mathrm{PF1B}} \sim 1.7\cdot 10^7\ \mathrm{s}. \tag{7}$$

Using the formula below, we obtain a gain factor over the former PF1 position:

$$Gain(1) = \left(\frac{F_{PF1B}}{F_{PF1}}\right)\cdot\left(\frac{t_{PF1B}}{t_{PF1B}}\right)^2\cdot\left(\frac{T_{PF1B}}{T_{PF1B}}\right) \sim 1.2, \tag{8}$$

$$Gain(2) = \left(\frac{F_{PF1B}}{F_{PF1}}\right)\cdot\left(\frac{t_{PF1B}}{t_{PF1B}}\right)^2\cdot\left(\frac{T_{PF1B}}{T_{PF1B}}\right) \sim 2.5. \tag{9}$$

These estimations imply that a repetition of the $n-\bar{n}$ experiment at the PF1B neutron beam would give a factor of 1.2 or 2.5 improvement in the sensitivity. However, there are also other gain factors to be considered and taken into account. These are an eventual higher neutron flux and a different spectrum at the entrance to the experiment, better transport of slow neutrons due to the $n/\bar{n}$ guide, a longer experiment duration, a higher efficiency of $\bar{n}$ detection. We estimate these factors using direct simulations presented in Section IV.

2.2. The new experimental approach based on a $n/\bar{n}$ guide

Using the new idea of a guide for both n and $\bar{n}$ [15], [16], [17], the experiment can become more compact in the transverse directions and less expensive and thus more feasible. The theoretical uncertainties associated with the interaction of $\bar{n}$ with the walls of a short guide are small. However, they should be taken into account.

One uncertainty is associated with the imaginary part of the $\bar{n}$ scattering length. It accounts for the annihilation of subcritical $\bar{n}$ in the guide walls. To minimise this effect, materials are preferred with a large critical velocity for $\bar{n}$ and a guide shape that decreases perpendicular-to-surface velocities of $n/\bar{n}$ as explained in more detail in Section 4. Virtually all subcritical $\bar{n}$ produced in the $n/\bar{n}$ guide would reach the annihilation detector. The terms "subcritical" and "above-critical" $\bar{n}$ in this context are intuitively clear by analogy with normal n; they will be defined more rigorously at the end of Section IV. A fraction of annihilated subcritical $\bar{n}$ is approximately equal to the ratio

$$\frac{t_{PF1B}}{2\tau_{\bar{n}}} \sim 1.5\%, \tag{10}$$

where $\tau_{\bar{n}}$ is the storage time of $\bar{n}$ in the guide, typically ~2 s. A better knowledge of $\bar{n}$ annihilation rates [18] reduces further this uncertainty.

Another uncertainty is associated with the real part of the scattering length. It accounts for the validity of condition that $\bar{n}$ are subcritical at all collisions with the $n/\bar{n}$ guide walls. To decrease it, one essentially needs to meet the same conditions as above.

First, the guide wall material should provide a large enough critical velocity for both n and $\bar{n}$. For $\bar{n}$, this condition favors materials with a large atomic number [15], for instance, copper, which is a material routinely used for early neutron guides (before the super-mirror era). Several other materials could be also considered with roughly same performance. We limit the present analysis to only copper for simplicity.

Second, the guide shape has to be specially designed. As the spread of perpendicular components of $n/\bar{n}$ velocities in the initial super-mirror section of the PF1B neutron guide is much larger than the critical velocity of the $n/\bar{n}$ guide material for $\bar{n}$, the guide cross-section has to be gradually increased along the guide. It follows from the Liouville theorem that the increase in size, in the adiabatic case, would be equal to the decrease in the perpendicular velocity spread. In the realistic non-adiabatic case, this factor is a bit larger.

More details about the PF1B guide and neutron beam are given in ref. [14]. At the entrance to the proposed $n-\bar{n}$ experiment, the neutron guide has a rectangular cross section with the vertical size of h_{in} = 20 cm and the horizontal size of w_{in} = 9 cm, or smaller, depending on the exact point where the experiment starts. The spread of perpendicular neutron velocities at the exit of the PF1B guide is ~15 m/s to any direction. At the entrance to the $n/\bar{n}$ guide it is larger and can be simulated.

The gravitational energy of a $\bar{n}$ falling from the top of the $n/\bar{n}$ guide to its bottom is about equal or even larger than the Fermi potential of a $n/\bar{n}$ guide material. If the guide is long enough, it should be subdivided into a few superimposed guides in order to decrease gravitational effects on $n/\bar{n}$ trajectories. If the length of the diverging part of the $n/\bar{n}$ guide appears to be sufficiently long to shape the perpendicular components of $n/\bar{n}$ velocities then further upstream sections would be straight.

The actual shape of the $n/\bar{n}$ guide is optimized in this work by direct simulations described in Section IV. Before doing this, we consider in Section III the interaction of $\bar{n}$ with the guide walls, provide parameters of this interaction and estimate lifetimes of $\bar{n}$ in this experiment.

3. Interaction with a straight guide in $n/\bar{n}$ oscillation experiments

The interaction of $\bar{n}$ with a wall is described using an optical antineutron-nucleus ($\bar{n}$A) Fermi potential which can be evaluated using the optical model approach described in ref. [19] and developed to describe the low energy interaction of antinucleons ($\bar{N}$) with nuclei. At very low energies, it can be presented in terms of scattering length:

$$\mathrm{Re}\, a(\bar{N}\mathrm{A}) = (1.54\pm0.03)\mathrm{A}^{0.311\pm0.005}\ \mathrm{fm}, \qquad \mathrm{Im}\, a(\bar{N}\mathrm{A}) = -(1.00\pm 0.04)\ \mathrm{fm}. \tag{11}$$

Annihilation in such systems is very strong so this A-dependence allows a simple geometrical interpretation: the real part of the scattering length corresponds to simply the scattering of $\bar{n}$ on a black disc with about the nucleus radius, whereas the imaginary part is about the same for all nuclei and proportional to the diffuseness of the $\bar{N}$A interaction.

Using eq. (11) one can calculate the $\bar{n}$Cu Fermi potential:

$$V_{\mathrm{F}}(\bar{n}\mathrm{Cu}) \equiv V_0 - i\mathrm{W} = (104\pm2)\cdot\, i(22\pm1)\ \mathrm{neV}. \tag{12}$$

The real part corresponds to the critical velocity of ~ 4.5 m/s. The imaginary part is responsible for $\bar{n}$ annihilation in Cu.

In this simple approach $\bar{n}$ moves in a one dimension square well with a complex Fermi potential. In the following, we perform calculations for a guide with a constant cross section as this approach allows us to get an analytical solution. A diverging guide effectively decreases perpendicular velocities, thus leading to even smaller losses of $\bar{n}$. A real configuration of the experiment will have to be analysed using direct simulations.

For a short $n/\bar{n}$ guide, the most important parameter is the real part of Fermi potential. As subcritical $\bar{n}$ have no time to annihilate, main losses are associated with above-critical reflections.

To be conservative, we reduce the estimated real part of Cu Fermi potential (12) by 5σ and also increase its imaginary part by 5σ. Thus, the most conservative estimation of the Cu Fermi potential is:

$$V_F(\bar{n}\mathrm{Cu}) \equiv V_0 - i\mathrm{W} = 94 - i27 \text{ neV}, \tag{13}$$

and the form of the well potential is:

$$V(x) = \begin{cases} V_F, & x < -\frac{L}{2}, \\ 0, & -\frac{L}{2} < x < \frac{L}{2}, \\ V_F, & x > \frac{L}{2}. \end{cases} \tag{14}$$

The vertical potential is modified by gravity:

$$V(x) = \begin{cases} V_F - \frac{mgH}{2}, & x < -\frac{H}{2}, \\ mgx, & -\frac{H}{2} < x < \frac{H}{2}, \\ V_F + \frac{mgH}{2}, & x > \frac{H}{2}. \end{cases} \tag{15}$$

Note that $mgH = 32$ neV and $m|V_F|H^2$ and $m|V_F|L^2$ are very large numbers of the order $10^7 - 10^8$.

Strictly speaking, potential inside the bulk is a sum of Fermi and optical potentials. On the left side $x = -H/2$, $\bar{n}$ could tunnel through if their energy is very close to Fermi potential and escape from the guide. However, this tunneling effect is very small and is important only for the energies of a few peV close to the top of the Fermi potential (of the same order as energies of bound states of neutrons in a gravity field [22]). Our conservative estimation of Fermi potential renders this a negligible effect.

We are not interested in the energy spectrum very close to Fermi potential, so we neglect all these modification of the potential outside the box.

3.1. Square well problem

A solution for the square well potential is well known and can be found in textbooks. It can be easily generalized to the complex potential. As usually, there two families (symmetric and anti-symmetric) of wave functions obeying standard transcendental equations:

$$\sqrt{R^2 - X^2} = X \tan X \quad \text{and} \quad \sqrt{R^2 - X^2} = -X \cot X,$$

with $X^2 \equiv \frac{mL^2}{2\hbar^2}E$ and $R^2 \equiv \frac{mL^2}{2\hbar^2}V_F$. For the states far from Fermi potential, these equations can be solved analytically. The width of the levels due to imaginary part W of Fermi potential is equal to

$$\Gamma = \frac{4\hbar}{\sqrt{2mL}}\frac{E}{(V_0-E)^{3/2}}W. \tag{16}$$

For simplicity we assumed $W << V_0 - E$; we also noted $E \equiv E_n^{(0)}$ the real part of the quantum level energy. Let us note that $\Gamma \rightarrow 0$ when $E \rightarrow 0$.

For larger values of W, the last expression is more complicated:

$$\Gamma = \frac{4\hbar}{\sqrt{2mL}}\frac{E}{(V_0-E)^{\frac{3}{2}}}W\frac{\sqrt{2}\sqrt{\sqrt{1+\eta^2}-1}}{\eta\sqrt{1+\eta^2}}, \tag{17}$$

with $\eta = W/(V_0-E)$.

3.2. Step-linear problem

For the lowest states in the gravitation plus box potential (15), one can use an approximation neglecting the right wall of the box:

$$V(x) = \begin{cases} V_0, & x < 0, \\ mgx, & x > 0. \end{cases} \tag{18}$$

The energy spectrum of this problem can be found within the WKB-approximation [20], which is very suitable for the linear potential as usual:

$$\frac{E(V-E)^{1/2}}{\varepsilon^{3/2}} = \frac{\sqrt{2}}{16} - \frac{E^{\frac{3}{2}}}{\varepsilon^{\frac{3}{2}}}\, cot\left(\frac{E^{\frac{3}{2}}}{\varepsilon^{\frac{3}{2}}} + \frac{\pi}{4}\right), \tag{19}$$

where $\varepsilon = \frac{\hbar^2}{md^2} \approx 1.2$ peV and $d = \left(\frac{\hbar^2}{2mg^2}\right)^{1/3}$ are the characteristic energy and distance of the problem.

Both the real and imaginary parts of potential (12) are larger than $\varepsilon \approx 1.2$ peV. One can thus solve the last equation using the small parameter $\varepsilon \ll V_0, W$. In the zero order approximation, one obtains the well-known pure real expression

$$E_n^{(0)} = \varepsilon\left[\frac{3\sqrt{2}}{8}\pi\left(n-\frac{1}{4}\right)\right]^{2/3}, \qquad n = 1,2,\ldots.$$

The imaginary part (width) appears in the next order. One obtains:

$$\Gamma = \frac{1}{2\sqrt{2}}\left(\frac{\varepsilon}{V_0-E}\right)^{3/2}W, \tag{20}$$

where for simplicity we set $W << V_0 - E$, and we note $E \equiv E_n^{(0)}$. This is the same behavior as a function of V as in (8) in [15].

For larger values of W, the last expression is:

$$\Gamma = \frac{1}{2\sqrt{2}}\left(\frac{\varepsilon}{V_0-E}\right)^{3/2} W\,\frac{\sqrt{2}\sqrt{\sqrt{1+\eta^2}-1}}{\eta\sqrt{1+\eta^2}}, \tag{21}$$

with $\eta = W/(V_0-E)$.

Let us note that contrary to the case of a pure box, this width tends to a constant value when energy tends to zero. In our case (13), this constant value is equal to

$$\Gamma = 4.2\cdot 10^{-16}\,\text{eV}, \tag{22}$$

which corresponds to the $\bar{n}$ survival time in the lower quantum states

$$\tau_{\bar{n}} = \frac{\hbar}{\Gamma} \approx 1.6\ \text{s}. \tag{23}$$

For the highest energy accessible in this approximation $E = mgH$, one obtains $\Gamma = 7.3\cdot 10^{-16}$ eV and $\tau_{\bar{n}} = 0.9$ s. Let us be reminded that the time of flight of neutron in the guide is as small as 0.060–0.085 s (5).

3.3. Linear potential in a box

To obtain a more general expression for a linear potential in a finite size box (an exercise for a box with infinite potential is usually called "'quantum bouncer in a closed court") let us note that quantification condition (19) can be rewritten in a more general way which relates the Bohr-Sommerfelfeld integral to the obtained one at the turning points:

$$\sqrt{2m}\int_0^{E/mg}\sqrt{(E-mgx)}\,dx = (n + C_L + C_R)\hbar\pi, \tag{24}$$

where C_L and C_R are the constants related to the potential form at the classical turning points.

For a "linear" function, their values are equal to 1/4, for an "infinite" wall to 1/2. For a finite abrupt wall, in the leading term on E/V, one can rewrite

$$C_{L,R} = \frac{1}{2} - \frac{1}{\pi}\,arctan\frac{k_{in}}{k_{out}}, \tag{25}$$

where k_{in} and k_{out} are the momenta (real and complex) inside and outside the well on its left and right side.

For instance, in the previous example, on the left abrupt turning point $k_{\text{out}} = \sqrt{2m(V-E)}$ and $k_{in} = \sqrt{2mE}$.

Let us note that expression (25) covers the limits of a "linear" function ($k_{in} = k_{\text{out}}$, $C_{L,R} = 1/4$) and of an "infinite" wall ($k_{in}/k_{\text{out}} = 0$, $C_{L,R} = 1/2$).

For particles of higher energies, the turning points are those of box boundaries $x = 0$ and $x = h$. Thus the quantification condition can be rewritten in the form:

$$\sqrt{2m}\int_{-E/2mg}^{E/2mg}\sqrt{(E-mgx)}\,dx = (n + C_L + C_R)\hbar\pi, \tag{26}$$

and the integral can be easily calculated

$$\sqrt{2m}\frac{2}{3}\left[\left(E+\frac{mgH}{2}\right)^{3/2}-\left(E-\frac{mgH}{2}\right)^{3/2}\right]=(n+C_L+C_R)\hbar\pi, \tag{27}$$

For a box with the infinite potential well (“a quantum bouncer in a closed court”), $C_L = C_R = 1/2$, the problem was studied in detail (see [21] and references therein). In particular, it is shown that for high energies $E > mgH$, the spectrum finds its usual n^2-behavior corresponding to the spectrum in a pure box.

For a box with a finite height and complex potential (which makes k_{in} and k_{out} complex), the energies also become complex with the imaginary part which is directly calculated from (27):

$$\Gamma = 2\hbar\sqrt{\frac{g}{H}}\frac{\sqrt{\frac{mgH}{2}}}{\sqrt{E+\frac{mgH}{2}}-\sqrt{E-\frac{mgH}{2}}}\times Im\left\{arctan\frac{\sqrt{E+\frac{mgH}{2}}}{\sqrt{V_0-iW-\left(E+\frac{mgH}{2}\right)}}+arctan\frac{\sqrt{E-\frac{mgH}{2}}}{\sqrt{V_0-iW-\left(E-\frac{mgH}{2}\right)}}\right\}, \tag{28}$$

In the limit of low energies, $E<<V_0$, $W<<V_0$, and $mgH << E$, one obtains again eq. (16).

After some algebra calculations, one can write eq. (28) in a more explicit form:

$$\Gamma = 2\hbar\sqrt{\frac{g}{H}}\frac{\sqrt{\frac{mgH}{2}}}{\sqrt{E+\frac{mgH}{2}}-\sqrt{E-\frac{mgH}{2}}}\{\varphi(\vartheta_+,\omega_+)+\varphi(\vartheta_-,\omega_-)\}, \tag{29}$$

$$\varphi(\vartheta,\omega)=\frac{1}{4}ln\frac{1+\sqrt{\vartheta^2+\omega^2}+\sqrt{2}\sqrt{\sqrt{\vartheta^2+\omega^2}-\vartheta}}{1+\sqrt{\vartheta^2+\omega^2}-\sqrt{2}\sqrt{\sqrt{\vartheta^2+\omega^2}-\vartheta}}, \tag{30}$$

$$\vartheta_\pm=\frac{V_0}{E\pm\frac{mgH}{2}}-1, \qquad \omega_\pm=\frac{W}{E\pm\frac{mgH}{2}}. \tag{31}$$

Let us note that the width tends to a constant value when the energy is approaching the Fermi potential corrected by gravity ($\vartheta_+ \to 0$ or $E \to V_0 - mgH/2$). This is due to the contribution of the imaginary part of potential to the reflection.

We will use this formalism to conservatively estimate the value of the effective critical velocity of the guide walls for $\bar{n}$, which separates the ranges of "subcritical" and "above-critical" $\bar{n}$. With the parameters from (13) and $H = 30$ cm, the annihilation time for the highest energy $E=V_0-mgH/2$, or perpendicular velocity ~3.9 m/sec, appears to be $\tau_{\bar{n}} \approx 0.077$ s which is slightly larger than the time of flight of $n/\bar{n}$ through the "short" guide (0.06 s) and slightly smaller than the time of flight through the "long" guide (0.086 s) (5). Thus the natural choice for the maximum allowed perpendicular velocity is ~3.9 m/sec corresponding to ~75 neV. We use it for the design the $n/\bar{n}$ guide as described in Section 4. "Fine tuning" of the effective critical velocity/energy of the guide wall for $\bar{n}$ is not important at the stage of this feasibility study. Moreover, this value would not depend significantly on the parameters of the guide. It can be done later, as soon as the guide configuration is fixed. This "fine tuning" is expected to slightly increase the experiment sensitivity. Also we will use this formalism in further developments of this analysis, in particular for the cases of long $n/\bar{n}$ guides, where the second straight section of the guide provides the dominant contribution to the experiment sensitivity. Note that a much longer $n/\bar{n}$ would slightly decrease the value of the effective critical velocity as defined here.

4. Design of the $n/\bar{n}$ guide

The neutron guide H113 and beam parameters that feed the PF1B facility are described in ref. [14]. The guide consists of a long ballistic middle section that is enclosed by straight entry and exit sections. There are two different possibilities, given the constraints of the facility, to install the ideal guide for performing the $n/\bar{n}$ oscillation experiment, starting from 11.6m from the source with a special diverging guide with length of 75 m or starting from 31.6 m from the source with a guide of 55 m.

Based on these constraints the ideal layout of the guide for the proposed experiment has been optimized. In the simulations, we consider all $n/\bar{n}$ with perpendicular-to-surface velocities at each bounce below $V_{\perp}^{cutoff} \sim 3.9$ m/s to be reflected and reach the annihilation detector and we consider lost all $n/\bar{n}$ with perpendicular-to-surface velocities above this cut-off value. This is a conservative estimate since some $n/\bar{n}$ with velocities above this value could still be able to reach the annihilation detector and contribute to the sensitivity. However, systematic uncertainties associated with this contribution would start increasing rapidly with increasing the perpendicular component of velocity. Therefore, we ignore this small sensitivity gain at this stage of the feasibility study.

The design of the guide was performed using McStas 2.7 [25], a popular neutron ray tracing code ideal for this kind of study. As a starting point, we use the previously developed McStas instrument files describing the ILL cold source, the H113 guide and the PF1B experimental area (instrument file provided in a private communication by Torsten Soldner). The flux produced by the source component of the simulation (2.6×10^{10} n/cm^{2}s) is higher than the results of actual measurements at nominal reactor power (2.2×10^{10} n/cm^{2}s). Therefore a correction factor of 2.2/2.6 = 0.81 is applied to the output intensity of the simulations. Notably, the over-prediction is not necessarily related to the source brightness since several imperfections of the H113 guide (e.g. waviness, alignment imperfections) are not included in the simulation and they are likely to be the dominant source of the disagreement. Hence, even though we are replacing the H113 guide with a new guide, this factor was still applied to keep a conservative approach. The code used to generate the different geometries was written in Python, exploiting the interface provided by McStasScript, which is the McStas API for creating and running instruments from python scripting [23]. The gravitational fall is taken into account throughout the whole optimization process.

The aforementioned perpendicular-to-surface velocity condition on the copper guide walls corresponds to setting the Q_c value of the guide to $0.56\cdot Q_c^{Ni} = 0.0122$Å^{-1} ($Q_c^{Ni}$corresponds to $v_{Ni} = 6.9$ m/s) with a hard cut-off of the reflectivity for scattering vectors greater than Q_c. The reflectivity is hence computed by McStas using the empirical formula derived from experimental data in [24]:

$$I(Q)=\begin{cases} R = R_0, & Q \leq Q_c \\ R = \frac{1}{2}R_0(2 - tanh[(Q - mQ_c)]/W)(1 - \propto(-mQ_c)), & Q < Q_c' \end{cases} \tag{32}$$

where $R_0 = 0.99$, $m = 1$, slope $a = 3.2$Å and width of cut-off $W = 0.0015$Å^{-1}. The need for a gradual increase in the guide cross-section required by the Liouville theorem, along with the necessity of keeping the height small, lead the optimization problem in the direction of a "fixed entry and exit size" approach, in which, given the parameters that define the geometry of the guide, the number of sections is calculated such that the cross-section constraints at the entry and at the exit of the guide are respected. The approach used can be described as follows.

- The total divergent length L_{div}, the dimensions of the guide at the entry w_{in}, h_{in} (respectively the width and the height), at the exit w_{out}, h_{out}, the divergence angle for the vertical a_v and the horizontal a_h plane are given.

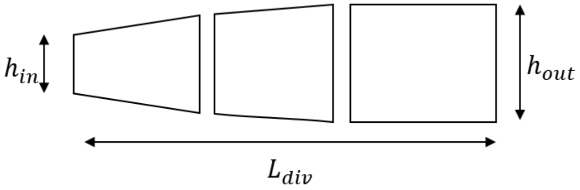

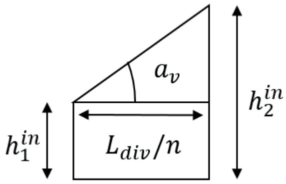

- Assuming n sections with length L_{div}/n and halving divergence at each step, the height (as well width) of each section is defined as:

$$h_1^i = h_2^{i-1}, \quad h_2^i = h_1^i + 2\frac{L_{div}}{n} tan\left(\frac{a_v}{2^i}\right). \tag{33}$$

- The following relation (showed for the vertical plane, but true for the horizontal too) links the starting and the ending section.

$$h_2^{out} = h_1^{in} + 2\frac{L_{div}}{n}\tan(a_v) + 2\frac{L_{div}}{n}\tan\left(\frac{a_v}{2}\right) + \cdots + 2\frac{L_{div}}{n}\tan\left(\frac{a_v}{2^{n-1}}\right) \approx$$

$$\approx h_1^{in} + 2\frac{L_{div}}{n} a_v \sum_{i=0}^{n-1}\frac{1}{2^i} = h_1^{in} + L_{div}a_v\left(\frac{4-2^{2-n}}{n}\right). \tag{34}$$

- Let us impose $h_1^{in} = h_{in}$ and then the condition:

$$h_2^{out} \leq h_{out}. \tag{35}$$

From (34) it is clear that one can always find a value of n large enough for (35) to be true, where in the limit → ∞ the guide is simply a straight guide. The interesting solution is the minimum integer n, which would give the biggest h_2^{out} allowed;

- The same applies to ω_2^{out}. It is important to notice that n_{min}^h and n_{min}^v can be considerably different, hence, the algorithm determines the final number of sections of the guide in such a way to halve independently the angles based on $n_{min}^h$and n_{min}^v. For example, if the 75m-guide requires n_{min}^h =1 and $n_{min}^v = 2$, then it will end up generating a 2-sections guide, where a_v is halved once after 37.5 m, while the vertical mirrors keep the same ah for the whole length;

- if L_{div} is less than the total length of the guide, a straight guide is inserted for the remaining distance.

The 99.7% of the beam of the previous experiment at PF1 was contained within the target of a 1.1 m [13] diameter surrounded by the detector. Therefore the first interesting guide exit to study is a square of 1×1 m^2. In addition, two smaller (0.4×0.4 m^2 and 0.8×0.8

m^2) and one bigger (1.2×1.2 m^2) exit windows were also considered. The cross section at the end of the $n/\,\bar{n}$ guide defines the size of the annihilation detector to be developed (see Section 5). The parameters left to optimize are L_{div} and the divergences a_v and a_h. The figure of merit (FOM) for the optimization used in this analysis is the same used for the optimization of the NNBAR experiment at ESS [12] and is given by the following quantity

$$FOM = \sum_i N_{ni} \cdot t_{ni}^2, \tag{36}$$

where for velocity spectrum bins i, N_{ni} is the number of neutrons per unit time reaching the annihilation detector after t_{ni} seconds of flight.

The parameter space to be explored by the simulations was chosen to be wide enough to include also its surroundings. In table 1 the optimal FOM value for each guide exit and guide total length (55 m and 75 m), along with the quasi-free time of flight (TOF) expectation value, the intensity at the exit and gain factor for a one-year-long experiment (section 2.1) are summarized. For convenience, the guide parameters that produced the optimal FOM values for all the different designs of table 1 are not reported in this work, but in fig. 1 two graphical representations of the 55 m and 75 m guide with $1\times1\mathrm{m}^2$ exit are shown. Overall, we observe that the requirement of a smaller guide cross section at the exit of the beamline, produces a higher number of sections as well as a lower divergence in both the vertical and the horizontal plane. The optimal divergent length, instead, is in general always close to the maximum allowed, but hits earlier a plateau for small exit sizes where the high number of sections makes the guide almost straight.

In fig. 2 we show the neutron wavelength and velocity distribution at the guide exit, both weighted using the FOM defined in eq. (36), for the configuration with the exit window of 1 m^2 and a 75m-long guide. The important feature to notice is that no wavelength cut-off is present in the distribution and the contribution of low energy neutrons stays relevant even when the source absolute intensity drastically drops, as expected by the t^2 factor in the calculation of the FOM (see eq. (36)).

	Exit square side, m							
	0.4		0.8		1		1.2	
	short	long	short	long	short	long	short	long
TOF(s)	7.98E-02	1.20E-01	6.94E-02	1.02E-01	6.94E-02	9.49E-02	6.95E-02	9.27E-02
I (n/s)	4.66E+11	3.92E+11	8.89E+11	6.85E+11	1.02E+12	8.73E+11	1.11E+12	9.79E+11
FOM	4.68E+09	8.45E+09	6.69E+09	1.14E+10	7.47E+09	1.26E+10	8.13E+09	1.37E+10
Gain	1.68	3.20	2.43	4.04	2.78	4.46	3.04	4.77

Table 1: Optimal FOM value for each guide cross section at the exit and guide total length (55 m and 75 m indicated as short and long, respectively), along with the quasi-free TOF expectation value, intensity at the exit and gain factor for one-year-long experiment defined in section 2.1. Gravitational fall was considered at all stages of the study.

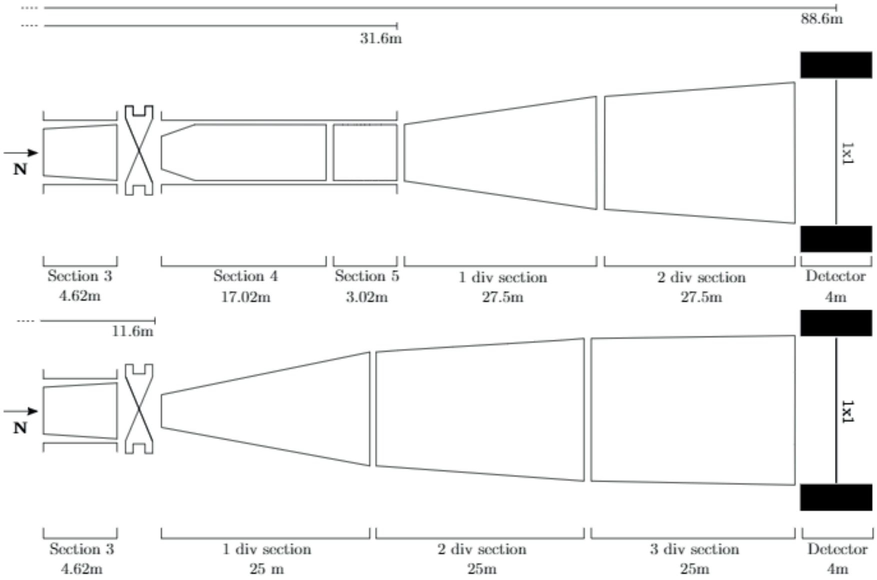

Figure 1. Graphical representations lateral view (not-to-scale) of the 55 m (top) and 75 m bottom) guide with a 1×1 m^2 exit. The short guide starts at 31.6 m from the neutron source and has w_{in} = 0.09 m, h_{in} = 0.2 m, horizontal and vertical initial divergences of 0.01 rad and 0.009 rad, respectively. There are two sections for a total divergence length of 55 m, w_{out} = 0.915 m and h_{out} = 0.942 m. Similarly, the long guide starts at 11.6 m from the neutron source and has w_{in} =0.077 m, h_{in} = 0.2 m, and horizontal and vertical initial divergences of 0.011 rad and 0.009 rad, respectively. There are three sections for a total divergence length of 75 m, w_{out} = 0.852 m and h_{out} = 0.987 m.

5. Design of the $\bar{n}$ annihilation detector

Using the $n/\bar{n}$ guide simulations and the geometrical constraints in the experimental zone of PF1B, we estimate the external size of the annihilation detector in both directions to be below ~ 2.8 m.

The maximum sensitivity of the experiment is achieved when the expected background is well below one event for the duration of the complete experiment and the efficiency of detection of $\bar{n}$ is maximized. A conservative estimation is that a new annihilation detector should at least achieve the 52% detection efficiency of the previous ILL [13] experiment, but most likely, due to the use of new technologies, it is expected to surpass it.

The detector must be sensitive to the characteristic antineutron-nucleon annihilation signal. The final state consists mainly of charged pions and photons from neutral pion decays. The detector consists of a thin (~ 100 μm) carbon foil in which the $\bar{n}$ would annihilate, a tracking chamber, which will allow particle identification as well as determination of the primary vertex, and a calorimeter.

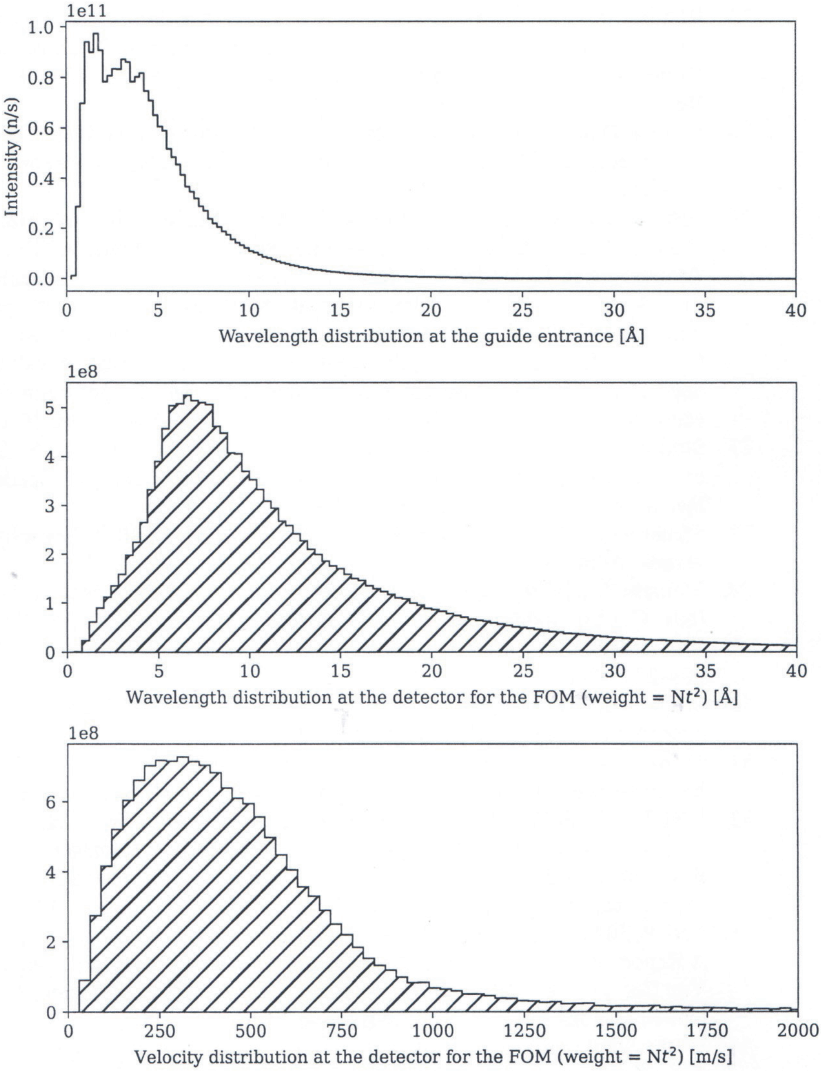

Figure 2. From top to bottom: neutron wavelength distribution at the guide entrance, wavelength and velocity distribution at the guide exit, weighted by the FOM, for the configuration with 1×1 m^2 exit window and 75m-long guide shown in fig.1. Notably, the absence in the distribution of a wavelength cut-off suggests that the contribution of low energy neutrons stays relevant even when the source absolute intensity drastically drops.

The tracking chamber will consist mainly of a Time Projection Chamber (TPC) which will provide three dimensional tracking and a measurement of the mean energy loss *dE/dx*. The calorimeter comprises arrays of plastic scintillators and lead-glass modules. The primary function of the scintillators will be to identify hits originating outside the inner detector volume, which will be important for particle identification via range determinations and for the rejection of cosmic ray background events. Electromagnetic calorimetry is provided by lead-glass modules and uses the Cerenkov effect. A high precision electromagnetic calorimeter is needed to identify neutral pion production via the decay $\pi^0 \rightarrow \gamma\gamma$. The calorimeters would be position sensitive, with a segmentation to be determined by simulation. This design is therefore in essence the same as being planned for the HIBEAM experiment at the European Spallation source [26]. A simulation and analysis software framework [27], which is based on detector simulation using GEANT-4 [28–30], can also be used for a search at the ILL. A complete analysis with simulated datasets is beyond the scope of this work. Here, distributions of sensitive observables in signal and one of the major sources of background (cosmic ray muons) are shown to demonstrate that a feasible detector design concept exists.

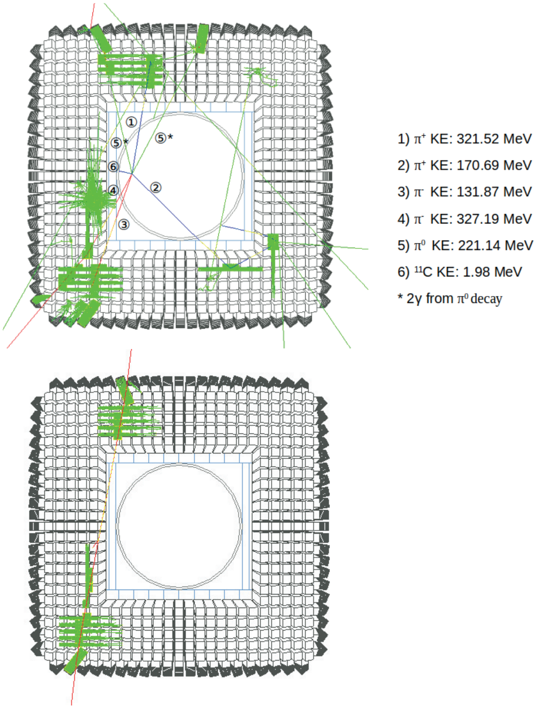

Figure 3. Event displays with the ILL detector showing (top) a signal event with five pions and (bottom) a cosmic muon.

Fig. 3(a) shows a signal event with five final-state pions in the ILL detector with a nuclear fragment from the carbon target. The pions' kinetic energies range from around 220–320 MeV. The antineutron-carbon annihilation signal was calculated with the model in Refs.[31,32]. Fig. 3(b) shows a cosmic muon of kinetic energy 495 MeV impinging the ILL detector. The cosmic muon enters from the top detector module and leaves the detector from the bottom. This was made using the CRY [33] cosmic ray program.

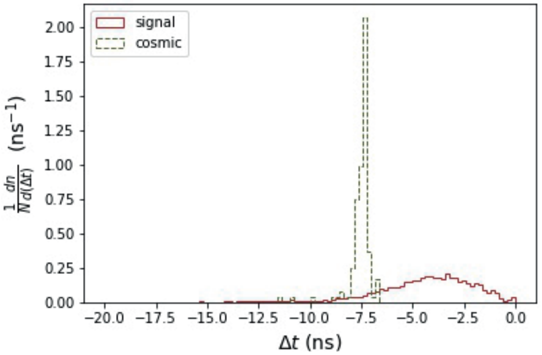

Figure 4. Timing quantity, Δt, for signal and cosmic muon background for the ILL detector.

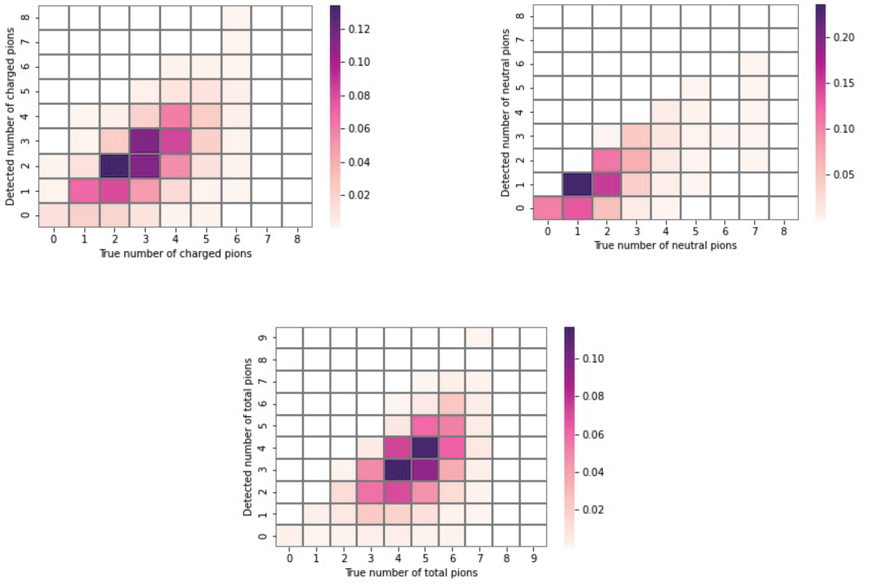

Figure 5. True and detector level multiplicities for (top left) charged, (top right) neutral and (bottom) all pions.

Fig. 4 shows the quantity $\Delta t = t_2 - t_1$, defined as the difference between the timing of the first (t_1) and last (t_2) signal in the scintillators. The spectra are shown for an annihilation event and a cosmic muon background event. Each cosmic event contains one charged cosmic muon passing through the ILL detector. Since the cosmic muons cross the top and bottom of the detector, Δt for cosmic background is expected to be larger than the signal. As expected, clear separation between the two distributions is observed.

Fig. 5 shows the multiplicities of neutral and charged pions for 1500 annihilation events. Measurements of pion multiplicity represent important evidence that an annihilation event has occurred.

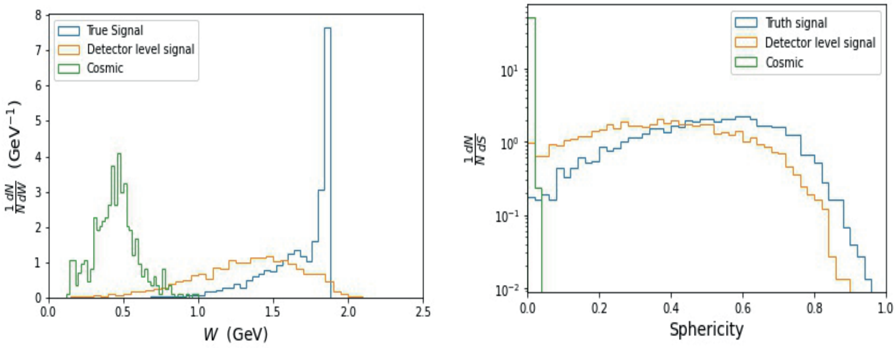

Figure 6. Left: the invariant mass distributions from the signal and cosmic background events. Both truth level and detector level results are shown. Right: the expected distribution of sphericity for signal events at the generator level and detector level and for cosmic ray muons at the detector level.

Fig. 6(a) shows the invariant mass distributions annihilation events at truth level and at detector level i.e. using information available from the detector such as energy loss and particle range. Detector-level background predictions for cosmic muons misidentified as pions are also shown for single muon events. The truth level invariant mass has a peak 1.88 GeV while the distribution of the reconstructed invariant is spread broadly and has a peak around 1.45 GeV in the ILL detector. The cosmic muon event distribution has a far lower invariant mass (typically around 500 MeV). Fig. 6(b) shows the sphericity distribution calculated for the same sets of events as shown in Fig. 6(a). As expected, the pure cosmic ray events have small values of sphericity, closer to zero, while signal (and signal with cosmic) events have larger sphericity.

6. Conclusion

We explore the feasibility of an experiment to search for n–$\bar{n}$ oscillations at the PF1B instrument at ILL. The main gain factors over the best experiment performed earlier at PF1 instrument at ILL are: a stronger neutron beam and a new operating mode based on coherent n and $\bar{n}$ mirror reflections. We show that the overall configuration is feasible. Due to the relatively short length available at PF1B, systematic uncertainties of the method are negligible. Virtually all subcritical $\bar{n}$ would be transported without losses to the annihilation detector. A major fraction of all the initial n could be converted to subcritical ones in a special diverging $n/\bar{n}$ neutron guide.

All the following estimations are preliminary and a more precise future analysis can change them slightly. The estimated statistical sensitivity for the $n\text{–}\bar{n}$ transition rate is up to an order of magnitude higher than that in the best performed experiment [13]. As a conservative estimate, the gain factor is ~2.8 for the "short" neutron guide and the middle-size $\bar{n}$ detector of 1 m, see Table 1. Potentially it can be further improved by a longer measuring time (say, a factor of ~2), a more efficient $\bar{n}$ annihilation detector, a longer $n/\bar{n}$ guide (a factor of ~1.6, see Table 1), a more accurate consideration of n and $\bar{n}$ transport and the account of their interaction with the guide walls (say, a factor of ~1.3), giving all together an additional gain factor of ~ 4.1), or the total gain factor of up to ~10.

This is large enough to provide a discovery potential. If, however, the actual transition rate is beyond the sensitivity of this experiment, it would be a significant step towards a future more sensitive larger-scale experiment at the ESS [12]. It would allow one to test the main experimental approaches and components of a future experimental setup. In such an experiment, the length can be increased using a guide with a constant cross section that is put after the diverging part of the $n/\bar{n}$ guide. This would lead to a nearly quadratic gain with regard to the increased length in the experimental sensitivity, as far as $\bar{n}$ annihilation losses are not too large. Such a saturation of the sensitivity corresponds to experiment lengths much larger, or neutron spectra much softer than those considered in this paper.

7. Acknowledgements

The authors are grateful to Torsten Soldner and Michael Kreuz for their very important help in this analysis. W. M. Snow acknowledges support from US National Science Foundation grant PHY-1913789 and the Indiana University Center for Spacetime Symmetries. This work is also funded by the HighNESS project at the European Spallation Source. HighNESS is funded by the European Framework for Research and Innovation Horizon 2020, under grant agreement 951782. The authors also gratefully acknowledge project grant support from Vetenskapsrådet.

References

1. A.D. Sakharov. Violation of CP Invariance, C asymmetry, and baryon asymmetry of the universe. Pisma Zh. Eksp. Teor. Fiz. **5**, 32(1967); [Usp. Fiz. Nauk **161**, 61 (1991)].
2. G.L. Smith, et al. Short range tests of the equivalence principle. Phys. Rev. D **61**, 022001 (2000).
3. S. Schlamminger, et al. Test of the equivalence principle using a rotating torsion balance. Phys. Rev. Lett. **100**, 041101 (2008).
4. A. Dolgov. Non-GUT baryogenesis. Phys. Rept. **222**, 309 (1992).
5. G. ’t Hooft. Computation of the Quantum Effects Due to a Four-Dimensional Pseudoparticle. Phys. Rev. D **14**, 3432 (1976). [Erratum: Phys. Rev. D**18**,2199(1978)].
6. V.A. Kuzmin, V.A. Rubakov, and M.E. Shaposhnikov. Anomalous Electroweak Baryon Number Nonconservation and GUT Mechanism for Baryogenesis. Phys. Lett. B **191**, 171 (1987).
7. K.S. Babu, R.N. Mohapatra, and S. Nasri. Post-Sphaleron Baryogenesis. Phys. Rev. Lett. **97**, 131301 (2006).
8. K. Babu, P.S.B. Dev, and R. Mohapatra. Neutrino mass hierarchy, neutron-antineutron oscillation from baryogenesis. Phys. Rev. D**79**, 015017 (2009).
9. K.S. Babu, P.S.B. Dev, E.C.F.S. Fortes, and R.N. Mohapatra. Post-Sphaleron Baryogenesis and an Upper Limit on the Neutron-Antineutron Oscillation Time. Phys. Rev. D **87**, 115019 (2013).

10. P.S.B. Dev and R.N. Mohapatra. TeV scale model for baryon and lepton number violation and resonant baryogenesis, Phys. Rev. D**92**, 016007 (2015).
11. R. Allahverdi, P.S.B. Dev, and B. Dutta. A simple testable model of baryon number violation: Baryogenesis, dark matter,
2. neutron–antineutron oscillation and collider signals. Phys. Lett. B **779**, 262 (2018).
12. A. Addazi et al. New high-sensitivity searches for neutrons converting into antineutrons and/or sterile neutrons at the HIBEAM/NNBAR experiment at the European Spallation Source. J. Phys. G **35**, 070501 (2021).
13. M. Baldo-Ceolin et al. A new experimental limit on neutron-antineutron oscillations. Zeit. Phys. C **63**, 409 (1994).
14. H. Abele et al. Characterization of a ballistic supermirror neutron guide. Nucl. Instr. Meth. A **562**, 407 (2006).
15. V.V. Nesvizhevsky et al. Experimental approach to search for free neutron-antineutron oscillations based on coherent neutron and antineutron mirror reflection. Phys. Rev. Lett. **122**, 221802 (2019).
16. V.V. Nesvizhevsky et al. A new operating mode in experiments searching for free neutron-antineutron oscillations based on
3. coherent neutron and antineutron mirror reflections. Eur. Phys. J. Web Conf. **191**, 01005 (2018).
17. V.V. Nesvizhevsky et al. Comment on B.O. Kerbikov, "The effect of collisions with the wall on neutron-antineutron transitions".Phys. Lett. B **795**, 362 (2019).
18. K.V. Protasov et al. Theoretical analysis of antineutron-nucleus data needed for antineutron mirrors in neutron-antineutron oscillation experiments, Phys. Rev. D **102**, 075025 (2020).
19. C.J. Batty, E. Friedman, and A. Gal. Unified optical model approach to low energy antiproton annihilation on nuclei and to antiprotonic atoms. Nucl. Phys. A **669**, 721 (2001).
20. A. Amthong. WKB approximation for abruptly varying potential wells. Eur. J. Phys. **35**, 065009 (2014).
21. R.W. Robinett. WKB energy quantization and first order perturbation theory. Am. J. Phys. **65**, 320 (1997).
22. V.V. Nesvizhevsky et al. Quantum states of neutrons in the Earth's gravitational field. Nature **415**, 297 (2002).
23. PaNOSC-ViNYL/McStasScript,https://github.com/PaNOSC-ViNYL/McStasScript.
24. K.N Clausen, et al. The RITA spectrometer at Risø –design considerations and recent results. Physica B: Condensed Matter **241-243**, 0921–4526 (1997).
25. K. Lefmann and K. Nielsen. McStas, a general software package for neutron ray-tracing simulations. Neutron News **10**, 1044–8632 (1999).
26. S.-C. Yiu, et al. Status of the design of an annihilation detector to observe neutron-antineutron conversions. Symmetry (MDPI), in preparation.
27. J. Barrow, et al. Computing and Detector Simulation Framework for the HIBEAM/NNBAR Experimental Program at the ESS, EPJ Web Conf. **251**, 02062 (2021), doi:10.1051/epjconf/202125102062.
28. S. Agostinelli et al. GEANT4–a simulation toolkit, Nucl. Instrum. Meth. A **506**, 250 (2003), doi:10.1016/S0168-9002(03)01368-8
29. J. Allison, et al. Geant4 developments and applications, IEEE Trans. Nucl. Sci. **53**, 270 (2006), oi:10.1109/TNS.2006.869826
30. J. Allison, et al. Recent developments in Geant4, Nucl. Instrum. Meth. A **835**, 186 (2016), doi:10.1016/j.nima.2016.06.125
31. E. Golubeva, et al. Model of $\bar{n}$ annihilation in experimental searches for ¯n transformations. Phys. Rev. D **99**, 035002 (2019).
32. J.L. Barrow, et al. Progress and simulations for intranuclear neutron-antineutron transformations in 40Ar, Phys. Rev. D **101**, 036008 (2020), doi:10.1103/PhysRevD.101.036008
33. C. Hagmann, et al. 2007 IEEE Nuclear Science Symposium Conference Record (Vol. 2, pp. 1143–1146). IEEE.

Review of the Experiments Related to the Radiative Neutron Decay

Khafizov R.U.[a], Kolesnikov I.A.[a], Nikolenko M.V.[a], Tarnovitsky S.A.[a],
Tolokonnikov S.V.[a], Torokhov V.D.[a], Trifonov G.M.[a], Solovei V.A.[a],
Kolkhidashvili M.R.[a], Konorov I.V.[b]

[a]*NRC «Kurchatov Institute», Russia*
[b]*Technical University of Munich, Munich, Germany*

khafizov_ru@nrcki.ru

The report gives an overview of the experiments related to the radiative decay of a neutron. Emphasis is placed on our 2005 experiment conducted at the Technical University of Munich at the FRMII research reactor. Our methodology is focused on measuring the spectra of triple coincidences of radiative gamma-quantum, beta electron, and recoil proton and double coincidences of beta electron and recoil proton. The peak on the spectrum of triple coincidences shows the number of radiative neutron decays, while the peak on the spectrum of double coincidences shows the number of regular neutron beta-decays. This methodology enabled us to become the first team to measure the branching ratio (B.R.) of radiative neutron decay B.R. = $(3.2\pm1.6)10^{-3}$ (where C.L. = 99.7% and gamma quanta energy exceeds 35 Kev) [1] in 2005 on our old experimental equipment.

The spectrum of double coincidences obtained in our experiment shows a fairly significant ion background, the fluctuations of which indicate the precision of measurement for the number of recoil protons. Because the ion background specifically is quite significant, it appears even under super deep vacuum as beta electrons ionize the highly rarified air inside the chamber. The value of the ion background very slowly decreases with decreasing density of air inside the equipment. Besides, we discovered an additional wide peak on the spectrum of triple coincidences. This peak consists of delayed gamma quanta created during the ionization of rare gas by beta-electrons. So, this experiment allows us to study another important phenomenon, the ionization of rarified gas by beta electrons with emission of gamma quanta. Our last experiment showed that these two phenomena, radiative neutron decay and ionization with gamma quanta emission, are distinguishable in the case of high time resolution and can be studied separately. This is another important result of our last experiment and in this report we mention that the authors of articles registered namely the ionization with gamma radiation events.

This report compares our results with those of the two NIST research groups. Our results agree quite well with those of the emiT group for the conventional mode of neutron decay. We and the emiT group obtained similar time spectra for the double coincidences of the usual neutron decay products, beta electrons and recoil protons. However, if we compare our results with the results obtained by the other NIST group, we will find out that they are in strong conflict with each other; the spectra of both double and triple coincidences do not agree at all. The reason for this is that we identified radiative neutron decay events by triple coincidences of radiative neutron decay products. The NIST group published only the spectra of double coincidences of the electron with ion and electron with gamma quantum; they do not have any spectra of triple coincidences. Thus, this group has studied the process of ionization of rarefied air with the emission of trapped gamma rays. In nature, this phenomenon is observed as polar lights and has nothing to do with radiative neutron decay.

Introduction

Presently, the characteristics of the ordinary decay mode are measured with precision of tenths of a percentage point. Under these circumstances, the experimental data obtained by different groups of experimentalists can be reconciled only by taking into account the corrections calculated within the framework of the standard theory of electroweak interactions. This means that the experimental research of the ordinary mode of neutron decay have exhausted their usefulness for testing the standard model. To test the theory of electroweak interaction independently, it is necessary to move from the research of the ordinary branch of decay to the next step, namely, to the experimental research of the radiative decay branch.

The radiative decay branch of elementary particles, where an additional particle, a radiative gamma quantum is formed along with the regular decay products, has been discovered for practically all elementary particles. This has been facilitated by the fact that among the rare decay branches the radiative branch is the most intensive, as its value is proportional to the fine structure constant α and is only several percent of the intensity of the regular decay mode (in other words, the relative intensity B.R. of the radiative decay branch has the value of several hundredths of a unit.)

However, for the neutron this decay branch had not been discovered until recently and considered theoretically only [1–4]. Our first attempt to register the radiative neutron decay events was made on intensive cold neutron beam at ILL [5]. But our experiment conducted in 2005 at the FRMII reactor of Munich Technical University became the first experiment to observe this elementary process [6]. We initially identified the events of radiative neutron decay by the triple coincidence, when along with the two regular particles, beta electron and recoil proton, we registered an additional particle, the radiative gamma quantum

$$n \rightarrow p + \bar{e} + \nu + \gamma ,$$

and so could measure the relative intensity of the radiative branch of neutron decay B.R.= $(3.2\pm1.6)\cdot10^{-3}$ (with C.L.=99.7% and gamma quanta energy over 35 kev; before this experiment we had measured only the upper limit on B.R. at ILL [5]).

Below (see Fig. 1) follow the Feynman diagrams describing neutron decay. The first diagram describes the usual beta decay of the neutron, which produces three particles: a recoil proton, an electron and an unregistered neutrino. The next three diagrams describe a rare mode of decay, the radiative branch, which produces a third particle, the radiative gamma quantum, represented by the wavy line in the diagram. The second and third diagrams describe radiation of bremsstrahlung gamma quantum, emitted by charged particles, electrons and protons flying in each other's decelerating field. The contribution of these diagrams is calculated using the standard electroweak model. Finally, the last graph, which is of the greatest interest, describes the emission of structure gammas, which carry information about the structure of the elementary particles themselves. It is these extra gammas that are responsible for the deviation of the theoretical value of the branching ratio, calculated within the standard model, and further investigation of their spectrum will give valuable information about the structure of the neutron. Looking further forward, we note that our last experiment produced an average value of the relative intensity which deviates noticeably upwards from the one calculated using the standard model.

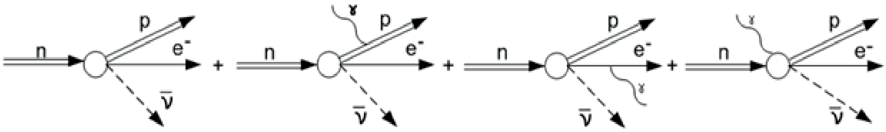

Fig.1. The Feynman diagrams describing neutron decay. Last one describes the emission of structure gammas.

The main characteristic of any rare mode of elementary particle decay is its relative intensity, branching ratio (BR). By definition, BR is equal to the ratio between the intensity of the rare decay mode and the intensity of the ordinary mode. In the case of neutron, this intensity ratio can be reduced to the ratio between the number of triple coincidences between the registration of beta-electrons, radiative gamma-quantum and the delayed proton N_T to the number of double coincidences between the registration of the ordinary decay products, beta electron and recoil proton N_D :

$$BR = I(\text{radiative decay}) / I(\text{ordinary decay}) = N(e,p,\gamma) / N(e,p)/k = N_T / N_D/k$$

These two values can be determined only from the analysis of double and triple coincidences spectra, which form corresponding peaks. Identifying these peaks and distinguishing them from the significant nonhomogeneous background with response peaks is the central problem in the methodology of BR measurements for neutron radiative decay. The geometry factor k should be determined by simulation of our computer experiment with using famous package of CERN programs GEANT IV.

Further, this experimental BR value needs to be compared with the theoretical value, estimated within the framework of the electroweak model. Any difference between these two values would mean that we are observing a deviation from the electroweak interaction theory.

Our group calculated the neutron radiative spectrum in the framework of standard electroweak theory in the following papers [1–4]. The calculated branching ratio for this decay mode as a function of the gamma energy threshold was published in these papers. BR value for the energy region over 35 keV was calculated to be about $2.1\cdot10^{-3}$.

It follows that to measure the main characteristic of radiative neutron decay it is necessary to obtain and analyze the spectra of double and triple coincidences.

Analysis and comparison of double coincidences spectra

Here let's pause to analyze the spectra of double coincidences between beta-electron and recoil proton, and compare our spectrum with the results obtained by other authors. We have published the diagram of our experimental equipment in the past [5–6, 8]. Here we will simply note that in its sizes our equipment is comparable to the equipment used by the two other groups and the distance between the observed decay zone and the proton detector in our equipment is about 0.5m. The accelerating potential of the electric field is also approximately the same in all three equipment sets, so all three experiments should lead to similarly forms of double and triple coincidences spectra.

Fig.2 demonstrates the summary statistics on double e-p coincidences (coincidences of electron with delayed proton). Fig.2 clearly shows two major peaks: one peak with a maximum in channels 99–100, which is the peak of zero or prompt coincidences [6, 8]. The position of this peak marks the zero time count, namely the time when the electron detector registered the electron. This peak is not physics-related in its nature. Instead, it is a reaction of the detectors and the electronic system to the registration of the beta electron. It is namely the pulse from the electron channel that opens the time windows on spectra Fig.2 for 2.5 μs forward and backwards. The next peak visible in Fig. 2 has a maximum in channel 120 and is the peak of e-p coincidences of beta-electron with delayed proton.

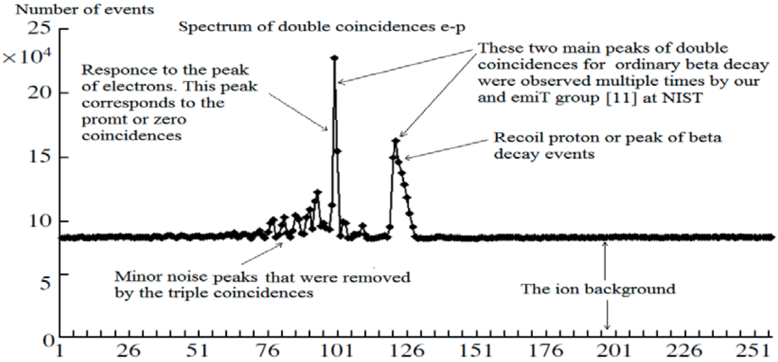

Fig.2. Timing spectrum for e-p coincidences. Each channel corresponds to 25 ns. The peak at channel 99–100 corresponds to the prompt (or zero) coincidences. The coincidences between the decay electrons and delayed recoil protons (e-p coincidences) are contained in the large peak centered at channel 120.

An analogous situation was observed in experiments on the measurement of the correlation coefficients by two independent groups at ILL [10] and emiT group at NIST [11], and it was also mentioned at [12]. We would especially like to emphasize the correspondence of our spectrum of double coincidences with an analogous spectrum from the result obtained by the emiT group from NIST [11]. In Fig. 3 we present their spectrum and diagram for the registration of the beta electron and the recoil proton. A comparison of our results with the results of the emiT group shows their unquestionable similarity. Moreover, the position of the second proton peak in Fig. 3 (emiT group), like in Fig. 2 (our result), corresponds well to the simple estimate obtained by dividing the length of a proton trajectory by its average speed.

Here we will also note the presence of a significant homogenous ionic background in Fig.2 and Fig.3. However, in both cases this background allows to easily distinguish the neutron decay peak. As we will shortly demonstrate, this ionic background will play a dominant role in the presence of a strong magnetic field and it will become impossible to distinguish events of ordinary neutron decay against it.

Following Avogadro's law, even in the case of a very deep vacuum under pressure of 10^{-6}–10^{-8} mbar, air molecule concentration remains very high. In fact, it is sufficient for beta-electrons produced in neutron decay to create a significantly high ionic background. Here one must note that the probability of ion creation along the trajectory of beta-electron in inverse proportion to the average distance between neighboring ions, i.e. proportional not to the molecule concentration but to the cubic root of this value. From this observation it follows that the value of the ionic background does not significantly depend on the vacuum conditions inside the experimental chamber. In our case, pressure was two orders of magnitude greater than the pressure in the emiT experiment. However, we observed an ionic background of only 4–5 times their background. This estimate is confirmed when one compares the spectra in Fig. 2 and Fig.3. Our spectrum, presented in Fig.2, has a 1:1 ratio of the value of e-p coincidences peak and the value of the background. The emiT group (Fig.3) spectrum has a ratio of 4:1 – 5:1, i.e. only 4–5 times our number, that is equal to the cubic root of pressure ratio in both teams' work (see Introduction).

We will present the specific calculations using the GEANT4 package in a separate paper, where we will consider the ionization process in more detail. It is noteworthy that in our case it is impossible to isolate and track individual tracks of electrons ionizing the residual air in the chamber due to their multiple reflections and scattering on the walls of the chamber, the neutron guide and other structural elements of the installation. As shown by concrete calculations, in this case it makes more sense to talk about the steady-state electron density ρe inside the chamber and, accordingly, the ion density ρ_i. The density of ions ρ_i is proportional to the density of electrons ρ_e, with the proportionality factor being the probability of the formation of the ion *P* (n) (see Introduction): $\rho_i = P(n)\cdot\rho_e = 2(\pi\sigma_i)^{1/2}\cdot n^{1/3}\rho_e$. Thus, the ratio of the ionic background value to the proton peak value also decreases in proportion to the cube root of density or pressure.

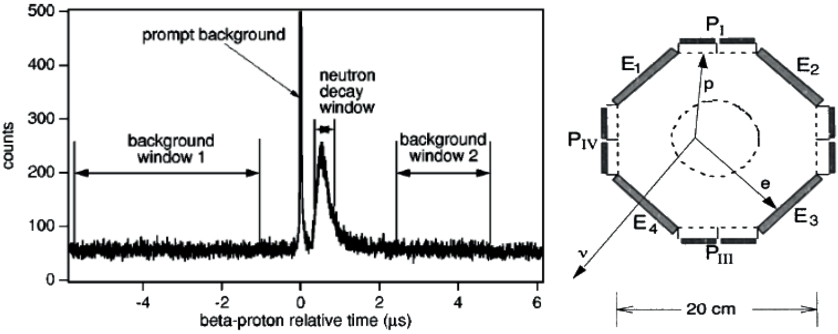

Fig.3. Spectrum of double electron-proton coincidences obtained by emiT Group [11] with two peaks and ion background value comparable to the neutron decay peak; emiT group scheme for registering beta electron and recoil proton.

Fig.2 shows that the total number of events in e-p coincidences peak in our experiment equals $N_D=3.75\cdot10^5$. This value exceeds the value we obtained in our previous experiment conducted on beam PF1 at ILL by two orders of magnitude. It was precisely because of the low statistics volume that we could not identify the events of radiative neutron decay in that experiment and instead defined only the upper B.R. limit [5]. It is very important to note that the peak of double coincidences between electron and the delayed proton is observed against a non-homogenous background (see Fig.2 and Fig.3): besides the homogenous ionic background, which has a value comparable to the value of the e-p coincidences peak, there is an obvious peak in channels 99–100. In essence, this peak is a response peak to the time spectrum of electron registration, which contains just one peak in channels 99–100, signifying the time when the electron detector registered the electron. We will shortly see that the radiative peak of triple coincidences appears against a non-homogenous background with not one, but two response peaks.

The remaining peaks in Fig.2 are small, with just seven peaks distinct from the statistical fluctuations. These occurred because of the noise in the electric circuits of the FRMII neutron guide hall. There are no other physics-related reasons for their occurrence. These peaks appeared and disappeared depending on the time of day, reaching their maxima during the work day and disappearing over the weekends. Such behavior was observed throughout the experiment as we collected statistics. Since the nature of these seven small peaks is in no way related to radiative and ordinary decay, we did not emphasize them in our article.

The comparison conducted demonstrates that the spectra of double coincidences obtained in our experiment completely correspond with the results obtained by the emiT group. Now we will compare these two spectra with the spectrum of double coincidences obtained by the third group. Unfortunately, the authors did not publish the spectrum of double coincidences in their original article [7], instead it was only published in paper [13]. Fig.4 displays the spectrum of double coincidences and the diagram of their experimental equipment.

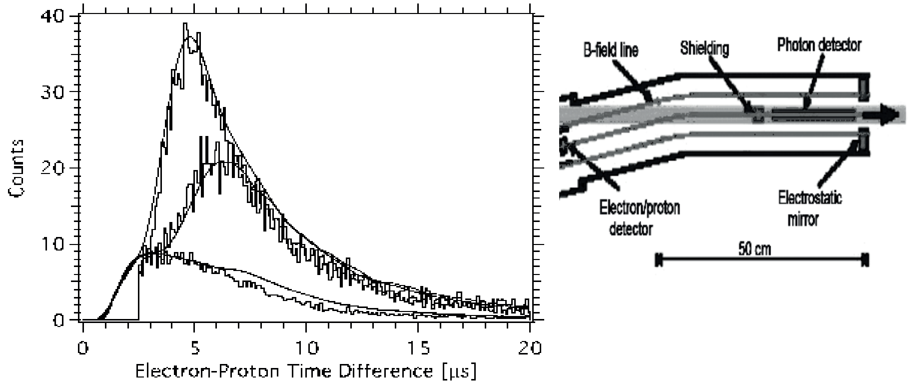

Fig.4. Equipment diagram and the single peak of "electron-proton" coincidences, published in [13]. The lower curve corresponds to 0 volts, the middle curve corresponds to 300 volts and the highest curve corresponds to 500 volts in an electrostatic mirror. The location of the peak's maximum and its significant width differ from our and the emiT results subsequently by one and two orders of magnitude. The location and the width of the peak also deviate by one and two orders of magnitude from the elementary estimates of delay times (see below).

The significant deviation obtained is explained by the fact that the peak in the NIST experiment consists not of beta-decay protons, but rather of ions. The density of gas molecules inside the equipment is proportional to pressure and according to the Avogadro's Law is at the order of 10^7 mol/cm^3 even at the pressure of 10^{-8}–10^{-9} mbar. This is a very significant number, which quite enough for creation the large ionic background in the presence of ionizing radiation. The energy of beta-electrons significantly exceeds the energy of ionization. Besides, the probability of ion creation by electrons is inverse proportional not to volume taken up by one molecule but to the average distance between molecules. It is precisely due to this reason that the ionic background falls proportionally to the cubic root of the pressure and not proportionally to pressure. In the emiT group experiment the pressure was the same as in the NIST experiment, i.so the ionic background should be the same too. The light ions, together with the beta protons, should have a delay time comparable to 1 μs. The pulses from these particles are simply not visible in the spectrum due to the NIST group's use of combined electron-proton detector (see Figure 5 with the shape of electron and ion pulses). The maximum of the "proton" peak in the NIST experiment, according to the delay times estimations (delay time is proportional to square root of ion mass), falls exactly to the air ions 4–6 μs.

Fig.5 presents the pulse forms on the electron-proton detector. As was pointed out above, the significantly delayed pulses of low amplitude correspond to ion pulses, and the pulses from protons are simply invisible due to a presence of a wide electron pulse of high amplitude. Namely this fact explains the dead zone around zero on the spectrum of electron-ion coincidences in Fig.4.

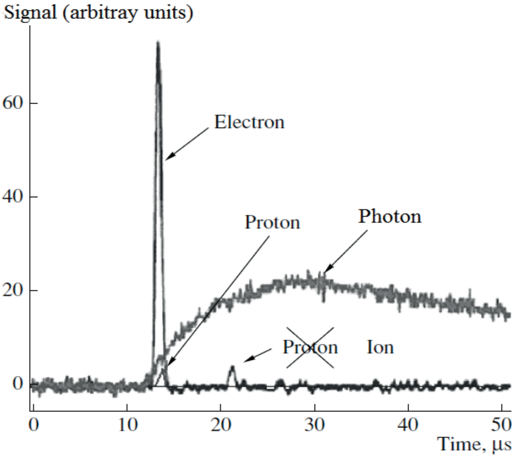

Fig.5. The signal from the decay proton has to be delayed by less than one microsecond, which is why it is located at the base of the electron pulse (see line number 2) and so cannot be registered by the combined electron-proton detector. The pulses that are delayed by longer than 1 microsecond are pulses not from decay protons, as it was indicated in ref. [7], but rather from ions, formed in the decay zone. The line number 1 shows the shape of pulses from the gamma detector.

Analysis and comparison of triple coincidences spectra

In paper [11] the emiT group researched only the ordinary decay mode, thus this comparison is limited to our spectrum of triple coincidences, presented in Fig.5, and the only peak published by the NIST authors in Nature [7], presented in Fig.7. Analysing the double coincidences spectra obtained by our and the emiT groups (both of which present two main peaks) shows that in the spectrum of triple coincidences we should observe not two but three main peaks. Namely, along with the sought after radiative peak, the triple e-p-gamma coincidences spectrum should show two response peaks to the registration of beta-electrons and the registration of protons, other words, the spectrum of triple coincidences should be similar the spectrum of double coincidences.

Let us review this similarity in more detail. We have two channels carrying background noise with some average signal frequency f_1 and f_2. Then the probabilities for the signal hitting the time window of value T are equal for both channels $p_1=f_1T$ and $p_2=f_2T$ respectively. If we now apply the electronic coincidence scheme, then the probability of random coincidence p_c of signals on the first and second channel in the coincidence scheme with the same value of time window T is equal to product of two independent events probabilities $p_c= p_1p_2 = f_1Tf_2T$ and frequency of coincidence respectively is equal to $f_c=f_1f_2T$. Suppose now on the first channel there is not a homogeneous horizontal background of pulses with mean frequency f_1, but some input spectrum with its peaks S_{in} then after the coincidence scheme an output spectrum proportional to the input $S_{out}= S_{in}f_2T$ with a ratio f_2T appears, note that the higher the homogeneous background on the second channel f_2, the more frequent the coincidence and the higher this ratio. Thus, all the peaks in the input spectrum also appear in the output spectrum from the coincidence scheme. However, as we will see below when analysing real triple match spectra, simply multiplying the input spectrum by a number does not fully describe the output spectrum and requires replacement of the simple multiplication function by a functional multiplication with the introduction of the response function $R_\gamma(t,t')$. For example, simple multiplication of the spectrum by a number describes an ideal pattern; it only changes the height of the peak, but both its width and its position remain unchanged. The real electronic coincidence circuit with the detector unit, however, also makes hardware changes to the shape of the spectrum itself, in particular to the widths of the peaks and their positions. Let us review these changes in more detail on our triple coincidence spectrum, shown in Figure 6.

Fig.6 of triple coincidences clearly shows three peaks, and the leftmost peak with the maximum in channel 103 is connected to the peak of the radiative gamma-quanta in question, as this gamma-quantum is registered by the gamma detectors in our equipment before the electron.

It is also important to note that while both teams' double coincidences spectra show the peaks at a distance from each other and easily distinguishable, in the spectrum of the triple coincidences the radiative peak is on the left slope of the response peak to electron registration. This means that we observe the peak of radiative neutron decay events against a heterogeneous background. At the same time, both response peaks on the spectrum of triple coincidences are significantly wider and located closer to each other than in the original spectrum of double coincidences. As we demonstrate below, one must take into account such spectrum behavior (related to the presence of a response in the electron detector system of data collection) by introducing the non-local response function. Using this well known method it is possible to distinguish N_T the number of triple coincidences from the heterogeneous background, arriving at the experimental BR value.

Comparing Fig.2 and 6, it becomes clear that if we ignore the first leftmost peak with the maximum in channel 103 in Fig. 6, the spectrum of double e-p coincidences will resemble the spectrum of triple e-p-γ coincidences in Fig.2. The peak with the maximum in channel 106 in Fig.6 is connected to the left peak of false coincidences in Fig.2, and the peak with the maximum in channel 120 in Fig.6 is connected to the right peak of e-p coincidences in Fig.2. The emerging picture becomes obvious when one uses a standard procedure, introducing a response function for gamma channel $R_\gamma(t,t')$ [6] , which is also necessary for calculating the number of triple radiative coincidences N_T in radiative peak:

$$S_{out}(t) = \int S_{in}(t')R_\gamma(t,t')dt'$$

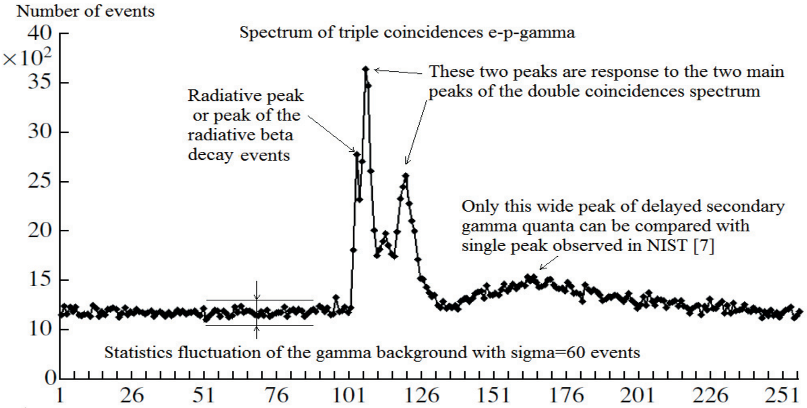

Fig.6. Timing spectrum for triple e-p-γ coincidences. Each channel corresponds to 25 ns. In this spectrum, three main peaks in channels 103, 106 and 120 can be distinguished. The leftmost peak in 103 channel among these three main peaks is connected with the peak of radiative decay events.

Using the method of response function, one can confidently define our double-humped background: the narrow peak with the maximum in channel 106 in Fig.6 is the response to the narrow peak of zero coincidences (by other words this peak is response to beta-electron registration) in channels 99–100 in Fig.2, and the second peak in this double-humped background in Fig.2 is the response to the peak in channels 117–127 in Fig.2 (or this peak is response to proton registration).

It must be noted that in our case we have to use the non-local response function, as the peaks on the original spectrum $S_{in}(t)$ of double coincidences are significantly narrower than those in the spectrum $S_{out}(t)$ of triple coincidences and also are shifted relatively their initial positions. In this case we use "functional" multiplication, however if we use the local response function, the triple coincidences spectrum is arrived at by simple multiplying the double coincidences spectrum by a number, in which case neither the width of the peaks nor their position change. It is also evident that the local response function approach leads to an erroneous number of triple coincidences N_T and, therefore, the wrong BR value.

When discussing the similarities between the spectra in Fig.2 and Fig.6, it is important to note that the response peak in Fig.6 with a maximum in channel 106 is shifted to the right or delayed in comparison to the peak responding to electron registration in channel 100 in Fig.1. This is due to the fact that in our electron diagram we used a constant fraction discriminator (CFD). CFD has its own delay line and the location of the time-pickoff signal it generates is determined by the method of comparing the fraction of the original signal to the delayed (CFD method [14]). Thus, there is a shift in the first response peak with a maximum in channel 106 in Fig.6 versus the first peak in Fig.2 with the maximum in channel 100. The value of this delay is equal to the front duration of the gamma quantum signal and is on average 150 ns. The CFD method obviously also shifts the radiative peak, but it should be located to the left of the response peak, as is observed in Fig.6.

As for the wide, almost indistinguishable peak in channel 165 in Fig.6, its influence on the radiative peak in channel 103 is negligible. Its nature is in no way related to the researched phenomenon, so we do not discuss it in our article [6]. This peak is created by the radioactive gamma quanta delayed on average by 1.25 μs and emitted during ionization of rare atmosphere within our experimental chamber. The molecular of this medium is ionized by registered beta-electrons. This event of artificial, induced radioactivity has been known for over 100 years and does not have anything in common with the new event of radiative neutron decay which is the subject of current research. As we demonstrate in Fig.6, only this 1 microsecond peak and delayed from the registration time by about the same time can be compared to the peak observed by the authors of paper [7] at NIST (see Fig.7). Thus, the authors of this experiment observed not the events of radiative decay but rather the event of artificial radioactivity, already well known in the time of Joliot-Curie. For our case in nature we can observe this phenomenon as polar light.

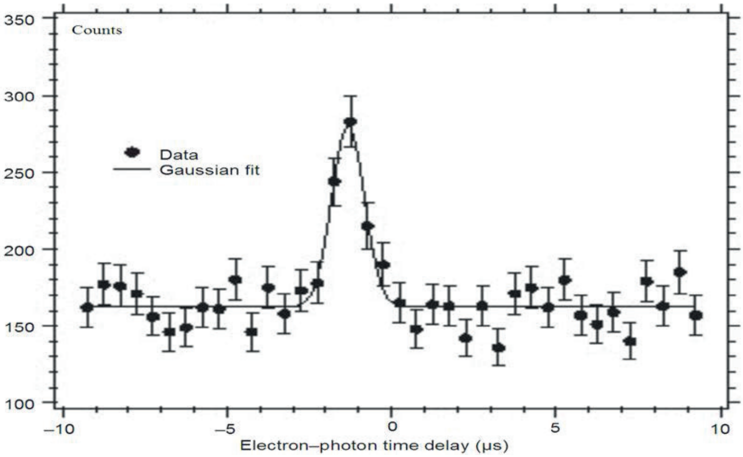

Fig.7. Only peak of "electron-photon" coincidences, shifted to the left of 0 – the time of beta-electron registration – by 1.25 microseconds, published in [7, 11].

After analyzing our triple coincidences spectra with the help of the non-local response function $R_\gamma(t,t')$ we finalize the average value for the number of radiative neutron decays N_T=360 with a statistics fluctuation of 60 events. B.R. can be expressed as a ratio of N_T to N_D as BR = k (N_T/N_D), where coefficient k=3.3 is the geometrical factor that we can calculate by using anisotropic emission of radiative gamma-quanta [4]. With the number of observed double e-p coincidences $N_D = 3.75 \cdot 10^5$ and triple e-p-γ coincidences $N_T = 360$, one can deduce the value for radiative decay branching ratio of $(3.2 \pm 1.6) \cdot 10^{-3}$ (99.7 % C.L.) with the threshold gamma energy ω=35 keV. The average B.R. value we obtained deviates from the standard model, but because of the presence of a significant error (50%) we cannot make any definite conclusions. The measurements must be made with greater precision. According to our estimates, in the future experiment we will be able to make more definite conclusions about deviation from the standard electroweak theory with experimental error less than 10%.

The difference between the NIST experiment and our experiment becomes immediately apparent. First and foremost, they did not get triple coincidence spectrum, they published double coincidences electron-gamma and electron-ion spectra only, so they could not identify radiative decay events at all! Besides that, it is the time scale: in our spectra, the scale is measured in nanoseconds, while in the other experiment the scale is in microseconds. Besides, we used three types of detectors, each of which registered its own particle: one detector for the electrons, one for the protons, and six identical detectors for the radiative gamma-quanta (see [6]). The duration of the front pulse from the electron and proton detectors is 10 nanoseconds in our experiment and 100 times greater than that in the NIST experiment, in the order of 1 μs. The rise time of gamma signal from our gamma-detectors is on average 150 ns, and from avalanche diode on the NIST equipment greater than 10 μs, besides that the diode pulse arrives with significant noise, which makes the thickness of the front pulse line equal to more than 0.5 μs (see the photon line in Fig.7 from [7]). All of this leads to our factual time resolution being two orders of magnitude better than the resolution achieved in the NIST experiment. However, as the two experiments used equipment which was practically the same in size and smaller than 1 meter, the choice of the time scale is a matter of principle. Given this geometry, it is impossible to get microsecond signal delays from all of the registered charged particles, i.e. electrons and protons. In this light, it is surprising that the peak identified by the authors of the NIST report [7] as the peak of radiative gamma-quanta, is shifted by 1.25 microseconds to the left. The expectation that magnetic fields of several tesla in magnitude delay all electrons and protons, are absolutely ungrounded.

Indeed, the magnetic field cannot change the speed of charged particles. It can only twist a line trajectory into a spiral. The length l of this spiral depends on angle θ between particle velocity and magnetic field direction. In beta decay, electrons can fly out under any angle θ, therefore the magnetic field can increase the time of delay by several orders of magnitude only for a negligible portion of the charged particles. Even this negligible number of particles that flew out at an almost 90 degree angle to the direction of the magnetic field that coincides with the direction of the narrow neutron guide (see Fig.4) will most likely end up on the walls of the neutron guide rather than reach and hit the detector due to the presence of the strong electrostatic field. Because the distance between the point of decay and the detector is about 0.5 meter and electron velocity is comparable with speed of light, the electron time of delay should be less than a microsecond by two orders of magnitude.

Thus, both the 1 microsecond shift and the width of the only peak in Fig.7 in the experiment conducted at NIST, is in sharp contradiction to elementary estimates. We, on the other hand, did not observe any wide peaks before electron registration and our gamma background is very even in this part of the spectrum (see Fig.6). However, when we assume that the NIST experiment authors observed the wide peak, shifted by 1 microsecond, not before, but after the registration of beta-electrons. In that case, the wide peak on our spectrum in Fig.6 completely corresponds to the wide peak in Fig.7. However, as noted above, density of gas molecules remains high even with the pressure of 10^{-8}–10^{-9} mbar and this residual gas is activated by beta-electrons. The wide peak in our spectrum is formed by the delayed gamma quanta from this induced artificial radioactivity. These delayed gamma quanta are produced by the ionization of the rarefied atmosphere by beta electrons in the experimental chamber. In nature, such a phenomenon can be observed in the form of polar lights and the NIST researchers did everything to observe exactly this phenomenon; they used strong magnetic fields, rarefied atmosphere and ionizing radiation inside their experimental chamber. It follows from what has been said that this group of researchers used their spectra of electron-ion and electron-gamma-quantum double coincidences to study the ionization process, with which the radiative neutron decay has nothing to do.

Conclusion

The main result of our experiment is the discovery of the radiative peak namely in the location and of the width that we expected. The location and the width of the radiative peak correspond to both estimates and the detailed Monte Carlo simulation of the experiment. Thus, we can identify the events of radiative neutron decay and measure its relative intensity, which was found to be equal B.R. = $(3.2\pm1.6)\cdot10^{-3}$ (with C.L.=99.7% and gamma quanta energy over 35 keV).

At the same time, the average experimental B.R. value exceeds the theoretical value by 1.5 times. However, due to a significant error we cannot use this result to assert that we observe a deviation from the standard model. Therefore, our most immediate goal is to increase experiment precision, which we can improve by several percents according to estimates.

For the last years we were preparing this new experiment and conducted number of tests for our new electronics. We constructed multi channel generator what can generate the pulses with the same forms as our electron, proton and gamma detectors. During these tests we got the same responses as during our last experiment on real neutron beams at FRMII. It means that all additional peaks on our spectra have no any physics reasons and It proves once more that we were absolute correct when applied the response function method for explaining these peaks as response ones and for developing our experimental spectra.

We created and tested our new electronic system for obtaining experimental spectra. By using this new programmable electronics we can significantly reduce the influence of response peaks on peak with radiative decay events. Now we can get this peak almost isolated from responses. On our estimations all these allow us to reach accuracy for our new experiment about 1%. So, on the base of our new electronics we can confirm or refuse the deviation of our average experimental value of BR from the standard model one.

As concerning the comparison of our experimental results with others we can make the following two main conclusions. The main parameters of our spectrum of double electron-proton coincidences identifying the events of ordinary neutron decay fully coincide with an analogous spectrum published by emiT group in [11].

Unfortunately we cannot say same for another experiment measuring the radiative neutron decay published in [7]. Particularly vexing is the authors' unsubstantiated assertion that they observe their only wide peak of gamma quanta before the registration of beta-electrons. Both the position and the width of this peak are located in sharp contradiction to both the elementary estimates, and the results of our experiment. In the course of our entire experiment we did not observe such a wide peak in the triple coincidences spectrum, located before the arrival of electrons at a huge distance of 1.25 μs. However, it is possible to reconcile our spectra of triple coincidences with the one isolated peak observed at NIST if we assume that at NIST, the gamma-quanta were registered after the beta electrons. Only in this case does the NIST peak almost completely coincide with the peak we observed in the spectra of triple coincidences with the maximum in channel 165, both in terms of the huge delay of 1.25 μs and in terms of its huge width. This peak is created by the delayed secondary radioactive gamma-quanta, arising from the activation by beta electrons of the media inside experimental chamber, which was the real object of the NIST experimentalists' observation. We strongly recommend that the authors of this experiment withdraw their work and instead publish a paper which indicates the position of the only broad peak on the spectrum of double electron-gamma coincidences which they observe in fact not before but after the electron registration.

Despite the recent disagreements [15], which we consider to be subjective in nature [16], we acknowledge the contribution of our Western colleagues Profs. N. Severijns, O. Zimmer and Drs. H.-F. Wirth, D. Rich to our experiment conducted in 2005. Here it is important to note that the authors of the article published in Nature [7] consciously misled first our Western colleagues and then the physics community at large by insisting that their only wide peak is removed by 1.25 microseconds to the left from the time of electron registration, when in reality this peak was formed by delayed gamma-quanta, emitted by the activated medium inside the experimental equipment, and corresponds to our wide peak with the maximum in channel 165 (refer to Fig.6) [15, 16]**.** The authors would like to thank Profs. D. Dubbers and Drs. T. Soldner, G. Petzoldt and S. Mironov for valuable remarks and discussions. We are also grateful to the administration of the FRMII, especially Profs. K. Schreckenbach and W. Petry for organizing our work. We would especially like to thank RRC President Academician E.P. Velikhov and Prof. V.P. Martem'yanov for their support, without which we would not have been able to conduct this experiment.

References

1. Gaponov Yu.V., Khafizov R.U., Phys. Lett. B **379** (1996) 7–12.
2. Yu.V. Gaponov, R.U. Khafizov, *Radiative neutron beta-decay and experimental neutron anomaly problem*. Weak and Electromagnetic Interactions in Nuclei (WEIN'95): Proceedings. Edited by H. Ejiri, T. Kishimoto, T. Sato. River Edge, NJ, World Scientific, 1995, 745p.
3. R.U. Khafizov, N. Severijns, *About the possibility of conducting an experiment on radiative neutron beta decay*, Proceedings of VIII International Seminar on Interaction of Neutrons with Nuclei (ISINN-8), Dubna, May 17–20, 2000 (E3-2000-92),185–195.
4. Khafizov R.U., Physics of Particles and Nuclei, Letters **108** (2001) 45–53.
5. M. Beck, J. Byrne, R.U. Khafizov, et al., JETP Letters **76** (2002) 332.
6. R.U. Khafizov, N. Severijns, O. Zimmer et al., JETP Letters **83** (2006) 5.
7. J.S. Nico, et al. Nature **444** (2006) 1059–1062.
8. R.U. Khafizov, N. Severijns et al., *Discovery of the neutron radiative decay*, Proceedings of XIV International Seminar on Interaction of Neutrons with Nuclei (ISINN-14) Dubna, May 24–25, 2006.
9. B.G. Yerozolimsky, Yu.A. Mostovoi, V.P. Fedunin, et al., Yad. Fiz. **28**, 98 (1978); [Sov. J. Nucl. Phys. **28**, 48 (1978)].
10. I.A. Kuznetsov, A.P. Serebrov, I.V. Stepanenko, et al., Phys.Rev.Lett. **75** (1995) 794.
11. L.J. Lising, S.R. Hwang, J.M. Adams, et al., Phys. Rev. C. v.**6** (2000) 055501.
12. J. Byrne, R.U. Khafizov, Yu.A. Mostovoi, et al., J. Res.Natl. Inst. Stand. Technol. **110**, 415 (2005).
13. R.L. Cooper, T.E. Chupp, M.S. Dewey, et al, Phys. Rev. C **81**, 035503 (2010).
14. T.J. Paulus, IEEE Transactions on Nuclear Science, v.NS-32, no.3, June, p.1242, 1985.
15. N. Severijns, et al., e-print arXiv:nucl-ex/0607023; J. Nico, private communication.
16. R.U. Khafizov, V.A. Solovei, e-print arXiv:nucl-ex/0608038.

THE PROBLEM OF CREATING NEUTRON MATTER AND HYPERHEAVY NUCLEI IN THE LABORATORY. POSSIBLE INSTRUMENTAL APPROACH

G.B. Ryazantsev[1], V.I. Vysotskii[2], G.K. Lavrenchenko[3], S.S. Nedovesov[2]

[1]*Lomonosov Moscow State University, Russia*
[2]*Taras Shevchenko National University of Kyiv, Ukraine*
[3]*LLC «Institute of Low Temperature Energy Technology», Odessa, Ukraine*

ryazantsevgb@gmail.com; vivysotskii@gmail.com; lavrenchenko@gmail.com

Possible mechanisms of creation of both hyperheavy nuclei by electron-nuclear collapse and neutron matter by condensation of ultracold neutrons are discussed. The possibility of such objects creation was previously justified by A.B. Migdal, who suggested that the known set of proton-neutron nuclei with mass numbers from 0 to 300 and a maximum specific binding energy of about 8 MeV/nucleon at A≈60 corresponds to the first region, beyond which (starting from about the charge $Z \approx (\hbar c/e^2)^{3/2} \approx 1600$) there is an additional region describing a possible state of nuclear matter, stabilized by a pion condensate. In this region, the maximum specific energy corresponds to ≈15 MeV/nucleon at A ≈ 100000. It is shown that neutron matter can be obtained under certain conditions, and its systematization can be realized as an addition to the Periodic Table. When solving such problems, it becomes quite real to study not only physical, but also chemical, and possibly engineering and technical properties. Analysis shows that the stability of neutron matter at the microlevel is ensured by the Tamm interaction and the Hund beta equilibrium. Such matter can be quite stable not only on the mega-level (neutron stars) due to gravitational interaction, as was a priori assumed earlier, but also on the scale of "ordinary" matter. The process of neutronization is possible not only with critical gravitational interaction, but also by other mechanisms (supercritical increase in the atomic number of elements due to electron-nuclear collapse and condensation of ultracold neutrons), which opens the way to the fundamental possibility of obtaining both neutron matter in laboratory conditions and superheavy nuclei.

Based on the works of Migdal, Tamm and Hund, the possibility of the existence of stable neutron matter (with $Z \gg 175$, $N \gg Z$, $A > 10^3$–10^5 and a size of 200–300 femtometers and more) is argued at the microlevel, and not only at the mega-level, as is now considered in astrophysics. The following technical approaches to the implementation of UCN condensation are considered: 1) slow isothermal compression; 2) refrigerator for dissolving helium-3 and helium-4; 3) use of a conical concentrator for UCN focusing (Vysotsky cone); 4) magnetic trap; 5) additional UCN laser cooling. Neutron matter is considered as a potential cosmological candidate for dark matter. One should take into account the possibility of the formation of fragments of neutron matter as dark matter (neutral, femto-, pico- and nanoscale, the cooling of relics makes it difficult to detect them by now) already at the initial origin of the Universe, which is the dominant process. The observable part of the Universe is formed by the residual part of protons, and then by decayed single neutrons and unstable fragments of neutron matter (with $Z > 175$, $N \gg Z$, but $A < 10^3$–10^5).

Key words: hyperheavy nuclei, neutron matter, electron-nuclear collapse, condensation of ultracold neutrons, primary cosmogenic matter, dark matter.

1. INTRODUCTION

Hyperheavy nuclei [1–7] as well as neutron matter [8–14], nowadays is a specific physical reality that requires the study of not only physical, but also chemical, and, possibly, in the near future, engineering and technical properties. Let us consider the possible mechanisms of the creation of hyperheavy nuclei by electron-nuclear collapse and neutron matter by condensation of ultracold neutrons (UCN). The fundamental possibility of creation of such objects was previously justified by A.B. Migdal, who suggested that the known set of proton-neutron nuclei with mass numbers from 0 to 300 and a maximum specific binding energy of about 8 MeV / nucleon at $A \approx 60$ corresponds to the first region, behind which (starting from the charge $Z \approx (\hbar c/e^2)^{3/2} \approx 1600$) there is still one additional area with a large value of the maximum binding energy at $A \approx 100{,}000$, which describes a possible state of nuclear matter, stabilized by a pion condensate.

Neutron matter, or rather the corresponding element, begins (zero period) and ends (supercritical atoms) of the Periodic System of Chemical Elements (PS). Neutron matter is given stability already at the micro level Tamm interaction, and it is stable not only at the mega level (neutron stars) due to gravitational interaction, as is usually believed in astrophysics. Neutronization is possible not only due to gravitational interaction, but also through other mechanisms (supercritical increase in the atomic number of elements [15] and condensation of ultracold neutrons [16,17]. These circumstances show that there is a fundamental possibility of obtaining neutron matter in terrestrial conditions [8–14]. Neutron matter is consistent with the original concept of the Periodic Law (PL) and PS, proposed by Dmitry Ivanovich Mendeleev [18–20].

From the standpoint of general chemistry, a neutron substance can be classified as chemically simple (that is, it cannot be decomposed into simpler substances by chemical means or reduced to allotropic modifications of already known substances), then the question inevitably arises about the corresponding element and its place in the PS. Proceeding from the logic of PL – (ordinal number - electric charge) – the ordinal number of neutron matter in the PS will correspond to zero, which makes us recall and develop the ideas of Dmitry Ivanovich Mendeleev about the zero group and the period.

D.I. Mendeleev did not have time and opportunity to solve this problem, and his students and followers tried to forget this topic as "erroneous." Modern knowledge about neutron stars and neutron matter persistently makes one recall his ideas about the elements disposed before hydrogen and assert the truth of his brilliant prediction, which more than 100 years ahead of the natural science of his time.

2. STABILITY OF HYPERHEAVY NUCLEI AND NEUTRON MATTER

In a neutron substance of sufficient size (more than a layer of complete absorption), an electron emitted during decay with its sufficient energy is captured by the remaining protons, which, in turn, are converted into neutrons, thereby maintaining the dynamic equilibrium of the system. In fact, this corresponds to both the theory of Igor Evgenievich Tamm [21], which he put forward in his time (1934) to explain the mechanism of nuclear forces for ordinary nuclei, and the ideas of Frederick Hund [22]. It should be noted that the theory of I.E. Tamm was not satisfactory for ordinary atoms (but he himself valued his "unsuccessful" theory of nuclear forces more than the Nobel work on Cherenkov radiation and considered his best theoretical achievement), but it is consistent and can be realized for neutron matter of the corresponding scale (200–300 or more femtometers), giving it additional stability.

In strongly interacting systems, there are many virtual particles and all kinds of interactions that are allowed invariance considerations are realized. So, in our opinion, Igor Tamm's "primordial" theory of β-nuclear forces (lepton exchange between nucleons), and not only its modification by Hideki Yukawa (π-exchange of nucleons), is still awaiting its recognition (because, besides the π-meson cloud, there are certainly other particles around each nucleon) and "dominates" in the neutron matter of the Universe, ensuring its stability and wide distribution.

The initial study of this problem was also given by Frederick Hund [22] in the first microscopic description of the equation of state of nuclear matter in beta equilibrium in the article "Substance at very high pressures and temperatures", only if Tamm has virtual electrons, Hund realizes beta equilibrium completely real particles, but most importantly, both mechanisms contribute to the stability of supercritical ($Z >> 175$, $N > 10^3–10^5$) nuclear matter, and, in strongly interacting systems, there is no fundamental difference between virtual and real particles.

It is the additional interaction due to nuclear β - forces that gives stability to the neutron matter already at the micro-level, and not only at the macro-level due to the gravitational interaction, as it is now believed in astrophysics!

The possibility of the existence of a superdense neutron nucleus was also considered in the work of A.B. Migdal [23] “Theory of finite Fermi systems and properties of atomic nuclei” in the section “Application of the Theory of finite Fermi systems in nuclear physics”. Migdal believed: “*... neutron nuclei can be stable with respect to beta decay and fission, with* $Z << N$ *and* $N> 10^3–10^5$. *Such nuclei could be observed in cosmic rays in the form of large fragments.*” Migdal suggested looking for neutron nuclei in the form of exotic traces in photographic emulsions after exposure to cosmic rays.

The theories of Tamm, Hund and Migdal admit the stable existence of hyperheavy neutron nuclei at $Z >> 175$, $N > 10^3–10^5$ and sizes of 200–300 and more femtometers.

Nevertheless, it is widely believed that the minimum mass for the stable existence of a neutron object is 0.1 solar masses [24]. It is believed that the equations of state used in this case are based on supposedly rich (?) Experimental material and therefore give a fairly accurate value for the minimum mass. The very fact of the existence of the minimum mass of a neutron star is justified by the fact that at low densities, neutrons, due to their susceptibility to beta decay, cannot be the predominant component of matter, and a high neutron density in them is provided only by gravitational interaction.

Most models of the neutron stars structure were based on the solution of the Tolman - Oppenheimer - Volkov equation [24]. Currently, there are several dozen models, ranging from the so-called "soft" equations of state (derived from models in which, at densities of the order of nuclear, the average interaction energy corresponds to attraction) to rigid equations of state (obtained for models in which there is repulsion). Since different models corresponding to different equations of state lead to a fairly wide range of parameters characterizing a neutron star, one might hope that an accurate determination of such parameters would make it possible to concretize the very equation of state of neutron matter, the very nature of internucleon interaction.

Unfortunately, until now it has not been possible to obtain reliable estimates of the main characteristics of neutron stars. Thus, the accuracy in determining the radius R is on average 50–100%. To date, the equation of state has not been obtained in the framework of quantum chromodynamics. Thus, the minimum mass of a neutron star, which is considered equal to 0.1 of the solar mass, is obtained from extremely approximate equations with an error of 100% or more, as indicated in many works on this topic, nevertheless, this number is widely replicated. Based on the conclusions from the theories of Tamm, Hund and Migdal, we can expect the stable existence of microscopic neutron objects ($Z >> 175$, $N > 10^3–10^5$) and neutron stars with a mass of less than 0.1 of the Sun. The author of the very concept of neutron stars, Fritz Zwicke [25], wrote about the possibility of the existence of neutron objects of much smaller sizes (3–10 m) under certain conditions. He believed that further analysis of matter at nuclear density is important not only for our understanding of eruptions in stars, from ordinary star explosions to supernovae, but it also promises to radically change some of the current ideas on the formation of elements in the theory of the evolution of the Universe.

The question of the possibility of obtaining neutron matter in laboratory conditions on Earth is partly rhetorical. The point is that it is necessary to distinguish between two aspects: mononeutron (ultracold neutrons) and polineutron (similar to stellar cosmic) matter. As for the mononeutron matter, it has long been obtained in Earth conditions (Shapiro, 1968), although it is not stable [16]. It is interesting to note that on the one hand, a mononeutron substance, or rather an element corresponding to it, occupies a place in the PS before hydrogen, which corresponds to the element Coronium proposed by D.I. Mendeleev. On the other hand, the polyneutron matter closes the PS, thus in the general case, the neutron matter both opens and also closes the PS. The question of obtaining polineutron matter is to be solved in the near future [8]. The situation is now similar to that at the end of the 30s of the last century, when a breakthrough was made in the mastery of nuclear energy, although many doubted the possibility of this.

3. OBTAINING HYPERHEAVY NUCLEI BY ELECTRON-NUCLEAR COLLAPSE

In the works of A.V. Migdal [23] it was shown that for very heavy nuclei (starting from nuclei with a charge $Z \approx (\hbar c/e^2)^{3/2} \approx 1600$) there is a condensation of pions, which under this condition become real (not virtual) particles. Under this condition, a very significant rearrangement of the nuclear structure occurs, and the maximum specific binding energy is shifted from the range of standard parameters ($Z \approx 60$, $E_{\text{bond}} \approx 8$ MeV / nucleon) to the range of mass numbers A=100,000, reaching the value of $E_{\text{bond}} \approx 15$ MeV / nucleon.

The main problem in the creation of such nuclei is the initial achievement of the $Z \approx 1600$ threshold, which corresponds to the conditional boundary (local minimum of the specific binding energy) between the “traditional” and “Migdal” regions of the mass numbers of nuclei. The scale of this problem is easy to imagine if we take into account the colossal efforts that are being made to create heavy nuclei with very moderate (on the scale of the Migdal model) charges $Z = 116–118$ due to the collision of lighter nuclei. It is quite obvious that such a "frontal" way of creation of hyperheavy nuclei due to the collision of lighter accelerated nuclei is absolutely unpromising.

In the articles [1–3,7], a radically different method of “soft” (non-impact) step by step nuclear fusion of superheavy nuclei was proposed, which does not require the use of accelerators and special donor mother nuclei.

This method uses two processes:

a) Coulomb electron-nuclear collapse, based on the application of the nonlinear law of the Coulomb interaction of charges

$$U_{\mathrm{eff}} = -Ze^2/r - (Ze^2/r)^2/2m_ec^2,$$

the action of which is realized at a small distance $r < Ze^2/m_ec^2$ or, respectively, at a high density of electron-nuclear matter, compressed to the state of a degenerate relativistic electron gas;

b) the action of a strong axial shock wave providing the required compression ratio of the target at its front.

It is shown in [1–5,7] that when such a compression is performed, a self-controlled collapse of the electronic and nuclear components of the medium takes place, which sharply increases the degree of screening of the nuclear charge and provides the possibility of repeated (with a multiple increase in mass and charge) nuclear fusion with the participation (absorption) neighboring atoms and nuclei of the target. In addition, when these conditions are met, the process of protonization of nuclei becomes energetically favorable.

The combined action of these two processes leads to a continuous shift in the position of the maximum binding energy within the complete nuclear-electronic subsystems from the initial value $Z = 60$, typical for any matter under "standard" conditions, to values that can reach (and exceed) the critical value $Z \approx 1600$, upon reaching which the process of increasing the charge and mass of the nucleus will be provided mainly by the mechanism of pion condensation of Migdal.

Such a scheme was implemented under the leadership of S.V. Adamenko in Kiev at the «Proton-21» Laboratory [4–7], in which nuclei with mass numbers in the range $A \approx 400$–4000 were created and registered in the course of experiments with the action of an axially symmetric electron beam on a needle target. On the basis of detailed mass spectrometric and spatial analysis of secondary light nuclei generated during rapid evolution in the vicinity of these hyperheavy nuclei, there are good reasons to believe that, upon entering the "ordinary" substance (storage screen located next to the target), these nuclei continued to grow, absorbing neighboring nuclei of the screen material (copper in conducted experiments) and "dumping" excess binding energy in the form of these secondary light nuclei [6,7].

We have also shown [3] that such a process, under certain (real) conditions, can occur on stars in the process of gravitational collapse, which can lead to the creation of proton-electron stars as an astrophysical alternative to neutron stars.

The main condition for the realization of such a scenario is an accelerated gravitational collapse, the duration of which should be significantly shorter than the duration of the stage of neutronization of nuclei. Analysis [3] shows that with successive compression of the stellar matter, these stages follow one after another. If the compression in the process of gravitational collapse occurs rather slowly, then the compression process ends at the stage of formation of a neutron star. However, in the case of anomalously fast compression, only a small fraction of protons is converted to neutrons, and the subsequent compression will correspond to the stage of protonization of all nuclei with synchronous generation of electrons and antineutrinos. This stage begins from the moment when the main process of interaction of nuclei with electrons is the nonlinear Coulomb interaction, which corresponds to the concentration of electrons $N_{\mathrm{critical}} = (2m_ec^2/Ze^2)^3$ as part of a degenerate electron gas.

Direct estimates have shown that for the formation of such anomalous stars, the final stage of gravitational collapse should be significantly less than 1 sec, which can be realized only with a very optimal ratio of the stellar parameters before its gravitational collapse.

If the compression process is long enough, then the state of the star will stop at the stage of complete neutronization of all nuclei without “switching on” the mechanism of nonlinear Coulomb interaction, which is realized only during subsequent compression.

4. OBTAINING OF HYPERHEAVY NUCLEI BY NEUTRON CONDENSATION

It should be noted that Georgy Antonovich Gamov [26] was the first to speak about the condensation of cold neutrons. This idea is rarely mentioned, which eventually found application in the theory of neutron stars. G.A. Gamow in the late 30s of the last century showed that when a neutron gas is compressed, a new superdense state of matter arises. Gamow's main hypothesis: “*We can anticipate that neutrons forming this comparatively cold cloud were gradually coagulating into larger and larger neutral complexes…*”.

In further development, the theory of the initial cold universe was discarded and together with it the idea of neutron condensation was forgotten. However, is this true? Neutron condensation is possible not only at low temperatures (ultracold neutrons), but also at ultrahigh pressures at temperatures below critical.

Usually we on Earth deal with neutron radiation of various energies, but not with neutron matter. This was the case until 1968, when an experiment was carried out in the Laboratory of Neutron Physics under the leadership of Corresponding Member of the USSR Academy of Sciences Fedor Lvovich Shapiro [16], in which the phenomenon of very slow neutron confinement in vessels, predicted by Academician Yakov Borisovich Zel'dovich [17], was first observed. The behavior of neutrons trapped in evacuated vessels resembles the behavior of a highly rarefied gas in a vessel. Such neutrons are called ultracold (UCN). The confinement of UCN in vessels attracts researchers by the possibility (in comparison with a single flight of a neutron through the experimental volume) to observe this particle for a longer time in an experimental setup, which gives a significant increase in the sensitivity and accuracy of experiments on studying the interaction of neutrons with fields and matter.

For example, the use of UCN made it possible to significantly lower the limit of the existence of the electric dipole moment of the neutron, which is necessary to test the law of conservation of temporal parity; to more accurately measure the lifetime of a free neutron before β-decay. The most important feature of UCNs is that they behave not like radiation, but like matter, and you can work with them as with matter, similar to a rarefied inert gas. Moreover, you can study both physical and chemical properties. The physical properties are already being studied, but it seems that the question of UCN chemistry is not even raised, since by default it seems somehow obvious that they should be similar to inert gases. This seems to be true, but now we already well know that inert gases under certain conditions (in particular, in an excited state) can enter into chemical reactions and form, albeit not stable, chemical compounds of the excimer type. Could something like this happen with UCN? If we proceed from the fact that Chemistry is only the interaction of the electronic shells of atoms, as many believe, then a categorical negative answer follows. But, if chemistry is understood more broadly, in general, the ability of micro- (nano-, pico- or even femto-) objects to interact and form relatively stable compounds, then why not?

Of course, neutrons have no electric charge and no free electrons, so all ideas about possible classical chemical bonds (ionic, covalent, etc.) immediately disappear. But, neutrons have exactly a magnetic moment and possibly an electric dipole moment (the essential role of which is well known in chemistry). This can facilitate the formation of quasi-stable multi-neutron complexes.

Some aspects of this problem were considered in [27] when analyzing and substantiating the possibility of creating neutron molecules.

Another option may be associated with the interaction of UCNs with molecules of substances with an odd number of electrons, and an experiment to detect the products of this interaction is quite realistic [13]. If someone finds it difficult to go beyond the concepts of traditional chemistry, then we can call it the quasi-chemistry of UCN.

New UCN sources are being actively developed all over the world, some of them are based on the use of solid deuterium at a temperature of 4.5 K (LANL, USA; PSI, Switzerland), and others – on the accumulation of UCN in superfluid helium (KEK-RCNP-TRIUMF, Japan-Canada; ILL, France) [28]. Similar work is being intensively carried out in Russia: the Neutron Laboratory at the Joint Institute for Nuclear Research (Dubna) and at the Petersburg Institute of Nuclear Physics (PNPI). In Gatchina, work is underway to create a high-intensity UCN source. With its help, they hope to obtain data that will provide answers to the most important questions of modern physics. The projected source will make it possible to obtain an ultracold neutron (UCN) flux with a density of 10^4 cm^{-3}, which is many times higher than the currently reached maximum densities [28]. This task – obtaining intense UCN fluxes – is today considered one of the priorities in neutron physics. An ever increasing increase in the UCN density will inevitably lead to the formulation of the question of their possible condensation and the production of condensed neutron matter in laboratory conditions, similar to space.

Not so long ago, a decisive breakthrough was made into a new field: a radically new type of matter was created, the so-called Bose condensates of atoms. Are neutron condensates possible? Condensates, the density and strength of which will be comparable to the density and strength of atomic nuclei. In other words, how close are we today to the stage of creating cosmic neutron matter in the laboratory?

The 2001 Nobel Prize in Physics was awarded to researchers Eric A. Cornell, Wolfgang Ketterle and Carl E. Wieman for obtaining and studying the properties of the fifth state of matter, the Bose-Einstein condensate: they were able to obtain for the first time the Bose condensate [29]. It was possible to do this with the help of the methods of supercooling of particles by laser beams and a magnetic field, developed not long before. The Bose condensate of atoms was obtained in a form convenient for research and laboratory analysis. Soon, methods were found for obtaining Bose condensates of particles of half-integer spin, fermions. In them, the particles are combined in pairs, then collecting in a Bose condensate. Neutrons are similar in many properties to the lightest atoms. For example, the mass of a neutron is practically equal to the mass of a hydrogen atom, the Bose condensate of which was obtained by Ketterle in 1997. But, unlike atomic Bose condensates, the natural compression of which during Bose condensation is impeded by their electron shells, nothing prevents the compression of a neutron Bose condensate. In such a condensate, the UCN gas forms pairs with opposite spins, upon reaching the critical density and temperature, it will spontaneously shrink to almost nuclear density when nuclear forces come into play, forming a stable state – condensed neutron matter. If in space a stable polineutron substance is formed at ultrahigh pressures, then on Earth it will be obtained at ultralow temperatures with a sufficient concentration of UCN, which sooner or later researchers will come to obtain.

The following technical approaches to the implementation of UCN condensation are considered:

1. Slow isothermal compression;
2. Refrigerator for dissolving helium-3 and helium-4;

3. Use of a conical concentrator for UCN focusing (Vysotsky cone) [30];
4. Magnetic trap;
5. Additional UCN laser cooling.

5. NEUTRON MATTER IN COSMOLOGY AND ASTROPHYSICS

The importance of neutron matter can hardly be overestimated in the astrophysics of neutron stars. It is now believed that all medium and heavy mass chemical elements almost appeared in the “thermonuclear reactors” of stars and supernovae. The Big Bang provided only fuel for them: a few of the lightest elements. The lion's share fell on hydrogen, which still (and by a large margin) remains the most abundant in the Universe. However, in small quantities, helium, beryllium, and lithium were formed at the same time.

Theorists explained with good accuracy why they formed in one or another quantity. With one exception: current concentration of lithium in the Universe cannot be predicted. The isotope of lithium-7 is three times less than it turns out in theory, and lithium-6 is 300–500 times more. This discrepancy remains a real headache for cosmology: it is not possible to "fit" the Big Bang model to it, and some suitable explanations call into question the Big Bang itself.

In the theory of the Big Bang of a hot Universe, the formation of nucleons begins approximately from time $t = 10^{-5}$ s, temperature $T = 10^{12}$ K and particle energy $E = 0.1$ GeV. This implies protons and neutron potentially could be in the form of neutrons, but for some reason they mainly consider only protons for possible thermonuclear fusion. Even if we calculate the density of matter at this moment [31], then it exceeds the density of a neutron star. That is, under these conditions the overwhelming majority of nucleons potentially could be in the form of neutrons since the conditions of neutronization are fulfilled.

It is more likely to expect the possibility of collective condensation of neutrons (for the most part, rather than sequential addition of individual neutrons, as Gamov and co-workers believed) upon reaching a critical temperature (which is an energetically more favorable process) than thermonuclear fusion from a minimum number of protons in those the same conditions. Fragmentary condensation of neutrons due to quantum-gravitational density fluctuations occurs with the release of additional energy, which enhances the formation of hyperheavy stable neutron nuclei, which are the source of non-relativistic dark matter (neutrality, femto-, pico- and nano-sizes, relic cooling to our time make it difficult detection with $Z >> 175$, $N >> Z$ and $N > 10^3–10^5$, stable dark matter – SDM). The observable part of the Universe is formed from the residual part of protons and subsequently decayed single neutrons and unstable fragments of neutron matter (with $Z > 175$, but $N < 10^3–10^5$, decaying dark matter – DDM).

Thus, it is necessary to take into account the possibility of the formation of fragments of neutron matter as dark matter (neutrality, femto-, pico- and nano-sizes, relict cooling complicate their detection) already at the initial moments of the birth of the Universe, which is the initial dominant process in primary nucleosynthesis, and not thermonuclear fusion from the initial negligible amount of protons. However, further, as it cools, the process proceeds according to the generally accepted scenario with thermonuclear fusion against the background of decay of an unstable component of neutron matter [32,33].

6. CONCLUSION

Summing up a brief summary, it can be noted that hyperheavy nuclei and neutron matter in our time is a very specific physical reality, which urgently requires its rightful place in the PS and the study of not only physical, but also chemical, and possibly in the near future, and engineering properties. Neutron matter, or rather an element corresponding to it, begins (zero period) and ends (supercritical atoms) of the PS of elements. Neutron matter is given stability already at the micro-level due to additional (Tamm, Hund, Migdal) interaction, and not only at the macro-level due to gravitational interaction, as is now believed in astrophysics. The possibility of polineutronization is shown not only due to gravitational interaction, but also by other mechanisms (supercritical increase in the ordinal number of elements and condensation of UCNs), thus, there is a fundamental possibility of obtaining neutron matter under terrestrial conditions (at $Z >> 175$, $N > 10^3$–10^5 and size 200–300 and more femtometers). Neutron substance is a necessary link connecting (throwing a bridge) from micro- to macro- and mega World, from free neutron to neutron stars and Black holes. Such an extremely concentrated substance is thermodynamically and statistically the most stable state of matter as such. This substance can be thought of as a multitude of tightly packed neutrons, with scattered residual protons and electrons among them.

It is necessary to take into account the possibility of the formation of fragments of neutron matter as dark matter (neutrality, femto-, pico- and nano-sizes, relic cooling make them difficult to detect) already at the initial moments of the birth of the Universe, which is the dominant process, and not thermonuclear fusion from an initial insignificant amount protons. Further, as it cools, the process proceeds according to the generally accepted scenario. Neutron matter consistently fits into the original concept of PZ and PS put forward by Dmitry Ivanovich Mendeleev, whose 150th anniversary we recently celebrated [8,9,19].

REFERENCES

1. S.V. Adamenko, V.I. Vysotskii, Foundations of Physics Letters.17, No.**3**, 203(2004).
2. S.V. Adamenko, V.I. Vysotskii, Foundations of Physics. 34, No.**11**, 1801(2004).
3. S.V. Adamenko, V.I. Vysotskii, Foundations of Physics Letters. 19, No.**1**, 21(2006).
4. S.V. Adamenko, V.I. Vysotskii, A.S. Adamenko, Synthesis of superheavy nuclei and conditions for their identification. Book: Controlled Nucleosynthesis. Breakthroughs in Experiment and Theory, (Editors S.V. Adamenko, F. Selleri, A.van der Merwe), Series: Fundamental theories in Physics, v.**156**, Springer, Chapter 10.1, 363(2007).
5. S.V. Adamenko, V.I. Vysotskii, Stability of Electron-Nucleus form of matter and methods of controlled collapse. Book: Controlled Nucleosynthesis. Breakthroughs in Experiment and Theory, (Editors S.V. Adamenko, F. Selleri, A.van der Merwe), Series: Fundamental theories in Physics, v.**156**, Springer, Chapter 11, 415(2007).
6. S.V. Adamenko, V.I. Vysotskii, Anomalies of the spatial distribution of extrinsic elements in the accumulating screen and the synthesis of superheavy nuclei. Book: Controlled Nucleosynthesis. Breakthroughs in Experiment and Theory, (Editors S.V. Adamenko, F. Selleri, A.van der Merwe), Series: Fundamental theories in Physics, v.**156**, Springer, Chapter 10.7, 401(2007).

7. S.V. Adamenko, V.I. Vysotskii, The problem of the Coulomb collapse in electron-nuclear system in condensed targets. Journal of Surface Investigation. X-ray, Synchrotron and Neutron Techniques, №**4**, 30 (2005) (in Russian).
8. G.B. Ryazantsev, G.K. Lavrenchenko, I.N. Beckman, I.M. Buntseva, S.S. Nedovesov, Odessa Astronomical Publications, **31**, 33(2018).
9. G.B. Ryazantsev, I.N. Beckman, G.K. Lavrenchenko, I.M. Buntseva, S.S. Nedoves, ISINN-26. 26th International Seminar on Interaction of Neutrons with Nuclei. Dubna, JINR, Russia, 37–44 (2019).
10. G.B. Ryazantsev, G.K. Lavrenchenko, Tehnicheskie gazy, №**1**, 3(2014) (in Russian).
11. G.B. Ryazantsev, G.K. Lavrenchenko, Tehnicheskie gazy, №**4**, 41(2016) (in Russian).
12. G.B. Ryazantsev, Nauka i zhizn', № **2**, 76(2016) (in Russian).
13. G.B. Ryazantsev, G.K. Lavrenchenko, M.A. Khaskov, I.N. Beckman, ISINN-24. 24th International Seminar on Interaction of Neutron with Nucle. Dubna, JINR, Russia, 65–74 (2017).
14. G.B. Ryazantsev, G.K. Lavrenchenko, I.N. Beckman, I.M. 18-th Gamow Summer School. Odessa, Ukraine, Abstrats, 15(2018).
15. Ya.B. Zel'dovich, V.S. Popov, Uspehi Fizicheskih Nauk, **105**,403(1971) (in Russian).
16. F.L. Shapiro, Nejtronnyje issledovanija, Sobranie trudov, Moskva: Nauka, 2: 348 (1976) (in Russian).
17. V.K. Ignatovich, Uspehi Fizicheskih Nauk, **166**, №3, 303(1996) (in Russian).
18. D.I. Mendeleev, Periodicheskij zakon. Sochinenija, tom 2, L: Goshimtechizdat, 520 c. (1934) (in Russian).
19. D.I. Mendeleev, Sobranie rabot, Sostavitel' Soloviev Yu. I., M. (1991) (in Russian).
20. R.B. Dobrotin, N.G. Karpilo, L.S. Kerova, D.N. Trifonov, Letopis' zhizni I dejatel'nosti D.I. Mendeleeva. Red. Storonkin A.V., L.: Nauka (1984) (in Russian).
21. I.E. Tamm, Teorija jadernuh sil i atomnigi jadra. Sobranije nauchnuh trudov, t.1, Nauka, M., 283–326 (1975) (in Russian).
22. F. Hund, Ergebnisse der exakten Naturwissenschaften **15**, 189(1936).
23. A.B. Migdal, Teorija konechnuh Fermi system i svojsnva atomnuh yader, izd. 2, M.: Nauka, **54**(1983) (in Russian).
24. A.Yu. Potehin, Uspehi Fizicheskih Nauk, **180**, №12, 1279(2010) (in Russian).
25. F. Zwicky, Publications of the Astronomical Society of the Pacific. Printed in USA, **70**, № 416, 506(1958).
26. G. Gamow, Phys. Rev. **70**, 572(1946).
27. V.I. Vysotskii, M.V. Vysotskii, Journal of Surface Investigation. X-ray, Synchrotron and Neutron Techniques, **5**, №2, 330 (2011).
28. A.P. Serebrov, S.T. Boldarev, A.N. Erykalov, Physics Procedia **17**, 251(2011).
29. E.A. Kornell, K.E. Viman, V. Ketterle, Uspehi Fizicheskih Nauk, **173**, №12, 1319 (2003) (in Russian).
30. Vusotskii V.I., Kuz'min R.N., Sposob formirovanija impul'snogo potoka nejtronov (in Russian).
31. Certificate of authorship №1346031 (in Russian).
32. A.D. Chernin, Uspehi Fizicheskih Nauk, **164**, №8, 889 (1994) (in Russian).
33. A. Chudaykin, D. Gorbunov, I. Tkachev, Phys. Rev. D **94**, 023528 (2016).
34. A. Chudaykin, D. Gorbunov, I. Tkachev, Phys. Rev. D **97**, 083508 (2018).

On History of the Fermi Pseudopotential Concept in Atomic and Neutron Physics

Sharapov E.I.

Frank Laboratory of Neutron Physics, JINR, Dubna, Russia

1. Introduction

This report will bear a touch of history. Enrico Fermi introduced the pseudopotential concept about 85 years ago. The Collected Papers of Fermi [1, 2], published in 1962 by the University of Chicago Press, revealed that this happened in 1933–1934. Fermi group just finished their studies in atomic spectroscopy, published their results and switched to a search of radioactivity induced by neutrons. Besides Fermi the Photo of [3] shows also physicists Franco Rasetti, Eduardo Amaldi, Emilio Segre and chemist Oscar D'Agostino.

Photo of [3]: Fermi group in 1934.

On January 27, 1934 Amaldi and Segre published the paper [4] on the shifts of high terms of alkaline atomic spectra in the presence of an additional ("foreign") gases H, He, Ar, O_2, and N_2. After active discussions with Amaldi and Segre, Fermi had found the explanation of the effect. In the end of 1933 he sent the paper [5] to Nuovo Cimento. The following quotation is from comments of Emilio Segre to paper [5] in [1]: *"We meet there for the first time the concept of the scattering length and of 'pseudopotential'. This theoretical development is remarkable… it gives a technique that Fermi used many times in connection with his neutron works"*. However, according to numerous reviews and books in neutron physics, Fermi introduced the pseudopotential for the first time in his seminal paper [6] in

1936 on physics of thermal neutrons behavior in paraffin and water. There is an unsettled issue here. Therefore, I'll give some details of both papers first, and then will proceed to rather general examples of how Fermi pseudopotential became a powerful concept for the latest developments in several research fields, such as ultracold neutrons, ultracold atoms, and condensed matter.

2. Fermi's paper of 1934

The most essential goal of paper [5] was to explain the shift of the spectral lines due to the interaction of the alkali atom valence electron with 'foreign' neutral atoms. Fermi estimated that due to a rather large radius of such electron orbit and the gas pressure of ≈ 1 atm, there should be about 10^3 of foreign atoms in the alkali atom volume where the electron can collide through the potentials $V_i(r)$. Using the Schroedinger equation in its historic form of 1926:

$$\Delta\psi(r) + \gamma(E - V(r))\psi(r) = 0, \text{ with: } \gamma \equiv 8\pi^2 m/h^2, \ \Delta \equiv \Delta^2,$$

Fermi, for his problem, wrote

$$\Delta\psi(r) + \gamma(W - U - \sum V_i(r))\psi(r) = 0. \tag{1}$$

The energy W here is the full energy E for the alkali atom, U is a weak remnant of the closed shell potential and r is the electron distance relative to neutral atom. As an example, the Lennard-Jones potential for interaction of two neutral molecules is shown in Fig.1. Its effective range value is $\rho \approx 6$ Å and its known analytical form allows exact solutions of practical problems.

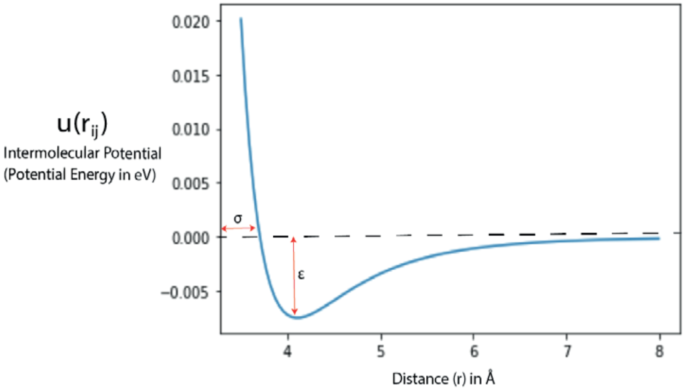

Fig.1. The Lennard-Jones potential.

To solve the Schroedinger equation with unknown potential $V_i(r)$, Fermi formulated an approximation presently known as one of simple forms of the boundary condition method. He considered a spherically symmetric (s-wave scattering) potential $V_i(r)$ and introduced, in addition to the exact wave function $\psi(r<\rho)$, the function Ψ by averaging ψ over the distances r in a broad region included the potential "well" $V_i(r)$ (at $r<\rho$) and the space outside (where $V_i(r) = 0$). This region was taken to be less than the de Broglie wavelength for the electron (λ_B

≈ 100 Å here), but large enough to contain many foreign atoms. The function Ψ, as opposite to ψ, has no singularities through all the considered space. Using the relationship $\Delta\Psi = <\Delta\psi>$ for averaging Eq. (1), Fermi wrote the Schroedinger equation for the averaged function in the form:

$$\Delta\,\Psi(r) + \gamma(W - U)\Psi - \gamma < \textstyle\sum_i V_i(r))\psi(r)> \, = 0. \tag{2}$$

To calculate the value of the last term in this equation he introduced another function, u(r), by the replacement $\psi = u(r)/r$, usually used for the case when $V_i(r) = 0$, and applied it for all r. The reasons for the replacement was the linear behavior $u(r) \sim (a + r)$ for this function outside the potential “well” and the obvious boundary condition $u(r{=}0) = 0$.

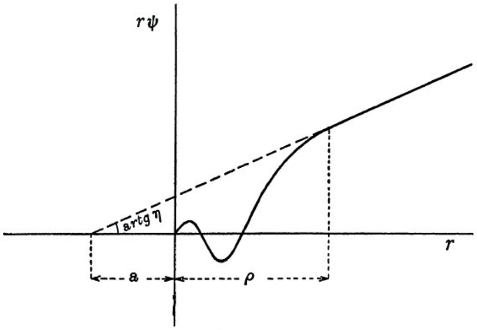

Fig.2. Interpretation of the scattering length *a* in [5].

The constant *a* was already used in the theory of atomic collisions as the limit of the ratio $a = \delta(k)/k$ at $k \to 0$, with $\delta(k)$ the phase shift of the scattered wave and k is the wave number. By plotting the function $u(r) = r\psi$, Fermi introduced another interpretation of *a* as the ‘scattering length’. This fames plot is shown in Fig. 2.

Using Eq.(2) without the small term U, Fermi deduced the differential equation for u(r) at ($r < \rho$)

$$u''(r) = \gamma V(r)u(r). \tag{3}$$

All these relationships where used to calculate the contribution of an one i-term (one ‘well’) in the sum, Eq.(3), by taking the volume integral

$$\gamma \int V\psi d\tau = 4\pi\gamma \int V u dr = 4\pi \mid u''r - u|0^{r} = -\,4\pi a\,\Psi. \tag{4}$$

Introducing *n* as the number of foreign gas ‘potential wells’ per cm³, Fermi finally obtained the equation

$$\Delta\,\Psi + \gamma(W - U - \frac{h^2 a\, n}{2\pi m})\Psi = 0. \tag{5}$$

The third term in Eq.(5) is *presently* often called the ‘optical potential’ and written as

$$V = \frac{2\pi\hbar^2}{m} an. \qquad (6)$$

With known values of a, n, m and Eq.(5) Fermi had explained the shifts of spectral lines in the Amaldi and Segre experiment.

3. Fermi's paper of 1936

The 1936 paper [6] was also published in the Italian translated into the English later in [1]. The paper is well known, referenced in all books, therefore the details will be omitted, and only the salient points, which distinguish it from the paper of 1934 will be given here. The goal was to introduce an average potential for interaction of neutrons with protons chemically bound in a hydrogen medium. While the scale of the nuclear potential range is of the order of, 10^{-12} cm, the regions where the chemical bounding forces work is of the order of amplitudes of atoms vibrations in the molecule, that is, about 10^{-9} cm. Using now U(X,Y,Z) as the potential energy of chemical forces, introducing again, in addition to the full true wavefunction ψ , the new function Ψ by performing an appropriate averaging this time over a large sphere of radius R around the neutron position, assuming that the length R simultaneously satisfies the inequalities

$$\boldsymbol{R} \ll \lambda; \quad R \gg \rho; \quad R \gg a, \qquad (7)$$

Fermi proceeded further in exactly the same way as in 1934 paper [5], however without any reference to it, and had shown the drawing, Fig. 3, analogous to Fig. 2:

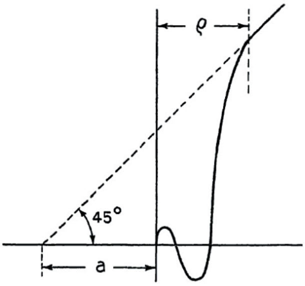

Fig.3. Interpretation of the scattering length a in [6].

Finally, Fermi obtained the desired equation for Ψ, which we show in a slightly different form than given in [6]:

$$\Delta\,\Psi + \gamma(W - U - (h^2 a/\pi M)\delta_R(r))\Psi = 0. \qquad (8)$$

The new function $\delta_R(r)$ he defined to be the equal to $3/(4\pi R^3)$ everywhere for $r < R$ and to be zero for $r > R$. Its volume integral extended over all space is equal to 1. And since the quantities in Eq.(8) vary slowly in the region where $\delta_R(r) \neq 0$, Fermi wrote the statement that, in the first Born approximation, we quote, *"... when calculating the matrix elements of the interaction term in Eq.(8), the function $\delta_R(r)$ may be identified with the Dirac delta-function in three dimensions"*. This is the essence of the Fermi pseudopotential concept. The pseudopotential itself, in the modern notation, is

$$V_F = 2\pi \frac{\hbar^2}{m} a\delta^{(3)}(r). \tag{9}$$

Fermi applied the first Born approximation with this potential for tackling the problem of inelastic scattering of neutron in paraffin while treating the hydrogen atoms as harmonic oscillators of frequency v. He calculated, for the first time, the elastic and inelastic cross sections in the function of the neutron energy w, which are shown in Fig.4. The curves 1, 2, 3 correspond to excitations of the oscillator in the corresponding exited states. This theoretical prediction was confirmed experimentally only about fifteen years later.

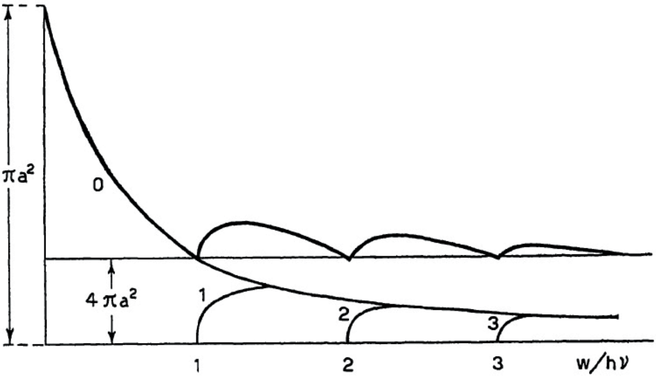

Fig.4. Neutron elastic and inelastic cross sections in paraffin.

4. Further developments in neutron and atomic physics

The neutron physics field. Ten years later, Gregory Breit [7], considering the Fermi method as the first approximation to the possible more accurate equations, formulated the same problem in terms of the boundary conditions method with the integral equations. The paper [7] is entitled:

G. BREIT

The scattering of slow neutrons by bound proton.

To describe nuclear properties within the exact approach, Breit applied the 'intercept' quantity a, which he named the *Fermi scattering length*. For the free protons case, the Fermi result was obtained again. For the bound protons, Breit calculated the correction of only 0.3%. The final resume was that the application of the first Born approximation with the Fermi pseudopotential doesn't increase the typical inaccuracy of the Born method. Later J.M. Blatt and V.F. Weisskopf [8] in their *Theoretical Nuclear Physics* came to the same conclusion.

The next fruitful phase in developing of the theory was focused mainly on properties of the many body wave functions of scattering, in particular on multiscattering corrections to the optical potential. This is a separate topic for recollections and reviews, requiring a special mathematical background. For an introduction to it one may start with the paper [9]:

A.L.BARABANOV, S.T. BELYAEV

Multiple scattering theory of slow neutrons (from thermal to ultracold).

The recent papers of Yu. Pokotilovski [13] and H. Abele [14] review the present status of the experimental researches with ultracold neutrons. In this field, the so-called ‘optical potential’, based on the Fermi method, is widely used and serves nowadays in precision studies of neutron beta-decay for the Standard Model tests and for searches of a ‘new physics’.

Atomic physics field. After the invention of the laser sources of the coherent light (with the Nobel Prize awarded in 1964), the atomic physics experienced a second birth, especially when techniques of cooling and trapping atoms with laser light and magnetic fields (the Nobel Prize awarded in 1997) became widely available at universities of the USA, Europe and Asia. The explosion of research in atomic and molecular physics, that followed the new technology, was culminated by the experimental demonstration of the phenomenon of Bose-Einstein condensation in dilute gases of ultracold alkali atoms (with the Nobel Prize awarded in 2001). Essential for this progress were new approaches to modeling and new methods to calculate the atom-atom interactions in environments, such as magnetic and optical traps. As an introduction to the achieved results in this prolific field, one may see the paper [10] by S. Inouye et al., entitled “Observation of Feshbach resonances in a Bose-Einstein condensate”, the paper [11] by N.T Zinner, entitled “Effective potential for ultracold atoms at the zero crossing of a Feshbach resonance”, or the review [12] by Cheng Chin et al., entitled “Feshbach resonances in ultracold gases”. In atomic physics, the Schroedinger equation $\boldsymbol{H}\,\Psi = \mathrm{E}\,\Psi$ for the relative motion of two cold atoms contains, generally, a more complicated operator $\boldsymbol{H}$:

$$\boldsymbol{H} = -\frac{\hbar^2}{2m}\Delta + \sum \frac{\omega^2}{2m} r^2 + \mu B(r_i) + 2\pi \frac{\hbar^2}{m} a \delta^{(3)}(\boldsymbol{r}) \frac{\partial}{\partial r} r. \tag{10}$$

The second term here is the harmonic oscillator potential of the interacting atoms at the positions r_i in a trap, the third term is the interaction with the magnetic field B and the last term is the so-called *regularized* zero-range potential. It is required for the mathematical correctness when using the $\delta^{(3)}$ function in three dimensions.

The phenomenon of the Feshbach resonances in nuclear physics is due to the coupling of the two channels in the collision: discrete nuclear state and the continuum region of the potential. The Feshbach resonances in atomic physics came into the play because the magnetic interactions in atoms are dependent on the magnetic moments of nuclei through the hyperfine splitting of the energy levels of the atom total angular momentum. Theorists developed the coupled two channel zero-range potential, calculated the scattering length a, and found the resonance behavior in dependence of the external magnetic field.

The result of the experiment for sodium atoms, shown in Fig.5 [10], demonstrates such behavior: at the resonance position B_0, the scattering length diverges ($a \to \pm \infty$). Near the resonance, the function $a(\mathrm{B})$ can be described as $a(\mathrm{B}) = a_{\mathrm{bg}}(1 - \Delta/(\mathrm{B}-\mathrm{B}_0)$. The physical output from this phenomenon is the association of interacting cold atoms into the cold molecules with a corresponding decrease of the initial atomic density (the upper part of Fig. 5).

This phenomenon was confirmed experimentally in several cases and opened the way to study the Bose-Einstein condensation in gases by tuning effective atomic interactions.

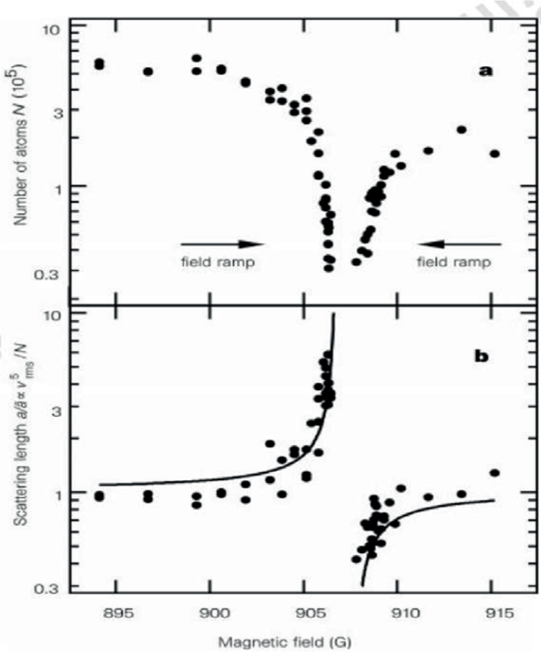

Fig.5. Feshbach resonance in Na.

Conclusion

From the outlined history of the Fermi pseudopotential concept one can conclude the following:

- The so-called effective or averaged potential, **V**, in the Schroedinger equation for interaction of electrons with the media was first introduced by Fermi in 1934. About twenty years later, in neutron optics, it got the name optical potential.
- The *pseudopotential* with the *Dirac Delta*-function, $\mathbf{V_F}$, allowing calculations in the first Born approximation, appeared in the neutron physics paper published in 1936. Under the notation $\mathbf{V_F}$ it is known since the G. Breit's paper of the year 1947.
- To use the effective potential **V** under the name "the *Fermi optical* potential" is not correct in a strict sense. History definitely made the choice of the Fermi name for "the Fermi pseudopotential" $\mathbf{V_F}$, in another words – "the Fermi zero-range potential".
- The most active use and development of the Fermi pseudopotential concept is going on presently in the field of the ultracold atoms physics.

5. Acknowledgment

Finally, many thanks are to Alexander Vladimirovich Strelkov. He often drew my attention to the physics beyond neutrons and, in particular, through his paper in [15], initiated this report and helped to work on it.

REFERENCES

1. Enrico Fermi, *Collected Papers (Note e Memorie),* v. **I**. Italy 1921–1938; The University of Chicago Press – Academia Nazzionale dei Lincei, Roma (1962).
2. Enrico Fermi, Nauchnye Trudy, **I.** Italia 1921–1938; Izd. «Nauka», Moskva,1971 (in Russian).
3. https://en.wikipedia.org/wiki/Enrico_Fermi.
4. E. Amaldi and E. Segre, Nature (London) **133**, 141 (1934).
5. E. Fermi. Nuovo Cimento **11**, 157–166 (1934).
6. E. Fermi, Ricerca Scientifica **7(2)**, 13–53 (1936).
7. G. Breit, Phys. Rev., **71,** 215 (1947).
8. J.M. Blatt and V.F. Weisskopf, *Theoretical Nuclear Physics*, Wiley, New York (1952).
9. A.L. Barabanov, S.T. Belyaev, Eur. Phys. J. B **15,** 59 (2000).
10. S. Inouye *et al*., Nature **392**, 151 (1998).
11. N.T. Zinner, Journal of Atoms and Molecules **2012**, 241051 (2012).
12. A. Chin, R. Grimm, P. Juliennem E. Tiesinga, Rev. Mod. Phys., **82** (2), 1225 (2010).
13. Yu.N. Pokotilovski, arXiv:1805.05292v1 [physics.hist-ph] 14 May 2018.
14. H. Abele, H. Lemmel, T. Jenke, arXiv:1909.03349v1 [nucl.ex] 7 Sep 2019; EPJ Web of Conferences, **219**, 01001 (2019).
15. A.V. Strelkov. In collected lections Д3 14-91-154 «VI International school on Neutron Physics» (Alushta, 1990, October 8–18), V.**I**, p.325, Joint Institute for Nuclear Research, Dubna (1991).

Reactions with Neutrons, Properties of Compound States, Nuclear Structure

Isomeric Ratios in Several Inverse (γ, n) and (n, γ) Reactions

Bui Minh Hue[1,2,*] and Tran Duc Thiep[1,2]

[1]Graduate University of Science and Technology, VAST, 18 Hoang Quoc Viet, Hanoi
[2]Institute of Physics, VAST, 10 Dao Tan St., Ba Dinh Region, Hanoi, Vietnam
bmhue@iop.vast.ac.vn

We measured isomeric ratios of ^{137m,g}Ce, ^{115m,g}Cd, ^{109m,g}Pd, and ^{81m,g}Se produced by 25 MeV bremsstrahlung and thermal neutron induced reactions, namely from inverse (γ, n) and (n, γ) reactions. The bremsstrahlung and the neutron sources were constructed at the electron accelerator Microtron MT-25 of the FLNR, JINR, Dubna, Russia. The activation method combining with off-line gamma-ray spectroscopy was used in the experiment. To improve the accuracy of the isomeric ratio determination, data analysis and necessary corrections, such as the self-absorption and summing cascade effects, were made in gamma rays radioactivity measurements. The results were discussed and compared with those in the existing literature. The obtained results in the (γ, n) reactions were validated by comparison with the theoretical predictions using TALYS 1.95 code.

1. Introduction

The inverse nuclear reactions, when a projectile of one reaction is the ejectile of another reaction, have been subjects for many experimental and theoretical studies since 1960s [1,2]. Inverse reactions including photonuclear and thermal neutron capture reactions play an important role in astrophysics and the study of nuclear structure and nuclear reaction mechanisms [2–4]. So far, most investigations about photonuclear reaction and thermal neutron capture reactions have concentrated on the determination of reaction cross section or reaction yield, but the studies on isomeric ratio (IR) have been still limited. The isomeric ratio, the ratio of the probability for forming isomeric and ground states, provides diverse information about the nuclear structure and nuclear reaction mechanism [5–8]. This ratio is connected with many problems of modern nuclear physics and can be used to test different models of nuclear reactions induced by various projectiles.

The aim of this work was to investigate IR of ^{137m,g}Ce, ^{115m,g}Cd, ^{109m,g}Pd, and ^{81m,g}Se produced in inverse (γ,n) and (n,γ) reactions by activation method, namely ^{138}Ce(γ,n)^{137m,g}Ce, ^{136}Ce(n,γ)^{137m,g}Ce, ^{116}Cd(γ,n)^{115m,g}Cd, ^{114}Cd(n,γ)^{115m,g}Cd, ^{110}Pd(γ,n)^{109m,g}Pd, ^{108}Pd(n,γ)^{109m,g}Pd, ^{82}Se(γ,n)^{81m,g}Se, and ^{80}Se(n,γ)^{81m,g}Se. The experimental results are expected to examine the role of the reaction channel effect, intake momentum and impulse effects on the IRs. Moreover, the obtained results in the (γ,n) reactions were compared with the theoretical predictions using TALYS 1.95 code.

2. Experimental procedure

The bremsstrahlung source is obtained by interaction of 25 MeV electron beam produced from MT-25 Microtron accelerator [9] and a 3 mm thickness W disk detailed in refs. [7,10]. The end-point energy of bremsstrahlung is 25 MeV. The bremsstrahlung spectra, which were simulated by GEANT4 toolkit [11], are shown on Fig.1.

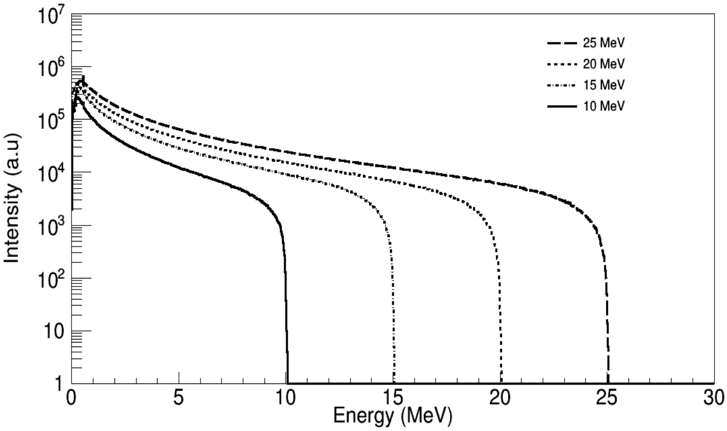

Fig 1. The bremsstrahlung spectra calculated by Geant4.10.06 version.

The thermal neutron source was also created at MT-25 Microtron described in ref. [8]. The uranium-beryllium converter was placed within a graphite cube, which served as a main neutron moderator to thermal and epithermal neutrons.

The high-purity natural Ce_2O_3, PdO, SeO_2 and Cd samples with the mass and diameter of 0.8 g, 0.323 g, 0.2484 g, 0.7143 g and 1.6 cm, 1.0 cm, 1.0 cm, 1.0 cm, respectively were irradiated in the photon and neutron sources with the definite time, which was preliminarily estimated by the activation method so that the interested gamma rays have good count statistics. Afterwards, the gamma-ray activities were measured for proper time of cooling and measurement by using the high-resolution gamma-ray spectroscopy consisting of the high-energy resolution HPGe detector (1.80 keV at γ- ray 1332 keV of ^{60}Co), the PC based 8192 channel analyzers for the data processing, the GENIE 2000 and Gamma Vision software used for the data acquisition and γ-ray spectra analysis [7,8].

3. Data analysis

The selected gamma rays and spectroscopic characteristic data [12,13] used for the IR calculation were determined and shown in Table 1. The losses of the interested gamma ray count due to the self-absorption and summing coincidence effects, which contribute to the IR determination error were corrected as the formulas (1) and (2) in ref. [8].

The IR was calculated below as in refs. [7,8,10]:

$$\frac{1}{IR} = \frac{\frac{S_g \varepsilon_m I_m}{S_m \varepsilon_g I_g} \Lambda_3 \Lambda_6 \Lambda_9 - \Lambda_1 \Lambda_5 \Lambda_8 - \Lambda_3 \Lambda_4 \Lambda_8 - \Lambda_3 \Lambda_6 \Lambda_7}{\Lambda_2 \Lambda_5 \Lambda_8} \tag{1}$$

Where m and g- the isomeric and ground states; *S*, ε and *I* - the counts, the efficiencies and the intensities of the gamma rays of interest and Λ_i ($i = 1 \sim 9$) are expressions related to the irradiation, cooling and measurement time.

Table 1. Selected gamma rays and spectroscopic characteristic data

Nuclear Reaction	Target Spin, Parity, [J^π]	Nuclear state	Spin Parity [J^π]	Decay Mode [%]	Half Life	γ-ray Energy [keV]	Intensity [%]
^{138}Ce(γ, n)^{137}Ce ^{136}Ce(n,γ)^{137}Ce	0^+	^{137m}Ce	$11/2^-$	IT: 99.2 EC: 0.78	34.4 h	254.3	99.2
^{138}Ce(γ,n)^{137}Ce ^{136}Ce(n,γ)^{137}Ce	0^+	^{137g}Ce	$3/2^+$	EC: 100	9.0 h	447.1	1.8
^{116}Cd(γ, n)^{115}Cd ^{114}Cd(n, γ)^{115}Cd	0^+	^{115m}Cd	$11/2^-$	β^- : 100	44.6 d	933.8	2.0
^{116}Cd(γ, n)^{115}Cd ^{114}Cd(n, γ)^{115}Cd	0^+	^{115g}Cd	$1/2^+$	β^- : 100	2.23 d	336.2 527.9	45.9 27.45
^{110}Pd(γ,n)^{109,}Pd ^{108}Pd(n,γ)^{109}Pd	0^+	^{109m}Pd	$11/2^-$	IT: 100	4.69 m	189.0	55.9
^{110}Pd(γ,n)^{109}Pd ^{108}Pd(n,γ)^{109}Pd	0^+	^{109g}Pd	$5/2^+$	β^- : 100	13.7 h	88.04	3.6
^{82}Se(γ, n)^{81}Se ^{82}Se(n, γ)^{81}Se	0^+	^{81m,}Se	$7/2^+$	IT: 99.95 β^- : 0.05	57.28 m	103.0	13.0
^{82}Se(γ, n)^{81}Se ^{80}Se(n, γ)^{81}Se	0^+	^{81g,}Se	$1/2^-$	β^- : 100	18.45 m	276.0 290.0	0.7 0.55

4. Results and Discussion

Table 2 presents the experimental results of this work together with the existing data, which were taken from refs. [7,14–23]. The product excitation energies were calcultate by using formula (5) in refs. [8]. The error of IRs came from two sources. The first included uncertainties related to the IR calculations using formula (1) and the second was from uncertainties related to systematics. The total error of the IR determination was estimated to be about 10.0%.

The experimental results show that the IRs in inverse (γ, n) and (n, γ) reactions, which lead to the same isomeric pairs ^{137m,g}Ce, ^{115m,g}Cd, ^{109m,g}Pd, and ^{81m,g}Se are different due to be reaction channel effect. The IRs in (γ, n) reactions are significantly higher than that in (n, γ) reactions. This trend can be explained by the intaken angular momentum and impulse, transferred to the target nuclei from the projectiles, namely the higher the intake angular momentum and impulse the higher the isomeric ratio.

For the (γ, n) reactions, the IRs of this work and that of refs. [15,16,19,22] in the error limit are in good agreement. Likewise, for the (n, γ) reactions, our result and the data from the references are in an agreement except for ^{81m,g}Se to be an agreement with refs. [14,23] and being considerably less than that from ref. [18].

Table 2. The isomeric ratio of the investigated (γ, n) and (n, γ) inverse reactions

Nuclear Reaction and Product	Type of Projectile	Product Exc. Energy [MeV]	Isomeric Ratio *IR*
^{138}Ce(γ, n)^{137m,g}Ce	25 MeV Bremsstrahlung	5.5	0.221(22) (This work) 0.19(2) [16]
^{136}Ce (n, γ)^{137m,g}Ce	Thermal neutron	7.4	0.112(11) (This work) 0.109(10) [7] 0.15(1) [17] 0.088(6) [18]
^{116}Cd(γ, n)^{115m,g}Cd	25 MeV Bremsstrahlung	5.8	0.165(16) (This work) 0.168(20) [19]
^{114}Cd(n, γ)^{115m,g}Cd	Thermal neutron	6.1	0.116(12) (This work) 0.099(33) [20]
^{110}Pd(γ, n)^{109m,g}Pd	25 MeV Bremsstrahlung	6.3	0.069(7) (This work) 0.065(3) [15]
^{108}Pd(n, γ)^{109m,g}Pd	Thermal neutron	6.1	0.023(2) (This work) 0.018(5) [21], 0.028(5) [14]
^{82}Se(γ, n)^{81m,g}Se	25 MeV Bremsstrahlung	6.9	0.556(55) (This work) 0.56(2) [22]
^{80}Se(n, γ)^{81m,g}Se	Thermal neutron	6.7	0.114 ± 0.014 (This work) 0.204(24) [17] 0.136(0.011) [14] 0.096(9) [23]

TALYS 1.95 code [24] and GEANT4 simulation tool were used for theoretical IR calculation of ^{137m,g}Ce, ^{115m,g}Cd, ^{109m,g}Pd, and ^{81m,g}Se produced from (γ, n) reaction. TALYS code simulates nuclear reactions that involve neutrons, gamma-rays, protons, deuterons, tritons, helions, and alpha-particles in the 1 keV–200 MeV energy range. In the thermal energy region of neutron, this code is completely unresolved. In case of bremsstrahlung induced nuclear reactions, the isomeric ratios could be analytically calculated by the expression below:

$$IR = \frac{Y_m}{Y_g} = \frac{N_0 \int_{E_{th}^m}^{E_\gamma^m} \sigma_m(E)\phi(E)dE}{N_0 \int_{E_{th}^g}^{E_\gamma^m} \sigma_g(E)\phi(E)dE}\,. \tag{2}$$

Here E_g^m - the bremsstrahlung end-point energy, ϕ (E) – the bremsstrahlung photon flux, N_0 - the number of the target nuclei; $\sigma_m(E)$ and $\sigma_g(E)$ - the cross sections of the isomeric and ground states; E_{th}^m and E_{th}^g - the threshold reaction energies for the isomeric and ground state, respectively.

By using the TALYS 1.95 code, $\sigma_m(E)$ and $\sigma_g(E)$ could be obtained. These data combining with the bremsstrahlung spectra simulated by GEANT4 (Fig. 1) could be caculated IR following the formula (2). The theoretical IR results were obtained by the calculation using six level density models of TALYS 1.95 as ldmodel 1: Constant temperature + Fermi gas model; ldmodel 2: Back-shifted Fermi gas model; ldmodel 3: Generalised superfluid model; ldmodel 4: Microscopic level densities (Skyrme force) from Goriely's tables; ldmodel 5: Microscopic level densities (Skyrme force) from Hilaire's combinatorial tables and ldmodel 6: Microscopic level densities (temperature dependent HFB, Gogny force) from Hilaire's combinatorial tables. The present experimental results are best suited to the predictions using the 6th level density model. The deviations between the experimental and calculated data using 6 level density models are less than 23% (see Fig. 2) except for ^{137m,g}Ce. The difference in the case of ^{137m,g}Ce requires the level density and strength function models to be more detailed.

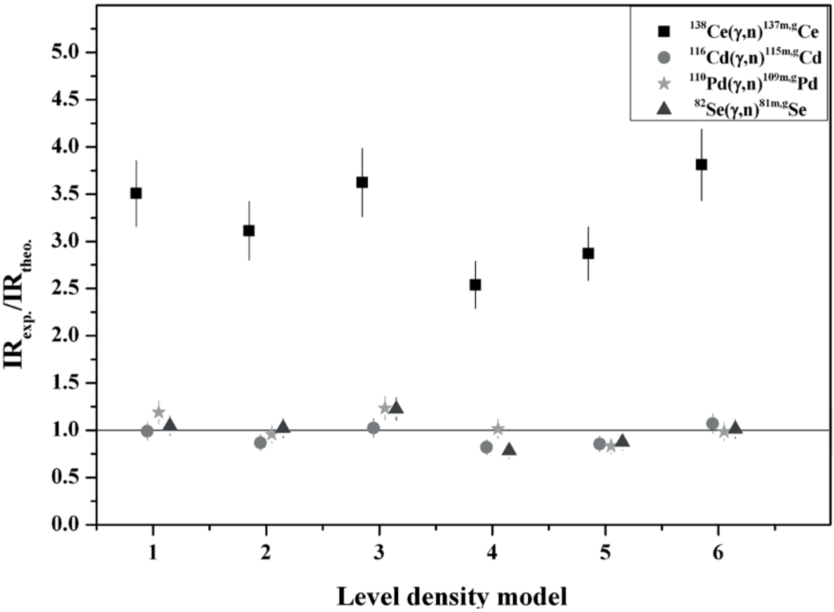

Fig. 2. Measured ($IR_{exp.}$) and calculated ($IR_{theo.}$) isomeric ratios of ^{137m,g}Ce, ^{115m,g}Cd, ^{109m,g}Pd and ^{81m,g}Se produced by (γ, n) reaction.

5. Conclusions

The IRs of ^{137m,g}Ce, ^{115m,g}Cd, ^{109m,g}Pd and ^{81m,g}Se in inverse (γ, n) and (n, γ) reactions have been measured by the activation method. The experimental results show that the IRs in (γ, n) reaction are higher than that in (n, γ) reaction. This trend can be explained by the effects of reaction channel, intaken angular momentum and impulse in nuclear reation.

The theoretical calculations for (γ, n) reactions based on TALYS 1.95 code are consistent with the experimental results, except in the case of $^{138}Ce(\gamma, n)^{137m,g}Ce$ reaction.

In order to reach a complete conclusion, it is needed more experiments to be performed as well as a nuclear reaction model, which includes detailed nuclear structure and nuclear reaction mechanisms as the compound, preequilibrium and direct.

Acknowledgment

This work has been performed at the Flerov Laboratory of Nuclear Reaction, Joint Institute for Nuclear Research, Dubna, Russia. The authors would like to express sincere thanks to the MT-25 Microtron group for operating the irradiation facility and the Chemical Department of the Flerov Laboratory of Nuclear Reaction for providing the measurement system. Bui Minh Hue was funded by Vingroup Joint Stock Company and supported by the Domestic PhD Scholarship Program of Vingroup Innovation Foundation (VINIF), Vingroup Big Data Institute (VINBIGDATA), code VINIF.2020.TS.18.

References

1. Cohen, S.G., Fisher, P.S. and Warburton E.K., 1961. Inverse Photonuclear Reactions $^{14}N(p, \gamma)^{14}O$ and $^{15}N(p, \gamma)^{16}O$ in the Giant Resonance Region. Phys. Rev. **121**(3), 858–865.
2. Wahsweiler H.G. and Greiner W. 1967. Angular distributions for the inverse photonuclear process in Si28 in the eigenchannel reaction theory. Phys. Rev. Lett. V. **19**(3), 131–134.
3. Mohr P., Angulo C., Descouvemont P. and H., 2006. Relation between the $^{16}O(\alpha, \gamma)^{20}Ne$ reaction and its reverse $^{20}Ne(\gamma, \alpha)^{16}O$ reaction in stars and in the laboratory, Eur. Phys. J. A **27**(1), 75–78.
4. Beard M., Frauendorf S., Kampfer B., Schwengner R. and Wiescher M., 2012. Photonuclear and radiative-capture reaction rates for nuclear astrophysics and transmutation: $^{92\text{-}100}Mo$, ^{88}Sr, ^{90}Zr, and ^{139}La. Phys. Rev. C **85**, 065808.
5. Huizenga J.R. and Vandenbosch R., 1960. Interpretation of Isomeric Cross Section Ratios for (n, γ) and (γ, n) Reactions. Phys. Rev. **120**(4), 1305–1312.
6. Do N.V., Luan N.T., Xuan N.T., Khue P.D., Hien N.T., Kim G., Kim K., Shin S.G., Kye Y., Cho M.H., 2020. Measurement of yield ratios for the isomeric pair $^{137m,g}Ce$ in the $^{141}Pr(\gamma, x)^{137m,g}Ce$ reactions with bremsstrahlung end-point energies of 50-, 60-, and 70-MeV. Radiation Physics and Chemistry, **176**, 1–9, 10901.
7. Thiep T.D., An T.T., Cuong P.V., Vinh N.T., Hue B.M., Belov A.G., Maslov O.D., 2017. Channel effect in isomeric ratio of $^{137m,g}Ce$ produced in different nuclear reactions. J. Radioanal. Nucl. Chem., **314**, 1777–1784.
8. Hue B.M., Thiep T.D., An T.T., Cuong P.V., Lukyanov S.M., Belov A.G., Mitrofanov S., 2020. The isomeric ratios in (n, γ) neutron capture reactions on ^{108}Pd and ^{110}Pd nuclei, J. Radioanal. Nucl. Chem., **326**(1), 503–509.
9. Belov A.G., Bondarenko P.G., Teteriev Yu.G. 1993. Preprint of JINR, D15-93-80, Dubna, Russia.
10. Thiep T.D., An T.T, Cuong P.V., Vinh N.T., Hue B.M., Anh L.T., Belov A.G., 2018. Isomeric Yield Ratio of $^{152m1}Eu(8\text{-})$ to $^{152m2}Eu(0\text{-})$ Produced from $^{153}Eu\ (\gamma, n)^{152}Eu$ Reaction in the Giant Dipole Resonance Region, J. Radioanal. Nucl. Chem., **317**, 1263–1271.

11. Geant4 Collaboration, Physics Reference Manual, Release 10.4, 2017.
12. Firestone R.B. 1996. Table of Isotopes, CD ROM Edn., Version 1.0, Wiley-Interscience, New York.
13. Radiation Search, http://ie.lbl.gov/toi/radSearch.asp53.
14. Bishop C.T., Vonach H.K. and Vandenbosch R.,1964. Isomer Ratio for Some (n, γ) Reactions. Nucl. Phys. A **60**, 241–249.
15. Palvanov S.R., Bozorov E.K., Mamajusupova M.I., Palvanova G.S., Saidimov Y.A., 2017. Excitation of Isomeric States in Reactions (γ, n) and (n, 2n) on ^{110}Pd Nucleus. World Journal of Research and Review, **5**(5), 28–31.
16. Gangrsky Yu.P., Zuzaan P., Kolesnikov N.N., Lukashek V.G., Tonchev A.P., 2001. Isomeric Ratios in Crossing (n, γ) and (γ, n) Reactions. Bull. Rus. Acad. Sci. Phys. **65**, 121–126.
17. Bernard K. 1963. Yield ratios of isomers produced by neutron activation. Phys. Rev. **129**(2), 769–775.
18. Torrel S. and Krane K.S., 2012. Neutron capture cross sections of ^{136,138,140,142} Ce and the decays of ^{137}Ce, Phys Rev. C **86**: 034340.
19. Kyryjenko A.V., Osipenko A.P., Parlag A.M., Pylypchenko V.A., Sabolchiy N.T., Sokolyuk I.V., Khimich I.V., 2006. Investigation of the cadmium nuclei isomers state excitation in the photonuclear reactions. Uzhgorod University Scientific Herald, Series Physics 19, 85–89.
20. Gicking A.M., Takahashi K., Krane K.S., 2019. Neutron capture cross sections of stable Cd isotopes, Eur. Phys. J. A **55**, 52–62.
21. Sehgal M.L., Hans H.S., Gill P.S., 1959. Thermal neutron cross-sections for producing some isomers, Nucl. Phys. **12**(3), 261–268.
22. Palvanov S., 2018. Cross Section of Excitation of Isomer States 81m,gSe in the Reaction (γ, n) and (n, 2n), Journal of Scientific and Engineering Research. **5**(1), 41–45.
23. Nakamura S., Furutaka K., Harada H., Katoh T., 2008. Thermal-Neutron Capture Cross Sections and Resonance Integrals of the ^{80}Se(n,γ)^{81m,g}Se Reaction. Journal of Nuclear Science and Technology **45**(2), 116–122.
24. Koning A.J. and Rochman D., 2012. Modern Nuclear Data Evaluation with the TALYS Code System, NUCLEAR DATA SHEETS, TALYS 1.8, p. 1–94. See also on: www.talys.eu.

CAPTURE NEUTRON CROSS SECTIONS MEASUREMENTS OF RARE EARTH ISOTOPES

Djilkibaev R.M., Khliustin D.V.

Institute for Nuclear Research, Russian Academy of Sciences, Moscow, Russia

denhlustin@gmail.com

Results of TOF measurements for total and capture neutron cross sections on isotope Ho^{165}, conducted on pulsed spallation neutron source RADEX, are presented. Pulse duration of accelerator's proton beam 250 nanoseconds, combined with 100 nanoseconds steps of data acquisition system and 80 nanosecond pulses of (n,γ) detector provided, at 50 meter base of vacuum neutron guide, value of TOF spectrometer resolution 6 nanoseconds per meter.

Measurements were done during linear proton accelerator's work for our task in years 2020 and 2021. Beam parameters were: proton energy 247 and 305 MeV, pulsed proton current 0.01 Amperes, pulse duration 250 nanoseconds, frequency 50 Hz. Average beam power 40 W provided average neutron intensity on Ho^{165} pattern 4000 n/(cm^2sec). Recycle neutrons were cut using cadmium filter.

Experimental results were compared with 4 world neutron databases: ENDF /B-VII.1, JEFF-3.1, JENDL-4.0, and ROSFOND. New experimental data on cross section resonance structure of Ho^{165} were achieved and are presented.

1. Introduction and description of the task

Neutron cross section measurements are necessary both for fundamental and applied nuclear physics. For fundamental purposes it's necessary to investigate detailed resonance structure and resonance parameters in the neutron energy region of resolved resonances, for each partial type of cross section: energy of each resonance, cross section at maximum point, it's gamma and neutron energy width, spin, average energy distance between resonances. This requires high energy resolution of TOF measurements.

For applied purposes the task is to measure partial components of cross section for each isotope in wide energy groups: both in resolved energy area and also in the high energy area of unresolved resonances.

Group cross sections, like ABBN-78, are used as initial data for calculation codes during creating the core of nuclear reactors of different types and radiation shield for them.

Group cross sections are used as coefficients in the system of 28 differential equations, solution of which defines neutron balance in the core of nuclear reactor. Precision for cross section measurements, requested by applied reactor physics, is determined by the share of delayed neutrons: 0.65% for U^{235}, 0.2% for Pu^{239}, 0.42% for fast breeder reactors. Criticality coefficient, critical mass and breeding ratio of fast neutron reactors must be calculated with precision defined by these values. This requires high statistical precision of TOF measurements.

In spite of good development of the fundamental theory of nuclear interactions, energy dependence curves for neutron cross sections with requested precision can be taken only from the experiment.

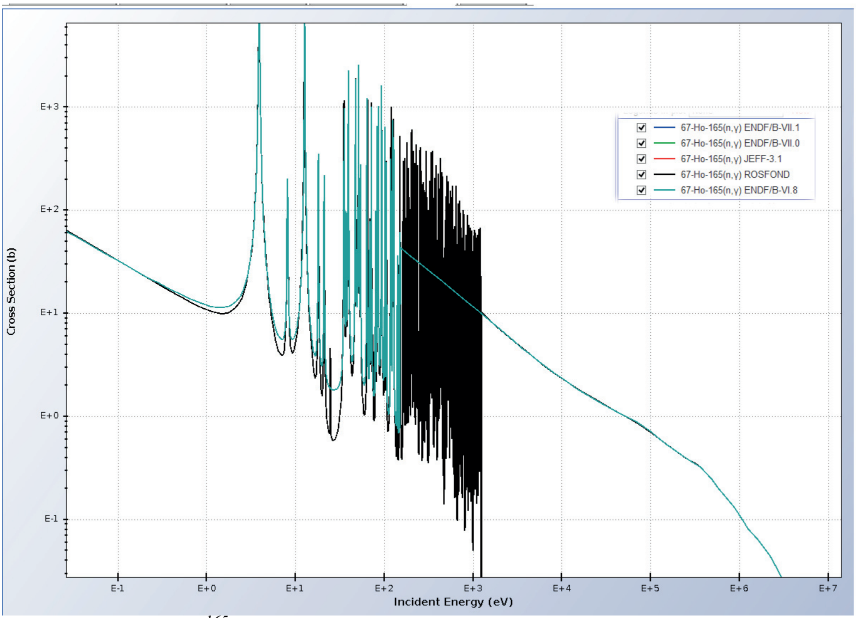

Figure 1. Ho^{165} neutron capture cross section in world data libraries [1].

Ho^{165} capture cross section BNL data [1] are shown of figure 1, in the neutron energy range 0.0253eV<E_n<14 MeV. ENDF/B-VII.1, ENDF/B-VII.0, JEFF-3.1, ROSFOND and ENDF/B-VI.8 data are compared. Upper energy border of resolved resonances in the best world data for Ho165 is 1250 eV. Several disputed resonances were found. Experimental TOF measurements were done to determine, what variant is more true and exact.

2. Experimental equipment

During measurements of Ho^{165} resonance structure, total cross section was measured by 4 Helium-4 based counters SNM-18. Another four counters SNM-18 with 4 atmospheres of He3 were used as monitors of intensity of the pulsed spallation neutron source RADEX. Capture cross section was measured by 40-liter 8-sectional liquid (n,γ) detector of the installation 'INES'. Cadmium beam filter was used in order to cut the recycle neutrons. To determine the background layer of experimental histograms in the low neutron energy area, Mn^{55} beam filter was used.

For determination of the background at high energies, aluminum Al^{27} filter was used. It allowed to determine the background up to neutron energy 140000 eV. Detailed description of the equipment, applied in these measurements, can be found in the sources [2–6].

Accelerator's proton pulse is shown on figure 3. It had duration 250 nanoseconds on half-altitude. Measurements were done during years 2020 and 2021 at the pulsed spallation fast neutron source RADEX, based on tungsten proton beam target of INR RAS 600 MeV proton linac. Metal Ho^{165} radiator pattern was installed inside the 8-sectional liquid (n, γ) detector, at the 50 meter TOF base.

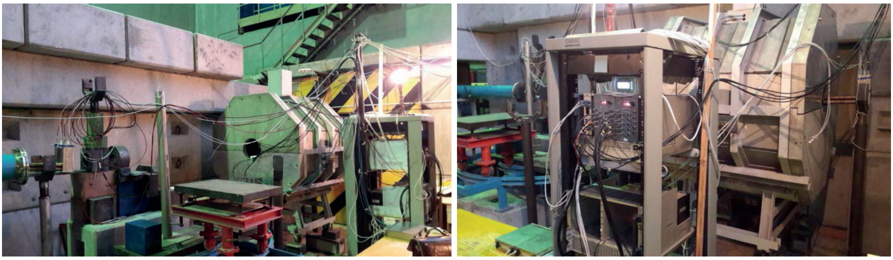

Figure 2. Experimental equipment at 50 meter TOF base, neutrons fly from left to right side.

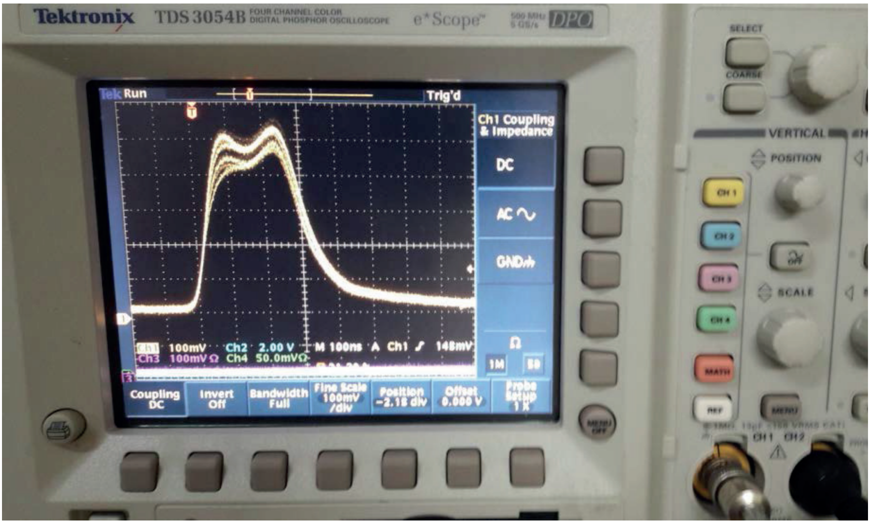

Figure 3. The 250 nanosecond proton beam during turning of the accelerator.

Duration of proton pulse (250 ns), detector's (80 ns) and data accumulation system's (100 ns steps) durations, at 50 meter TOF base provided spectrometer resolution factor: 6 nanoseconds per meter.

3. Analysis of existing world neutron data libraries for Ho^{165}

Comparison of Ho^{165} capture cross section structure in the energy region of resolved resonances showed that ENDF/B-VII.1, ENDF/B-VII.0 and the ROSFOND data for $Ho^{165}(n,\gamma)$ are similar to each other, and have upper border of resolved resonances at neutron energy 1250 eV. Also JEFF-3.1 and ENDF/B-VI.8 are similar to each other and have resolved area up to 152 eV.

Resolution of resonances at higher energies, requires better energy resolution of the spectrometer. At the same time, all differences between data libraries for Ho^{165} are below 152 eV. Between 152 eV and 1250 eV all world data are similar.

As shown on figure 5A, figure 5B and figure 5C, existences of resonances at 24.9 eV; at 75.07 eV; at 120 eV are disputed. Energy position of resonance at 64 eV or at 65.18 eV is disputed. Amplitude of the resonance at 126.9 eV is disputed between four main world data bases of neutron cross sections.

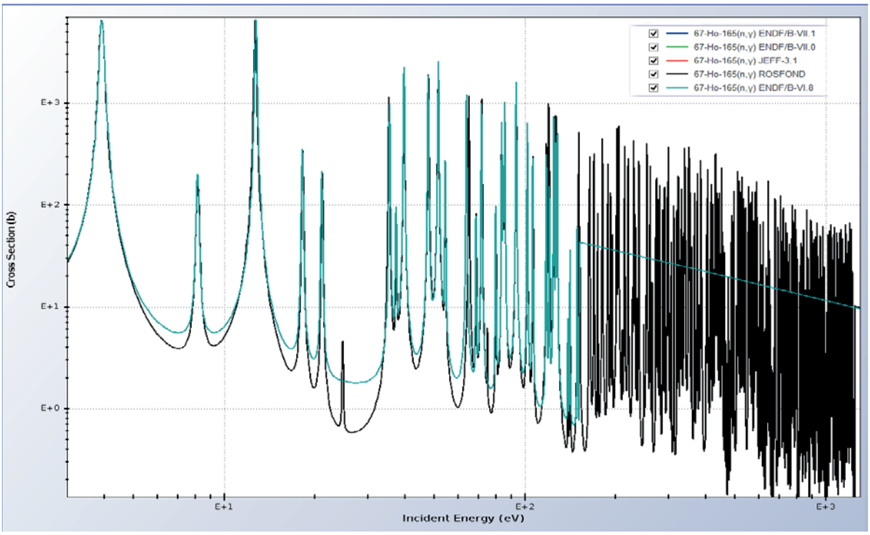

Figure 4. All resolved area of Ho^{165} capture cross section, shown 3 eV<E_n<1250 eV.

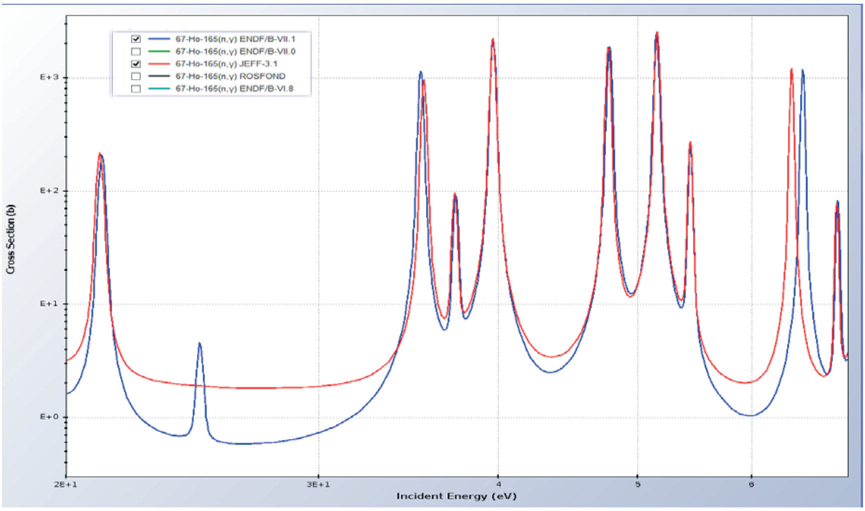

Figure 5A. Ho165 capture cross section debated resonances in the area 20 eV<E_n<70 eV.

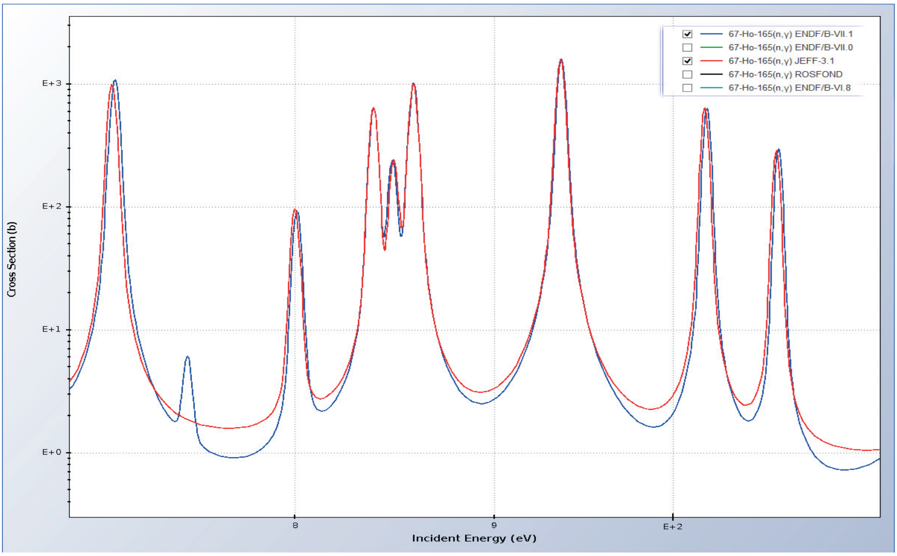

Figure 5B. Ho165 capture cross section debated resonances in the area 70 eV<E_n<120 eV.

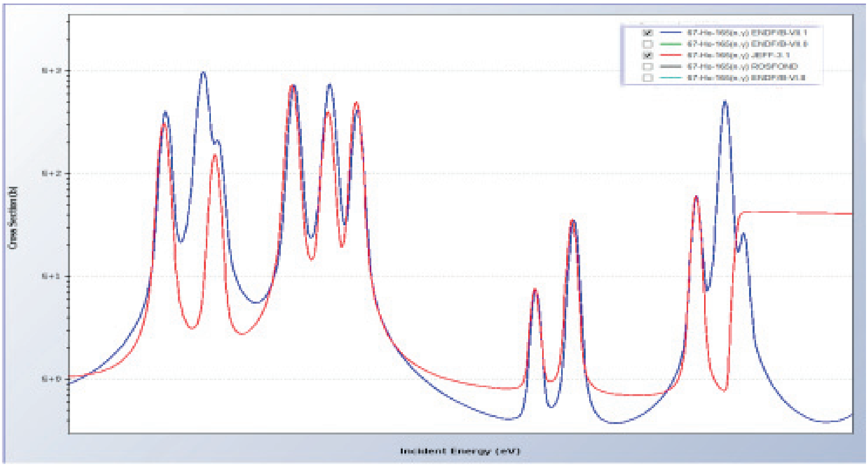

Figure 5C. Ho^{165} capture cross section debated resonances in the area 120 eV<E_n<160 eV.

4. Experimental results for Ho^{165} in the energy area of resolved resonances

Measurements results, collected by data acquisition system, are histogram of 200,000 columns. If we express each channel as one pixel on the computer's screen, wideness of the plot will be equal to 100 screens. We show only some of them.

In figures 6 and 7 we have combined experimental data (upper curve) and BNL ENDF/B-VII.1 data for $Ho^{165}(n,\gamma)$ cross section in barns on right axis, logarithmic scale. We can see that resonances at 24.8 eV, at 65.18 eV and at 75.07 eV exist. Resonance at 64 eV does not exist.

Also we experimentally confirmed, that resonance at 120 eV exists, and that cross section of the 126.9 eV resonance coincidences with the ENDF/B-VII.1 variant. As we can see of figure 8, experimental measurements show good coincidence with the best world data at low and intermediate neutron energies. At high neutron energies, shown on figure 9, resolution 6 nanoseconds per meter of our spectrometer 'INES' based on pulsed neutron source RADEX, allows to distinguish only groups of resonances to get resonance integral value, but some resonances with small energy interval merge.

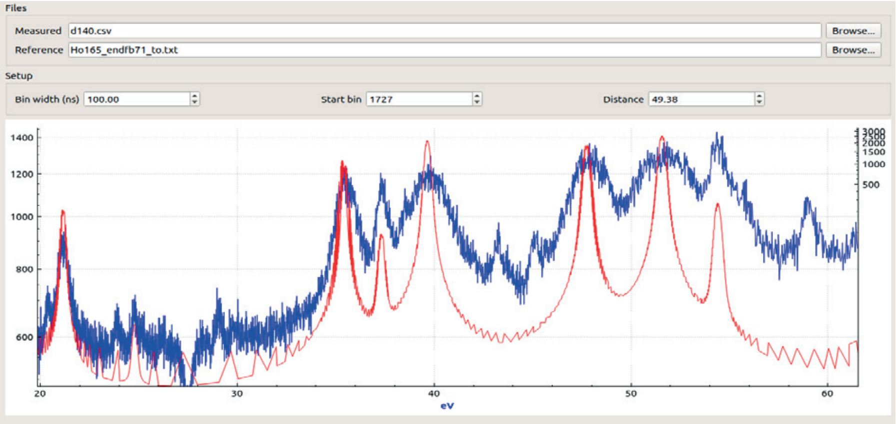
Files
Measured d140.csv
Reference Ho165_endfb71_to.txt
Setup
Bin width (ns) 100.00
Start bin 1727
Distance 49.38

Figure 6. Ho^{165} capture cross section experimental data, 20 eV<E_n<60 eV.

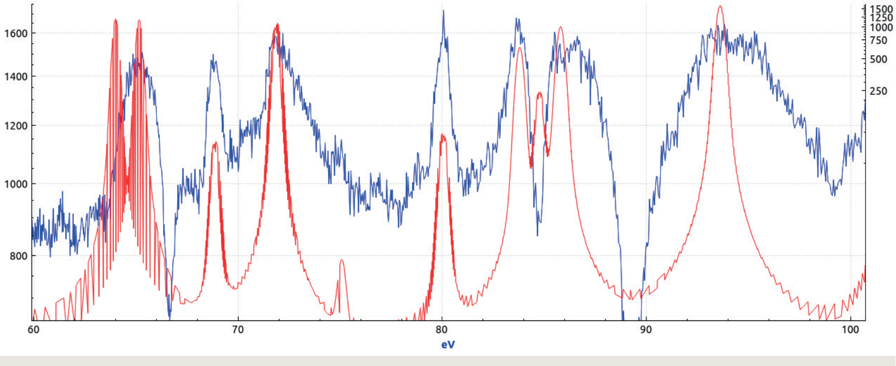

Figure 7. Ho^{165} capture cross section experimental data, 60 eV<E_n<100 eV.

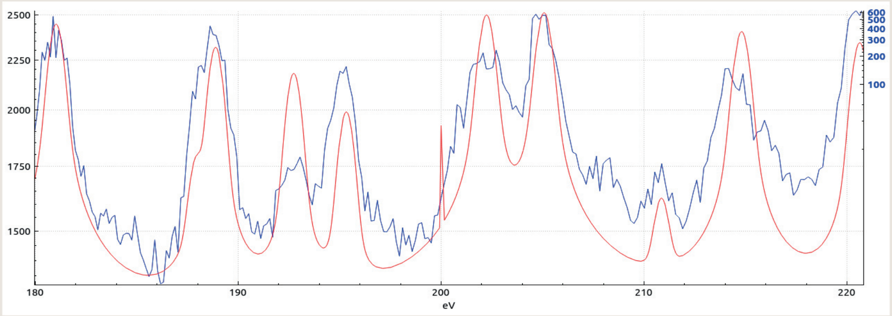

Figure 8. Ho^{165} capture cross section experimental data, 180 eV<E_n<220 eV.

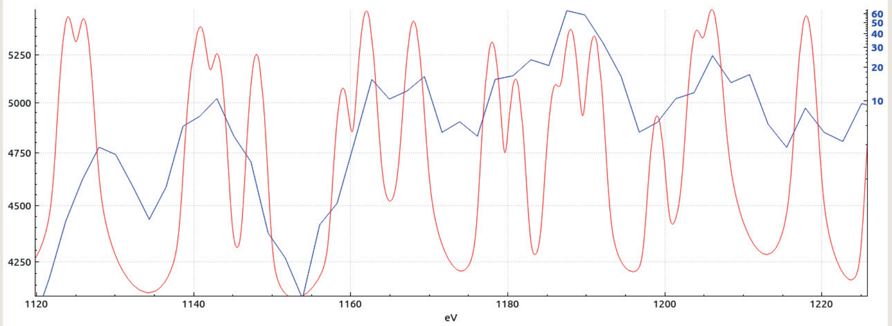

Figure 9. Ho^{165} capture cross section experimental data, 1120 eV<E_n<1200 eV.

Figure 10. Ho^{165} capture cross section experimental data, 1220 eV<E_n<1320 eV.

In figure 10 we can make sure, that our 'INES' spectrometer's resolution allows to observe Ho^{165} resonance structure, approximately, up to the same 1250 eV, as in the best world data for this isotope. Higher than 1250 eV we observe some histogram peaks, which obviously are groups of resonances.

Above 1250 in the best world data begins interval of unresolved resonances for Ho^{165}, although the Doppler-effect allows to distinguish resonances up to higher energy, what is the subject for future measurements with higher energy resolution.

5. High neutron energy area of unresolved resonances

World TOF spectrometers use pulsed neutron sources of different types: based on electron accelerators, on fission reaction, potentially on inertial thermonuclear synthesis and all their spectrums are well known in world literature [7].

In the case of current measurements on RADEX pulsed neutron source, initial fast particles injected into tungsten target are 247 MeV protons. Spectrum of spallation neutron sources, based on proton accelerators, consists of 2 components. Share of cascade neutrons is 8% of all initial neutrons, they have energy up to energy of protons, i.e. 247 MeV.

Another 92% of neutrons are spallation neutrons, they have average spectrum energy 3 MeV and, compared to fission reaction, less amount neutrons at $E_n < 1$ MeV. Share of delayed neutrons is 10^{-5} and background layer by this factor is very small, if compared to fission reaction as a neutron source where 0.23% for Pu^{239} core and 0.7% for U^{235} core are multiplied to ‘1-K’ factor.

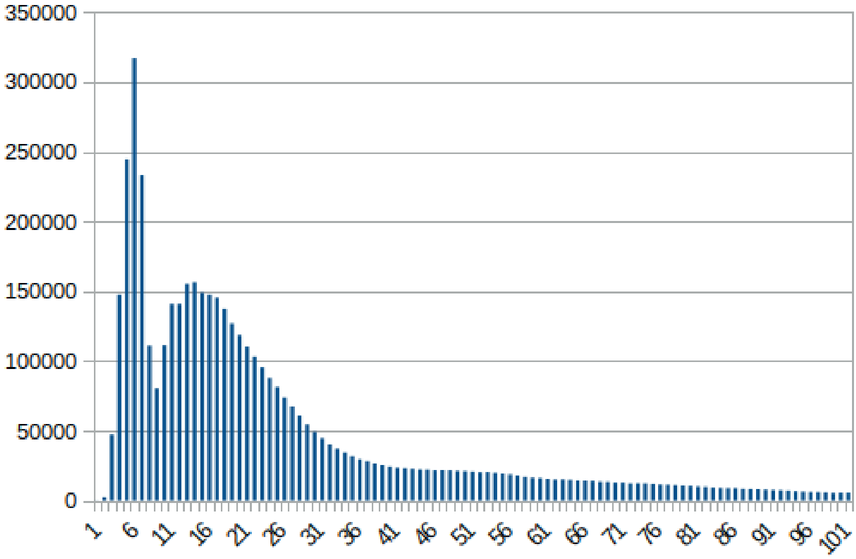

Figure 11. First 100 channels of the histogram.

In the figure 11 first 100 channels of histogram are presented: on horizontal axis channel number with 100 nanoseconds each channel, on vertical axis number of counts per channel. Horizontal axis is especially not transformed into MeV to show, that we distinguish cascade neutrons /first peak/ and spallation neutrons which are second peak, which goes over into Fermi’s ‘1/E’ spectrum at lower neutron energies due to availability of H_2O moderator after the tungsten target of RADEX. Also important factor is high value of counts per channel, around 150,000 in the spallation peak. Considering that accuracy of TOF measurements is proportional to $N^{(-0.5)}$, we can achieve precision of cross section measurements up to 0.5% in high energy interval, which is equal to the share of delayed neutrons in fissile materials, and is enough to improve fast breeder reactor multi-group neutron constants.

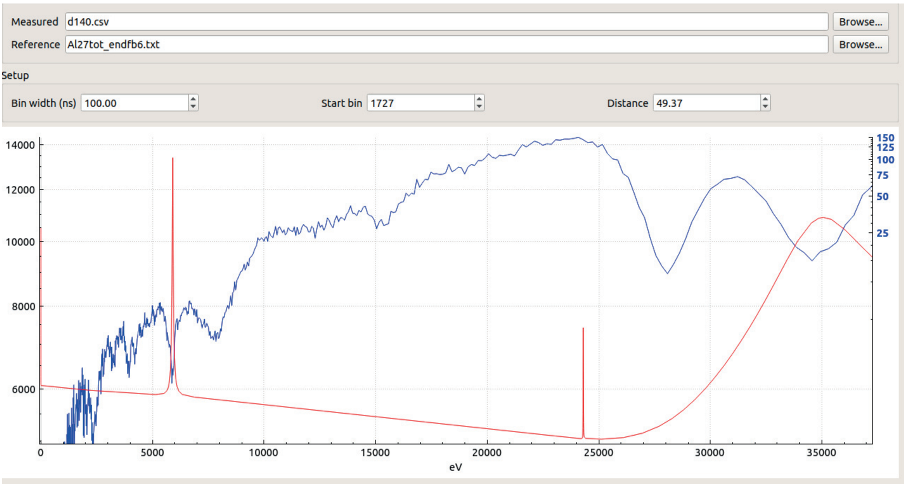

Measured d140.csv

Reference Al27tot_endfb6.txt

Setup

Bin width (ns) 100.00

Start bin 1727

Distance 49.37

Figure 12. Ho^{165} cross section with Al^{27}filter, $0<E_n<37000$ eV.

In figure 12, upper curve is Ho^{165} experimental histogram, counts per channel on the left axis. Lower curve is Al^{27} cross section with barns on right axis, Al^{27} resonances at neutron energy 5900 eV and at 35 keV are exactly observable and were used for calibration of the background curve at these energies. Spectrometer energy resolution allows to make measurements on this energy interval, of neutron group cross sections: both for ABBN-78 which has 28 groups. And for group constants based on ABBN-93, like ABBN-RF, which has 299 energy groups and is being developed in Russia for fast breeder reactor calculations.

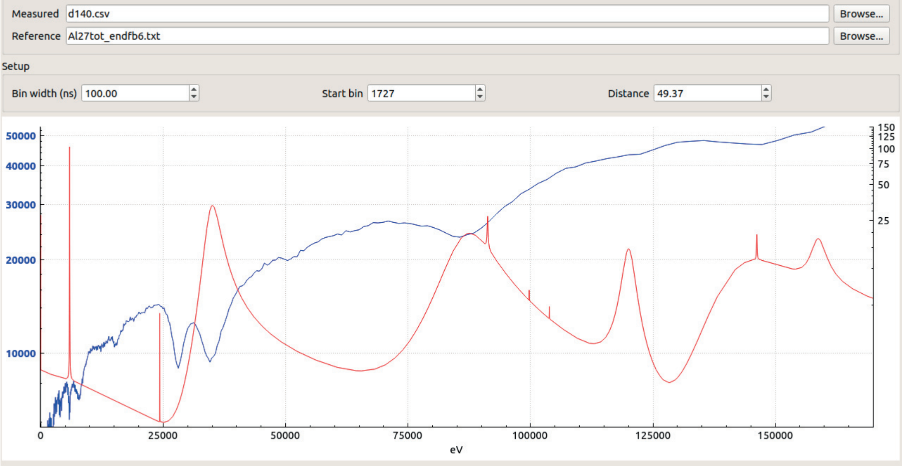

Measured d140.csv

Reference Al27tot_endfb6.txt

Setup

Bin width (ns) 100.00

Start bin 1727

Distance 49.37

Figure 13. Ho^{165} histogram with Al^{27}filter on lower curve, $0<E_n<0.17$ MeV.

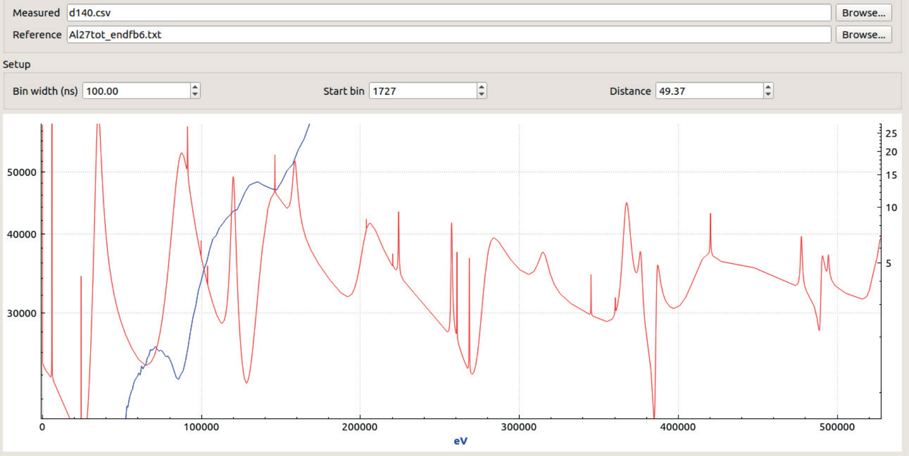

Measured d140.csv

Reference Al27tot_endfb6.txt

Setup

Bin width (ns) 100.00

Start bin 1727

Distance 49.37

Figure 14. Ho^{165} histogram with Al^{27}filter on lower curve, $0<E_n<0.52$ MeV.

Al^{27}(n,total) resonances, used as beam filter, are exactly observable at 5900 eV, at 35000 eV and at 87000 eV on figure 12. Resonance at 147000 eV is also observable on experimental curve on figure 13 and figure 14: counts per channel on left axis for experimental curve, and barns for Al^{27}(n, total) on right axis. This allows to calibrate the background curve in the region 140–170 keV and extrapolate it higher.

Al^{27} resonance at 147000 eV is exactly observable with the scale accepted on figure 14. It's necessary to note, that neutron energy region up to 0.5 MeV includes main part of spectra of fast breeder reactors. Initial fission spectrum has average energy 2 MeV and most probable energy 650 keV. In fast spectrum reactor, due to inelastic and elastic scattering on construction isotopes of the reactor's core, average spectrum energy is shifted to 150 keV. Resonance at 0.14 MeV of Al^{27} proves, that we can measure such energies on the INES TOF spectrometer of RADEX pulsed neutron source. Also, new method for background determination in the MeV region is currently investigated.

6. Conclusion

Ho^{165} capture resonances were experimentally confirmed at 24.8 eV; at 65.18 eV; at 75.07 eV; at 120 eV. Amplitude value for 126.9 eV resonance coincidences with ENDF/B-VII.1 data file.

Energy resolution of the spectrometer INES, based on neutron beam of the INR RAS pulsed neutron source RADEX, allows to observe all resolved area of Ho^{165} capture cross section. Up to 1250 eV, according to the best world data files.

At resolution 6 nanoseconds per meter we achieved separation between cascade neutrons and spallation neutrons. In the 'figure 11' first 100 histogram channels of (n,γ) detector are shown, 100 ns each step, energy of minimum point between components is 14 MeV.

Energy resolution of modern TOF spectrometers allows to make measurements in all practically important neutron energy region: $0.0253 \text{ eV} < E_n < 14 \text{ MeV}$.

It allows to resolve the resonance structure, of all 286 stable nuclides, up to energy, where Doppler-effect makes intersection of neighbor resonances at the temperatures of the core of nuclear reactors and radiation shield.

The same high energy resolution is necessary to make possible measurements in wide energy groups for multi-group neutron reactor constants in the practically important energy area of hundreds keV and several MeV.

7. Literature and cited sources

1. Brookhaven National Laboratory http://www.bnl.gov
2. http://isinn.jinr.ru/past-isinns/isinn-27/presentations/12/Khliustin.pdf
3. http://isinn.jinr.ru/past-isinns/isinn-26/0601PM_session%20A/A19.pdf
4. http://isinn.jinr.ru/past-isinns/isinn-25/24/Hliustin.pdf
5. http://isinn.jinr.ru/past-isinns/isinn-24/3_day/hlustin.pdf
6. http://isinn.jinr.ru/past-isinns/isinn-21/progr-23_05_2013/Hliustin.pdf
7. L.F. Curtiss ‘Introduction to Neutron Physics’. D. van Nostrand Book Company, Inc. Princeton, New Jersey.

GENERATION OF RADIOCARBON C-14 IN THE AIR IN CONDITIONS OF THUNDERSTORMS

V.I. Lyashuk [1, 2, §]

[1] *Institute for Nuclear Research of the Russian Academy of Sciences, Moscow, Russia*

[2] *National Research Center "Kurchatov Institute", Moscow, Russia*

The synthesis of isotopes is possible under conditions of power electric discharge in the atmosphere. It is extremely important to know the radioactive ^{14}C yield under thunderstorm conditions as additional channel of ^{14}C production relative to the main – cosmogenic one. Here we propose the gross model for evaluation of the upper limit of the ^{14}C yield, which creation was simulated for the altitudes up to 15 km. It is presented the results for yield of radioactive isotope ^{41}Ar which synthesis goes along with ^{14}C creation under thunderstorm conditions. It was obtained that the possible thunderstorm mechanisms of ^{14}C creation cannot compete with production originated from cosmogenic sources.

1. Introduction

The main mechanism of radiocarbon ^{14}C creation on the Earth is ensured by cosmogenic irradiation [1] with yield of 472 g-mole/year in the reaction of thermal neutrons with atmospheric nitrogen: ^{14}N(n,p)^{14}C. The generated isotope of ^{14}C is assimilated in the biomass (in the form of dioxide CO_2) and decays within it ($T_{1/2}$ =5700 y) that allows to date the age of the investigated organic materials.

Along with such cosmogenic generation it is possible the synthesis of the isotope ^{14}C under conditions of atmospheric thunderstorm: the electrons in the avalanche of the flash discharge slow down and escape bremsstrahlung *x*-rays; the escaped *x*-radiation produces the flux of photo-neutrons in interactions with air nitrogen in ^{14}N(γ,Xn)-reaction ($E_{\text{threshold}}$ = 10.6 MeV), where Xn – emission of X=1, 2 or more neutrons with maximal cross section at $E_\gamma \approx$ 23 MeV according to JENDL-3.3 nuclear reaction library [2]); the produced neutrons slow down and intensively create the radiocarbon in reaction ^{14}N(n,p) ^{14}C (cross section according to ENDF/B-VIII [3] is given in Fig.1; thermal cross section $\sigma_{np} \approx 1.8$ b).

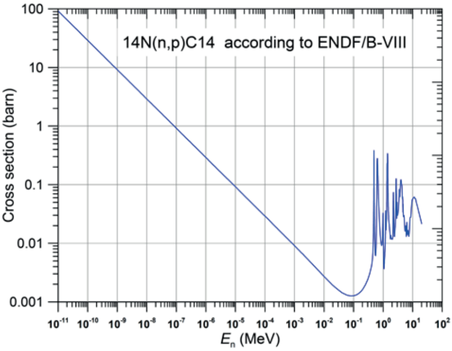

Fig. 1. Cross section of radiocarbon C-14 production in ^{14}N(n,p)^{14}C reaction according to the nuclear reaction library ENDF/B-VIII [3].

[§] lyashuk@itep.ru

As neutron production is the threshold process, the ^{14}C synthesis can be realized only by means the relativistic electrons with energy higher than threshold of the reaction. The spectrum of these energetic electrons was applied as $f \sim \exp(-\varepsilon[\mathrm{MeV}]/7.3)$ [4], where ε is the energy of the runaway electrons (i.e., electrons accelerated in the electric fields; the process was investigated by Wilson [5]). The spectrum spreads up to ~60 MeV ensuring the multiplication of the avalanche under condition of atmospheric electric fields in the thunderclouds. Namely relativistic electrons (E >1 MeV) move in the forward part of the flash discharge producing the low energy electrons in interactions (via ionization of the media), drawing them into the avalanche propagated and accelerated in the thundercloud electric field. In opposite the electrons, which energy decreases below the threshold about 100 eV, fall out the avalanche and form the dynamical equilibrium between involved and lost electrons. In the avalanche the number of low energy electrons N_{le} strongly exceed the relativistic ones N_{re}, the relation is $N_{le}/N_{re} \approx (1.3\times10^4)\times n$, where $n = \rho(H)/\rho(H=0)$ is the relation of the air density $\rho(H)$ at the altitude H to the density at the sea level ($H = 0$) [4]. So, the total charge of flashes is ensured namely by low energy electrons which part in the avalanche decreases for higher altitudes.

2. The Gross Model for Simulation of Isotope Creation

Taking into account the dependence of relation N_{le}/N_{re} from the air density the simulation was realized for the altitudes from the sea level up to the H =15 km (i.e., including approximately the upper charge layer at typical elevation H=(10–14) km) as the most of thunderclouds are distributed at these heights [6]. We use the spherical geometry with centers (the point source of energetic electrons of isotropic f-spectrum) at the indicated altitudes. The spheres are divided into plane layers (of 500 m thickness) with air density corresponding to their heights. In order to exclude the escape of the valuable part of neutrons (which were born in the sphere) the radii were increased up to 30 km. The scheme of geometry is given in the Fig. 2.

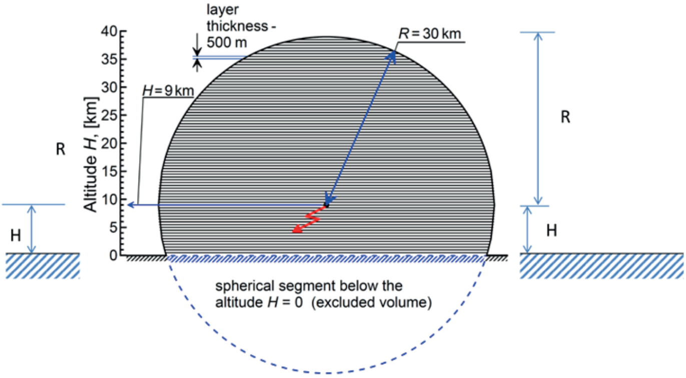

Figure 2. Geometry of the spherical-layers model for simulation of the particles transport and calculation of radiocarbon ^{14}C creation in the air under conditions of thunderstorms lightning (examples for lightning [indicated as arrow] origin at the altitude H = 9 km on the sea level). The spherical segment below the sea level (H =0) is excluded from ^{14}C accumulation.

As a result the percent of the escaping neutrons was lower than 1%. An example of the spectrum of generating neutrons at *H*=10 km is presented in the Fig. 3 (a). The maximum of the obtained spectrum ~ 23 MeV in Fig. 3 (a) is in good agreement with maximum of neutron production in ^{14}N(γ,Xn) reaction in Fig. 3 (b). Such a spherical-plane-layers formalism allowed to specify the yield of relativistic electrons N_{re} in the total $(N_{le} + N_{re})$ – flux that was necessary for correct evaluation of ^{14}C production.

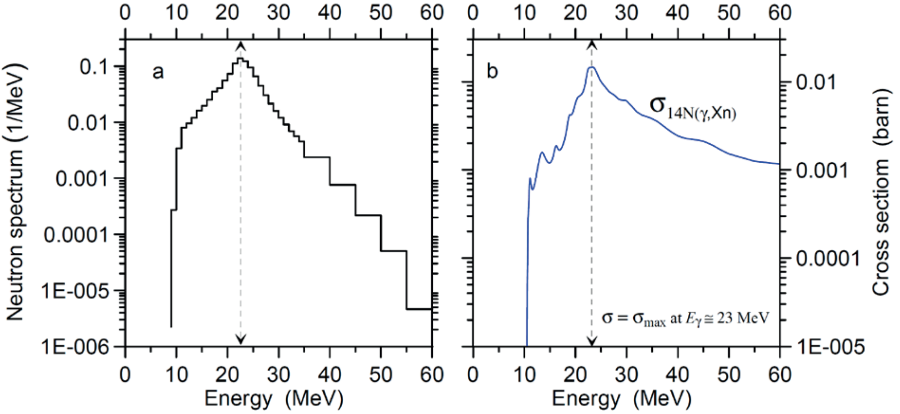

Figure 3. (a) Spectrum of neutrons produced in air under thunderstorm conditions. Generation of neutrons is accounted in the reactions: ^{14}N(γ,Xn), ^{16}O(γ,n) ^{15}O and ^{40}Ar(γ,n)^{39}Ar. (b) Cross section of the main channel of neutron production ^{14}N(γ,Xn) (according to JENDL-3.3 [2]) by bremsstrahlung from electrons under thunderstorm flashes. The spectrum maximum is in good agreement with the maximum cross section of the main channel of neutron production ^{14}N(γ,Xn) (see (a)).

The modeling results (by means the code [7]) for radiocarbon ^{14}C yield depending on the altitude are shown in the Fig. 4.

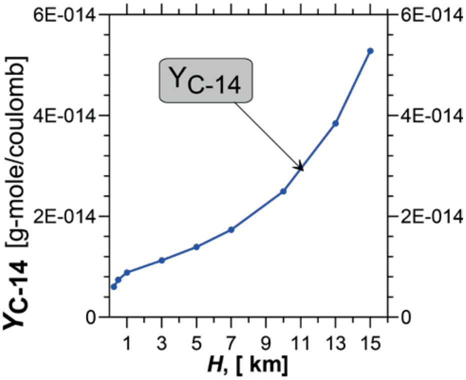

Figure 4. Yield of ^{14}C (in gram-molecules) depending on the altitude *H* (km) above the sea level. The yields correspond to one coulomb flash discharge under thunderstorm conditions.

For the equal discharges the drop of the low energy population N_{le} in the avalanche at increase of the altitude ensures rise of the ^{14}C yield. The results of isotope generation (in gramme-molecules) are normalized on the flash charge 1 coulomb. If the discharge occurs between thunderclouds in the horizontal plane (idealized case) then the normalized yield corresponds the function *Y*(*H*) in the Fig. 4. In common case the discharge goes between some altitudes *H1* and *H2*. The ^{14}C yield is calculated then as the integral along the discharge path and normalized yield will be between *Y(H1)* and *Y(H2)*.

3. The Upper Limit for Radiocarbon C-14 Production. Creation of Argon-41 under Thunderstorm Conditions

Let us evaluate the upper limit of ^{14}C production per year under the flash condition (knowing the number of flashes on the Earth per 1 year – 1.4×10^{9} [8] and considering that the average flash charge is ~ 20 coulombs [6] and mean $H = 7$ km [6]): then production during the year is $Y_{\text{C-14}} = 1.7\times10^{-14}\times20\times1.4\times10^{9} \simeq 5\times10^{-4}$ (g-mole/year) for the relation *R1*.
Creation of neutron flux ensures simultaneously also the production of ^{41}Ar isotope by the reaction ^{40}Ar(n,γ)^{41}Ar with significant cross section (see Fig.5).

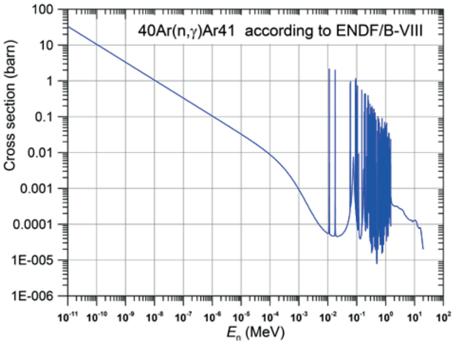

Figure 5. Cross section (barn) of the ^{40}Ar(n,γ)^{41}Ar reaction according to ENDF/B-VIII library.

In the similar way (as ^{14}C production) it was obtained the yield of radioactive ^{41}Ar (produced at neutron activation of the main argon isotope: ^{40}Ar(n,γ)^{41}Ar) – see Fig. 6. The upper limit of ^{41}Ar production per mean flash (20 coulombs) will be: $Y_{\text{Ar-41}} = 2.9\times10^{-17}\times20 \simeq 5.8\times10^{-16}$ (g-mole).

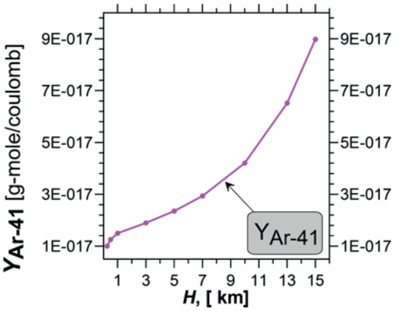

Figure 6. Yield of ^{41}Ar (in gram-molecules) depending on the altitude *H* (km) above sea level. The yields correspond to one coulomb flash discharge under thunderstorm conditions.

The curves of yields for ^{14}C and ^{41}Ar are very similar as: the main yield occurs at the thermal energy; $(N_{le}/N_{re}) \propto n$. As a result, $Y_{C-14,\,Ar-41} \propto \sigma_{C-14,\,Ar-41} \times n$. Note that cross sections for ^{14}C and ^{41}Ar production $\sigma \propto 1/\boldsymbol{v}$ (at $E < 2\times10^{-2}$ MeV for ^{14}C and $E < 1\times10^{-4}$ MeV for ^{41}Ar; $\boldsymbol{v}$ – neutron velocity).

The obtained upper limits for yields of ^{14}C and ^{41}Ar were evaluated basing on the relation $N_{le}/N_{re} \approx 1.3\times10^4$. According to the alternative model of electron avalanche this relation is more than factor of order larger: $N_{le}/N_{re} \approx 3\times10^6$ [9]. In case of this relation the yields for ^{14}C and ^{41}Ar will be smaller in ($3\times10^6/1.3\times10^4$) times. Taking into account two alternative theories, then for evaluation of the possible upper limits of ^{14}C and ^{41}Ar creation we have to use the first N_{le}/N_{re} relation.

Under thunderstorm condition the isotope ^{41}Ar is created in the atmosphere simultaneously with ^{14}C. Owing to relevant ^{41}Ar decay characteristics ($T_{1/2}$ = 109.34 m, β^-(100%)) it will be attractive to consider this isotope as an appropriate tracer of the radiocarbon ^{14}C generation. But the detection of such low and changing ^{41}Ar concentration is a very complicated task. In spite of debugged technique of ^{41}Ar monitoring (for example on the accelerators [10] and reactors) the detection of ^{41}Ar may be possible in cases of significantly larger atmospheric discharge phenomena (may be when population of neutrons reaches ~ 1E+15 as in case of large "terrestrial" gamma flashes [11]).

4. Conclusion

It was considered the synthesis of radiocarbon ^{12}C creation under the condition of thunderstorm flashes. We propose the gross model to evaluate the upper limit of isotope ^{14}C creation. The synthesis of ^{14}C is ensured by relativistic electrons in the flash avalanche. The yield of relativistic electrons in the total number of electrons is strongly model dependent. In case of $N_{le}/N_{re} \approx 1.3\times10^4$ (relation of low energy to relativistic electrons number) [4], the upper limit of ^{14}C creation on the Earth per year during the thunderstorm is evaluated as 5×10^{-4} (g-mole/year). Compared to ^{14}C isotope creation from the cosmogenic radiation (472 g-mole/year [1]) the production at the thunderstorm gives about 1×10^{-4} %. In case of realization of the alternative avalanche model [9] the relative number of relativistic electrons in the avalanche will be in two orders smaller (according to this theory the relation $N_{le}/N_{re} \approx 3\times10^6$) and ^{14}C synthesis on the Earth during the thunderstorm per year will be in two orders smaller too.

It was also shown [12] that dependence of bremsstrahlung yield (the bremsstrahlung is responsible for generation of neutron flux in (γ,n) reaction and generation of ^{14}C under neutron irradiation) on the air density (with change of the altitude) is very small.

Acknowledgements

We are grateful to I.N. Borzov and Yu.S. Lutostansky for helpful and useful discussion.

References

[1] Roth R., Joos F. (2013) *Clim. Past.* v.**9**, p.1879.

[2] K. Shibata, T. Kawano, T. Nakagawa, et al.,: "Japanese Evaluated Nuclear Data Library Version 3 Revision-3: JENDL-3.3," *J. Nucl. Sci. Technol.* **39**, 1125 (2002).

[3] Brown, D.A., Chadwick, M.B., Capote, R.,et al., 2018. ENDF/B-VIII.0: The 8th major release of the nuclear reaction data library with CIELO-project cross sections, new standards and thermal scattering data. Nucl. Data Sheets **148**, 1–142. https://doi.org/10.1016/j.nds.2018.02.001

[4] Dwyer J.R., Babich L.P. (2011) *J. Geophys. Res.*, v.**116**, p.A09301.

[5] Wilson C.T.R. (1925) *Proc. Cambridge Philos. Soc.*, v.**22**, p.534–538.

[6] Rakov V.A., Uman M.A., *Lightning: Physics and Effects* (2005) Cambridge Univ. Press.

[7] MCNPX User's Manual (2008) ed Denise B. Pelowitz LA-CP-07-1473.

[8] Christian H.J., et al. (2003) *J. Geophys. Res.* v.**108**, p**.**ACL 4–1.

[9] Gurevich A.V., Zybin K.P., Medvedev Yu.V. (2006), *Phys.Lett.* A v.**349.** p**.**331–339.

[10] Cicoria G., Cesarini F., Infantino A., Vichi S., Zagni F., Marengo M., (2017). Characterization of ^{41}Ar production in air at a PET cyclotron facility. Modern Phys. Lett. A **32** (17), 1740014-1 - 1740014-14.

[11] Babich L.P., (2006) Generation of neutrons in giant upward atmospheric discharges *JETP Letters*, v.**84**, p.285.

[12] Lyashuk V.I. (2021), arXiv: 2011.07417.

Analysis of Scattering Phase Shifts for Two-Cluster Systems

M. Odsuren[1], G. Khuukhenkhuu[1], A. Sarsembayeva[2], S. Davaa[1], Ch. Saikhanbayar[1],
T. Munkh-Erdene[1], J. Batmyagmar[1], N. Battsooj[1]

[1]School of Engineering and Applied Sciences and Nuclear Research Center, National University of Mongolia, 14201, Ulaanbaatar, Mongolia

[2]Department of Physics and Technology, Al-Farabi Kazakh National University, Almaty 050040, Kazakhstan

**e-mail: odsuren@seas.num.edu.mn*

I. INTRODUCTION

Study of resonances in the scattering problem of light nuclei has been carried out using various methods, one of which is the complex scaling method [1–2]. It is possible to investigate the resonance contributions and to obtain a deep understanding of resonance structure by separation of a scattering quantity. Suzuki et al. [3] showed that scattering phase shifts can be calculated from the continuum level density, which is expressed using the complex scaled Green's function.

We apply the complex scaling method to the calculation of scattering phase shifts and extract the contributions of resonances in a phase shift. The decomposition of the phase shift is shown to be useful in understanding the roles of resonant and non-resonant continuum states. We apply this method to the two-body alpha+nucleon systems. We discuss the explicit relation between the scattering phase shifts and complex-energy eigenvalues in the complex scaling method via the continuum level density. The results provide us with deeper understanding of the role of resonant states characterized by the widths described as an imaginary part of the eigen-energy.

II.THEORETICAL FRAMEWORK

A. Complex Scaling Method

In the complex scaling method the relative coordinate is rotated as $r \longrightarrow re^{i\theta}$ in the complex coordinate plane. Therefore, the *Schrödinger* equation

$$\hat{H}|\Psi\rangle = E|\Psi\rangle \tag{1}$$

is rewritten as

$$\hat{H}(\theta)|\Psi^{\theta}\rangle = E^{\theta}|\Psi^{\theta}\rangle, \tag{2}$$

where $\hat{H}(\theta)$ and Ψ^{θ} are the complex scaled Hamiltonian and wave function, respectively. The θ is scaling angle being a real number, $U(\theta)$ operate on a function Ψ^{θ}, that is

$$\Psi^{\theta} = U(\theta)\Psi(r) = e^{\frac{3}{2}i\theta}\Psi(re^{i\theta}). \tag{3}$$

The eigenvalues and eigenstates are obtained by solving the complex scaled *Schrödinger* equation Eq.(2). The eigenvalues of resonance states are found as $E^{\theta} = E_r - i\Gamma_r/2$, where E_r is resonance energy and Γ_r is width of the resonant state. More detailed explanation of the complex scaling method is given in Ref.[2].

To solve the eigenvalue problem of Eq. (2), we employ the Gaussian basis functions given as:

$$\phi_i(r) = N_l(b_i)r^l \exp\left(-\frac{1}{2b_i^2}r^2\right)Y_{lm}(\hat{r}), \tag{4}$$

where the range parameters are given by a geometric progression as $b_i = b_0\gamma^{i-1}$; $i = 1 \cdot\cdot, N$, and $N_l(b_i)$ is the normalization factor. We take $N = 60$ and employ the optimal values of $b_0$and γso as to obtain stationary solutions. All results are obtained with $\theta = 15°$.

B. Continuum Level Density and Phase Shift

The continuum level density $\Delta(E)$ is given as

$$\Delta(E) = -\frac{1}{\pi}\mathrm{Im}\{\mathrm{Tr}[G^{+}(E) - G_0^{+}(E)]\}, \tag{5}$$

where

$$G^{+}(E) = (E + i\epsilon - H)^{-1},$$
$$G_0^{+}(E) = (E + i\epsilon - H_0)^{-1}$$

are the full and free Green's functions, respectively. In this study, the Hamiltonian H and H_0 are transformed using the complex scaling method.

The continuum level density is related to the scattering phase shift $\delta(E)$, it can be expressed in the following form in the single channel case:

$$\Delta(E) = \frac{1}{\pi}\frac{d\delta(E)}{dE}. \tag{6}$$

Using this relation, we can obtain the phase shift as a function of the eigenvalues in the complex scaled Hamiltonian by integrating the continuum level density.

When we expand the wave functions in terms of the finite number N of the basis states, the discretized eigenstates are obtained with number N and the level density can be approximated as in [4]:

$$\Delta(E) \approx \Delta_\theta^N(E) =$$
$$-\frac{1}{\pi}\mathrm{Im}\left\{\sum_{b=1}^{N_b}\frac{1}{E+i0-E_b} + \sum_{r=1}^{N_r^\theta}\frac{1}{E-E_r^{res}+\frac{i\Gamma_r}{2}} + \sum_{c=1}^{N_c^\theta}\frac{1}{E-\epsilon_c^r+i\epsilon_c^i} - \sum_{k=1}^{N}\frac{1}{E-\epsilon_k^{0r}+i\epsilon_k^{0i}}\right\}, \tag{7}$$

where $N = N_b + N_r^\theta + N_c^\theta$ is the total number of N_b (bound states), N_r^θ (resonance states) and N_c^θ (continuum states) solutions. Then, we can obtain the phase shift:

$$\delta_\theta^N(E) = N_b\pi + \sum_{r=1}^{N_r^\theta}\left\{-\cot^{-1}\left(\frac{E-E_r^{res}}{\Gamma_r/2}\right)\right\} + \sum_{c=1}^{N_c^\theta}\left\{-\cot^{-1}\left(\frac{E-\epsilon_c^r}{\epsilon_c^i}\right)\right\} - \sum_{k=1}^{N}\left\{-\cot^{-1}\left(\frac{E-\epsilon_k^{0r}}{\epsilon_k^{0i}}\right)\right\}, \tag{8}$$

where $E \geq 0$. When we define δ_r, δ_c and δ_k as

$$\cot\delta_r = \frac{E_r^{res}-E}{\Gamma_r/2},\ \cot\delta_c = \frac{\epsilon_c^r-E}{\epsilon_c^i},\ \cot\delta_k = \frac{\epsilon_k^{0r}-E}{\epsilon_k^{0i}}, \tag{9}$$

respectively, we can write the phase shift as

$$\delta_\theta^N(E) = N_b\pi + \textstyle\sum_{r=1}^{N_r^\theta}\delta_r + \sum_{c=1}^{N_c^\theta}\delta_c - \sum_{k=1}^{N}\delta_k. \tag{10}$$

The geometrical indications for δ_r, δ_c and δ_k are given for two energy cases, larger or smaller than the real parts of the eigen-energies E_r, ε_c and ε_k, as shown in Fig. 1. The phase shift δ_r for the resonances is the angle of the r-th resonant pole measured at the energy E on the real energy axis. At $E = E_r^{res}$, we have $\delta_r = \pi/2$ for every resonant pole. In addition, $\delta_r = \tan^{-1}(\Gamma_r/2E_r^{res}) > 0$ at $E = 0$ and $\delta_r = \pi$ at $E = \infty$, for each resonance. Similarly phase shifts from continuum terms including the asymptotic part, δ_k, are given by the angles of the discretized continuum energies. At $E = \infty$, the continuum terms of the phase shifts go to $-(N_b + N_r^\theta)\pi$ because of the relation $N = N_b + N_r^\theta + N_c^\theta$.

III. RESULTS AND DISCUSSIONS

In our previous works [5-6], we proposed a new method to get information of the pole position of the virtual state applying the continuum level density, the phase shift obtained in the complex scaling method. Based on the proposed method, we discuss the contribution of each state into the scattering phase shifts calculating the decomposed phase shifts. In this work, we choose two-body two mirror nuclei for calculation of decomposed phase shifts. The KKNN (Kanada, Kaneko, Nagata, Nomoto) [7] potential is used for the effective nucleon-nucleon interaction of α+n and α+p systems.

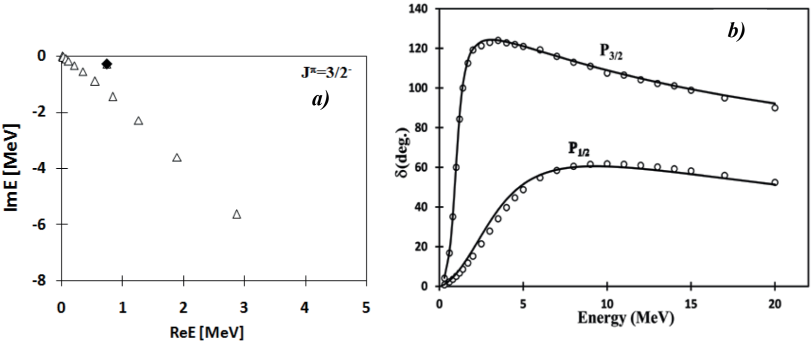

Fig. 1. In the left hand side: the calculated eigenvalue distribution on the complex energy plane for $J^\pi = 3/2^-$ of ^{5}He. In the right hand side: the scattering phase shifts of ^{5}He at the $J^\pi = 3/2^-$ and $1/2^-$ states for $\theta = 20^0$. The calculated phase shifts are displayed as solid curves and the experimental data are given by open circles.

At the first step, we calculate the scattering phase shifts and compared it with measured data. The calculated eigenvalue distribution on the complex energy plane and scattering phase shifts for the low-lying $3/2^-$ and $1/2^-$ states of α+n system are shown in Fig. 1. We can see from Fig. 1, our calculated scattering phase shifts well reproduce the measured data [8] in the low-lying states. The same trend is obtained on its mirror α+p system, too.

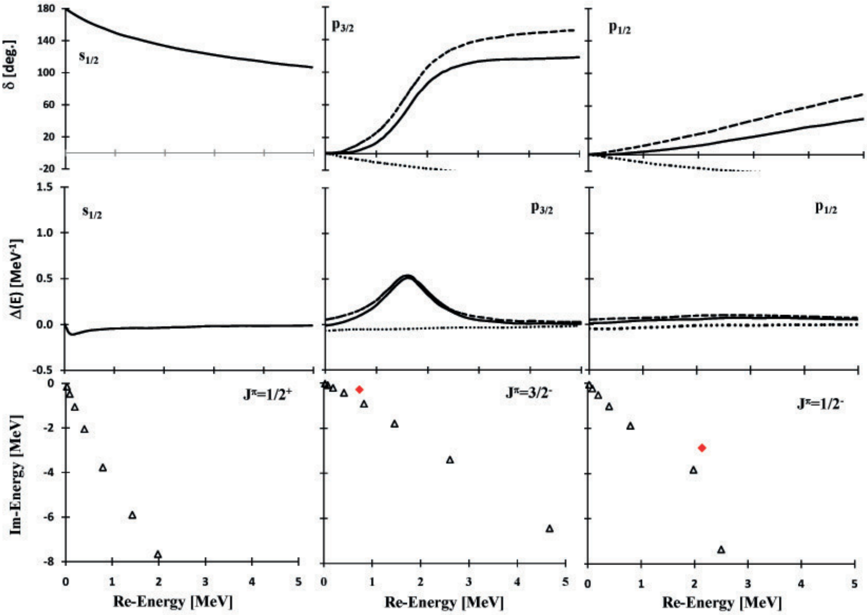

Fig. 2. Upper panel: the decomposition of scattering phase shifts of α–p (^{5}Li) system for the $J^\pi = 1/2^+; 3/2^-; 1/2^-$ states and middle panel: the decomposition of continuum level densities. The dashed and dotted lines represent the contributions of resonance and continuum terms, respectively. The solid lines display total scattering phase shifts or total continuum level densities. Lower panel: the distributions of eigenvalues are displayed in the complex energy plane. The diamond displays the resonance pole.

In the next step, we calculate the decomposed phase shifts by selecting the energy states and analyze its contribution into the scattering phase shifts. In Fig. 2, the energy eigenvalue distribution on the complex energy plane, decomposed phase shifts and continuum level density for the $J^\pi=3/2^-$ state of ^{5}Li system is shown. The resonance phase shift of $3/2^-$ increases rapidly due to the small decay width. Although $1/2^-$ has a larger width, the phase shift of $1/2^-$ shows a clear resonance behavior beyond $\pi/2$. The continuum phase shifts of both states are very similar. This trend seems due to the same p-wave scattering and a small effect of the $\ell \cdot s$ force to the background states. The property of the scattering phase shifts is determined from a sum of resonance and continuum terms. Therefore, the observed resonances depend on not only resonant states as poles but also the contribution from the non-resonant continuum states.

IV. SUMMARY

Applying Green's function, we can precisely extract the contributions of resonance and continuum terms from the total continuum level density. This analysis clarifies the physical role of resonances and non-resonant continuum states in the observables. We have also shown the application of the complex scaling method to the calculation of the decomposed continuum level density and the decomposed phase shifts. The role of resonance poles on the phase shifts and continuum level densities are discussed.

REFERENCES

1. S. Aoyama, T. Myo, K. Kato, and K. Ikeda, Prog. Theor. Phys. **116**, 1 (2006).
2. T. Myo, Y. Kikuchi, H. Masui, and K. Kato, Prog. Part. Nucl. Phys. **79**, 1 (2014).
3. R. Suzuki, T. Myo, and K. Kato, Prog. Theor. Phys. **113**, 1273 (2005).
4. M. Odsuren, K. Katō, M. Aikawa, T. Myo, Phys. Rev. C **89**, 034322 (2014).
5. M. Odsuren, G.Khuukhenkhuu, A.T. Sarsembayeva, N. Amangeldi, K. Katō, Indian Journal of Physics, 1 (2021).
6. M. Odsuren, Y. Kikuchi, T. Myo, H. Masui, K. Katō, Phys.Rev. C **99**, 034312, (2019).
7. H. Kanada, T. Kaneko, S. Nagata, M. Nomoto, Prog. Theor. Phys. **61**, 1327 (1979).
8. B. Hoop Jr., H.H. Barschall, Nucl. Phys. **83,** 65 (1966); Th. Stammbach, R.L. Walter, Nucl. Phys. A **180**, 225 (1972); D.C. Dodder et al., Phys. Rev. C **15**, 518 (1977); S. Ali, A.A.Z. Ahmand, N. Ferdous, Rev. Mod. Phys. **57**, 923 (1985).

FAST PROTON INDUCED PROCESSES ON NATURAL INDIUM

C. Oprea[1, 2] *, A. Mihul[2,3], I. Oprea[1], S. Zgura[4], M. Potlog[4], A. Neagu[4]

[1] *Joint Institute for Nuclear Research, Dubna (JINR), 141980 Russia*
[2] *Romanian Scientific Research Agency, Bucharest (ANCS), Romania*
[3] *European Center for Nuclear Research (CERN), 1211 Geneva 23, Switzerland*
[4] *Institute for Space Sciences, 077124 Magurele, Romania*

**E-mail: coprea2005@yahoo.co.uk*

Proton induced reactions with energies from threshold up to 25 MeV were investigated. Contributions of nuclear reaction mechanisms for each process are evaluated theoretically. For the protons up to 4–8 MeV, the compound processes are dominant and they are described by using a Hauser-Feshbach statistical approach. Contribution of direct mechanism to the cross section was determined using DWBA approach and pre-equilibrium processes by exciton model. At higher energies direct and pre-equilibrium mechanisms cannot be neglected. Parameters of optical potential and level density for incident and emergent channels were also extracted. The isotopes' production was analysed using cross sections calculated with Talys. Cross-section uncertainties provided by variation of optical potential parameters were also evaluated.

INTRODUCTION

Nuclear reactions induced by fast charged particles (protons, alpha particles, deuterons, etc) are for a long time investigated at JINR Dubna basic facilities. These processes represent an efficient tool for fundamental researches of structure of atomic nuclei and nuclear reactions mechanism [1]. Reliable nuclear data of charged particle nuclear reactions are necessary as well for a large number of applications like neutron sources, proton therapy, isotopes production, transmutation and energy projects, accelerator physics and astrophysics [2–4].

In the present work ^{113}Sn($p,2n$)^{112}Sn and ^{115}In(p,n)^{115}Sn nuclear reactions induced by fast neutrons with energies starting from threshold up to 25 MeV were investigated. Cross sections, Tin isotopes production and cross sections uncertainties were evaluated.

Indium is a chemical element with atomic $Z = 49$ and two natural stable isotopes, ^{113}In and ^{115}In. Abundance of ^{113,115}In nuclei are 4.29% and 95.71%, respectively. By interaction of Indium with fast protons followed by emission of gamma quanta and neutrons, Tin isotopes are obtained. This nucleus has a magic number of protons ($Z = 50$) and therefore Tin has ten natural isotopes with atomic masses $A = 112, 114, 115, 116, 117, 118, 119, 120, 122, 124$, and abundances 0.96%, 0.66 %, 0.35 %, 14,30%, 7.61%, 24.03%, 8.58 %, 32.85%, 4,72 %, 5,94 %, respectively [5, 6].

THEORETICAL BACKGROUND

Cross sections of ^{113}Sn($p,2n$)^{112}Sn and ^{115}In(p,n)^{115}Sn reactions and Tin isotopes production in the fast protons were evaluated with Talys computer code.

Talys is a free software working under Linux dedicated to structure of atomic and nuclear reaction mechanisms calculations. In this code are implemented all nuclear reactions mechanisms, a nuclear database for a large number of stable nuclei and isotopes containing spin, parity, energies, time of life of nuclear levels, parameters of density levels models and of Woods-Saxon potential with all components (volume, surface, spin-orbit, each with real and imaginary part) [7].

In Talys calculations all nuclear reaction mechanisms are enabled. Compound processes are described in the frame of Hauser-Feshbach approach [7, 8], exciton model is used for pre-equilibrium ones [7, 9], and Distorted Wave Born Approximation in the case of direct processes [7, 10].

Tin isotope production was modeled using cross section from Talys and charged particles energy loss in the target with finite given dimensions.

RESULTS AND DISCUSSIONS

Cross sections, astrophysical rates, production of Tin isotopes and other were evaluated for ^{113}Sn($p,2n$)^{112}Sn and ^{115}In(p,n)^{115}Sn processes with fast protons from threshold up to 25 MeV. For each reaction, contributions to the cross section of the nuclear reaction mechanisms and of the discrete and continuum states of residual nuclei were determined. Theoretical evaluations were compared with experimental data from literature. Production of Tin isotopes was modeled considering a target of natural Tin with transversal surface 1 cm^2. Protons maximum energy was 35 MeV and in this case thickness is about 3 mm (protons remain in the target). Number of ^{113}In nuclei is about 5 ×10^{20} and of ^{115}In is 1.1×10^{22}. Irradiation time is 24 h and the protons intensity was chosen 1 μA and 100 μA, respectively.

^{113}In(p,2n)^{112}Sn reaction. Production of ^{112}Sn

Tin isotope ^{112}Sn was obtained in the ^{113}In(p,2n)^{114}Sn reaction. Cross section energy dependence of ^{113}In(p,2n)^{114}Sn process with fast protons starting from the threshold up to 25 MeV is represented in Fig. 1.

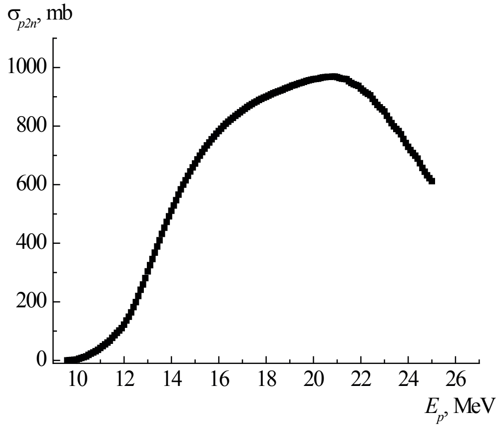

Fig. 1. Cross section of ^{113}In(p,2n)^{112}Sn reaction.

Contributions to the cross section of the nuclear reaction mechanisms and of discrete and continuum states of the residual nucleus were determined. Talys evaluations showed that "pure" compound and multistep compound processes are dominant and the contribution of other reaction mechanisms can be neglected for incident protons up to 25 MeV. Discrete states are important near the threshold ($Q = -9.56$ MeV) and up to around 12 MeV. At higher proton energies, cross section is given mainly by continuum states.

Cross section of ^{113}In($p,2n$)^{112}Sn reaction has enough large values but there are no experimental data in the literature. Computer simulation of natural Tin interaction with 35 MeV protons for the ^{112}Sn production given by ^{113}In($p,2n$) process contributes much greater than 1 ppm for 1 μA and 100 μA currents. Results are represented in Fig. 2.

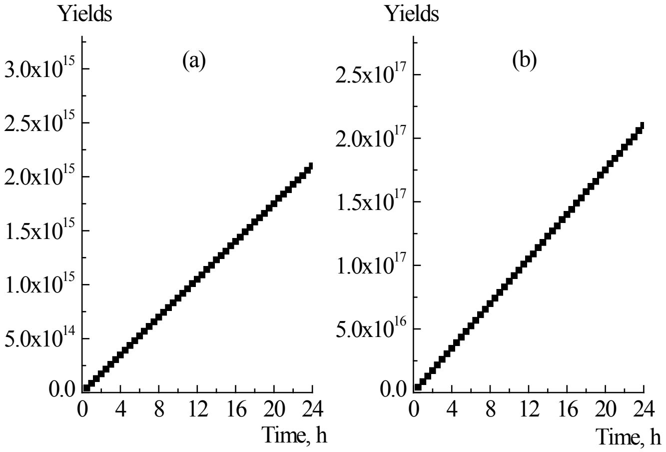

Fig. 2. Production of ^{112}Sn in ^{113}In(p,2n). Curent: a) – 1 μA; b) – 100 μA.

^{115}In(p,n)^{115}Sn reaction. Production of ^{115}Sn

In the interaction of fast protons with natural In, the Tin isotope with mass number 115 can be formed in ^{115}In(p,n)^{115}Sn reaction. Cross sections of ^{115}In(p,n)^{115}Sn process with protons, starting from threshold up to 25 MeV are presented in Fig. 3.

In Fig. 3*a* contributions of nuclear reaction mechanisms to the cross section are represented. Compound processes are dominant in the whole interval of incident protons energy (curve 3). Direct processes (curve 1) have very low values. Pre-equilibrium mechanism has higher values than direct processes but much lower value than compound ones in 10–15 MeV region. Usually, in this range, at other nuclear reactions, contribution of the compound processes is replaced by the pre-equilibrium mechanism.

In Fig. 3*b* cross section of ^{115}In(p,n)^{115}Sn reaction is represented as the sum corresponding to the discrete (curve 1) and continuum (curve 2) states of residual nucleus. Contribution of discrete states has very low values and practically the cross section of (p,n) process (curve 3) coincides with the cross section given by continuum states (curve 2). Curve 4 from Fig. 3*a* is practically the same with curve 3 from Fig. 3*b*.

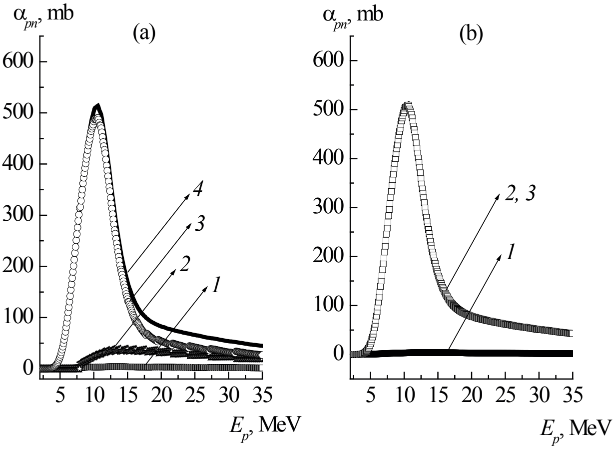

Fig. 3. Cross section of ^{115}In(p,n)^{115}Sn. Mechanisms : a) 1 – direct; 2- pre-eqiulibrium; 3 – compound; 4 – sum of 1, 2, 3. States: b) 1 –discrete; 2 – continuum; 3 – sum of 1, 2.

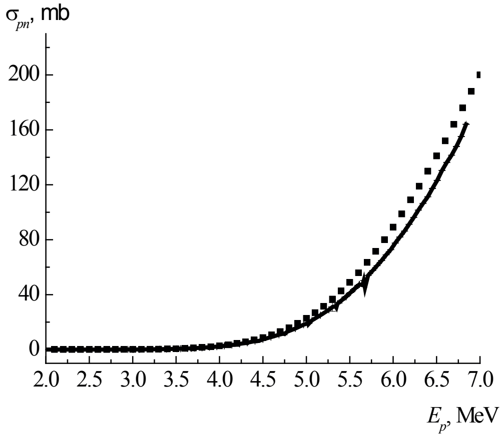

Fig. 4. ^{115}In(p,n)^{115}Sn. Talys evaluation – line. Experimental data – points.

In Fig. 4 the theoretical evaluations are compared with experimental data. The good agreement between theory and experiment was obtained mainly by variation of the parameters of optical potential. Experimental data are from [11].

Like for other two processes analyzed before, the production of ^{115}Sn in ^{115}In(p,n) processes by interaction of 35 MeV fast protons on a natural Indium target were determined for 1 μA and 100 μA currents. Results are shown in the Fig. 5.

Production of ^{115}Sn is higher than that of ^{112}Sn isotopes for both proton currents. Tin isotope with mass number 115 is obtained from ^{115}In which has a much larger abundance in natural Indium in comparison with ^{113}In, the source of $^{112,\ 114}$Sn, even when the cross section is larger.

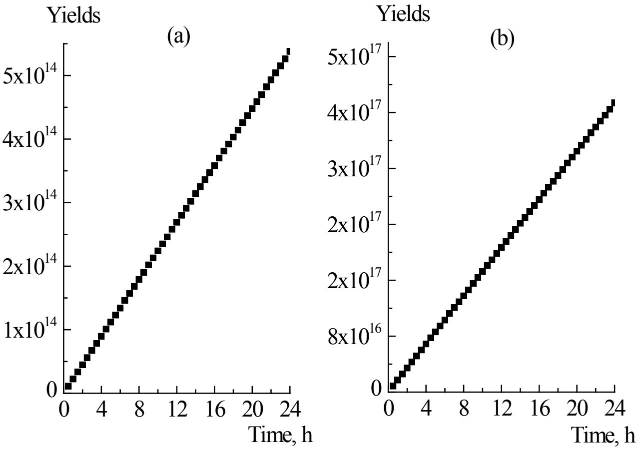

Fig. 5. Production of ^{115}Sn in ^{115}In(p,n)^{115}Sn. Current: a) 1 - μA; b – 100 μA.

Parameters of optical potential

Results presented in previous paragraphs were obtained with Talys using a large number of input parameters. In the cross section calculations were considered all open channels at the given incident energy. For elastic and inelastic channels, 30 levels of residual nucleus were taken into account and for reaction channels 10 levels. If the excitation energy is higher than excited states are considered in continuum [7]. Further, in this case, back – shifted Fermi gas model was chosen. The agreement between our evaluations and cross section data from literature was obtained by variation of optical potential parameters in the incident and emergent channels. In the calculations is used optical potential, with volume (V), surface (D) and spin-orbit (SO) components. Expression of Woods-Saxon potential (by components) is [7]:

$$\begin{aligned} U_{WS}(r) &= V_V f(r,R_V,a_V) + iW_V f(r,R_W,a_W) - i4a_D W_D \frac{d}{dr} f(r,R_D,a_D) + \\ & V_{SO}\left(\frac{\hbar}{m_\pi c}\right)^2 \frac{1}{r}\frac{d}{dr} f(r,R_{VSO},a_{VSO}) + iW_{SO}\left(\frac{\hbar}{m_\pi c}\right)^2 \frac{1}{r}\frac{d}{dr} f(r,R_{VSO},a_{VSO}) \end{aligned} \tag{1}$$

with the Wood-Saxon factor, f:

$$f(r,a_i,R_i) = \frac{1}{1+\exp\dfrac{r-R_i}{a_i}} \quad \text{and} \quad R_i = R_{0i}A^{1/3} \tag{2}$$

where i represents the components V, D, SO; A is the atomic mass; R_i is the radius; R_{0i} is the radius parameter; m_π is the pion mass; c is the speed of light.

Results with parameters of Woods-Saxon optical potential are presented in Table 1.

Process	V_V	W_V	W_d	V_{SO}	W_{SO}
$p + {}^{113}$In	62.42	0.11	4.25	6.09	-0.01
$p + {}^{115}$In	62.69	0.11	4.28	6.09	-0.01
$n + {}^{115}$Sn	50.74	0.14	3.94	6.09	-0.01

Table 1. Parameters of optical potential (in MeV) according with relation (3).

Analysis of Uncertainties

Cross sections for ^{113}In(p,$2n$)^{112}Sn and ^{115}In(p,n)^{115}Sn reactions where evaluated. For their uncertainties analysis, parameters of optical potential from Table 1 for neutron and proton channels were modified starting with the half of initial value up to two times of the initial value. Evaluations showed that the cross sections are most sensible to the variation of the real part of the volume Woods-Saxon potential. In the Fig. 6 are represented the results for relative variation of the real and imaginary part of the volume Wood – Saxon potential, for proton incident channel, for ^{115}In(p,n)^{115}Sn reaction. In Fig. 5 the R ratios are defined as:

$$R(k,V_V)=\frac{\sigma_{p\gamma}(kV_V)}{\sigma_{p\gamma}(V_V)} \quad \text{and} \quad R(k,W_V)=\frac{\sigma_{p\gamma}(kW_V)}{\sigma_{p\gamma}(W_V)} \tag{3}$$

where k = 0.25, 0.5, 0.75, 1, 1.25, 1.5, 1.75, 2; V_V, W_V are the real and imaginary part of volume Woods-Saxon potential with values from Table 1 *(k=1)*; $\sigma_{p\gamma}(V_V)=\sigma_{p\gamma}(W_V)$ are the ^{113}In(p,γ)^{114}Sn cross section (see Fig. 1a curve 4).

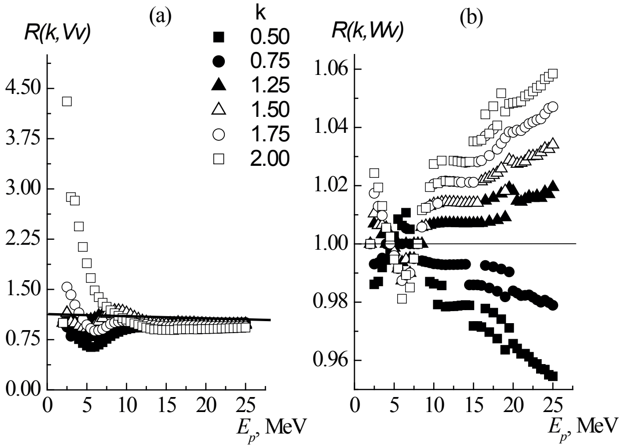

Fig. 6. The relative variation of the ^{115}In(p,n)^{115}Sn cross section by modifying the volume Woods-Saxon potential: a) real part; b) imaginary part. Line in both a) and b) represents the case k = 1.

Variation of the real part of the volume Woods-Saxon potential (given by *k* parameter) in the incident proton channel leads to the increasing of the cross section by four times near the threshold (Fig. 6.*a*). It is necessary to take into account the fact that near the threshold cross section has small values and the calculations can be affected by the computer codes precision here. Cross sections are influenced by the variation of the real part of volume Woods-Saxon potential starting from the threshold up to 10 MeV. This trend is maintained to other investigated processes from this work. Modification of the imaginary part of Woods-Saxon potential in the incident proton channel shows much lower changing in the cross sections (Fig. 6.*b*). As a general tendency, in the many investigated nuclear reactions, cross sections are the most sensitive to the modification of the real part of the volume Woods-Saxon potential in the incident and emergent channels, near the threshold up to 10–15 MeV.

CONCLUSIONS

Interaction of fast protons with natural Indium and production of Tin isotopes for nuclear astrophysics were investigated. Cross sections of ^{113}In(p,$2n$)^{112}Sn and ^{115}In(p,n)^{115}Sn processes, for protons, from threshold up to 25 MeV were evaluated using Talys. Contribution of the nuclear reaction mechanisms related to the discrete and continuum states of residual nuclei were obtained. A good agreement between theoretical calculation and experimental data from literature was obtained. Optical potential parameters, for incident and emergent channels were also extracted.

Production of Tin isotopes was simulated for the analyzed processes in the case of a real finite dimensions target and different proton currents. Obtained results in computer simulation showed that the concentrations of Tin isotopes depend on the cross section and abundance of nuclei in the target. For chosen initial conditions, some of Tin isotopes can be measured in the activation experiments.

Many nuclear investigations and applications necessitate precise nuclear data. For this reason cross section uncertainties, related to the variation of optical potential parameters were analyzed. Results have demonstrated that the cross sections data are mainly influenced by the modification of the real part of the volume component of Wood – Saxon potential near the threshold and few MeV higher.

Present evaluations accomplished the necessity of new experimental and theoretical evaluations of protons induced processes as well as computer modeling for nuclear structure, reaction mechanisms and other investigations correlated with uncertainties studies of the resulted nuclear data.

Acknowledgment. *The present researches are supported by JINR Dubna Annual Cooperation Program with Romanian Research Institutes coordinated by Romanian Plenipotentiary Representative and FLNP JINR Scientific Plan on 2021.*

REFERENCES

[1] A. Olacel, C. Borcea, M. Boromiza, Ph. Dessagne, G. Henning, M. Kerveno, L. Leal, A. Negret, M. Nyman, A.J.M. Plompen, *The European Physics Journal A*, Vol. **54**, p. 183 (2018).

[2] S. Cabral, G. Borker, H. Klein, W. Mannhart, *Nucl. Sci. Eng.*, Vol. **106**, p. 308, (1990).

[3] M. Salvatores, I. Slessarev, A. Tchistiakov, *Nucl. Sci. Eng.*, Vol. **130**, p. 309 (1998).

[4] I. Gheorghe, D. Filipescu, T. Glodariu, D. Bucurescu, I. Cata-Danil, G. Cata-Danil, D. Deleanu, D. Ghita, M. Ivascu, R. Lica, N. Margineanu, R. Margineanu, C. Mihai, A. Negret, T. Sava, L. Stroe, S. Toma, O. Sima, M. Sin, *Nuclear Data Sheets*, Vol. **119**, p. 245 (2014).

[5] J. Meija, T.B. Coplen, M. Berglund, W.A. Brand, P. De Bievre, M. Groning, N.E. Holden, J. Irrgeher, R.D. Loss, T. Walczyk, T. Prohaska, *Atomic Weights of Elements* (IUPAC Technical Reports) , *Pure Appl. Chem.*, 2016, Vol. **88** no. 3, p. 265 (2013).

[6] G. Audi, H.A. Wapstra, Nucl. Phys. A, Vol. **595**, p. 409 (1995).

[7] A.J. Koning, S. Hilaire, M.C. Duijvestijn, TALYS-1.0., *Proceedings of the International Conference on Nuclear Data for Science and Technology*, April 22-27, 2007, Nice, France, editors O. Bersillon, F. Gunsing, E. Bauge, R. Jacqmin, S. Leray, EDP Sciences p. 211.(2008).

[8] W. Hauser, H. Feshbach, *Phys. Rev.*, Vol. **87**, no. 2, p. 366 (1952).

[9] A.J. Koning, M.C. Duijvestijn, *Nucl. Phys. A*, 2004, Vol. **744**, p. 15 (2004).

[9] G.R. Satchler, *Direct Nuclear Reactions*, Oxford University Press: New York (1983).

[10] S. Harissopulos, A. Spyrou, V. Fonteinou, M. Axiotis, G. Provatas, P. Demetriou, *Phis. Rev. C*, Vol. **93**, p. 025804 (2016).

[11] R.L. Hershberger, D.S. Flynn, F. Gabbard, P.H. Johnson, *Phys. Rev. C*, Vol. **21**, p. 896 (1980).

ALPHA EMISSION IN FAST NEUTRONS REACTION ON NEODYMIUM NUCLEUS

C. Oprea, A. Oprea

Frank Laboratory for Neutron Physics (FLNP), Joint Institute for Nuclear Research (JINR),
141980 Dubna, Moscow Region, Russian Federation

Cross section, angular correlations and asymmetry effects in ^{143}Nd$(n,\alpha)^{140}$Ce process induced by fast neutrons with incident energies starting from 0.5 MeV up 25 MeV were investigated. Theoretical evaluations and modeling of (n,α) observables were realized with Talys combined with computer codes realized by authors. Contribution in the cross section and angular correlation of nuclear reaction mechanism were also determined. Cross section experimental data and theoretical evaluations are in a good agreement but similar comparison of forward – backward asymmetry effect results for few MeV neutrons energy revealed large discrepancy. The done calculations and computer modeling have demonstrated that the large asymmetry effect observed in the experiment cannot be explained by direct mechanism, rather the difference is coming from the presence of other open channels with participation of alpha particles. The results of present work were obtained in the frame of the fast neutrons scientific program of FLNP JINR Dubna.

INTRODUCTION

Nuclear reactions induced by the fast neutrons are for many years investigated at FLNP JINR Dubna. The fast neutron processes are of a great importance in fundamental and applicative researches. For theoretical investigations they represent an efficient tool in the investigation of nuclear reaction mechanism and structure of atomic nuclei. In the field of applicative researches the fast neutrons reactions offer precise nuclear data for fission and fusion reactors, reprocessing of Thorium and Uranium for nuclear transmutation, Accelerated Driven Systems projects and for Fast Neutrons Activation as a complementary method of Instrumental Neutron Activation Analysis with thermal and epithermal neutrons [1,2].

Neodymium is a chemical element with number of protons, $Z = 60$. This nucleus has five stable isotopes with atomic mass $A = 142, 143, 145, 146, 148$ and two long-lived isotopes with $A = 144, 150$. Isotopes of Neodymium are used in many applications such as manufacturing of powerful permanent magnets or in the Samarium–Neodymium dating as geochemical tracers and others [3,4].

In the present work nuclear process induced by fast neutrons with energies starting from 0.5 MeV up to 25 MeV on ^{143}Nd stable nucleus followed by the emission of charged alpha particles will be investigated (^{143}Nd$(n,\alpha)^{140}$Ce reaction).

ELEMENTS OF THEORY

Analysis of fast neutrons induced process on ^{143}Nd nucleus starts with the cross sections evaluations. In the theoretical calculations direct, compound and pre-equilibrium nuclear reactions mechanisms are considered. The direct processes are described by the Distorted Wave Born Approximations (DWBA), the compound processes are described in the frame of the statistical model of nuclear reactions and pre-equilibrium by the two exciton approach

[5–7]. The cross section of the (n,α) process with fast neutrons can be described in the frame of Hauser-Feshbach approach and has the following expression [6]:

$$\sigma_{n\alpha}(E_n) = g\pi ƛ_n^2 T_n T_\alpha W_{n\alpha}\left[\sum_c T_c\right]^{-1} \tag{1}$$

where $T_{n,\alpha}$ are the transmission coefficients in the incident and emergent channels respectively; g is the statistical factor; $ƛ_n$ = neutron reduced wave number; $W_{n\alpha}$ is the width fluctuation correction factor. In the sum of relation (1) are considered all open channels (c).

Width fluctuation correction factor, $W_{n\alpha}$, represents the correlation between incident and emergent channels. At low incident energies this coefficient is equal with one indicating no correlation between neutron and alpha channels (Bohr hypothesis of compound nucleus is working). With the increasing of the incident energy width fluctuation correction factor is slowly decreasing. There are few way for the calculation of fluctuation factor but in this work is used the method described in [8].

Transmission (or penetration) coefficient represents the probability of particles to pass a potential barrier. Usual transmission coefficient is lower than one, is increasing with incident energy and is constant at high energies. There are some methods in the evaluation of transmission coefficient and for this work the quantum mechanical approach (based on reflection factor) described in reference [9] was used.

In the case of (n,α) reaction with fast neutrons of few MeV, Hauser-Feshbach formalism was implemented by authors, considering a rectangular nuclear potential and ten levels of residual nucleus. Also, in the given incident neutrons energy intervals, the all open channels such as elastic, inelastic, protons and gamma were considered in the realized computer code [10].

For the cross sections and angular correlations from 0.5 MeV up to 25 MeV evaluation, Talys code was used [11]. A very useful database including parameters like levels energy, spin, parity, time of life, levels density for more than 2000 of stable nuclei and isotopes are implemented in the software database. The parameters of Woods-Saxon potential (with components volume, central and spin-orbit with real and imaginary part), extracted mainly from experimental data for many nuclei and channels are also included [11].

RESULTS AND DISCUSSIONS

Target nucleus ^{143}Nd is stable and has the spin and parity $J^{\Pi} = (7/2)^-$. In the software created by authors, in $^{143}\mathrm{Nd}(n,\alpha)^{140}\mathrm{Ce}$ reaction, is considered that fast neutrons have the orbital momentum $l_n = 0,1$. Residual nucleus ^{140}Ce has the spin and parity $J^{\Pi} = 0^+$. Heat of reaction for $^{143}\mathrm{Nd}(n,\alpha)^{140}\mathrm{Ce}$ process is $Q = 9.72$ MeV [3]. In the frame of quantum mechanical approach neutrons and alpha transmission coefficients were calculated by our soft. Results are shown in Fig. 1. Transmission coefficients have values lower than one and with the increasing of the incident energy they are also increasing tending to a constant value. With the increasing of orbital momentum the transmission coefficient are decreasing mainly due to centrifugal potential [7].

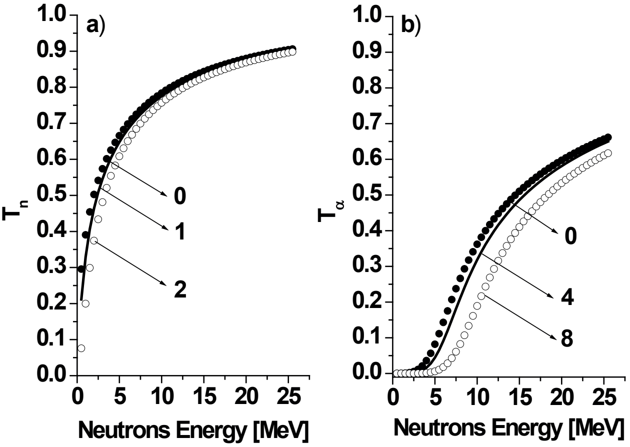

Figure 1. Transmission coefficients: a) neutrons (orbital momentum $l_n = 0, 1, 2$);
b) alphas (orbital momentum $l_\alpha = 0, 4, 8$).

Neutron transmission coefficients have higher values than for alpha particles for the all incident energy interval (see Fig 1.a) and Fig 1.b)). This fact results from the presence of the Coulomb potential term in the case of alpha particles which acts like a barrier [7].

Transmission coefficients are an important term of Hauser-Feshbach cross section from relation (1). In the Fig. 2 cross section was evaluated using the author soft, considering neutrons with orbital momentum, $l_n = 0,1$, ten levels of ^{140}Ce residual nucleus, rectangular optical potential, with real and imaginary part in the incident and emergent channels ($U = V + iW = (172+i0.1)$ MeV). Also, in the calculations, the elastic, inelastic, proton and gamma emergent channels were taken into account.

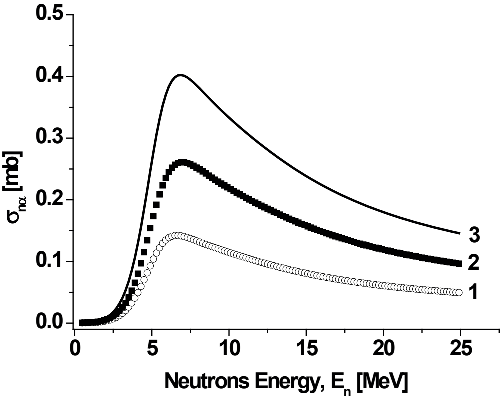

Figure 2. ^{143}Nd(n,α)^{140}Ce cross section (XS) : 1 – neutron orbital momentum $l_n = 0$;
2 – neutron orbital momentum $l_n = 1$; 3 – XS as sum of curves 1, 2.

In Fig. 2 cross sections of ^{143}Nd(n,α)^{140}Ce fast neutrons reactions are represented. Contribution of neutrons with *0* and *1* orbital momentum are given by the curves 1 and 2, respectively. For analyzed process, cross section of orbital momentum, $l_n = 1$ is larger than for neutrons with $l_n = 0$ results which differ from the similar case of other investigated fast neutrons reactions [10]. Total (n,α) cross section is shown by the curve 3. Cross sections from Fig. 2 are increasing with energies, reach a maximum value followed by a slowly decreasing, which are the usual dependences in fast neutron reactions. Cross section of ^{143}Nd(n,α)^{140}Ce process has small values which make the experimental measurements very difficult.

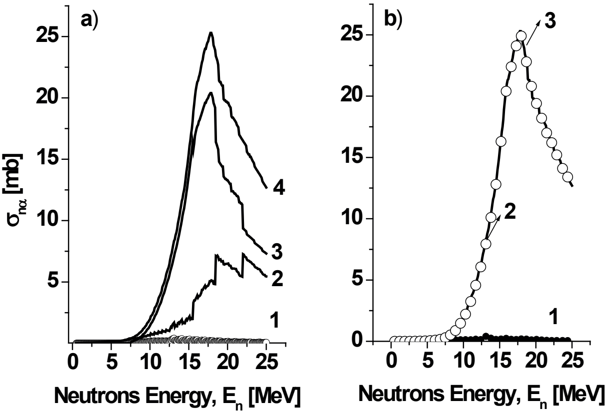

Figure 3. ^{143}Nd(n,α)^{140}Ce cross section (XS). Contribution to XS: 1 – of direct mechanism; 2– of compound mechanism; 3– of pre-equilibrium one; 4 – XS as sum of (1+2+3).

In Fig. 3 (n,α) the cross section calculated with Talys is shown. In Fig. 3.a contribution of nuclear reaction mechanisms to the cross section was obtained. Direct processes (dependence 1) have very low values and they are important at low energies. Compound processes are present in the whole energy interval (curve 2) with a consistent contribution to the cross section but pre - equilibrium multistep mechanism is the dominant one. In Fig. 3.b the (n,α) cross section is separated in contribution of discrete and continuum state of residual nucleus. Ten discrete levels of residual nucleus were taken into account (similar as in Fig. 2). At low energies the cross section is coming mainly from discrete levels (up to 7–8 MeV). At higher incident energies cross section is given by continuum states of residual nucleus. Contribution of discrete states from Fig. 2, evaluated with authors code is in good agreement with Talys calculations (Fig. 3.b – curve 1).

The evaluation of the (n,α) cross section with fast neutrons has small values, fact confirmed also in the experiment. The experimental cross section for the neutrons with the energy E_n = (4±0.23) MeV is $\sigma_{n\alpha}$ = (0.12±0.01) *mb* [12]. The cross section value obtained with author soft (Fig. 2) is $\sigma_{n\alpha}[E_n= 4$ MeV$] = 0.14$ *mb* and with Talys $\sigma_{n\alpha}[E_n= 4$ MeV$]=0.11$ *mb*. Both theoretical calculations are in a fair agreement with experimental data. The contribution of direct component cross section is $\sigma_{dir}[E_n= 4$ MeV$]=0.002$ *mb* and of compound one $\sigma_{n\alpha}[E_n= 4$ MeV$]=0.108$ *mb*. The cross section coming from discrete and continuum states of residual nucleus are $\sigma_{discr}[E_n= 4$ MeV$]= 0.105$ *mb* and $\sigma_{cont}[E_n= 4$ MeV$]= 0.005$ *mb*. At 4 MeV the main contribution to the cross section comes from the discrete states combined with the compound processes. The direct component is very low. The above results were used in the analysis of forward–backward (FB) asymmetry effects measured in the experiment. For the neutron incident energy E_n = 4 MeV, FB effect is $A_{FB}[(E_n= (4\pm0.23)]= (1.25\pm0.12)$ [12]. In the reference (12), experimental FB effect is the ratio between all forward and backward events registered by a gridded ionization chamber. Theoretical evaluation of FB effects, as defined in [12], necessitates the knowledge of the angular correlations. The differential cross section obtained using Talys is represented in the Fig. 4.

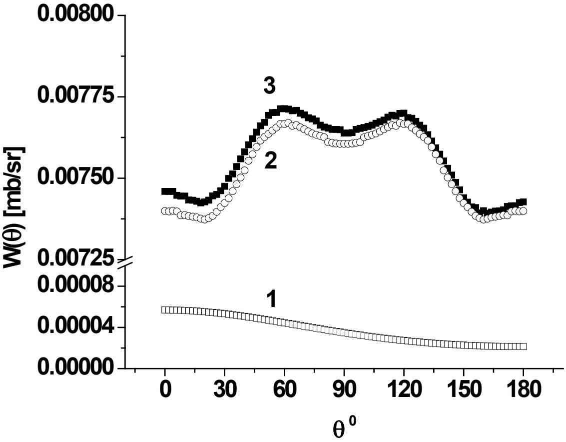

Figure 4. The differential XS of ^{143}Nd$(n,\alpha)^{140}$Ce. Nuclear reaction mechanism: 1 – direct; 2 – compound one; 3 – sum of (1+2).

Using the results from Fig. 4, the FB effect was evaluated in the case of a point like target. From differential cross sections, the angular correlations were extracted. Further, the angular distribution was modeled by direct Monte-Carlo method [13]. Simulated FB effect, for 4 MeV incident neutrons is $A_{FB}^{sim} = 1.0076$. The difference between experimental FB effect theoretical and experimental data is large. The calculated direct component is very low (see Fig. 4) and in consequence the measured FB effect is also small. The discrepancy can be explained qualitatively by the influence of the other open channel with participation of alpha particles. In the investigated reaction, formed compound nucleus is an even-even one which in principle favors alpha particles emission.

In our evaluations using Talys 30 levels for residual nucleus, in the case of elastic and inelastic scattering and 10 levels in the case of reaction channels were took into account. For the density levels, Fermi gas model was chosen. In the description of experimental data a large number of the parameters of the Wood-Saxon optical potential were tested. Theoretical results are the most sensible to the variation of central volume parameter and for emergent alpha channels they are $U = V + iW = (172+0.11)$ MeV (results are practically the same obtained by authors code).

RESULTS AND CONCLUSIONS

The cross sections, angular correlations and forward – backward asymmetry effects were analyzed in the ^{143}Nd(n, α)^{140}Nd nuclear reaction induced by fast neutrons with energies starting from 0.5 MeV up to 25 MeV. The theoretical results were obtained with programs realized by authors and with Talys code. The cross section for the investigated reaction has very low values and therefore the experimental data are poor. The experimental and theoretical cross section data are in good agreement. In the case of forward – backward asymmetry effects a large differences were observed which cannot be explained by the presence of direct mechanism. The large experimental forward–backward effect in comparison with theoretical evaluations and computer modeling can be the results of the influence of other open emergent channels with participation of alpha particles but this discrepancy remains an open issue for the future. The well description of cross sections experimental data allowed to extracting new parameters of Woods-Saxon optical potential for incident neutron channels and emergent alpha channel.

Acknowledgments. *The present researches are supported by JINR Dubna Annual Cooperation Program with Romanian Research Institutes coordinated by Romanian Plenipotentiary Representative and FLNP JINR Scientific Plan on 2021.*

REFERENCES

[1] G. Khuukhenkhuu, M. Odsuren, Yu. Gledenov, G. Zhang, B. Batchimeg, J. Munkhasaikhan, C. Saikhanbayar, E. Sansarbayar, M. Sedysheva, EPJ Web of Conference 239, 03007 (2020).

[2] G. Khuukhenkhuu, G. Unenbat, Yu. Gledenov, M. Sedysheva, Journal of Nuclear Science and Technology, Supplement 2, p, 782–784 (2002).

[3] G. Audi, O. Bersillon, J. Blanchot, A.H. Wapstra, Nucl. Phys. A, Vol. **729**, Issue 1, p. 3 (2003).

[4] M. Drak, L.A. Dobrzanski, Journal of Achievements in Materials and Manufacturing Engineering, Vol. **20**, Issue 1–2, p. 239 (2007).

[5] G.R. Satchler, Direct Nuclear Reactions, Oxford University Press, New York (1983).

[6] W. Hauser, H. Feshbach, Phys. Rev., Vol. **87**, Issue 2, p. 366 (1952).

[7] A.J. Koning and M.C. Duijvestijn, Nucl. Phys. A, Vol. **744**, p. 15 (2004).

[8] P.A. Moldauer, Rev. Mod. Phys., Vol. **35**, p. 1079 (1964).

[9] A. Foderaro, The Neutron Interaction Theory, MIT Press Cambridge Massachusets and London, England (1971).

[10] A.I. Oprea, C. Oprea, C. Parvutoiu, D. Vladoiu, Rom. Rep. in Phys., Vol. **63**, Issue 1, p. 107 (2011).

[11] A.J. Koning, S. Hilaire and M.C. Duijvestijn, TALYS-1.0., Proceedings of the International Conference on Nuclear Data for Science and Technology, April 22–27, 2007, Nice, France, editors O. Bersillon, F. Gunsing, E. Bauge, R. Jacqmin, S. Leray, EDP Sciences, p. 211 (2008).

[12] Yu.M. Gledenov, M.V. Sedysheva, V.A. Stolupin, G. Zhang, J. Zhang, H. Wu, J. Liu, J. Chen, G. Khuukhenkhuu, P.E. Koehler, P.J. Szalanski, Phys. Rev. C, Vol. **80**, 044602 (2009).

[13] C. Oprea, A. Mihul, A. Oprea, CERN Proceedings-2019-001, p. 125 (2019).

Systematical Analysis of (n,2n) Reaction Cross Sections for 14–15 MeV Neutrons

Ch. Saikhanbayar, G. Khuukhenkhuu and M. Odsuren

Nuclear Research Center, National University of Mongolia, Ulaanbaatar, Mongolia
School of Engineering and Applied Sciences, National University of Mongolia, Ulaanbaatar, Mongolia

Yu.M. Gledenov and E. Sansarbayar

Frank Laboratory of Neutron Physics, JINR, Dubna, Russia

Guohui Zhang

State Key Laboratory of Nuclear Physics and Technology, Institute of Heavy Ion Physics, Peking University, Beijing 100871, China

1. Introduction

Fast neutron induced nuclear reaction cross section data are necessary for both nuclear energy technology and the study of nuclear structure and reactions. The information of (n,2n) cross sections is quite essential in nuclear reactor technology as a significant portion of the fission neutron spectrum lies above the threshold of (n,2n) reaction for most of the structural materials. These cross section data are required in radiation shielding and nuclear fuel breeding calculations. Furthermore, the application of the fast neutron induced nuclear reaction cross section data have been increasing in the fields of biomedical applications, accelerator driven transmutation, material irradiation experiments concerning research and development for fusion reactor technology. On the other hand, systematics of fast neutron induced reaction cross sections is useful to clarify nuclear reaction mechanisms. Also, it is often necessary, in practice, to use the systematical analysis for evaluation of the neutron cross sections of the nuclides, for which no experimental data are available.

A systematic dependence of (n,2n) reaction cross sections on the neutron number excess parameter (N–Z)/A for target nuclei was studied in a number of works [1–11]. Purely empirical formulae [1–4,10] and semi-empirical formulae based on the statistical model [5–9,11], pre-equilibrium [7] and direct reaction [5] mechanisms were suggested to explain this regular behaviour of the (n,2n) cross sections. However, a strict and unified theoretical validity no up to now is available for explanation of the neutron cross section regularity which in the literature is termed as the isotopic effect.

In this work new formulae for the (n,2n) cross section are deduced using the concepts of statistical and non-statistical nuclear reaction mechanisms. In the calculation of the statistical part of the cross section the constant nuclear temperature approximation, evaporation model and Weizsäcker's formula for binding energy were utilized. Non-statistical part was obtained by subtraction of statistical model cross section from total one. The total cross section was determined by geometrical cross section of target nuclei as an upper limit of interaction of neutrons with nuclei.

2. Theoretical background

In the framework of the statistical model based on the Bohr's assumption of a compound mechanism the cross section formula for (*n,x*) reaction is expressed as [12]:

$$\sigma(n,x)=\sigma_c(n)\frac{2S_x+1}{2S_n+1}\frac{M_x}{M_n}e^{\frac{Q_{n,x}-V_x}{\Theta}}\left\{\frac{1-\frac{W_{n,x}}{\Theta}e^{-\frac{W_{n,x}}{\Theta}}-e^{-\frac{W_{n,x}}{\Theta}}}{1-\frac{E_n}{\Theta}e^{-\frac{E_n}{\Theta}}-e^{-\frac{E_n}{\Theta}}}\right\}, \qquad (1)$$

where: $\sigma_c(n)=\pi(R+\bar{\lambda}_n)^2$ is the compound nucleus formation cross section; R is the target nucleus radius; $\bar{\lambda}_n$ is the wavelength of the incident neutrons divided by 2π; S_n and S_x are the spins of the incident neutron and emitted x-particle, respectively; M_n and M_x are the masses of the neutron and x-particle, respectively; $Q_{n,x}$ is the reaction energy; V_x is the Coulomb barrier for x-particle; Θ is the thermodynamic temperature; E_n is the incident neutron energy; $W_{n,x}=E_n+Q_{n,x}-V_x$.

According to our evaluations, term in the curly brackets of the formula (1) approximately equals to 1 for the fast neutron induced (n,2n) reaction cross sections except a few very light nuclei. Then, from the formula (1) can be obtained following formula, which is similar to Cuzzocrea's *et al.* [13] and Ericson's [14] formulas:

$$\sigma(n,2n)=\sigma_c(n)\frac{2S_{2n}+1}{2S_n+1}\frac{M_{2n}}{M_n}e^{\frac{Q_{n,2n}-V_{2n}}{\Theta}}. \qquad (2)$$

Using the Weizsäker's formula for binding energy we can obtain following expressions for the target and residual nuclei:

$$E_i=\alpha A-\beta A^{2/3}-\gamma\frac{Z^2}{A^{1/3}}-\xi\frac{(N-Z)^2}{A}\pm\frac{\delta_i}{A^{3/4}} \qquad (3)$$

and

$$E_f=\alpha(A-1)-\beta(A-1)^{2/3}-\gamma\frac{Z^2}{(A-1)^{1/3}}-\xi\frac{(N-1-Z)^2}{A-1}\pm\frac{\delta_f}{(A-1)^{3/4}}. \qquad (4)$$

Then, we get the (n,2n) reaction energy $Q_{n,2n}$ as following:

$$Q_{n,2n}=-\alpha-\beta\left\{(A-1)^{2/3}-A^{2/3}\right\}-\gamma\left\{\frac{Z^2}{(A-1)^{1/3}}-\frac{Z^2}{A^{1/3}}\right\}-\xi\left\{\frac{(N-1-Z)^2}{A-1}-\frac{(N-Z)^2}{A}\right\}\pm\frac{\delta_f}{(A-1)^{3/4}}\mp\frac{\delta_i}{A^{3/4}}. \qquad (5)$$

where: α = 15.7 MeV; β = 17.8 MeV; γ = 0.71 MeV; ξ = 23.7 MeV; δ_i and δ_f depend on either odd or even number of neutrons and protons $|\delta|$ = 34 MeV or 0.

So, taking into account the Coulomb barrier for neutrons $V_{2n} = 0$, the spin and mass of neutrons, and reaction energy for formula (2) we get the (n,2n) cross section formula:

$$\sigma(n,2n) = 4\pi(R+\lambdabar_n)^2 \exp\left\{\frac{-\alpha-\beta\left((A-1)^{2/3}-A^{2/3}\right)-\gamma\left(\frac{Z^2}{(A-1)^{1/3}}-\frac{Z^2}{A^{1/3}}\right)-\xi\left(1-\frac{4Z^2}{A(A-1)}\right)\pm\frac{\delta_f}{(A-1)^{3/4}}\mp\frac{\delta_i}{A^{3/4}}}{\Theta}\right\}. \quad (6)$$

In the case of A >> 1 can be obtained the following formulae for systematical analysis of the (n,2n) cross sections:

$$\frac{\sigma(n,2n)}{\pi(R+\lambdabar_n)^2} = C\exp(-K\frac{Z^2}{A^2}) \quad (7)$$

where: *Z* and *A* are proton and mass numbers of the target nuclei; the parameters *K* and *C* are expressed as:

$$K = \frac{4\xi}{\Theta}; \quad (8)$$

$$C = 4\exp\left\{\frac{-\alpha-\beta\left((A-1)^{2/3}-A^{2/3}\right)-\gamma\left(\frac{Z^2}{(A-1)^{1/3}}-\frac{Z^2}{A^{1/3}}\right)\pm\frac{\delta_f}{(A-1)^{3/4}}\mp\frac{\delta_i}{A^{3/4}}+\xi}{\Theta}\right\}. \quad (9)$$

It can be, as a first approximation, assumed that for (n,2n) reactions induced by 14–15 MeV neutrons the pre-equilibrium and direct mechanisms predominate. In this case, we find out the non-statistical share of cross section by subtracting the (n,2n) cross section defined by compound mechanism from the total one as following:

$$\sigma^{nonstat}(n,2n) = \sigma^{tot}(n,2n) - \sigma^{comp}(n,2n) \quad (10)$$

If the total cross section is determined by geometrical cross section of the target nuclei as an upper limit of interaction of neutrons with nuclei:

$$\sigma^{tot}(n,2n) = \pi(R+\lambdabar_n)^2, \quad (11)$$

then the non-statistical part can be obtained as following:

$$\sigma^{nonstat}(n,2n) = \pi(R+\lambdabar_n)^2\left(1-C\exp(-K\frac{Z^2}{A^2})\right). \quad (12)$$

Then, the reduced (n,2n) cross section is expressed as:

$$\frac{\sigma^{nonstat}(n,2n)}{\pi(R+\bar{\lambda}_n)^2} = \left(1 - C\exp(-K\frac{Z^2}{A^2})\right). \tag{13}$$

3. Systematics of (n,2n) reaction cross sections and Discussions

We have analyzed 139 experimental (n,2n) cross section data for the neutron energy of 14–15 MeV from EXFOR [15]. The dependence of the reduced (n,2n) cross section on the parameter Z^2/A^2 is shown in the Fig. 1.

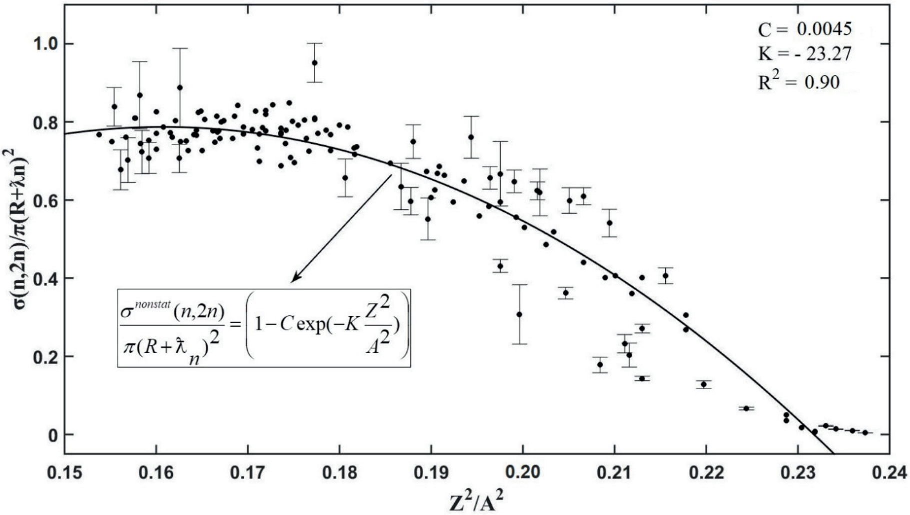

Fig. 1. The dependence of the reduced (n,2n) cross sections on parameter Z^2/A^2

It is seen from Fig. 1 that the theoretical curve is in satisfactorily agreement with the experimental data. Also, in Fig. 1 experimental errors of the cross sections for some isotopes are given, as example.

4. Conclusions

1. In the framework of the statistical model a theoretical formula for the (n,2n) reaction cross section was deduced. In addition, a non-statistical share of the total neutron cross section was obtained.
2. Known experimental data of the (n,2n) cross sections for 14 – 15 MeV neutrons were analyzed using the obtained formulae. It was shown that the non-statistical share of the total cross section is in satisfactorily agreement with experimental data.

5. Acknowledgement

This work has been supported by the Mongolian Science and Technology Foundation (Contract No: ShuSs-2019/6).

REFERENCES

1. J. Csikai and G. Peto, *Phys. Lett.*, Vol. **20**, No. 1, 1966, pp. 52–53.
2. A. Adam and L. Jeki, *Acta Phys. Hung*., Vol. **26**, No. 4, 1969, pp. 335–338.
3. S. Chatterjee and A. Chatterjee, *Nucl. Phys*. Vol. A**125**, 1969, pp. 593–612.
4. W.D. Lu, N. RanaKumar and R.W. Fink, *Phys. Rev. C*, Vol.**1**, No.1, 1970, pp. 350–357.
5. W.D. Lu and R.W. Fink, *Phys. Rev. C*, Vol. **4**, No. 4, 1971, pp. 1173–1181.
6. V.M. Bychkov *et al*., INDC(CCP)-146/LJ, NDS, IAEA, 1980, Vienna.
7. A.Yu. Konobeyev and Yu.A. Korovin, *Nuovo Cimento*, Vol. **112**A, No. 9, 1999, pp. 1001–1013.
8. Kh.T. Osman and F.I. Habbani, INDC(SUD)-004, NDS, IAEA, 2000, Vienna.
9. F.I. Habbani and Kh.T. Osman, *Appl. Rad. Isot*., Vol. **54**, No. 2, 2001, pp. 283–290.
10. E. Tel *et al*., *Int. J. Mod. Phys. E*, Vol. **17**, No. 3, 2008, pp. 567–583.
11. J. Luo *et al*., *Nuc. Inst. Meth. Phys. Res*. Vol. **266**B, No. 22, 2008, pp. 4862–4868.
12. G. Khuukhenkhuu and M. Odsuren, “Fast neutron induced nuclear reaction cross section” Ulaanbaatar, 2010, pp. 36–40, (in Mongolian).
13. P. Cuzzocrea *et al*., *Nuovo Cimento*, Vol. **4**A, No. 2, 1971, pp. 251–298.
14. T. Ericson, *Advances in Physics*, Vol. **9**, No. 36, 1960, pp. 425–511.
15. https://www-nds.iaea.org/exfor/

Excitation Functions of Neutron-Induced Reactions of Medical Isotopes ^{32}P, ^{55}Fe, ^{74}As, ^{97}Ru, ^{103}Ru and ^{109}Pd

Namrata Singh, A. Gandhi, Aman Sharma, Mahesh Choudhary and A. Kumar

Department of Physics, Banaras Hindu University, Varanasi-221005

Introduction

There are many stable and radioactive isotopes, each having their own physical and chemical properties, perform important roles in technology and actually existing in the field of research. The most common application is the use of radioisotopes in the medicine [1]. The medical radioisotopes are classified as therapeutic and diagnostic radioisotopes, depending on the decaying properties. The diagnostic radioisotopes, depending on the nature of radioisotopes, are used in two types of emission tomography, i.e. single photon emission computed tomography (SPECT) and positron emission tomography (PET).

The knowledge of the excitation function is necessary, to get a governed and optimized medical radionuclide. In this regard, the theoretical model calculation is very helpful. TALYS1.9 and EMPIRE-3.2 are used to determine the excitation functions of radionuclides ^{32}P, ^{55}Fe, ^{74}As, ^{97}Ru, ^{103}Ru and ^{109}Pd produced via $^{32}S(n,p)^{32}P$, $^{56}Fe(n,2n)^{55}Fe$, $^{58}Ni(n,\alpha)^{55}Fe$, $^{74}Se(n,p)^{74}As$, $^{98}Ru(n,2n)^{97}Ru$, $^{102}Ru(n,\gamma)^{103}Ru$, $^{103}Rh(n,p)^{103}Ru$, $^{104}Ru(n,2n)^{103}Ru$, $^{108}Pd(n,\gamma)^{109}Pd$, $^{109}Ag(n,p)^{109}Pd$, $^{110}Pd(n,2n)^{109}Pd$, and $^{112}Cd(n,\alpha)^{109}Pd$ reactions in the neutron energy range 1 – 20 MeV.

The calculated results are discussed and compared with the existing experimental data (EXFOR database) [2] as well as with the evaluated data. The excitation functions of ^{32}P, ^{55}Fe, ^{74}As, ^{97}Ru, ^{103}Ru and ^{109}Pd are medically important and widely used in bone disease treatment, heat source, in biomedical, monoclonal antibodies labelling, imaging, radio labelling and potential radio therapeutic agent [3].

Calculations

Theoretical calculations based on nuclear models play a very important role in the development of cross-section data. Calculations on the cross-sections have been carried out with TALYS-1.9 and EMPIRE-3.2 codes.

TALYS-1.9 [4] is a computer code system for the analysis and prediction of the nuclear reactions. The main purpose of the TALYS is to stimulate the nuclear reactions that involve gammas, protons, neutrons, deuterons, tritons, ^{3}He and α-particles as the projectiles over energy range $10^{-3} < E < 200$ MeV for the target nuclei for the mass ≥ 12. This code takes into account different reaction mechanisms like compound nucleus formation, pre-equilibrium and direct reactions as the function of the incident particle energy. This code uses the Hauser-Feshbach model to unify the effects of the compound nucleus reaction mechanism. The pre-equilibrium contribution has been included using the exciton model, which was developed by Kalbach.

EMPIRE-3.2 [5] is a computer code for the nuclear reactions, including different nuclear models, and designed for the calculations as a wide range of incident energies and incident particles. Photons, nucleons, deuterons, tritons, helium (^{3}He), α-particles, and light or heavy ions can be selected as projectiles. This code can be used for the nuclear data evaluation as well as for the theoretical calculations of the nuclear reactions. There are various input parameter libraries, FORTRAN codes, and experimental data library (EXFOR), which are operated through the Graphical User Interface (GUI). This statistical model is an advanced implementation of the Hauser-Feshbach theory for the compound nuclear reaction cross-section. EGSM is a default level density model used in the present calculations.

Results and Conclusions

In the paper, the calculations on the excitation functions of ^{32}S(n,p)^{31}P, ^{56}Fe(n,2n)^{55}Fe, ^{58}Ni(n,α)^{55}Fe, ^{74}Se(n,p)^{74}As, ^{98}Ru(n,2n)^{97}Ru, ^{102}Ru(n,γ)^{103}Ru, ^{103}Rh(n,p)^{103}Ru, ^{104}Ru(n,2n)^{103}Ru, ^{108}Pd(n,γ)^{109}Pd, ^{109}Ag(n,p)^{109}Pd, ^{110}Pd(n,2n)^{109}Pd and ^{112}Cd(n,α)^{109}Pd reactions in the 1–20 MeV energy range are presented. The calculated results are compared and discussed with the experimental as well as evaluated data.

Generally, the nuclear reaction cross-sections first increases with the increasing of neutron energy and get the maximum value and then decreases as a function of neutron energy in the case of (n,p), (n,2n) and (n,α) reactions. But in case of (n,γ) reactions, the cross-section values are higher at ~1 MeV neutron energy due to the contribution of compound nucleus as compared to the pre-equilibrium mechanism and direct reaction.

The shape of the theoretically predicted excitation functions for ^{32}P, ^{55}Fe, ^{74}As, ^{97}Ru, ^{103}Ru and ^{109}Pd radionuclides produced by (n,p), (n,2n), (n,α) and (n,γ) channels show a similar trend with the existing experimental data. It should also be noted that there is only one experimental data present for ^{102}Ru(n,γ)^{103}Ru reaction and for ^{108}Pd(n,γ)^{109}Pd reaction, no experimental data is present in this energy range. The data obtained by using EGSM model of EMPIRE-3.2 code can be used as a reference cross section and it is hoped that they can help in enterprising a well-controlled and optimized production of medical radionuclides in the energy range 5 – 20 MeV.

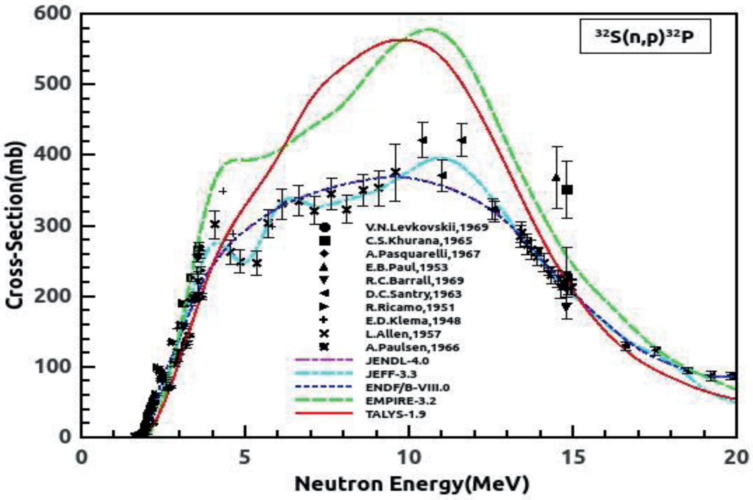

Fig.1. Theoretically predicted and experimentally measured as well as evaluated excitation functions for ^{32}P radionuclide.

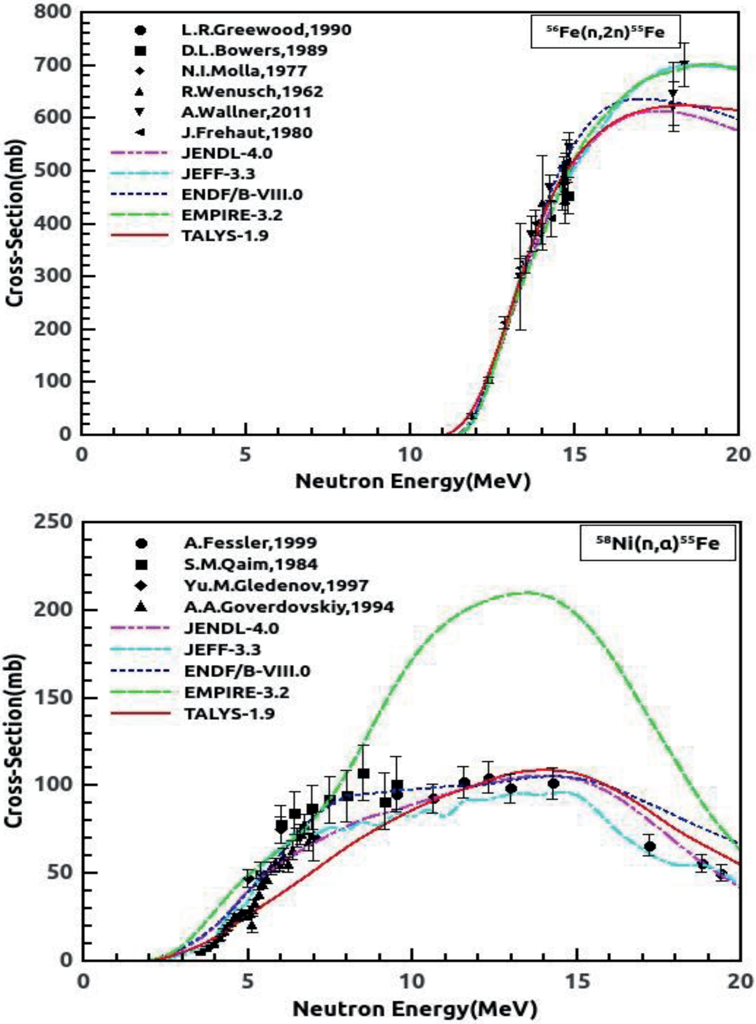

Fig.2. Theoretically predicted and experimentally measured as well as evaluated excitation functions for ^{55}Fe radionuclide.

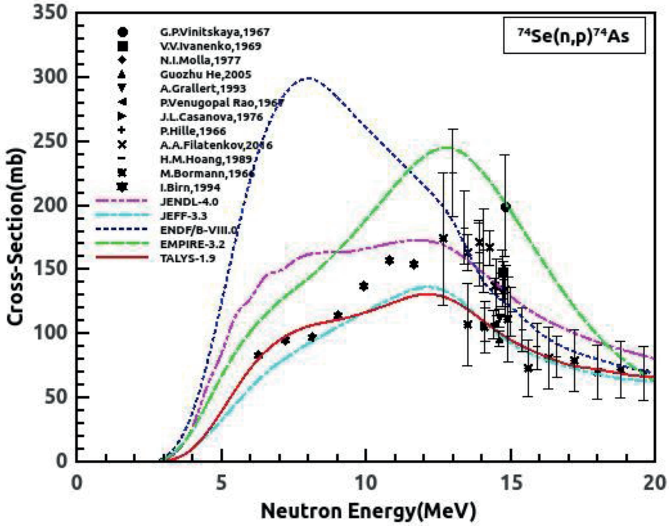

Fig.3. Theoretically predicted and experimentally measured as well as evaluated excitation functions for ^{74}As radionuclide

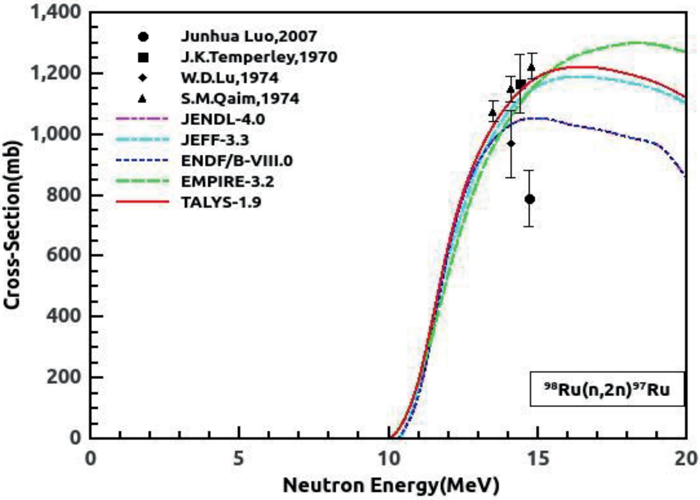

Fig.4. Theoretically predicted and experimentally measured as well as evaluated excitation functions for ^{97}Ru radionuclide.

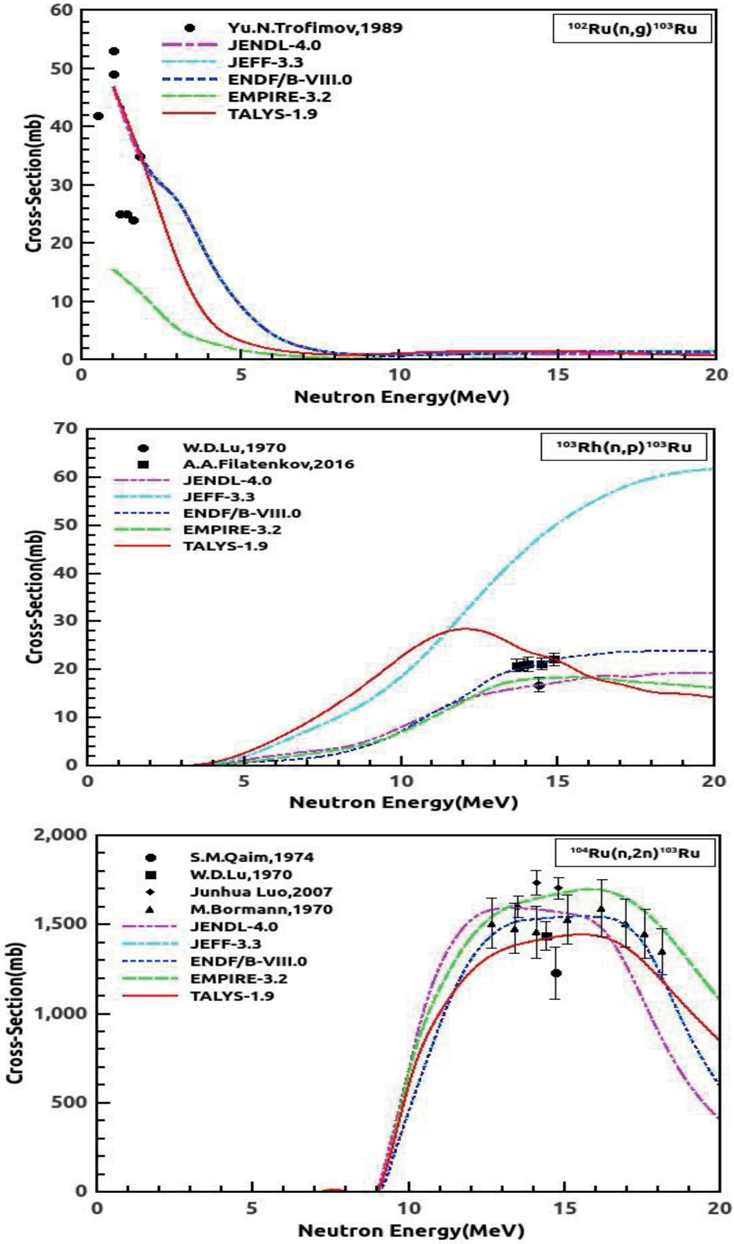

Fig.5. Theoretically predicted and experimentally measured as well as evaluated excitation functions for ^{103}Ru radionuclide.

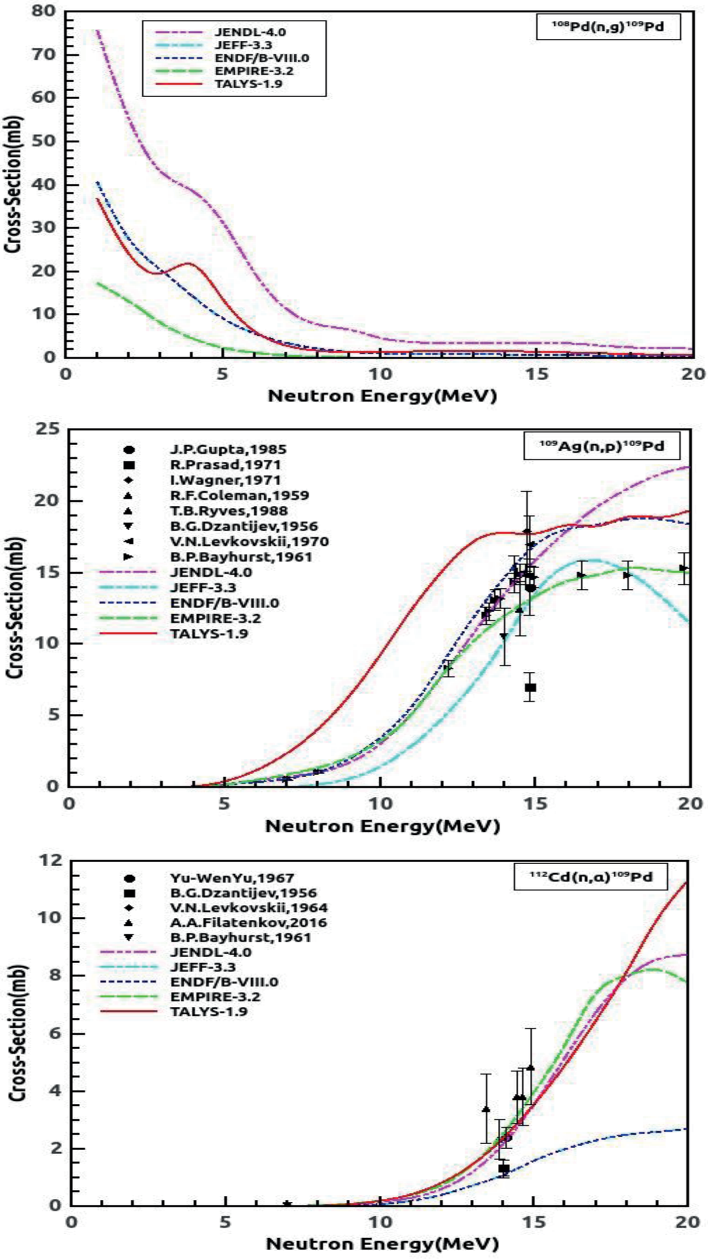

Fig.6. Theoretically predicted and experimentally measured as well as evaluated excitation functions for ^{109}Pd radionuclide.

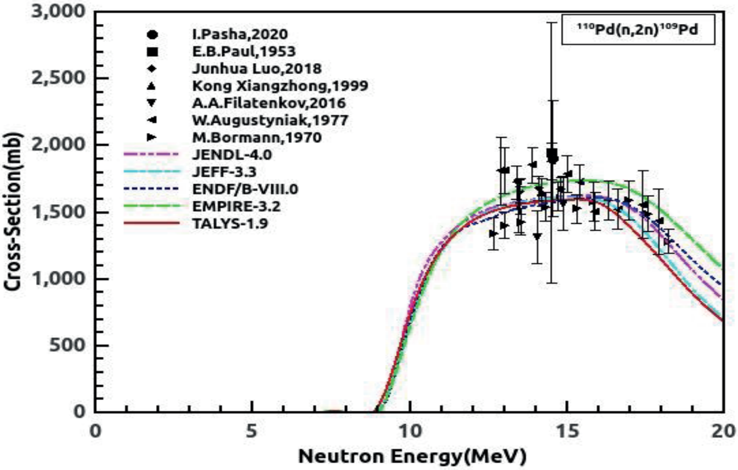

Fig.7. Theoretically predicted and experimentally measured as well as evaluated excitation functions for ^{109}Pd radionuclide.

Acknowledgement
One of the authors (A. Kumar) thanks to SERB-DST, Govt. of India (Sanction No. CRG/2019/000360) and Institutions of Eminence (IoE) BHU Grant for the financial support.

References

1. F.K. Amanuel, Appl. Rad. and Isotopes, 109674, 2021.
2. N. Otuka, E. Dupont, V. Semkova, B. Pritychenko, A.I. Blokhin, M. Aikawa, S. Babykina, M. Bossant, G. Chen, S. Dunaeva, and R.A. Forrest, Nuclear Data Sheets, 272, 2014.
3. A. Aydin, B. Şarer, and E. Tel, Appl. Rad. and Isotopes, 365, 2007.
4. A.J. Koning, S. Hilaire, S. Goriely, TALYS user manual, A nuclear reaction program, NRG1755 ZG PETTEN, The Netherlands, 2015.
5. M. Herman, R. Capote, B.V. Carlson, P. Oblozinsky, M. Sin, A. Trkov, H. Wienke, and V. Zerkin, Nuclear Data Sheets, 2655, 2007.

NEUTRON RESONANCES IN THE GLOBAL CONSTITUENT QUARK MODEL

S.I. Sukhoruchkin, Z.N. Soroko, M.S. Sukhoruchkina, D.S. Sukhoruchkin

Petersburg Nuclear Physics Institute, NRC "Kurchatov Institute", 188300 Gatchina

1. Introduction

Neutron resonance spectroscopy is part of nuclear physics based on the Standard Model (SM) as a theory of all interactions. In this work, we present the symmetry motivated and electron-based empirical approach to SM development. It was shown in [1], that nonstatistical effects, observed by different authors in the positions and spacing distributions of neutron resonances in many isotopes are systematic.

The high accuracy in determining the neutron resonance energy achieved by the time-of-flight method allowed us to consider together empirical correlations in nuclear data, namely the existence of fine and superfine structures, respectively, with periods of ε'=1.2 keV and ε''=1.4 eV=5.5 eV/4, which are equal to the first and second QED radiative corrections to the empirically found period 1022 keV=$\varepsilon_\circ$=2m$_e$ in few-nucleon excitations and the differences of the nuclear binding energies. The factor $\alpha/2\pi$ between them corresponds to the influence of the physical QED condensate known for the magnetic moment. The distinguished character of the electron mass m_e=511 keV was found in many empirical data: 1) The frequent appearance of stable nuclear intervals related to the values of m_e and $\delta m_N = m_n - m_p$=1293 keV, shown as maxima in Fig. 1, and as 2) the period $16m_e$ in the empirical relations between the nucleon and electron masses [2-4]

$$m_n = 115 \cdot 16m_e - m_e - \delta m_N/8 \qquad m_p = 115 \cdot 16m_e - m_e - 9(\delta m_N/8). \tag{1}$$

3) The discreteness in the nucleon separation energies shown in Figs. 2-4 and discussed later, as well as in many other effects with the parameter m_e.

The neutron mass shift $\delta_n = 161.6491(6)$ keV from $k \cdot 16m_e$ coincides with the nuclear tensor forces parameter $\Delta TF = 161$ keV, which corresponds to the one-pion exchange dynamics [3,4], and is equal to the radiative correction $\alpha/2\pi$ to the pion mass.

Nucleons and the electron are stable particles that determine the visible mass of the universe. They belong to the first and last components of the Standard Model, respectively, QCD and QED in the representation

$$SU(3)_{col} \otimes SU(2)_L \otimes U(1)_Y. \tag{2}$$

The masses of the neutron and the electron are in a ratio that is very accurately estimated by the CODATA commission as m_n/m_e=1838.6836605(11), see unexpectedly simple "CODATA relations" (1). Y. Nambu noted [5]: "a) When we discover new phenomena which we do not understand, the first thing to do is to collect data and try to find some empirical regularities among them, b) one next tries to build concrete models, c) finally there emerges a real theory ... Standard Model ...is theoretically unsatisfactory... a) the unification of forces is only partially realized, and b) there are too many input parameters. The nature can be at the same time more complicated than we think, and simpler in a way we do not know yet... ."

According to S. Weinberg [6], d: we are "still seeking a solution" for these problems.

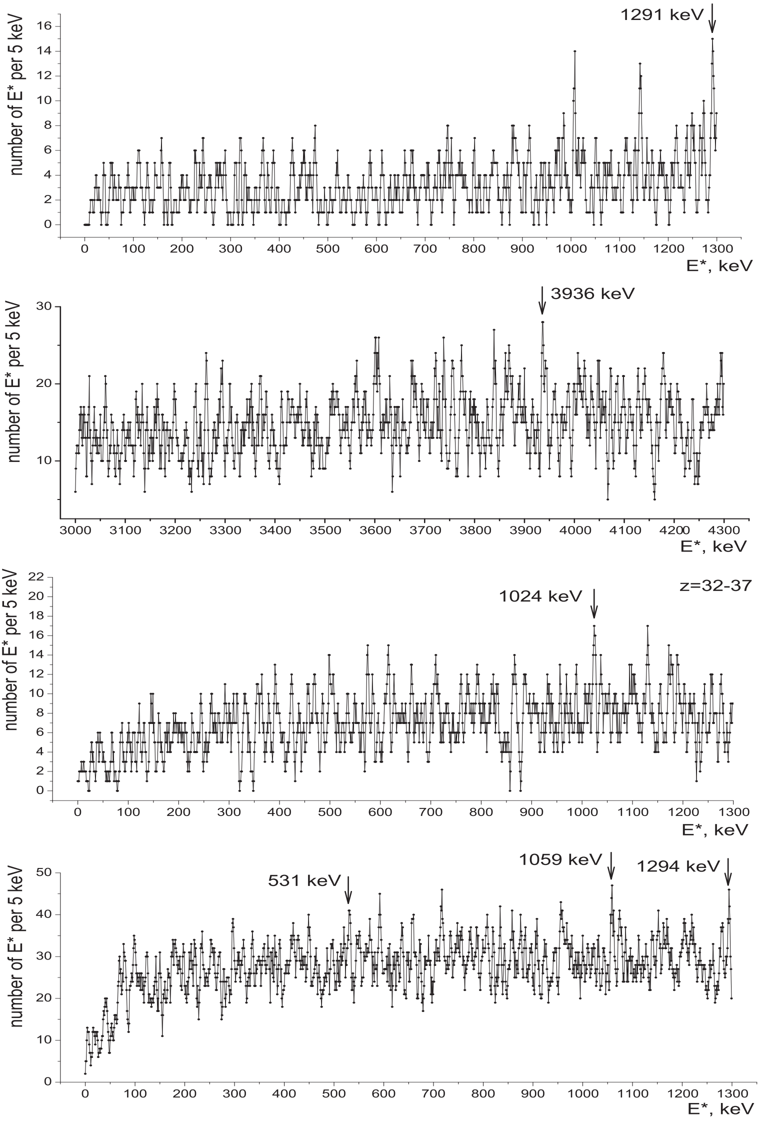

Figure 1: *Top and 2nd line*: E^*-distribution in nuclei with Z=4-29 for E^*<1300 keV and 3000-4300 keV. Arrows mark δm_N and $4\times8\times13\delta'$=3936 keV. Schematic diagram of the nuclear level system is shown in Fig. . The equidistant maxima at E^*=1008 keV=$2\times17\delta'$+$4\times18\delta'$, 1142 keV=$5\times17\delta'$ + $2\times18\delta'$ and 1291 keV=$8\times17\delta'$ are explained in the text. $S_{2\mathrm{p}}$ (Z) for Z=40-84. *Center:* The E^*-distribution in all nuclei with Z=32-35. The maximum at 1024 keV=$6\times18\delta'$. *bottom:* The excitation energy distribution in all nuclei with Z=61-73. Maxima at 531 keV=$4\times7\delta'$, 1059 keV=$8\times7\delta'$ and 1294 keV=$8\times17\delta'$=δm_N.

Fine and superfine structures observed in neutron resonances with parameters $\varepsilon' = 1.2$ keV and ε''=1.4 eV=5.5 eV/4 were introduced together with the parameters of "stabilizing effects of nuclear shells" [7] and empirical observations of many authors on the exact relations between the particle masses, namely the relations m_N=m_μ+6m_π and m_Λ=8m_π (by Y. Nambu), $m_\omega/2$=m_K-m_μ=m_N-m_η=391 MeV=M_q^ω (by G. Wick), m_η-m_μ= m_N-m_K=$m_\Xi/3$=M_q=441 MeV (by R. Sternheimer and P. Kropotkin), $m'_\eta - m_\eta = m_\eta - m_\pi$ (by T. Takabayasi) and $m_{\pi^\pm} - m_{\pi^\circ} = 9m_e$ (by the first author [1,8]).

This allowed us to introduce a common period of the mass discreteness $\delta = 16m_e$, close to the doubled value of the pion β-decay energy. Particle masses ($m_\mu = 13\delta, m_\pi = 17\delta$ and $m_N = 115\delta$), as well as large intervals 391 MeV=$M_q^\omega = 48\delta$ and $M_q = 54\delta$=441 MeV, later used as constituent quark masses in the Nonrelativistic Constituent Quark Model (NRCQM) [9,10]) are shown in Fig. 2 from [1].

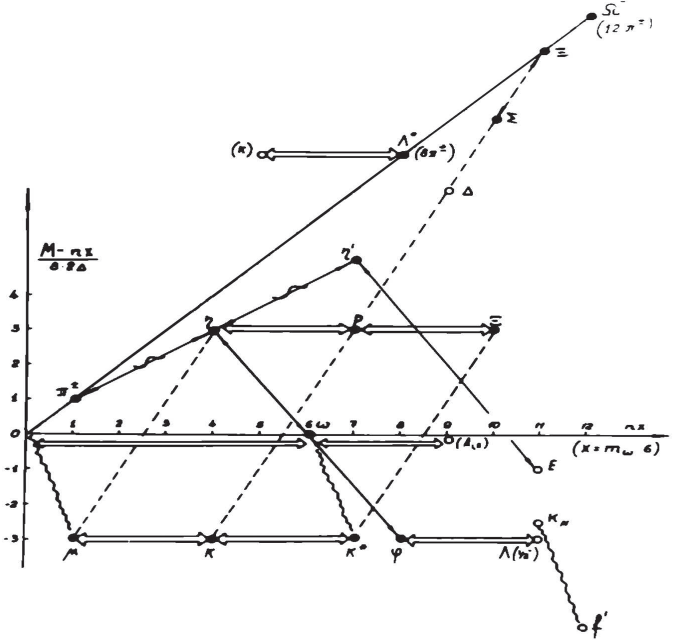

Figure 2: Stable intervals in particle masses found by G. Wick (double arrows) R. Sternheimer (dotted lines) and T. Takabaiasi (arrows). For convenience the integer number $16\delta = 16 \times 16m_e = m_\omega/6$ was subtracted from masses.

The presence of the main CODATA relations (1) for the nucleon masses allows one to consider the previously observed dependence of the two protons separation energies on Z for Z=40-58 and Z=76-84, shown in Figs. 3-4, marked with arrows at the ends of neutron shells at N=50, 82, 126 (see n$\varepsilon_o = 2m_e$ on the right axis and the reference value $S_{\rm 2p}$=10183 MeV in ^{212}Po close to 10ε_o=10220 MeV).

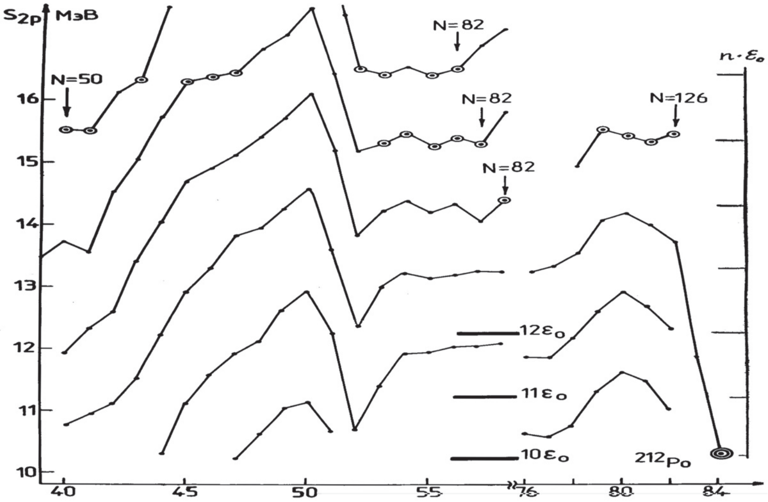

Figure 3: $S_{2\mathrm{p}}$ (Z) for Z=40-84. Double circled is the reference point value $S_{2\mathrm{p}}$=$10\varepsilon_o$ in ^{212}Po. Lines mark groupings in deformed region.

Grouping $S_{2\mathrm{p}}$ values by the number of periods n=10-16 is shown in Fig 3. Near constancy at the end of the closed shell takes place in nuclei differing by ΔZ=1,ΔN=2, and in nuclei differing by ΔZ=2, ΔN (or ^{4}He cluster), ΔE_B turns out to be close to integers $k\ \Delta$=$9m_e$=4.6 MeV. At N=82 for $k\ =\ 20$ ΔE_B=46 MeV (see Fig. 5, left). A similar ΔE_B=147 MeV=32Δ = 18 × 16m_e = 18δ grouping was found in light nuclei (Z ≤26), differing by 4^{4}He cluster (Fig. 5, right [11]). In Table 1 it is shown that the unexpected proximity of these empirical values ΔE_B to the symmetry motivated multiple values $k \times m_e$ is not contained in the existing theoretical models. Three empirical observation are used during production Electron-based Constituent Quark Model (ECQM):

1. Leptons are considered together with the parameters of a very successful Nonrelativistic Constituent Quark Model (NRCQM), namely pion parameters $f_\pi = 130\,MeV, m_\pi$=140 MeV and the constituent quark masses $M_q\ =\ m_\Xi/3$=441 MeV, $M_q^\omega\ =\ m_\omega/2$=391 MeV. The mass of τ-lepton is equal to $2m_\mu$+$4M_q^\omega$.
2. Leptons and hadrons are forming the observed correlations in the mass spectrum with a common period 8.176 MeV=δ = $16m_e$ (Fig. 1 [3,4]), where it is shown that the masses of the fundamental fields $M_Z = m_\mu(\alpha/2\pi)^{-1}$ and $M_{H^\circ} = m_e/3(\alpha/2\pi)^{-2}$, as well as the main parameter of the ECQM and NRCQM models, $M_q = m_e(\alpha/2\pi)^{-1}$, are interconnected by symmetry motivated relations and the common QED correction.
3. In this work, we consider additional empirical observation of the particle mass spectrum and nuclear data, including the important role of neutron resonance data in confirming the QED correction, which is a very important factor in the SM development.

In at least three cases: in the masses of leptons, in the masses of nucleons (CODATA relations), and in the masses of hadrons containing bottom quarks, unexpectedly accurate empirical relations with the electron mass m_e are observed.

Table 1: Proximity ΔE_{B} (keV) to $(45{=}5{\times}9)\varepsilon_o$=45.99 MeV in nuclei differing by $2\Delta Z{=}\Delta N{=}4$, N=82 *center* and to $144\varepsilon_o = 8 \times 18\varepsilon_o$=147.2 MeV, N=20 *right* In nuclei differing by 4α cluster. Small deviations from $k \times \varepsilon_\circ = 2m_e$=1022.0 keV in real values and large deviations in ΔE_{B} drom Finite Range Droplet Model *bottom*, are boxed [10].

Nucl.	^{137}Cs	^{135}La	^{137}La	^{139}La	^{136}Ce	^{138}Ce	^{140}Ce	^{139}La	^{39}K
Z	55	57	57	57	58	58	58	57	19
N	$\boxed{82}$	78	80	$\boxed{82}$	78	80	$\boxed{82}$	$\boxed{82}$	$\boxed{20}$
ΔE_{B}	45970	46018	45927	46024	46087	45997	45996	91975	147160
$n\varepsilon_o$	45990	45990	45990	45990	45990	45990	45990	91980	147168
diff.	$\boxed{-20}$	28	-63	$\boxed{34}$	97	$\boxed{7}$	$\boxed{6}$	$\boxed{-5}$	$\boxed{8}$
Theo.	46340	45950	46820	46970	45960	46850	47160	93200	147450
diff.	$\boxed{350}$	-40	830	$\boxed{980}$	-30	860	$\boxed{1170}$	$\boxed{1220}$	$\boxed{282}$

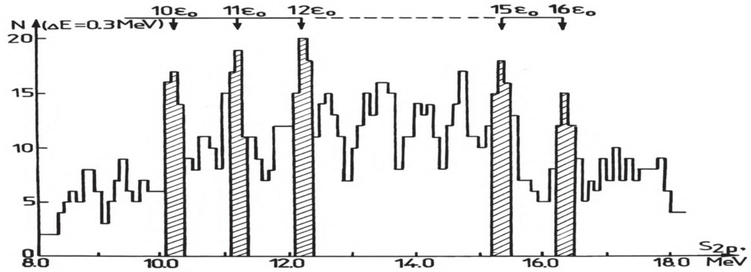

Figure 4: Distribution of $S_{2\mathrm{p}}$ (Z) (averaging 300 keV, step of the ideohistogram - 100 keV). The regions of groupings at multiples of ε_o=1022 keV are shaded.

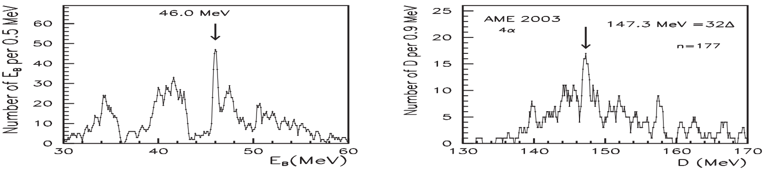

Figure 5: Grouping of ΔE_B in nuclei differing by ^{6}He-cluster (*left*) and by 4 ^{4}He-clusters.

Observed in Fig. 1 discreteness (fine structure) with numbers k=13,14,17 and 18 of the common period δ'=9.5 keV was similar to other empirically found discreteness in nuclear data and particle masses. In particle masses, k=13 corresponds to the masses of the muon and Z-boson (Table 2, periods $\delta = 16m_e$=8.176 MeV and δ°=3.50 GeV), while k=18 (with the same periods) corresponds to the difference in baryon masses due to the appearance of strangeness ($m_s \approx$150 MeV in NRCQM) and due to the residual quark interaction 147 MeV=$(m_Delta - m_N)/2$, as well as the scalar mass 125 GeV.

Here we show that discreteness with k=13 also exists in neutron resonance data. Symmetry motivated relations with k=13, 16-18 in addition to the proximity of the ratio $1/(32 \times 27)115.74 \times 10^{-5}$ to $\alpha/2\pi = 115.96 \cdot 10^{-5}$ provide the production of Table 2.

2. Electron-based Constituent Quark Model

The muon and tau-lepton masses, together with the mass of the constituent quark $M_q^\omega = m_\omega/2$=391.33 MeV, take part in the exact relation (3). There is a proximity of the ratio m_τ/m_{K^*}=1776.9 MeV/891.7 MeV=1.99 to 2.0.

$$m_\tau = 2m_\mu + 2m_\omega \approx 2m_\mu + 4 \cdot 48 \cdot 6m_e = 2m_{K^*} \tag{3}$$

It was found [3,8] that besides the m_μ/m_e=105.658 MeV/0.510.999 MeV=206.768 proximity to an integer (lepton ratio) L=207=16×13-1, the same ratio exists between the vector bosons and constituent quarks masses M_Z/M_q=206.8 and M_W/M_q''=207.3 for $M_q'' = m_\rho/2$=387.6 MeV. For an exactly integer value L one can get an estimate of the respective mass value 441.0 MeV close to $54\delta - m_e$. The initial mass of the baryon constituent quark in NRCQM is three times greater than ΔM_Δ, namely M_q=441 MeV=$m_\Xi/3$. The mass of the meson constituent quark M_q^ω in NRCQM is derived as half of the masses of ω-meson close to 780 MeV=$6f_\pi$, where f_π=130.7 MeV=16δ is the pion β-decay parameter.

Table 2: Presentation of particle masses (3 top sections) and nuclear data (bottom) by the expression n·16m$_e(\alpha/2\pi)^X$M with QED correction $\alpha/2\pi$. Boxed values m$_\mu$, M_Z, M_{H°, $\delta^\circ, \delta, \delta', \delta''$ and ΔM_Δ=m_s, m$_e$/3 are considered in [3.4,7,8]. Intervals in nuclear binding energies (X=0) and fine structure in nuclear states are considered elsewhere.

X	M	n = 1	n = 13	n = 16	n = 17	n = 18
-1	3/2			m_t=173.2		
GeV	1	$\boxed{16M_q=\delta^\circ}$	$\boxed{M_Z=91.2}$	M'_H=115		$\boxed{M_{H^\circ}=125}$
0	1	$16m_e$=$2m_d$-$2m_e$	$\boxed{m_\mu=106}$	f_π=130.7	m_π, Λ_{QCD}	$\boxed{\Delta M_\Delta=147}$
MeV	1	ΔE_B	106	130	140	147
	2	Figs. 6,7	212	262		296
	3	NRCQM		$\boxed{\boxed{M_q^\omega=391}}$		$\boxed{\boxed{M_q=441}}$
	4	Radial excit.			$(b\tilde{b})$=563.0	$(c\tilde{c})$=589.1
	6			m_ω=782		$2M_q$=882
	9				m_c=1270(20)	
	10	$m_\Lambda = 19m_\pi$			1390-1407	
	12	$m_\Omega = 12m_\pi$			1671-1688	
	60	Fig.? in [3]				8848
	64	$\eta_b(1S), \Upsilon(1S)$				9399-9460
1	1	$\boxed{16m_e=\delta=8\varepsilon_\circ}$			$k\delta$-m_n-m_e=	$\boxed{170 = m_e/3}$
keV	1,8,8 · 4	CODATA, Fig.1	3936	δm_N=1293.3	=161.651	
1	1	$\boxed{9.5=\delta'=8\varepsilon'}$	123	152	Δ^{TF}=161	170 (Sn)
keV	2		247 (^{91}Zr)		322 (^{33}S)	340 (^{100}Mo)
2	1, 4	$\boxed{11=\delta''=8\varepsilon''}$	143 (As)		749 (Br, Sb)	Neutron
eV	4, 8		570 (Sb)		1500 (Sb, Pd)	reson.

The above mentioned CODATA relations (1) and the empirical observation used for production of the Electron-based Constituent Quark Model (ECQM) are in agreement with direct observation of the parameters of the very successful Nonrelativistic Constituent Quark Model (NRCQM), namely, the pion parameters $f_\pi = 130\,MeV, m_\pi$=140 MeV and the constituent quark masses $M_q = m_\Xi/3$=441 MeV (maxima at 445 MeV, 3504-3962-4427 MeV), as well as $M_q^\omega = m_\omega/2$=391 MeV and 781 MeV on the total spacing distribution of masses all 198 particles from the PDG-2020 compilation shown in Fig. 6.

The muon and τ-lepton (equal to $2m_\mu$+$4M_q^\omega$ [3,8]) masses together with hadrons form the observed correlations in the mass spectrum with a common period of 8.176 MeV=δ = $16m_e$. The masses of the fundamental fields $M_Z = m_\mu(\alpha/2\pi)^{-1}$ and $M_{H^\circ} = m_e/3(\alpha/2\pi)^{-2}$ in symmetry motivated relations (1:3) with leptons and common QED correction. The important role of neutron resonance data in confirming QED correction and symmetry motivated relations will be seen in the further development of the Standard Model.

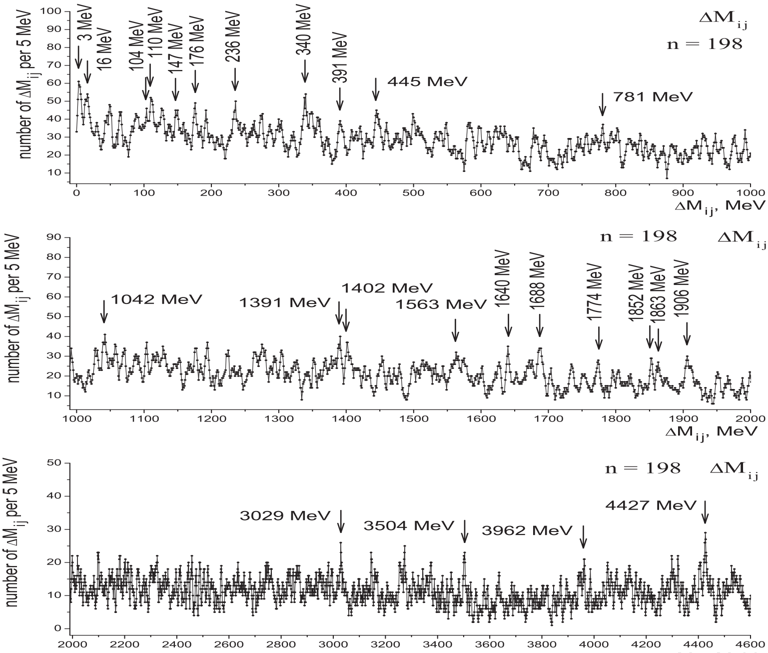

Figure 6: *Top:* ΔM distribution of all differences between particle masses from compilation PDG-2020 (averaging 5 MeV) for the energy region 0–1000 MeV. Maxima at 16 MeV= $2\delta = 2 \times 16m_e$, 391 MeV=$m_\omega/2$, 445 MeV=M_q, 781 MeV=m_ω. *Center:* The same for energy region 2000–4600 MeV. Maxima are at 1774 MeV≈ m_τ=1777 MeV. *Bottom:* The same for energy region 2000–4600 MeV. Maxima are at 3504 MeV≈ $8M_q = \delta^\circ/2$, 3962 MeV≈ $9M_q$ and 4427 MeV≈ $10M_q$.

3. Analysis of neutron resonance data

Resonance parameters, which are investigated within neutron resonance spectroscopy demonstrate the same symmetry motivated relations observed between stable nuclear intervals and in particle masses.

In [11] it was found that for some monoisotopic odd-odd targets, stable intervals can be observed (143 eV in As, 43 eV in Nb and 594 eV in Cs). The same values were found in the positions of strong resonances of many nuclei (43 eV in Nb, 570 eV in Th etc.). In the distribution of relatively strong neutron resonances in Z=33-56 nuclei, maxima at 44 eV and 572 eV were observed (Fig. 7), and in nuclei Z=51-94, maxima at 22 eV and 286 eV. We show here confirmation of the distinguished character of the 4:13 relation between stable intervals in neutron resonances.

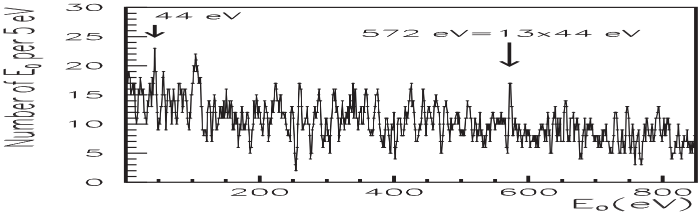

Figure 7: Distribution of positions of relatively strong neutron resonances of all nuclei with Z=33-56 [11]. There is strong resonance in ^{233}Th at 570 eV with $g\Gamma^{\circ}_{n}$=1.1 meV, which means, that neutron separation energy is correlated with the period 573 eV under consideration.

We use here the data for the ^{233}Th and $^{234-236}$U isotopes to check the 1:4:13 relation previously found between the stable intervals in the neutron resonances of many other isotopes. Some results of an earlier analysis of neutron resonance data for ^{233}Th were also given in [13]. These data for structurally important isotopes contain the most numerous lists of resonance parameters (evaluated by F. Gunsing and L. Leal).

Thorium isotopes have 90 protons, corresponding to the filled $f_{7/2}$ subshell. It was noted long ago that the spacing distribution of its L=0 resonances is clearly nonstatistical. On the histogram with the averaging parameter 5 eV in Fig. 8 (top), the equidistancy of the maxima at k=1, 2, 3, 5 of the estimated period 11 eV corresponds (as k=288/11=26) to the strongest maximum at D=288 eV (marked with an arrow). Fixing all such intervals (x=288 eV) in the spectrum of all s-wave resonances (see Fig. 8, center), we obtain maximum at a doubled value of 576 eV. Such an interval corresponds to the distance between strong neutron resonances (maximum at 573 eV in Fig. 2, bottom, with the selection of resonances with a reduced neutron widths greater than 1 meV, deviation from the random level $\approx 3\sigma$). A small maximum at 42 eV on the same distribution (Fig. 8, bottom) corresponds to a 1:13 ratio between strong resonances (between states with a relatively large single-particle component in the wave function). Similar correlations were found earlier in strong resonances of many different isotopes (Fig. 7).

The spectrum of highly excited ^{236}U states contains 3164 states with the spacing distribution shown in Fig. 9, top (all states have L=0). Neutron resonances were selected according to spin J (n=1438 for J=3 and n=1734 for J=4), and respective spacing distributions are given in Figs. 9 and 10.

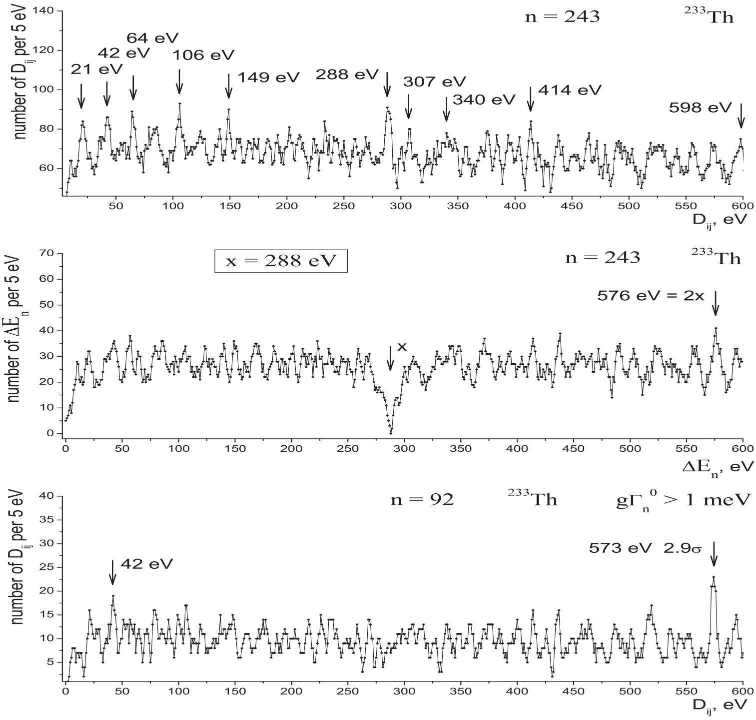

Figure 8: *Top:* Spacing distribution of all L=0 neutron resonances in ^{233}Th. *Center:* Spacing distribution of L=0 neutron resonances in ^{233}Th adjacent to intervals D'=x=288 eV. *Bottom:* Spacing distribution of all L=0 strong neutron resonances in ^{233}Th.

In spacing distribution of ^{236}U resonances with J=3 (Fig. 9, 2nd line) a grouping of 4 maxima at 55 eV=$5\delta''$ is situated at the doubled position of the maximum at 27.8 eV (see Fig. 9 center). Resonances forming the maximum at =393.5 eV (close to 396 eV=$4\times 9\times 11$ eV) are frequently appear together with another resonance situated 288 eV away from them (see maximum at 287.9 eV, close to 2×143 eV=$2\times 13\delta''$). This interval, coinciding with D'=288 eV in ^{233}Th (Fig. 8, top), has exactly twice the value of the interval 143.4 eV in independent spacing distribution for J=4 resonances (Fig. 10, top). This interval appears together with the interval 44.2 eV=$4\delta'' = 4\times 11$ eV.

In spectrum of ^{236}U (Fig. 9, top) there is a small maximum at 43 eV, but only by selecting resonances according to their spin and by using correlation analysis of their decay properties one can hope to obtain further fundamental information.

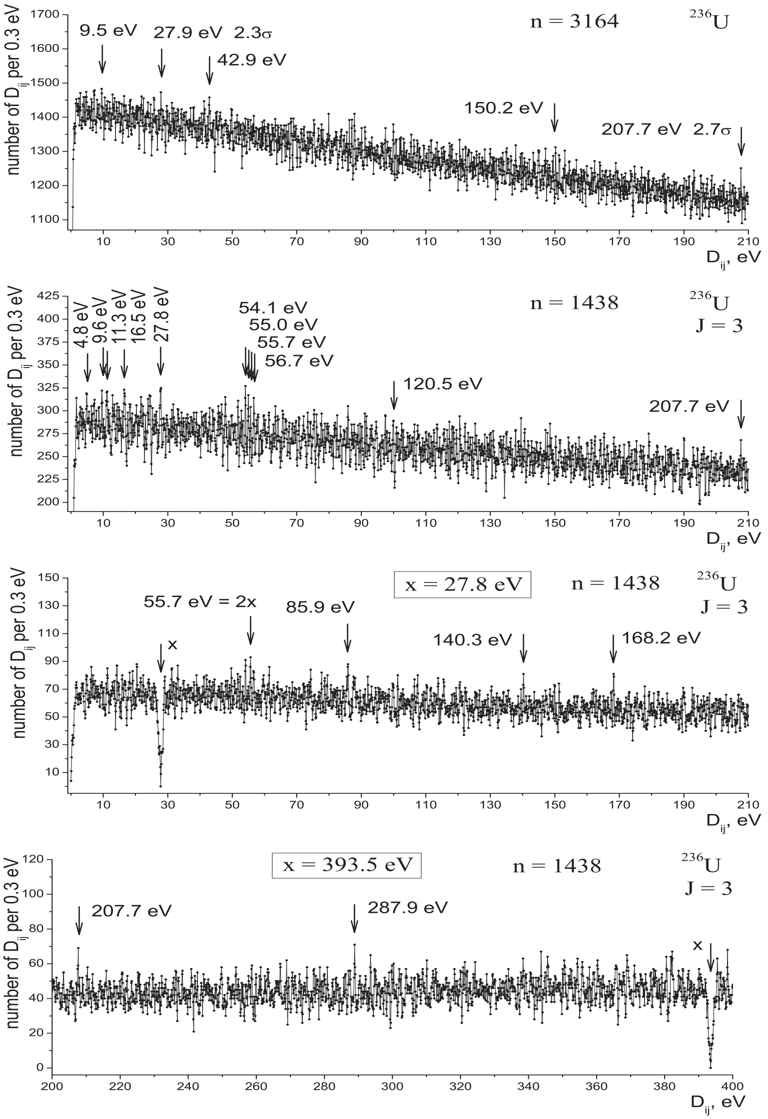

Figure 9: *Top*: Total spacing distribution in all ^{236}U resonances. *2nd line*: The same for resonances with J=3. *Center:* Adjacent interval distribution for J=3 ^{236}U resonances for x=27.7 eV=(55 eV=5δ'')/2. *Bottom*: The same for x=393.5 eV (close to 396 eV=4 × 9×11 eV). Maximum at 288 eV (close to 2 × 143 eV=2 × 13δ'') coincides with D'=288 eV in ^{233}Th (Fig. 8, top).

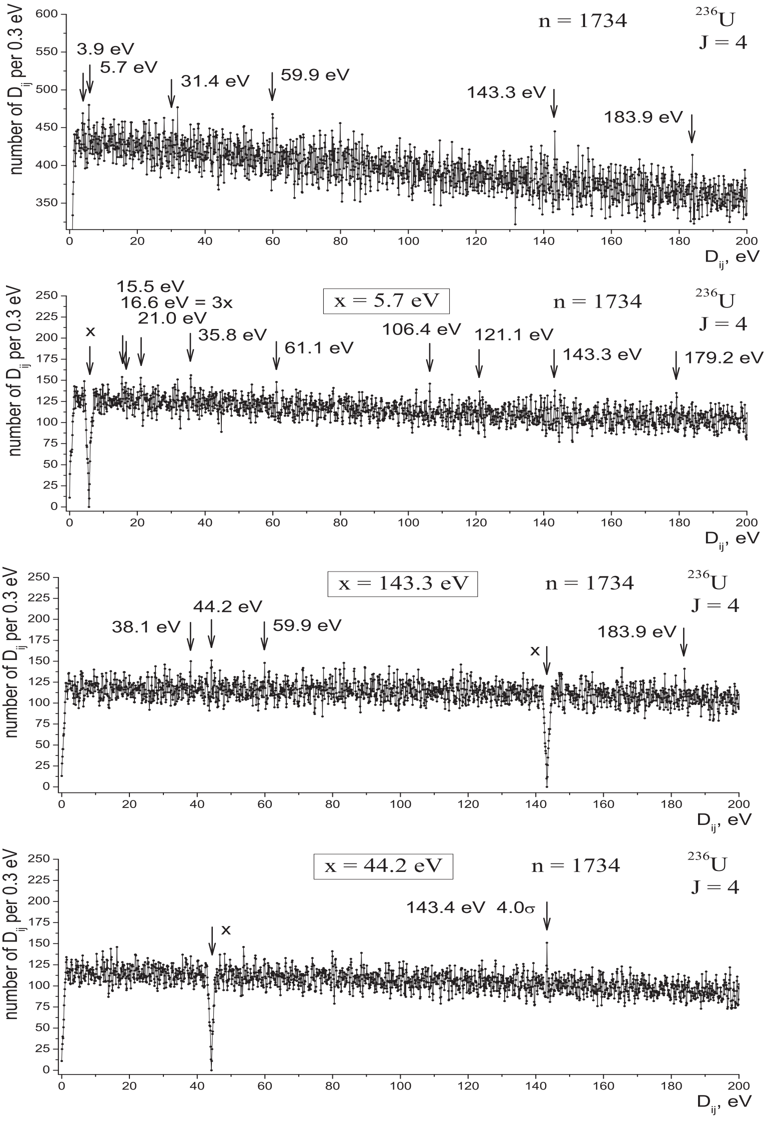

Figure 10: *Top*: Spacing distribution of all ^{236}U neutron resonances with J=4. *2nd line*: Adjacent interval distribution of ^{236}U resonances for x=5.7 eV. *Center:* Adjacent interval distribution for J=4 ^{236}U resonances for x=143.3 eV. *Bottom*: The same for x=44.2 eV. 4Σ deviation is marked. An exact ratio 13:4 = 143.4:44.2 is considered in the text.

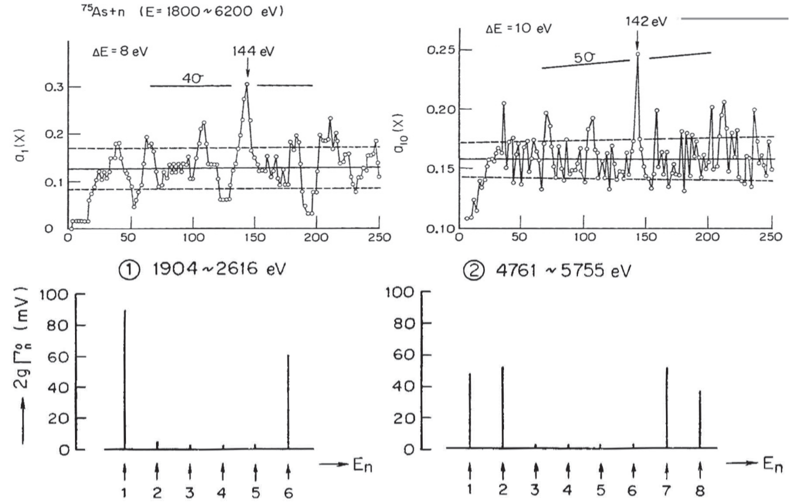

Figure 11: *Top:* The spacing distribution in neutron resonances of the compound nucleus ^{76}As with averaging interval ΔE. The response function of the program "Period" means the number of resonances coinciding with the periodic system (k is the number of periods x, one for the left distribution and ten for the right distribution) [14]. *Bottom:* The periodicity in the positions of neutron resonances of the target ^{75}As, found in [14].

Considering the role of the ratio k=13 in particle masses [8,12], discussed in the Introduction, we could mention observations of this ratio in neutron resonance spectra of other isotopes [13,14]. Observation by K. Ideno and M. Ohkubo of the periodicity in resonances of As [14] is shown in Fig. 11 (maxima at $D = k \times 13\delta'' = k \times 143\,\mathrm{eV}$ are given as deviation in units of σ). Two examples of long range correlations are presented.

Discreteness with k=10,12,14 of the period of $13\delta'$=123 keV in $E^*(0^+)$ of ^{108,110,112}Cd was noticed.

4. Conclusions

Symmetry motivated relations 1:9:13:16:17 between particle masses and stable nuclear intervals of the few-nucleon-, fine- and superfine-structures effects are considered here as an indirect check of the ECQM model with the parameter $\alpha/2\pi$ corresponding to the QED correction due to influence of the condensate. This factor can be indirectly studied in nuclear data. Important application of this factor can be seen in empirical analysis of particle mass data. In Table 3 from [8] a coincidence of two estimates of the mass of the constituent quark $M_q \approx 441\,\mathrm{MeV}$ used in NRCQM and ECQM models are presented. The first estimate is derived from the coincidence of the ratio m_μ to M_Z with $\alpha/2\pi$ and $L = 13 \times 16 - 1$. The second estimate is obtained from empirical mass of the scalar ($\tilde{\mathrm{bb}}$) meson ($m(\eta_b) = 64M_q$).

We see that any confirmation of different aspects of CODATA relations as multiple relations with the real mass of the electron, its symmetry and QED correction could be

Table 3: Comparison of the SM and NRCQM parameters m_μ=105.659375(35) MeV and m_e=510.998328(11) keV with QED radiative correction $\alpha/2\pi$=116.0·10^{-5} [8].

	Values	Mass and ratios
1	Ratio=m_μ/m_e	206.768
2	(L - ratio)/L	112.08·10^{-5}
3	m_μ/M_Z	115.9·10^{-5}
4	m_e/M_q	115.7·10^{-5}
5	$M_q = m_{\Xi^-}/3$	441.5 MeV=54 · 16m_e
6	M_Z/L=$M_q(1-\alpha/2\pi)-m_e$	$\boxed{440.5\,\mathrm{MeV}=M_q^{red}}$
7	$(3/64)m(\eta_b)$	$\boxed{440.6\,\mathrm{MeV}}$

used for SM development. The unexpectedly universal relations in the neutron resonance positions and spacings signal fundamental aspects of nuclear physics [16,17].

The symmetry motivated relations with k=13 in the nuclear data, manifested in the stability of the intervals, are associated with the same discreteness in the particle masses and result in the lepton ratios and masses of both heavy leptons.

References

1. S.I. Sukhoruchkin, *Stat. Prop. Nuclei*, Pl. Press, 1972, p. 215.
2. P. Mohr, D.B. Newell, B.N. Taylor, Rev. Mod. Phys. **88** (2016) 035009.
3. S.I. Sukhoruchkin, Nucl. Part. Phys. Proc. **312-317** (2021) 185.
4. S.I. Sukhoruchkin *et al*, Proc. ISINN-27, pp. 330.
5. Y. Nambu, Nucl. Phys. A **629** (1998) 3c.
6. S. Weinberg, CERN Courier **53** (2017) No 3, p. 31.
7. H. Schopper (Ed.), Landoldt-Börnstein New Series, vol. **I/25 E**. Springer, 2013.
8. S.I. Sukhoruchkin, Nucl. Part. Phys. Proc. (in press).
9. C. Itoh *et al.*, Phys. Rev. D **40** (1989) 3660.
10. L.A. Glozman, Nucl. Phys. A **629** (1998) 121c.
11. S.I. Sukhoruchkin *et al*, Proc. ISINN-19, JINR E3-20-12, p. 308.
12. S.I. Sukhoruchkin, Nucl. Part. Phys. Proc. **309-311** (2020) 67.
13. H. Schopper (Ed.), LB New Series, vol. **I/26A**, p. 59. Springer, 2015.
14. K. Ideno, M. Ohkubo, J. Phys. Soc. Jpn. **30** (1971) 620.
15. S.I. Sukhoruchkin *et al*, Proc. ISINN-3, Dubna, 1995. JINR E3-95-37, p. 330.
16. S.I. Sukhoruchkin *et al*, *Fundamental aspects of neutron spectroscopy*, these Proceed.
17. S.I. Sukhoruchkin, Z.N. Soroko, M.S. Sukhoruchkina, *Nonstatistical effects in resonances of heavy nuclei*, these Proceedings.

FUNDAMENTAL ASPECTS OF NEUTRON SPECTROSCOPY

S.I. Sukhoruchkin, Z.N. Soroko, M.S. Sukhoruchkina

Petersburg Nuclear Physics Institute, NRC "Kurchatov Institute", 188300 Gatchina

1 Introduction

Neutron resonance spectroscopy provides data on a large number of highly excited nuclear states. This information can be used to check nuclear microscopic models, including the Nonrelativistic Constituent Quark Model (NRCQM), which, according to R. Feynman, is successful [1]. Its extension, the Electron-based Constituent Quirk Model (ECQM), combines the properties of hadrons and leptons with the universal character of the influence of a physical condensate (vacuum) [2]. ECQM model provides a possibility to estimate the discreteness in particle masses and energies of nuclear states, as well as to explain nonstatistical effects in the neutron resonance positions and spacing distributions. The systematic character of these effects is due to the fundamental dynamics, which is manifested itself in the CODATA relations for the nucleon masses. Empirically, it was found that the QED correction $\alpha/2\pi$ coincides with the ratios between the parameters of NRCQM (M_q=441 MeV), single-particle structure ($m_e = \varepsilon_\circ/2$) and fine and superfine structures in neutron resonances [3]. In Tables 1 and 2 and in Figs. 1 and 2, the main empirical observations used in the development of the ECQM model are presented [4-7].

Table 1. Intervals in particle masses (MeV), noted by G. Wick, R.Sternheimer and P. Kropotkin.

Author	Part.$_{top}$	Mass	Part.$_{bottom}$	Mass	Interval	Mass	n	$n \times \delta$	diff.
Wick	K°	497.62	muon	106.16	$K^\circ - \mu$	391.45	48	392.45	1.00
Wick	neutron	939.57	η	547.86	$n - \eta$	391.71	48	392.45	0.71
Sternheimer	η	547.86	muon	106.16	$\eta - \mu$	441.70	54	441.50	0.20
Sternheimer	neutron	939.57	K°	497.61	$n - K^\circ$	441.96	54	441.50	0.46
$\boxed{\text{Kropotkin-CQM}}$	Ξ	1342 /3	M_q		$\boxed{M_q}$	$\boxed{441}$	$\boxed{54}$	441.50	
Sternheimer	Σ°	1383.7	neutron	939.57	$\Sigma^\circ - n$	441.1	54	441.50	0.4
Sternheimer	$K^{*\pm}$	891.55	ω	782.65	$K^{*\pm} - \omega$	109.01	13	106.29	2.72
	$K^{*\circ}$	895.81	ω	782.65	$K^{*\circ} - \omega$	113.16	13	106.29	
Fig. 2, top	K_3^*	1776(7)	$K^{*\circ}$	895.81	$K_3^* - K^*$	880(7)	108	883.0	3(7)
Fig. 2, bottom	ω_3	1667(4)	$\boxed{\omega}$	$\boxed{782.65}$	$\boxed{\omega_3 - \omega}$	884(4)	108	883.0	$\boxed{1(4)}$

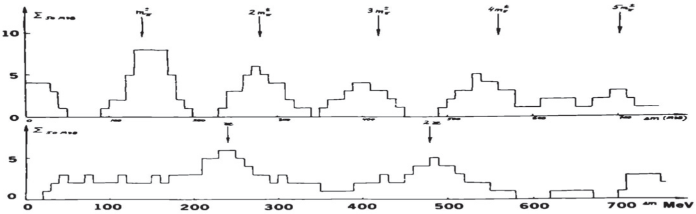

Figure 1: Ideohistograms of distribution of differences between masses of baryon singlets (top, ΔM with the averaging interval 25 MeV). Arrows mark the period 140 MeV=$m_{\pi^\pm}$.

Y. Nambu was the first who noticed that the mass of a pion is a common parameter of the particle mass spectrum [4]. The representation of baryon singlet masses as an integer pion mass is shown in Fig. 2 as a straight line passing through the hyperons Λ, Ξ, Ω and the charmed quark $m_c \approx 9m_\pi$ (dark circle in Fig 2). In the previous report at this conference it was shown that the neutron mass m_n deviates from the integer m_n by 161 keV$=m_\pi(\alpha/2\pi)$. The factor $\alpha/2\pi = 115.96 \cdot 10^{-5}$, which is very close to the ratio $1/(32 \times 27)115.74 \times 10^{-5}$, was found empirically [3] as the ratio between the stable mass/energy intervals shown in lines 3-6 of Table 2.

The initial mass of the baryon constituent quark in NRCQM $M_q = m_e(\alpha/2\pi)^{-1}$ was introduced by P. Kropotkin (under the name ”gammon”) long before NRCQM [8,9]. With the stable interval 391 MeV$=m_\omega/2 = 3f_\pi$, introduced by G. Wick (Table 1 [7]), it corresponds to the discreteness in particle masses with periods 130-140-147 MeV (close to f_π, m_π, Fig. 1) and nucleon mass evolution from $3M_q$ to $m_\omega + M_q/3$=932 MeV (Fig. 2).

Table 2. Comparison of the parameter $\alpha/2\pi$=115.96$\cdot 10^{-5}$ with the anomalous magnetic moment of the electron $\Delta\mu_e/\mu_e$ [8-10] (top line), parity nonconservation parameter $\eta_\pm/2$ (observation by J. Bernstein [8-10], second line) and with the ratios between the mass/energy values introduced in [3] (lines No 4-6) and other parameters mentioned in literature (below).

No.	Parameter	Components or the ratio	Value $\times 10^5$
	$\Delta\mu_e/\mu_e$	$=\alpha/2\pi$-0.328 α^2/π^2	$\boxed{115.965}$
	$\eta_{+-}/2$ [10]	2.232(11)$\times 10^{-3}/2$	112(1)
	$2\delta m_\pi - 2m_e$	$\boxed{(81652(10)\,\text{keV})/(16m_e{=}\delta)}$	132(12)
1	$\delta m_\mu/m_\mu$	$(23\times 9m_e\text{-}m_\mu)/m_\mu$	112.1
2	m_μ/M_Z	$\boxed{m_\mu/M_Z{=}91182(2)\,\text{MeV}}$	$\boxed{115.87(1)}$
3	$\delta m_n/m_\pi$	$\boxed{(\text{k}\times m_e\text{-}m_n)/m_\pi{=}161.649\,\text{keV}/m_\pi}$	$\boxed{115.86}$
4	$\varepsilon''/\varepsilon'$	1.35(2) eV/1.16(1) keV	116(3)
5	$\varepsilon'/\varepsilon_o$	1.16(1) keV/ε_o=1022 keV	114(1)
6	$(\varepsilon_o/6)/\Delta M\Delta$		116.02
7	$(\Delta M_\Delta{=}M_q/3)/M_{H^\circ}$	147 MeV/125 GeV	118
8	δ/δ°	$\delta^\circ = 16M_Z/(L = 207)$=7.048 GeV	116.0
9	m_d/m_b, [10]	m_d=4.78(9) MeV/ m_b=4.18(3) GeV	114
10	m_u/m_c, [10]	m_u=2.2(5) MeV/ m_c=1275(25) MeV	173(40)
11	Sb, D(187 eV)/161 keV	(373 eV/2=187 eV)/160 keV	114
12	Pd, D(1497 eV)/1293 keV		115.7
13	Hf, D(1501 eV)/δm_N	^{172,176}Hf $E^*(0^+)$=1293 keV=δm_N	116.1
14	Os, D(1198 eV)/$2m_e$	^{178,180}Os $E^*(0^+)$=1023 keV=$2m_e$	117
14	Pd,Cd D(1501 eV)/δm_N	^{97}Pd $E^*(2^+)$=1293 keV	
15	D(1585 eV)/$8m_e/3$[12, 13]	^{even}Sn $E^*(0^+)$=$4m_e$	
16	Cd-Xe D(1437 eV)	^{112}Cd $E^*(0^+)$ 1222 keV	117
17	D(1723 eV) [12,13]	^{110}Cd $E^*(0^+)$ 1473 keV	116
18	D(2007 eV) [12,13]	^{108}Cd $E^*(0^+)$ 1721 keV	117
19	Te D(2375 eV)/$4m_e$ [20]	^{even}Te $E^*(0^+)$=$4m_e$	116
20	N=90 D(793 eV)/$4m_e/3$	$E^*(0^+)$=682 keV=$(4/3)m_e$	
21	D=1.19 keV/$\varepsilon_\circ$ [14]	ΣE^*=$\varepsilon_\circ$=1022(2) keV)	117
22	D=1188 keV/$\varepsilon_\circ$ [15]	ΣE^*=$\varepsilon_\circ$=1022(2) keV)	117
23	ε'=1.276 keV, Fig. 4	$\varepsilon' \cdot (A/A+1) : \varepsilon_\circ$	119
24	^{241,242,243}Pu, Figs. 8-10	D=99(2) eV)/2($E^*(2^+)$=42.5 keV)	117
25	^{239}U	D=1506 eV/1295 keV	116

Parameters of the ECQM model $M_q^\omega = m_\omega/2 = 3f_\pi = 48\delta$=391 MeV and $M_q = m_\Xi/3 = 3\Delta M_\Delta = 54\delta$=441 MeV are boxed in Table 1. Important relations between these parameters and lepton masses are shown at the top of Fig. 2, where a coincidence of the difference between the masses of the ω_3 meson and ω meson (boxed in bottom line of Table 1) and the corresponding difference between the masses of K^* and K_3^* mesons to the value of $2M_q$=882 MeV, shown by three parallel lines in Fig. 2 (and the difference between them of 1 MeV, boxed in bottom line of Table 1) is observed. The evolution of the nucleon mass from $M_q \approx m_\Xi/3$ ends at the mass of the nucleon in the nuclear media $m \approx m_N$-8 MeV=932 MeV=$m_\omega + \Delta M_\Delta$ [21,22]. So, we see that the components of the ratio, found by P. Kropotkin, $m_e/M_q = \varepsilon_\circ/3\Delta M_\Delta = \alpha/2\pi$ (line in Table 2) correspond to several clearly interpreted parameters.

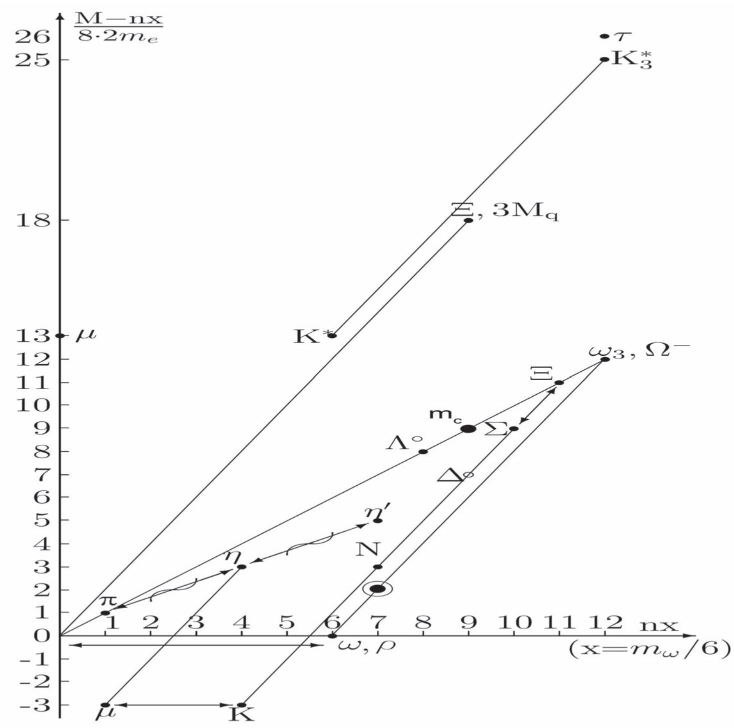

Figure 2: The evolution of the baryon mass from $3M_q$ to the nucleon mass M_N is shown in a two-dimensional presentation: the values in the horizontal direction are given in units of $16 \cdot 16m_e = f_\pi$=130.7 MeV, the remainders M_i-n$(16 \cdot 16m_e)$ are plotted along the vertical axis in $16m_e$. The nucleon mass in a nuclear medium (circled point) is close to the sum ΔM_Δ+$6f_\pi$. Three different slopes correspond to three pion parameters: $f_\pi = 16\delta$, $m_{\pi^\pm} = 17\delta$ and $\Delta M_\Delta = 18\delta$. The mass of the τ lepton is close to $2m_\mu + 2m_\omega$.

2 Fine structure in neutron resonances

Using a special table BNL-325 [14] where ten strong resonances in each nucleus are presented, the grouping was found at E_n=$2\varepsilon'$ and $4\varepsilon'$ with the fine structure parameter ε'=1.188 eV. This common parameter was determined from the correlations noticed by M. Ohkubo [15] in the positions of resonances in the compound nuclei ^{82}Br, ^{124}Sb, and ^{141}Ce. Other stable intervals in spasing of neutron resonances were observed in [16-20].

The strong neutron resonance position E'_n (after recoil correction) is the difference between the E^* state with a relatively simple wave function structure and S_n. The value 18.8 keV=$2\delta'$ (found as a maximum in the distribution of positions of relatively strong neutron resonances of light N-even nuclei Z$\leq$28, Fig. 30, top) corresponds to the 4th maximum in spacing distribution of neutron resonances in the near-magic ^{61}Ni (Fig. 30). 6 out of 14 values E_n=E^*-S_n, forming a maximum at 18.8 keV, were obtained from Z-magic nuclei (Z=20, 28). Parameters δ'=19 keV/2=9.5 keV and ε'=δ'/8=1.2 keV [21] are given in Table 3 (bottom).

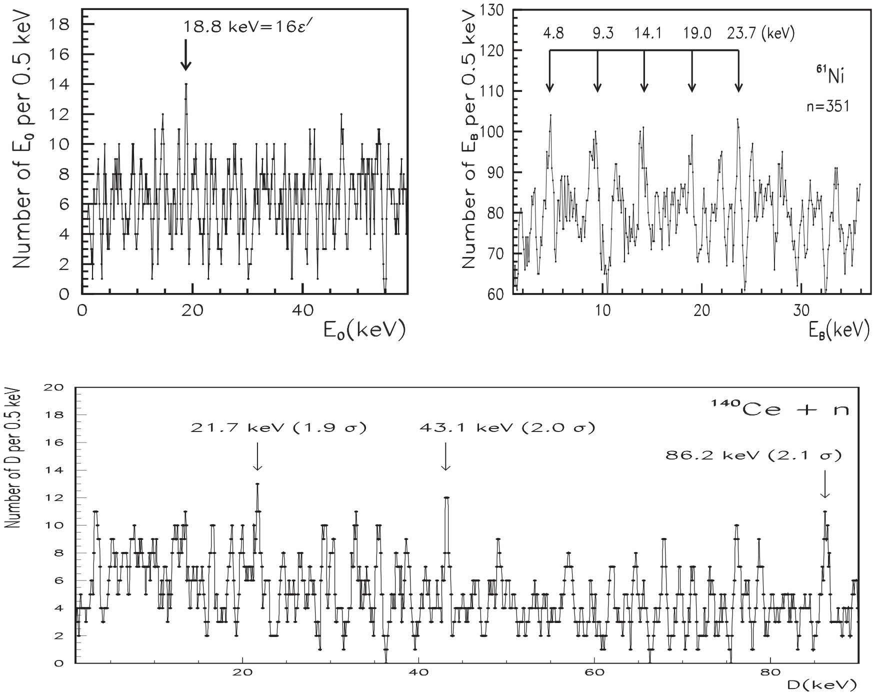

Figure 3: *Top:* Distribution of resonance positions in all N-even light nuclei. *Center:* Distribution of neutron resonance spacing in the target ^{60}Ni (the number of resonances n=351). *Bottom:* Spacing distribution of ^{141}Ce neutron resonances (period 21.7 keV).

Table 3. Comparison of positions and spacings in light and near-magic nuclei with integer values of the fine structure parameter $\varepsilon' = \delta'/8 = 1.188\,\mathrm{keV}$. *Top:* Positions E'_n of strong neutron resonances in light and magic nuclei and periodicity in the spacing distributions in resonances ^{61}Ni (top right). *Center:* Values E_n in nuclei with N=83=82+1, maxima in spacing distributions ^{141}Ce. *Bottom left:* The positions of strong neutron resonances in isotopes with Z=35-39 are compared with the integer of the period ε'=1.188 keV=9.505 keV/8, found in the positions of strong resonances in Z=57-59, N=83 nuclei (center). *Bottom right:* Excitation energies E^* of ^{143}Ce. Boxed are values ε'=1.188 keV=9.505 keV/8, δ', $2\delta'$ and $(9/4)\delta'$ discussed in the text.

Nucl.	Ca-Ni	^{61}Ni	^{61}Ni	^{61}Ni	^{61}Ni	^{61}Ni Fig. 3, center
l_n	l_n=0	D(keV)				
E_n	18.8	4.8	9.3	14.1	19.0	24.7
$k(\varepsilon')$	16	4	8	12	16	20
$k \times \varepsilon'$	19.0	4.8	9.6	14.4	19.0	24.7

Nucl.	^{141}Ce	^{141}Ce	^{142}Pr	^{141}Ce	^{141}Ce	^{141}Ce Fig. 3, bottom
J^π_i	$1/2^+$	$1/2^+$	$(5/2^-)$			
Γ^o_n,meV	660*	3060*	160	D	D	D
E_n	9.573	21.570	9.598	21.7	43.1	86.2
E^*,E'_n	$\boxed{9.505}$	$\boxed{21.418}$	$\boxed{9.530}$			
$k(8\varepsilon')$	1	9/4	1	9/4	9/2	9
$k{\times}8\varepsilon'$	$\boxed{9.504}$	21.384	$\boxed{9.504}$	21.4	42.5	85

Nucl.	^{140}La	^{80}Br	^{82}Br	^{86}Rb	^{143}Ce	J^π_o=3/2$^-$
J^π_i	3^+	l_n=0	l_n=0	l_n=0	$7/2^-$	$5/2^-$
Γ^o_n,meV	54	72.0	120	159	E^*	E^*
E_n	1.179	1.201	1.209	2.398		
E^*,E'_n	$\boxed{1.170}$	$\boxed{1.186}$	$\boxed{1.194}$	2.370	$\boxed{18.9}$	42.3
$k(8\varepsilon')$	1/8	1/8	1/8	2/8	2	9/2
$k{\times}8\varepsilon'$	1.188	1.188	1.188	2.376	19.0	42.77

It was noticed [15] that in ^{141}Ce, the positions of the two strongest resonances (marked with * and ** in Table 2) are in the ratio 9:4=2.25 (2.253, in fact). The same ratio (2.237) exists between the energies of low-lying excitations ^{143}Ce (Table 2, center). The triplet of these closely spaced levels (the next E^* is at 633 keV) is the result of the residual interaction between three valence neutrons. One could notice a 1:2 ratio of the values E'_n in ^{141}Ce to E^* in ^{143}Ce (ratio 0.505). E'_n of strong s-resonances in some other N=83 nuclei are related to these E'_n. For example, E'_n in ^{142}Pr is close to that of ^{141}Ce (marked as $8\varepsilon'=8\times1.188$ keV), while E'_n in ^{140}La is close to ε' (see Table 2).

In the near-magic ^{145}Sm (N=83), the position of the p-wave resonance with the largest Γ^1_n is close to ε', while the stable spacing of its s-wave and p-wave resonances (n=143, D=3689 eV and n=62, D=2485 eV, see Fig. 3) are close to $3\varepsilon'$=3564 eV and $2\varepsilon'$=2376 eV.

Stable intervals D=595 eV=$\varepsilon'/2$ and D=294 eV=$\varepsilon'/4$ were found in resonances ^{134}Cs and ^{128}I.

It was found that the clustering of strong resonances in ^{82}Br [15] has a small (0,03) occasional probability of grouping. It is shown in Table 3 that E'_n of the strongest resonances in ^{80}Br, ^{82}Br and ^{86}Rb are close to ε' and $2\varepsilon'$. In ^{182}Ta, E'_n of the two strongest s-resonances are ε' and $\varepsilon'/2$.

In this work, we show that in the D-distributions of neutron resonances in ^{145}Sm (for orbital momenta L=0 and 1, Fig. 2, top and bottom), the maxima are located exactly at $3\varepsilon'$ and $2\varepsilon'$.

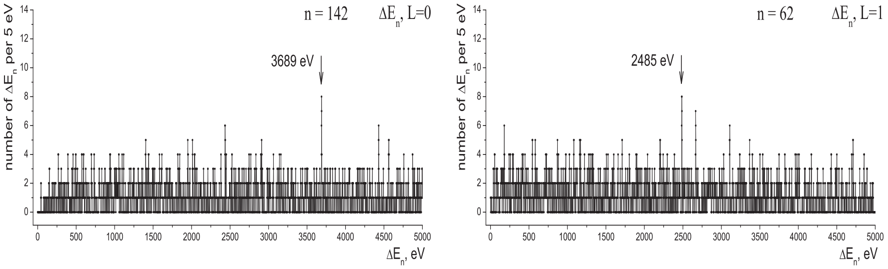

Figure 4: Spacing distributions of neutron resonances in ^{145}Sm (for orbital momenta L=0 and L=1 with maxima at $3\varepsilon'$ and $2\varepsilon'$ (3689 eV/2485 eV=1.48≈3/2, ε'=1.226 keV).

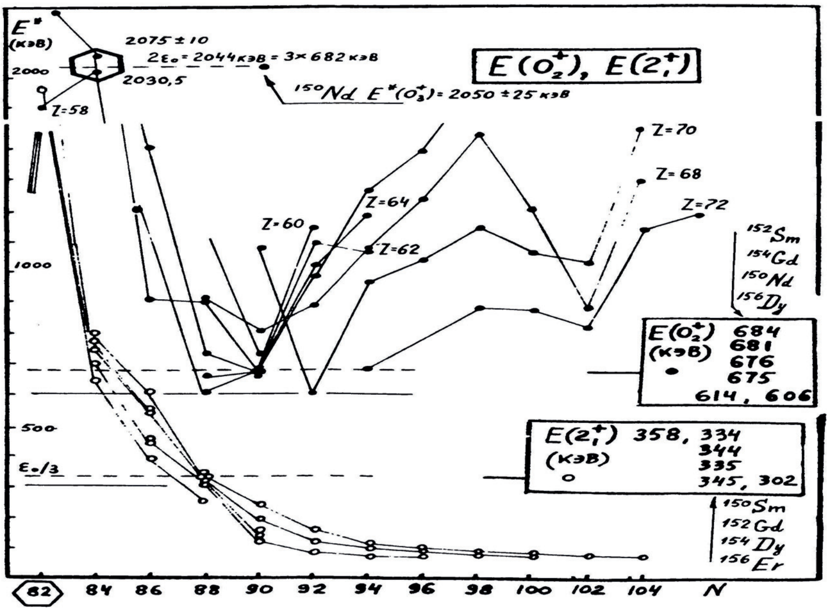

Figure 5: Bunching of energies of 0^+ excitations of nuclei with the number of neutrons 90 (filled $2f_{7/2}$ neutron subshell) at a value of $2/3\varepsilon_o$=682 keV. The values of the excitations are indicated by dark circles and are connected by lines for each serial number with the corresponding Z on the right side. In the same nuclei (neutrons number N = 62-104), the first excitations (2^+) are shown in the figure with light circles. When the number of neutrons is 88 = 90-2, the grouping of the values of 2^+ excitations occurs at a value of 340 keV=$\varepsilon_o/3$. The $\varepsilon_o/3$, $(2/3)\varepsilon_o/3$ and $2\varepsilon_o$ energy levels are shown with dashed lines. The top of the figure shows the closeness to $2\varepsilon_o$ of the energies of the nuclei levels ^{132}Ce (N = 84 = 82 + 2) and ^{150}Nd (N=90).

3 Superfine structure in neutron resonances

The superfine structure in the position and spacing distribution of neutron resonances was found in different nuclei by many authors [15-20]. Selecting the reduced widths of neutron resonance, the positions and the spacing distributions shown in Fig. 6 were obtained. There is a proximity of the maximum in positions of resonances at 5 eV to four intervals $\varepsilon'' = 5.5\,\mathrm{eV}/4{=}1.34\,\mathrm{eV}$, observed in sum spacing distribution [3]. For example, in the niobium, the position of the strongest resonance (Γ_n^o=218 meV) at 5.78 eV (close to 5.5 eV=$\delta''/2$=11 eV/2) is four times the position of the resonance at 1.34 eV=ε''.

An example of superfine structure in the spacing distribution of strong neutron resonances (corresponding to highly excited states with a relatively simple wave function structure) was found in ^{238}Np. Selecting the reduced widths of neutron resonance larger than 50 and 100 meV, we obtained the spacing distributions shown in Fig. 7. From the proximity of the doublet of resonance positions at 1.32 eV and 1.48 eV to $\varepsilon'' = 5.5\,\mathrm{eV}/4 = 1.38\,\mathrm{eV}$ and the position of the strongest resonance (Γ_n^o=218 meV) at 5.78 eV to 5.5 eV, we see that stable intervals 4.1 eV, 5.6 eV and 16.4 eV are close to $3\varepsilon''$, $4\varepsilon''$ and $12\varepsilon''$.

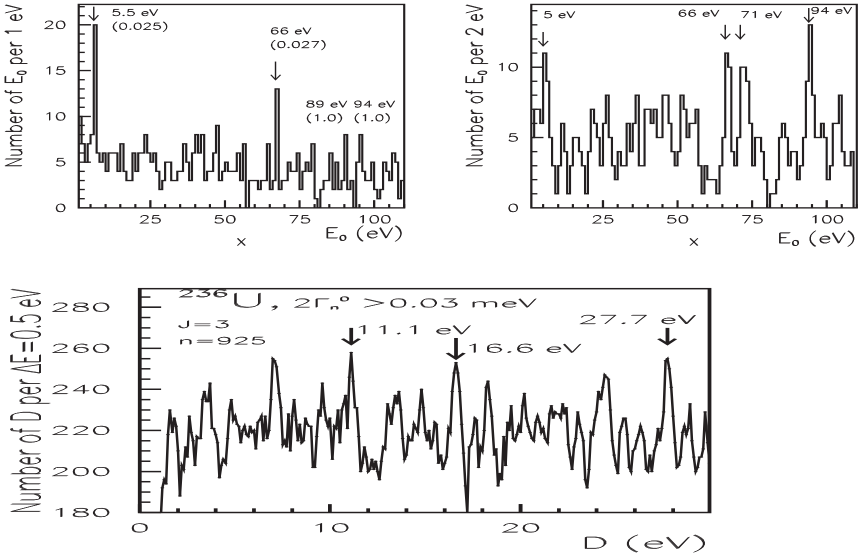

Figure 6: *Top*: Distribution of neutron resonance positions (1970s) by selection of one resonance (max Γ_n^o) in the interval 10 eV and 100 eV. *Bottom*: Spacing distribution of J=3 ^{235}U resonances. Integers k=1, 2, 3, 5, 12, 13 and 17 of the period of 5.5 eV=$\delta''/2$ are marked.

In Nb (Fig. 7), positions of the doublet of resonances at 1.32 eV and 1.48 eV are close to the maximum (at 1.1 eV) in the spacing distribution (top), while in the distributions for more strong resonances maxima are observed at 4.1 eV=$3\varepsilon_\circ$, 5.6 eV=$4\varepsilon_\circ$ and 16.4 eV=$12\varepsilon_\circ$, as well as at 54.8 eV=$5\delta'$=$40\varepsilon_\circ$ and 87.8 eV, close to 88 eV=$8\delta'$=$64\varepsilon_\circ$.

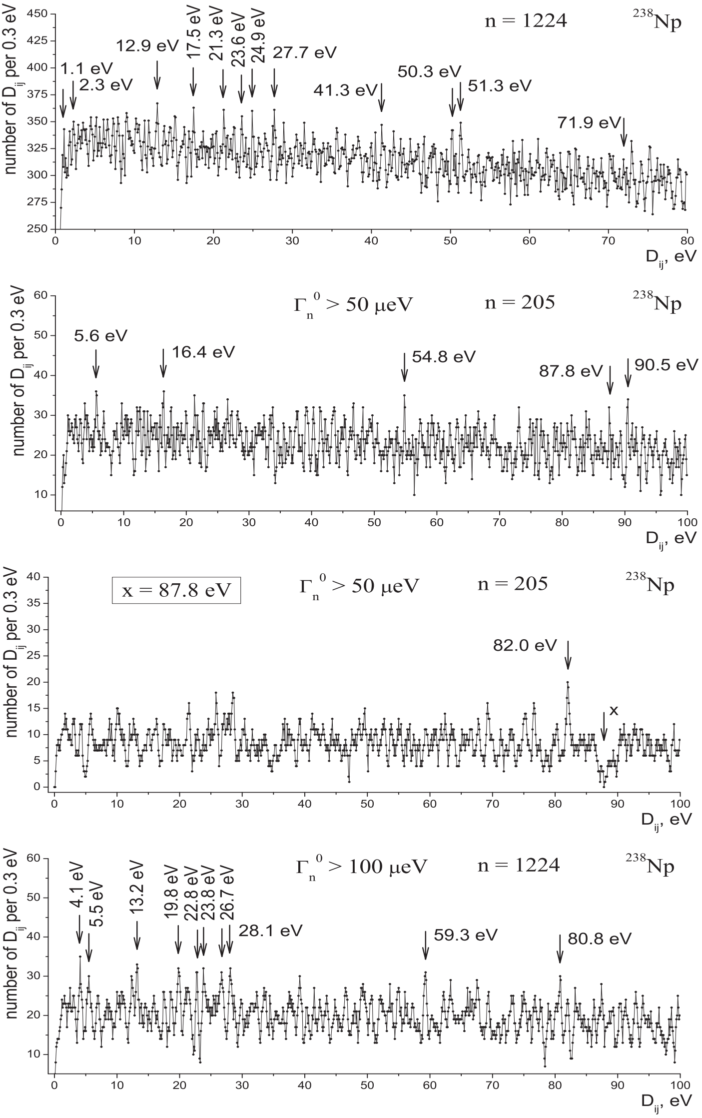

Figure 7: *Top*: Total spacing distribution of all resonances in ^{238}Np. *2nd line*: Spacing distribution of resonances in ^{238}Np with $\Gamma_n^\circ \geq 50\mu$eV. *Center*: Adjacent spacing distribution of resonances in ^{238}Np with $\Gamma_n^\circ \geq 50\mu$eV for the fixed interval x=87.8 eV. *Bottom*: Spacing distribution of resonances in ^{238}Np with $\Gamma_n^\circ \geq 100\mu$eV.

The stable interval D=99 eV=9δ'' was observed in Pu isotopes, in which stable excitation 43 keV=6×6δ' is well known and is shown in Fig. 8 ,top (maximum in the spacing distribution of all 188 low-lying states). The correspondence between intervals 99 eV (see Figs. 9, 10) and 43 keV are shown in the bottom lines Table 2, where similar correspondence between levels of the neighbour nucleus ^{239}U is shown (considered in the work that follows).

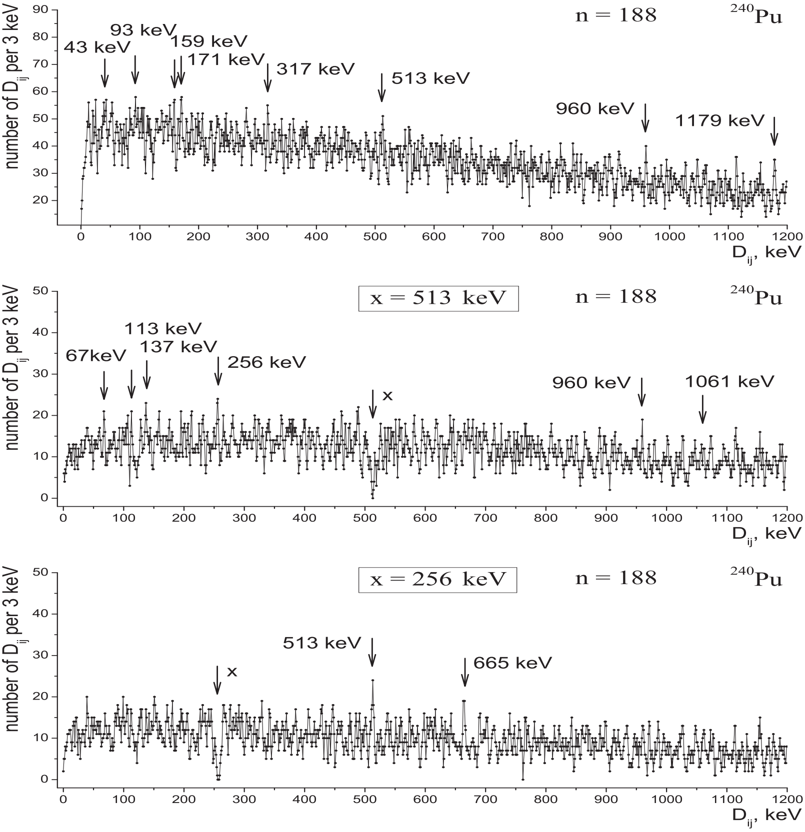

Figure 8: *Top*: Total spacing distribution of low-level ^{240}Pu states with the maximum at 43 keV corresponding to stable excitations in many heavy nuclei. *Center and bottom*: Distribution of intervals adjacent to x=513 keV and 256 keV.

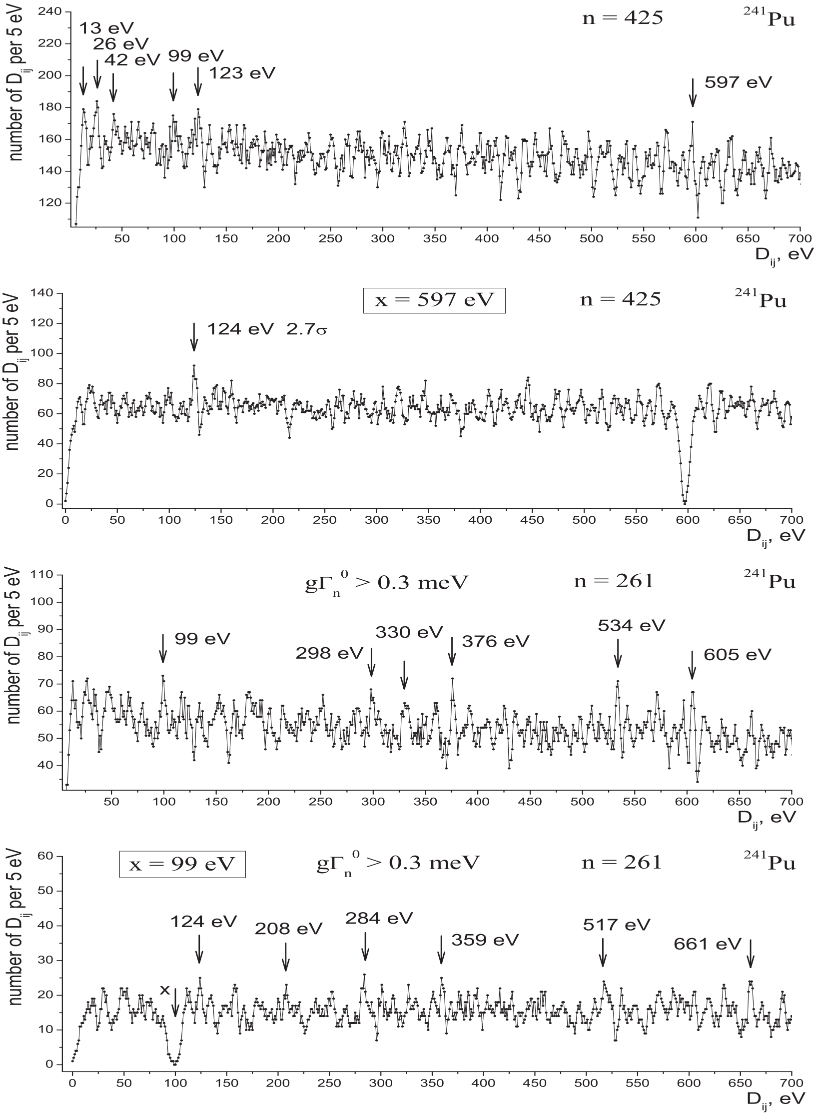

Figure 9: *Top*: Total spacing distribution of all resonances in ^{241}Pu with the maximum at 99 eV=9δ'. *2nd line*: Resonance spacing distribution in ^{241}Pu adjacent to x=597 keV. *Center*: Resonance spacing distribution in ^{241}Pu with g$\Gamma_n^o \geq$0.3 meV with the maximum at 99 eV=9δ''. *Bottom*: Resonance spacing distribution in ^{241}Pu with gΓ_n^o $\geq$0.3 meV adjacent to x=99 eV.

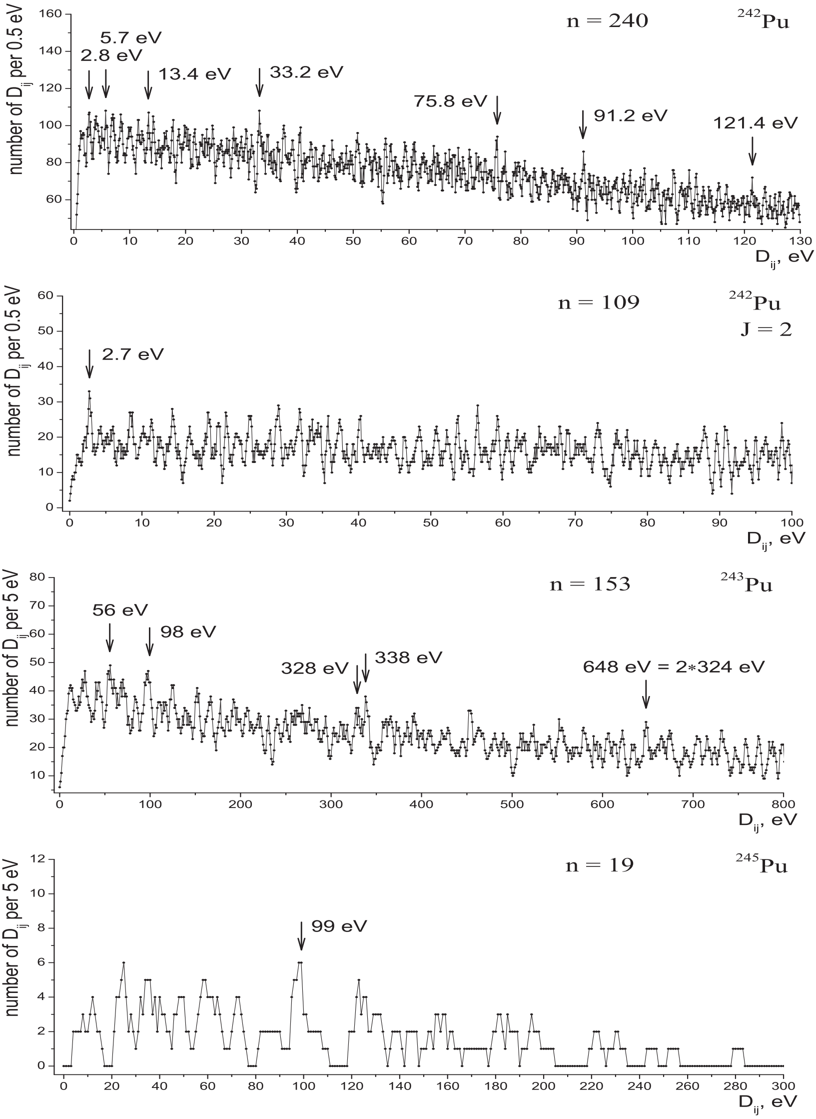

Figure 10: *Top*: Total spacing distribution of all resonances in ^{242}Pu. *2nd line*: Total spacing distribution of all resonances in ^{242}Pu for J=2 with the maximum at 2.7 eV. *Center*: Total spacing distribution of all resonances in ^{243}Pu with the maximum at 98 eV=$9\delta''$. *Bottom*: Total spacing distribution of all resonances in ^{245}Pu with the maximum at 99 eV=$9\delta''$.

4 Conclusions

The recently presented analysis of fine and superfine structures in the spacing of neutron resonances (all data from [25], see also introductions there) confirmed the results obtained in [3,8,9,11-13,20-24] that the coincidence of the ratio between the parameters of these structures demonstrate the important role of the influence of physical condensate (vacuum). Empirically established accurately known CODATA relations [21,22]:

$$m_n = 115 \cdot 16 m_e - m_e - \delta m_N/8 \qquad m_p = 115 \cdot 16 m_e - m_e - 9\delta m_N/8 \tag{1}$$

show two symmetry motivated factors $16 : 1 = \delta : m_e$ and $3 : 1 = m_e : 170\,\mathrm{keV}$, where $170\,\mathrm{keV}{=}m_e/3$ and $161\,\mathrm{keV}{=}\delta m_N/8$ are related to the real fundamental mass splitting.

A near coincidence of the QED radiative correction $\alpha/2\pi = 115.96 \cdot 10^{-5}$ to the ratio $1/(32 \times 27) = 115.74 \cdot 10^{-5}$ allows to suggest that the nuclear data, including neutron resonance data, can indirectly verify the presence of fundamental relations observed in the particle mass spectrum, for example, the lepton ratio as a reflection of the mass discreteness and symmetry.

References

1. F. Close, CERN Courier **53** (2017) No 3, p. 31.
2. V. Belokurov, D. Shirkov, *Theory of Particle Interactions.* AIP, 1991.
3. S.I. Sukhoruchkin, *Statistical Properties of Nuclei.* Pl. Press, 1972, p. 215.
4. Y. Nambu, Progr. Theor. Phys. **7** (1952) 595.
5. P. Kropotkin, *Field and Matter*, Moscow Univ., 1971, p. 106.
6. P. Kropotkin, Doklady Ac. Nauk URSS **206** (1972) 304.
7. R. Sternheimer, Phys. Rev. **136** (1964) 1364; **170** (1968) 1267.
8. S.I. Sukhoruchkin *et al.*, Proc. ISINN-27, JINR E3-2020-10, pp. 40, 54.
9. S.I. Sukhoruchkin *et al.*, Proc. ISINN-9, JINR E3-2001-192, pp. 314, 342, 351.
10. P.A. Zyla *et al.*, Progr. Theor. Exp. Phys. **2020** (2020) 083C01.
11. S.I. Sukhoruchkin *et al.*, Proc. ISINN-3, Dubna, 1995. JINR E3-95-37, pp.182, 330.
12. S.I. Sukhoruchkin, Proc. ISINN-2, JINR E3-94-192, pp. 234, 326.
13. Z. Soroko *et al.*, Proc. ISINN-5, JINR E3-97-213, p. 370.
14. S. Mughabghab, *Neutron Cross Sections*, **1**, part B, p. A-1, 1984.
15. M. Ohkubo *et al.*, J. Nucl. Sci. Techn. **18(10)** (1981) 745; JAERI-M-93-012, 1993.
16. F.N. Belyaev, S.P. Borovlev, Yad. Fiz. **27** (1978) 289.
17. G. Rohr, Proc. 8th Symp. Capt. Gamma-Rays, Fribourg, 1993. W.Sc., 1994, p. 626.
18. G. Rohr, in: *Low Energy Nuclear Dynamics*, p. 130. World Scientific, 1995.
19. K. Ideno, J. Phys. Soc. Jpn. **37** (1974) 581 .
20. Z.N. Soroko *et al.*, Proc. ISINN-7, Dubna, 1999. JINR E3-99-212, p. 313.
21. S.I. Sukhoruchkin, Nucl. Part. Phys. Proc. **312-317** (2021) 185.
22. S.I. Sukhoruchkin, Nucl. Part. Phys. Proc. (in press).
23. S.I. Sukhoruchkin *et al.*, Proc. ISINN-8, Dubna. JINR E3-2000-192, pp. 420, 428.
24. S.I. Sukhoruchkin *et al.*, Proc. ISINN-10, Dubna. JINR E3-2003-10, pp. 290, 299.
25. S.I. Sukhoruchkin, Z.N. Soroko, in: *Neutron resonance parameters*, Landoldt-Börnstein New Series, vols. **I/24**, **I/26A**. Springer, 2009, 2015. Ed. H. Schopper.

NONSTATISTICAL EFFECTS IN RESONANCES OF HEAVY NUCLEI

S.I. Sukhoruchkin, Z.N. Soroko, M.S. Sukhoruchkina

Petersburg Nuclear Physics Institute, NRC ”Kurchatov Institute”, 188300 Gatchina

1. Introduction

In the report of the Kurchatov Institute (Moscow) [1] at the First Geneva Conference (1955) on the Peaceful Use of Atomic Energy, attention was drawn to the proximity of the positions of neutron resonances of different heavy isotopes (at $E_n \approx 0.3$ eV in target nuclei ^{239,241}Pu and ^{241,243}Am). This effect was later studied by Yu. Konakhovich and M. Pevsner in ^{229}Th [2] (this work was supported by I.V. Kurchatov), but as a result, no resonance was found in this isotope at this energy.

The systematic character of the proximity of the resonances positions (at 0.296 eV, 0.265 eV, 0.205 eV and 0.419 eV) in the compound nuclei ^{240,242}Pu and ^{242,244}Am cannot be checked using spacing distributions due to the very small interval under consideration. But the grouping of resonance positions at 5 eV was discussed in [3-6], and a combined study of spacing D distributions of Pu and Am isotopes was possible. In ^{242}Am (Fig. 1), fine structures were observed with intervals D=9 keV, 76 keV, 38 keV, 45 keV and 101 keV (at low excitations) and D=1.32 keV, 2.07 keV, 2.76 keV and 10.24 keV (in resonances).

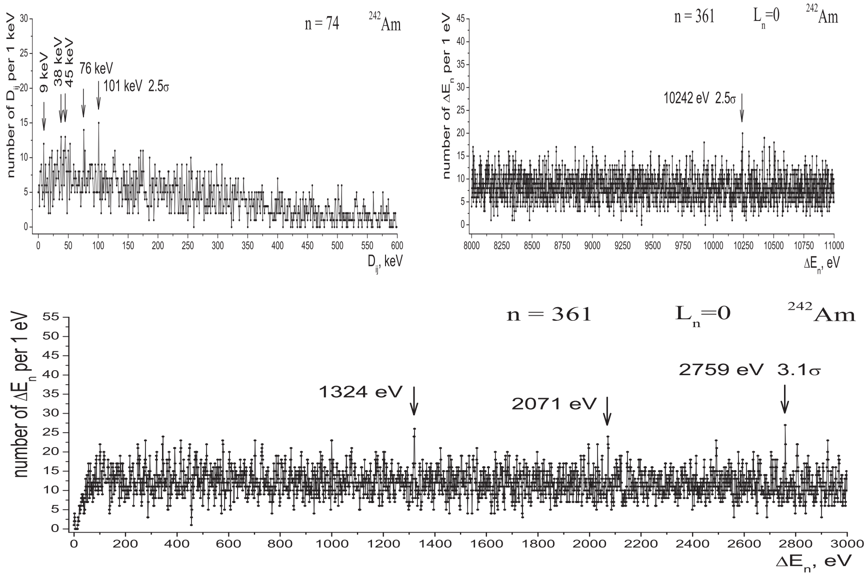

Fig. 1. *Top left:* Spacing distributions in low-lying states of ^{242}Am.
Top right and bottom: Spacing distribution in ^{242}Am neutron resonances.

The superfine structure in the neutron resonance spectra of plutonium isotopes is shown in Fig. 2. Here the coincidence of the maxima in the resonance spacing distributions in three neighbouring isotopes ^{241,243,245}Pu with D=99 eV=18×5.5 eV is shown (the Figure is from [5], where the specific properties of heavy nuclei were discussed). Many authors reported the observation of a grouping of small intervals in the neutron resonance spacing and the resonance positions (called hyperfine structure in [6]). Such effects (with stable intervals of 1 eV and larger) can be considered as the next order effects in the spectra of nuclei, where fine structure effects (with intervals of the order of 1 keV and larger) take place. For example, in heavy isotopes, a fine structure in mass values (with intervals of about 170 keV) was found by V. Andreev [7]. Stable intervals with values 1 eV and larger were attributed to superfine structure (the name was proposed by I.M. Frank [8]). First this effect was considered by W. Havens [9]. The presence of the grouping effect at 5.5 eV, 66 eV and 94 eV in the positions of resonances (see Fig. 6, top in the previous report at this meeting [10,11]) was reported in [3,4]. The superfine structure in the resonance spacing of many nuclei (with the parameter 11 eV=$\delta'' = 8\varepsilon'' = 8\times1.34$ eV) was discussed in [12-15]. Considering the stable intervals of the hyperfine structure (with the value less than the superfine parameter 1.3 eV=ε''), as the next order effect of the observed superfine structure in the ^{240}Pu 0^+ levels (Fig. 2), one estimates their values as 650 eV×$\alpha/2\pi$ ≈0.75 eV. For obtaining a meaningful result, very accurate data are needed.

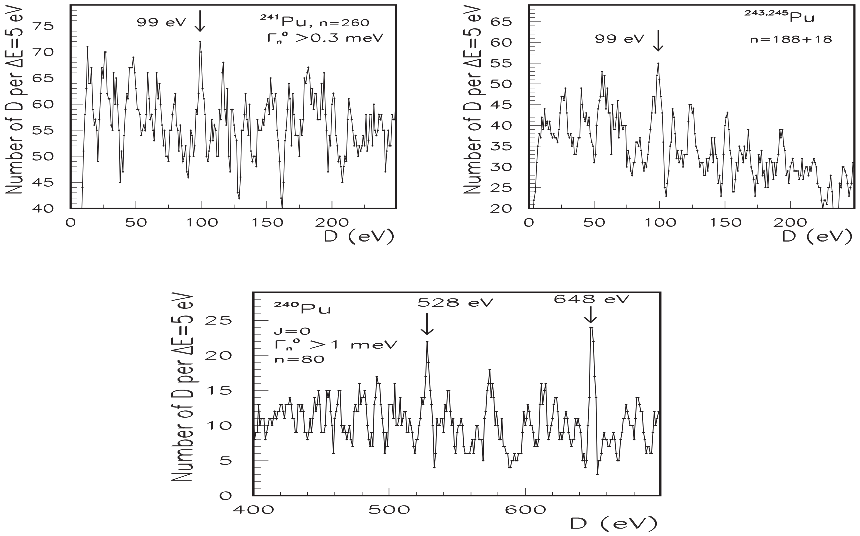

Fig. 2. *Top: D* distributions in ^{241,243,245}Pu resonances. *Bottom:* The same for ^{240}Pu.

Stability of 2^+ excitation values 42.8-42.0-44.5-44.2 keV ^{240,241,242,244}Pu (see the double boxed values in Table 1) is in the ratio 99(1) eV/86(2) keV=115$\cdot10^{-5}$, which is close to the QED radiative correction $\alpha/2\pi = 116\cdot10^{-5}$ (see the first and last lines of Table 2 in the previous work [10]). Such interconnection of the ratios between the superfine and fine structure nuclear intervals and the QED radiative correction is observed in many other heavy nuclei, as shown in the bottom part of this Table in [10].

Table 1. Excitations in heavy nuclei close to 42.5 keV=$\varepsilon_o/24$ and m(85 keV=$\varepsilon_o/12$) [5].

Nucleus	^{229}Th	^{230}Th	^{231}Th	^{232}Th	^{233}Th	^{231}U	^{232}U	^{233}U	^{234}U	^{235}U	^{236}U
J_o^π,J_i^π,$2J_i^\pi$	5^+,7^+	0^+,2^+	5^+,7^+	0^+,2^+	5^-,7^-	5^-,7^-	0^+,2^+	5^+,7^+	0^+,2^+	7^-,9^-	0^+,2^+
E^*,keV	$\boxed{42.4}$	53.2	$\boxed{42.0}$	49.4	44.3	45.1	47.6	40.3	43.5	46.3	45.2
m	1/2	1/2	1/2	(1/2)	(1/2)	(1/2)	1/2	1/2	1/2	1/2	1/2
m·85 keV	42.5	42.5	42.5	42.5	42.5	42.5	42.5	42.5	42.5	42.5	42.5
Nucleus	^{237}U	^{238}U				^{239}U					^{240}U
J_o^π,J_i^π,$2J_i^\pi$	3^+,5^+	0^+,2^+	1^-	D	D	5^+,7^+	(7^+)	D	D	1-5	0^+,2^+
E^*,keV	44.9	44.9	680	45	680	$\boxed{42.5}$	169	43	170	1295	45(1)
m	1/2	1/2	8	1/2	8	1/2	2	1/2	2	δm_N	1/2
m·85 keV,	42.5	42.5	682	42.5	682	42.5	170	42.5	170	1293	42.5
Nucleus	^{235}Pu	^{236}Pu	^{237}Pu	^{238}Pu	^{239}Pu	^{240}Pu	^{241}Pu	^{242}Pu	^{243}Pu	^{244}	^{246}Pu
J_o^π,J_i^π,$2J_i^\pi$	5^+,7^+	0^+,2^+	7^-,9^-	0^+,2^+	3^+,5^+	0^+,2^+	5^+,7^+	0^+,2^+	7^+,9^+	0^+,2^+	0^+,2^+
E^*,keV	$\boxed{41.9}$	44.6	47.7	44.1	49.4	$\boxed{42.8}$	$\boxed{42.0}$	44.5	58.1	44.2	46.7
m	1/2	1/2	1/2	1/2	1/2	1/2	1/2	1/2	1/2	1/2	1/2
m·85 keV	42.5	42.5	42.5	42.5	42.5	42.5	42.5	42.5	42.5	42.5	42.5

The possibility to check the influence of physical condensate within a nuclear medium should be studied in different regions of the nuclear chart. In the regions of collective excitations, such an analysis can be based on the expected relation between fine structure and superfine structure ($D = k{\times}5.5$ eV) corresponding to next order effects with the QED radiative correction parameter $\alpha/2\pi$. The proximity of neutron resonances was first noticed in uranium (5.98 eV, 5.16 eV, 5.45 eV, 6.67 eV in the target $^{232-238}$U). The period in the superfine structure intervals 5.5 eV/4=1.38 eV=ε'' is close to the positions of the first neutron resonances ^{238}Np (1.32-1.48 eV) [6,16,17]. The superfine period $\varepsilon_\circ \cdot (\alpha/2\pi)^2$ corresponds to a stable $E(8^+) = \varepsilon_\circ/2 \approx$511 keV (497-522=518-518-516-514-497-518 keV in $^{234-238}$U, $^{236-242}$Pu), due to the relation 6:20:42:72 for excitations with J=2, 4, 6, 8.

The observed discreteness in the spectrum and the possible appearance of an additional hyperfine structure, similar to that observed as resonance positions in isotopes with Z=92-95 (as the next order effect to the established stability of superfine structure excitations), is the subject of further analysis. Besides the role of real nuclear excitations considered in connection with nonstatistical effects in $^{241-245}$Pu spectra (42.5 keV$\times 2 \cdot (\alpha/2\pi)$=99 eV) and maxima at 43-45 keV in D-distributions for many isotopes (see Fig. 8 [10], Figs. 2, 3) it was noticed that the parameter k in the relation $E^*(2^+) = 6k$ coincides with the QED correction to the stable nuclear interval $6m_e$ found in many nuclei [16].

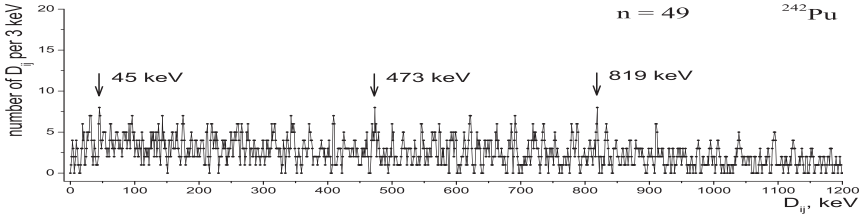

Fig. 3. Spacing distributions in levels of ^{242}Pu, maximum at 45 keV is considered in text.

2. Analysis of spectroscopic data of ^{238,239}U

Analysis of the spacing distributions of low-lying levels of different heavy nuclei allows to confirm the stable character of the parameter 42.5 keV=$6\times6\varepsilon'$.

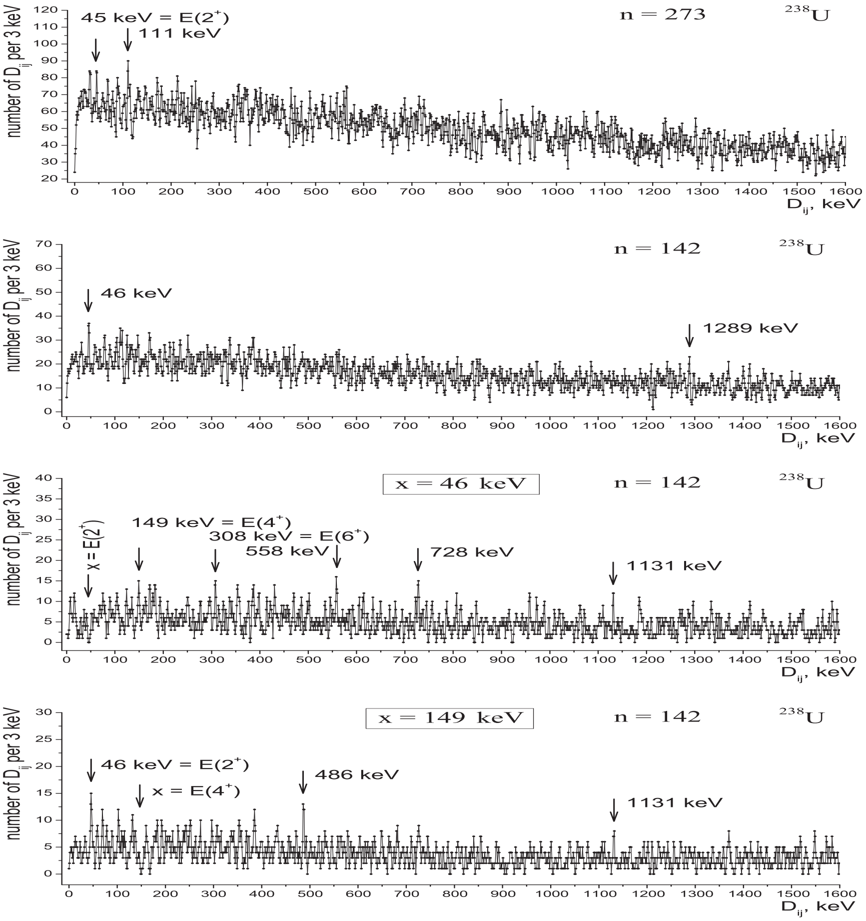

Fig. 4. *Top*: *D*-distributions in all 273 levels and in 142 positive-parity levels of ^{238}U. *Bottom*: Adjacent spacing distributions in levels of ^{238}U for x=46 keV and x=149 keV.

First levels ^{238}U, E^{*}=44.916 keV and ^{239}U, E^{*}=42.543 keV=1.182 eV×36 have corresponding maxima in the spacing distributions of their low-lying levels (Figs. 4 and 5). The value 42.5 k3V is close to the excitations of many nuclei (Table 1, 6 double boxed values).

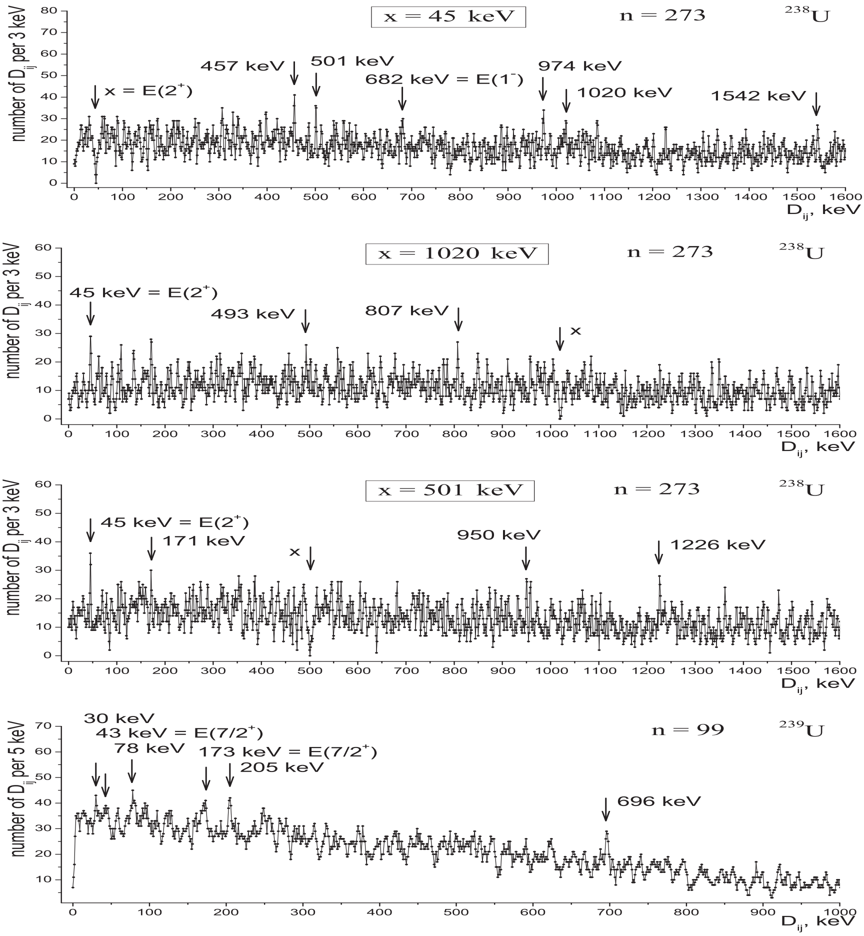

Fig. 5. *Top*: Adjacent spacing distributions in levels ^{238}U for x=45 keV, 1020 keV, 501 keV. *Bottom*: Spacing distributions in levels of ^{239}U.

3. Additional analysis of neutron resonance data

All existing neutron resonance data collected in Springer Compilations [7] on the target ^{238}U (n=897 for s-wave and n=2661 p-wave resonances) were analyzed and compared with data on low-lying levels ^{239}U (Fig. 5, bottom). The interval D=97 eV$\approx 9\delta''$ in the resonance spectrum (Fig. 8, top) is analogous to the interval 99 eV in the data for plutonium (Fig. 2, top).

The spacing distributions in all 897 L=0 neutron resonances ^{239}U and in 233 resonances with $\Gamma_n^\circ \geq 1$ meV are shown in Fig. 5. The exact equidistance between the maxima at 193-388-583-776 eV in the D-distribution for strong resonances (Fig. 6, bottom) and the proximity of the maximum at 776 eV to 793 eV$\approx 4\times198\,eV = 4\times18\delta''$ means confirmation of the superfine structure in the spectrum of strong resonances found earlier in Th [10].

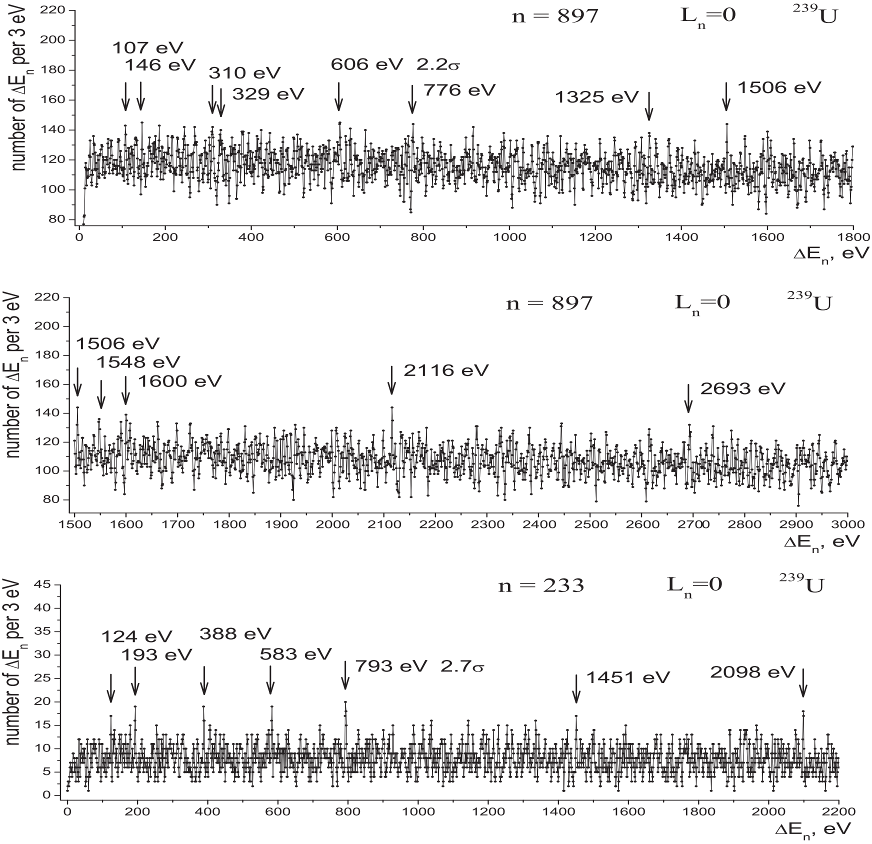

Fig. 6. *Top and center:* Spacing distribution in all 897 L=0 neutron resonances of ^{239}U. *Bottom:* The same for 233 strong resonances with $\Gamma_n^\circ \geq 1$ meV.

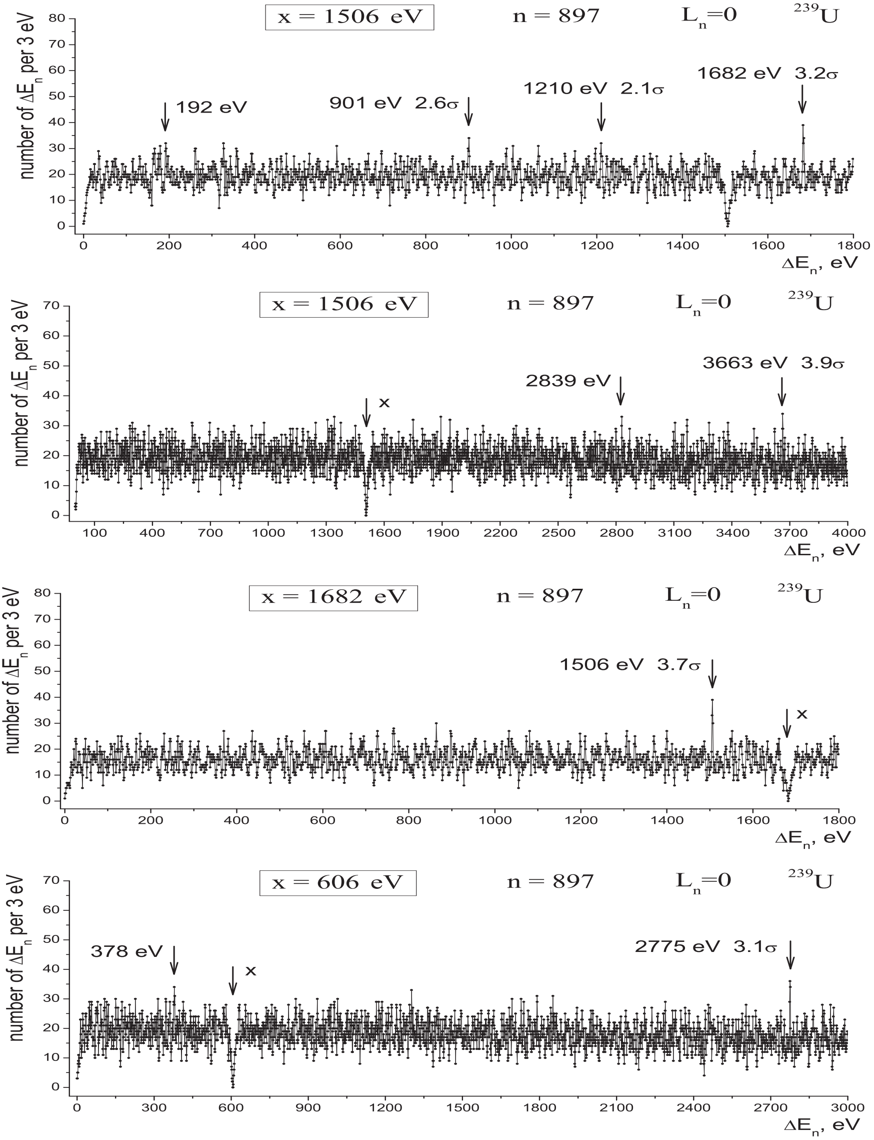

Fig. 7. Adjacent spacing distributions in L=0 neutron resonances of ^{239}U for x=1506 eV (two regions), for x= 1682 eV and for x=606 eV.

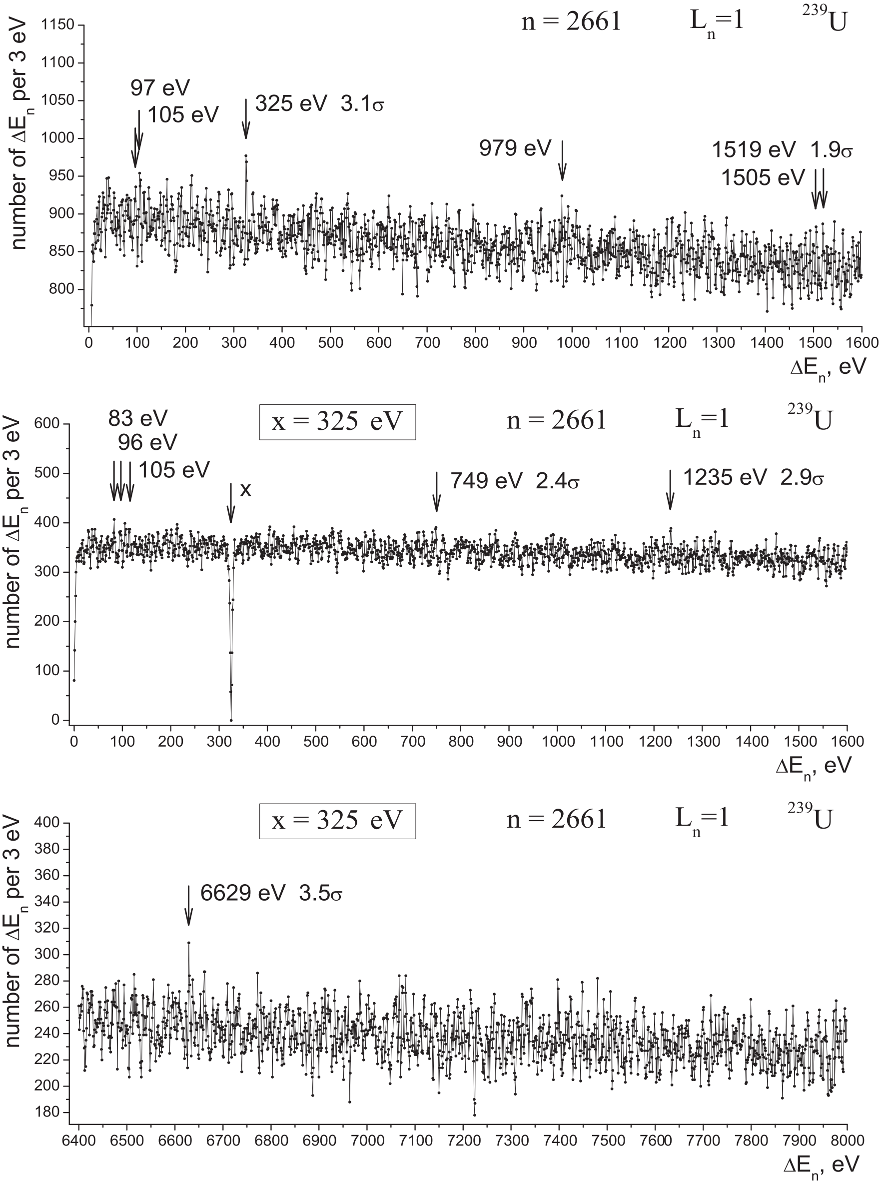

Fig. 8. *Top*: Spacing distributions in L=1 neutron resonances of ^{239}U.
Bottom: Adjacent spacing distributions in L=1 neutron resonances of ^{239}U for x=325 eV (two regions).

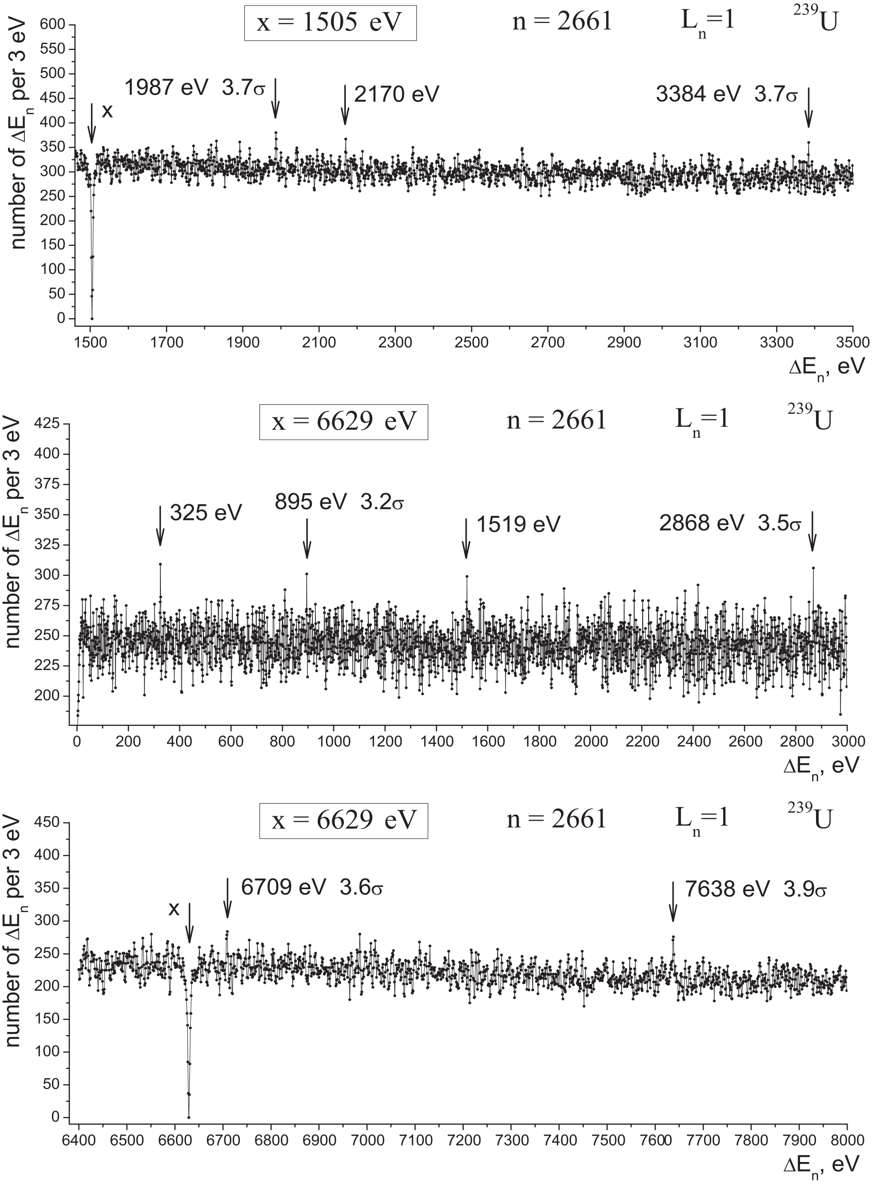

Fig. 9. Adjacent spacing distributions in L=1 neutron resonances of ^{239}U for x=1505 eV and for x=6629 eV (two regions).

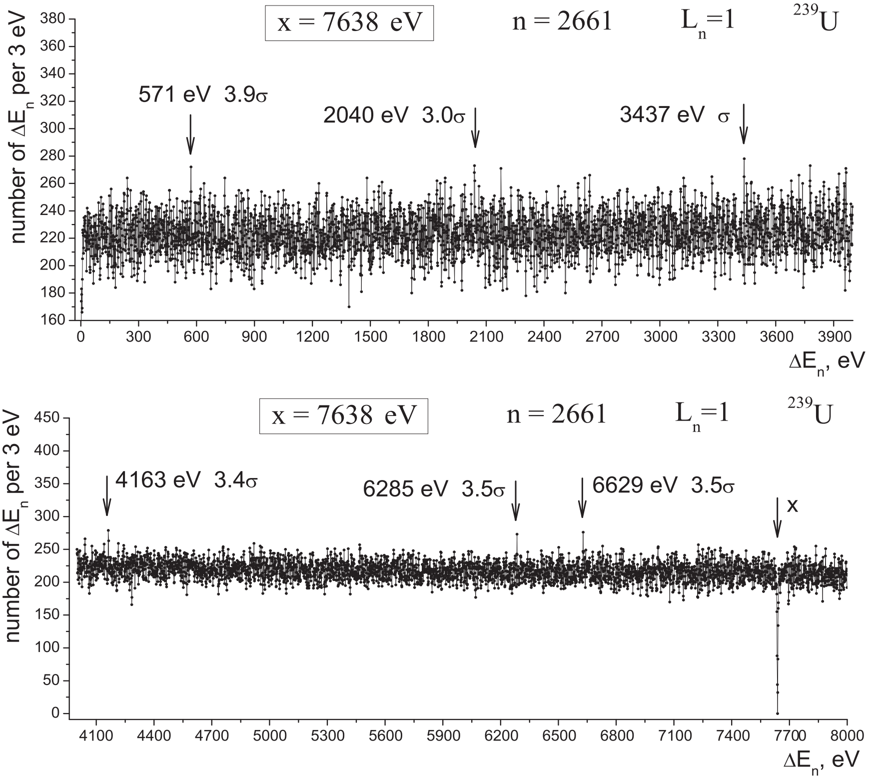

Fig. 10. Adjacent spacing distributions in L=1 neutron resonances of ^{239}U for x=7638 eV (two regions).

Nucleons and the electron are stable particles that determine the visible mass of the universe. They are in a ratio that is very accurately estimated in the CODATA review as m_n/m_e=1838.6836605(11). The electron-based SM development considered here is derived from the fact that the exactly known shift of the neutron mass from $115{\cdot}16m_e$ - m_e is δm_n = 161.6491(6) keV, which is equal to 1/8 of the nucleon mass splitting δm_N=1293.3322(4) keV. The unexpectedly exact ratio $\delta m_N : \delta m_n = 8.00086(3) {\approx} 8{\times}1.0001(1)$ allows the following representation:

$$m_n = 115 \cdot 16m_e - m_e - \delta m_N/8 \quad m_p = 115 \cdot 16m_e - m_e - 9\delta m_N/8 \qquad (1)$$

Y. Nambu noted that " a) When we discover new phenomena which we do not understand, the first thing to do is to collect data and try to find some empirical regularities among them, b) one next tries to build concrete models, c) finally there emerges a real theory ... Standard Model qualifies as such a theory ". We discuss here the development of the Electron-based Constituent Quark Model and some aspects of modern Standard Model. Y. Nambu continued: " Standard Model ... is theoretically unsatisfactory ... a) the unification of forces is only partially realized, and b) there are too many input parameters, especially concerning the masses, which are not explained. The nature can be at the same time more complicated than we think, and simpler in a way we do not know yet. ... we are now at the step of a new cycle. The mass problem is already an early signal for it." According to S. Weiberg, we are "still searching a solution " for the mass problem in the Standard Model.

Analysis of neutron resonance data allows us to confirm two main conclusions from empirical observations on particle properties.

1. There is a distinguished role of the electron mass, its correction and symmetry motivated relations in the particle masses. CODATA relations concern particle physics, as well as nuclear spectroscopy, the appearance of nuclear parameters related to $m_e = 3{\times}170\,\mathrm{keV}$ and $\delta m_N = 8{\times}161\,\mathrm{keV}$ (CODATA structure parameters $m_e/3$ and $\delta m_N/8$ became common for all nuclear parameters). In the spacing distribution for all positive-parity states of ^{238}U (Fig. 4, 2nd line), only two maxima were observed: at 46 keV, which corresponds to stable 2^+ excitations, and D=1289 keV$\approx$ $\delta m_N = 8{\times}161\,\mathrm{keV}$, the second CODATA parameter.

2. It was suggested by R. Feynman and D. Shirkov, that QED radiative correction, known as $\alpha/2\pi = 116\cdot 10^{-5}$ in the case of an anomalous magnetic moment of the electron, can be applied to the electron mass. Empirically, the ratios equal to $\alpha/2\pi = 116\cdot 10^{-5}$ were found between the constituent quark mass, the electron mass, and the parameters of the fine and superfine structure [6].

In the spacing distribution of all 897 L=0 neutron resonances ^{239}U (Fig. 6, top) and in the spacing distribution of 2661 L=1 resonances, the same stable interval D=1505-1506 eV was found. Its appearance can be connected with the stable character of CODATA parameters (in ^{239}U there is an excitation of 1295 kev$\approx$ δm_N). In these works [10,11], we try to check the stable nuclear excitations related to CODATA fine structure parameters.

In the spacing distribution for 233 L=0 strong resonances ($\Gamma_n^\circ \geq 1\,\mathrm{meV}$), the exactly equidistant maxima are observed at 193-388-583-776 eV (Fig. 6, bottom), where the maximum at 776 eV (in all resonances, Fig. 6, top) is close to the maximum at 793 eV$\approx$ $4\times 198\,eV = 4\times 18\delta''$. The probability of the random appearance of four equidistant maxima (in resonances with $\Gamma_n^\circ \geq 1\,\mathrm{meV}$), shown in Fig. 6, bottom, is very small. K. Ideno and M. Ohkubo developed the "Period" program to study such effects [14].

Neutron resonance spectroscopy was developed in response to practical demands. Massifs of resonance data for thorium, uranium, neptunium and plutonium isotopes are the results of measurements performed due to practical applications and world-wide scientific traditions of information collection. In our case, it was W. Furman's initiative to continue the collection of nuclear data started at JINR to be published by Springer (editors W. Martienssen, H. Schopper).

There is a large amount of neutron resonance data for other construction isotopes, but now is the time to measure the resonance structure of many other elements. For example, the cross section of near-magic antimony was measured and analyzed by M. Ohkubo many years ago. The possibility of using neutron resonance data to solve some fundamental problems is shown here.

4. Conclusions

The well-known effect of stability of low-lying excitations in heavy nuclei was used in this work to confirm the discreteness in the neutron resonance spacing distribution due to the possible influence of physical condensate considered by D. Schirkov. The application of new physics based on the distinguished role of the electron was discussed by F. Wilczek [19]. The fundamental aspects of nonstatistical effects in neutron resonance spectra discussed here are considered in [20,21].

The pion parameters $(f_\pi, m_\pi, \Delta M_\Delta)$ corresponding to N=16, 17 and 18 of the period $\delta = 16m_\pi$ (Table 2 in [11] and Table 5 in [18]) were considered here together with the basic parameters of the NRCQM model ($N = 3 \times 16 = 48$ and $N = 3 \times 18 = 54$). All of them manifest themselves directly as maxima in the spacing distribution between the particle masses (from the PDG–2016 and PDG–2020 compilations), similar to what was done earlier with the masses of baryon isosinglets [6]. CODATA relations and discreteness in particle masses and parameters are the main elements of a ”data-driven science” approach in production of the Electron-based Constituent Quark Model (ECQM).

References

1. Y.B. Adamchuk *et al*, Proc. Int. Conf. on Peaceful Uses of Atomic Energy, P/645, **Vol. 4**, p. 223. N.-Y., 1956.
2. Yu. Konakhovich, M. Pevsner, At. En. **8** (1960) 47.
3. S.I. Sukhoruchkin, Proc. Conf. Nucl. Data for Reactors, Paris, 1966. **Vol. 1**, p. 159. IAEA, 1967.
4. S.I. Sukhoruchkin, in: *Neutron Cross Sections*, Washington DC, 1968, **Vol. 2**, p. 923.
5. S.I. Sukhoruchkin, 17th Int. Spin Phys. Symp., Kyoto, 2006. AIP **915** (2007) 272.
6. S.I. Sukhoruchkin, in: *Stat. Prop. of Nuclei.* Ed. G. Garg. Pl. Press, 1972, p. 215.
7. V. Andreev, Nucl. Phys. **39** (1962) 318 and priv. commun.
8. I.M. Frank, Proc. Int. Conf. Struct. Study with Neutrons, Budapest, 1972. Eds. J. Ero, J. Szucs. Acad. Kiado, Budapest, 1974, p. 17.
9. W.W. Havens Jr., *Progr. Fast Neutron Phys.*. Univ. Chicago Press, 1963, p. 215.
10. S.I. Sukhoruchkin *et al.*, *Fundamental aspects of neutr. spectr.*, these Proc.
11. S.I. Sukhoruchkin *et al.*, *Neutron res. in Global Const. Quark Model*, these Proc.
12. S.I. Sukhoruchkin *et al.*, Proc. 2nd Int. Workshop On Nuclear Data Evaluation for Reactor applications (Wonder2009), CEA Cadarache Chateau, France, 2009, p. 88.
13. S.I. Sukhoruchkin, *Discreteness in particle masses and parameters of the Standard Model.* Lambert Ac. Publ., 2017. ISBN 978-620-2-02258-3.
14. K. Ideno, M. Ohkubo, J. Phys. Soc. Jpn. **30** (1971) 620.
15. K. Ideno, Proc. Conf. Neutr. Research, SPIE Proc. Ser. Vol. **2867**, 1997, p. 398.
16. S.I. Sukhoruchkin, Sov. J. Nucl. Phys. **10** (1969) 251, 496.
17. S.I. Sukhoruchkin, Izv. Akad. Nauk SSSR Ser. Fiz. **36** (1972) 885.
18. S.I. Sukhoruchkin *et al.*, Proc. ISINN-27, 2019. JINR **E3-2020-10**, pp. 40, 54.
19. F. Wilczek, Nature **520** (2015) 303.
20. S.I. Sukhoruchkin, Nucl. Part. Phys. Proc. **312-317** (2021) 185.
21. S.I. Sukhoruchkin, Nucl. Part. Phys. Proc. (in press).

AN INVERSE-PROBLEM SOLVING BY THE EXAMPLE OF ^{238}U(n,2γ)^{239}U REACTION ANALYSIS

A.M. Sukhovoj, L.V. Mitsyna, C. Hramko

Frank Laboratory of Neutron Physics, JINR, Dubna

1. Introduction

In spite of preserved representation that a nucleus is a system of non-interactive Fermi-particles, a modern theory supposes that the wave function of any excited level includes both quasi-particle and phonon components. So an experimental obtaining of the nuclear-physical parameters of ^{239}U nucleus is needed not only for practical application, but also for investigation of fundamental interaction between fermion and boson states of nuclear matter. Information about the nuclear-matter behavior can be received if only the strong-correlated nuclear-physical parameters (the nuclear level density ρ and partial widths Γ of reaction-products emission) are obtained simultaneously at the nuclear-reaction investigation.

As the required strong-correlated parameters enter into the measured spectrum as a product $\rho\times\Gamma$, their extraction from indirect experiment is a complicated problem of search for inverse solution. Analysis of data of indirect experiment in order to obtain the strong-correlated parameters ρ and Γ always leads to inevitability of unknown sizeable systematical errors. By the highest standards, reliable nuclear-physical parameters can be obtained in two independent experiments only.

When γ-quanta coincidences of the two-step cascades are recording, indeterminateness of the nuclear-physical parameters obtained from measured intensities of $\gamma\gamma$-cascades can be diminished in the presence of information about initial, final and intermediate cascade levels. And with all this going on, it is very important to ascertain the quanta sequence in the cascades in order to determine more reliable nuclear-parameters. But an ambiguity of the obtained nuclear parameters always exists in $\gamma\gamma$-coincidence experiment, even at essential difference of the $\rho(E_{ex})$ and $\Gamma(E_\gamma)$ functions, where E_{ex} and E_γ are energies of nuclear excitation and of γ-quantum.

The empirical method was created and developed in Dubna in order to enable an investigation of dynamics of nuclear-structure change below the neutron binding energy in a nucleus. The Dubna method allows simultaneous extraction of the nuclear level density and partial widths of γ-quanta emission from approximation of the experimental intensities of only primary transitions of the two-step γ-cascades, without using experimentally-untested hypothesis.

The Dubna empirical method was applied to analyze presented in [1] experimental γ-spectrum from the ^{238}U(n,2γ)^{239}U reaction, which has been measured using nearly 4π γ-ray calorimeter DANCE composed of a spherical array of 160 BaF$_2$ crystals.

2. Opening remarks concerning analyzable data

The multistep γ-cascade spectra at the decay of isolated *s*-wave ($J^\pi = 1/2^+$) resonances in compound-nuclei of three uranium isotopes are presented in [1] for multiplicities up to M=4. For reliability of extraction of the nuclear-physical parameters from experimental γ-cascade spectra it is necessary to determine the quanta sequence in the cascades. As for M-cascade quanta there is a possibility of $M!$ placing variants in the decay scheme, it makes the quanta-sequence determination impossible in the cascades with multiplicities M>2.

An uncertainty in the quanta sequence exists even for the cascades with multiplicities M=2, but the presence of energy-resolved cascades' peaks in the experimental spectrum allows the use of available information about known intense transitions. As far as an energy resolution of coincidences recording enables, the experimental spectra are composed of isolated peaks and continuum of unresolved ones. In the two-step cascade the γ-quanta sequence can be unambiguously determined in the experimental-intensity spectrum only for a part of energy-resolved cascades corresponded to available spectroscopic data. The part of such cascades in the experimental spectrum can be very sizeable if detectors of high energy resolutions (now HPGe-detectors only) are used to record γγ-coincidences. For example, used in our experiments HPGe-detectors of greatly high intensity allowed us to increase a part of energy-resolved cascades in the experimental γ-spectra up to 40–60% at statistics about of 40000 events (or more).

But energy-resolving power of scintillation counters, which are used in experiments with 4π-calorimeter, unfortunately doesn't allow a separation of individual intense transitions, so the decay-scheme application is impossible in the analysis. And what is more, in the experiment with 4π-calorimeter a sharp increase in a number of counts was always observed for experimental γ-spectra of the cascades of M=3 multiplicity as compared with ones of M=2. Underestimation of the intensities of the cascades of M=2 multiplicity is quite possible owing to redistribution of annihilation quanta between detector crystals at low energy resolution of the spectrometer.

In spite of insufficient-detailed spectrum recorded by scintillation detectors, which make impossible a separation of spectrum of primary γ-transitions with a fair degree of confidence, in spite of everything, we try to analyze presented in [1] experimental spectrum of M=2 multiplicity from the ^{238}U(n,2γ)^{239}U reaction.

3. The basis of the Dubna empirical method

A key concept of the Dubna empirical method is obtaining the $\rho(E_{ex})$ and $\Gamma(E_\gamma)$ functions from the fitting of the $I_{\gamma\gamma}(E_1)$-intensities of only primary transitions of the cascades (E_1 is energy of primary γ-quantum of the two-step γ-cascade), calculated when Monte-Carlo solving a system of nonlinear equations (1), to the experimental intensities of primary transitions. The use of high-aperture HPGe-detectors in the experiments allows a determination of the part of primary transitions of the two-step cascades with an uncertainty of 10–20% without distortion of the spectrum normalization, which was confirmed by negligibility of the effect of the systematic errors of $I_{\gamma\gamma}(E_1)$-spectrum separation, for example, for ^{172}Yb nucleus [2].

Each of the equation (1) connects $I_{\gamma\gamma}(E_1)$-intensities with the partial widths of γ-transitions between neutron resonance λ and a group of final levels f via all possible intermediate levels i in a small energy interval ΔE_j:

$$I_{\gamma\gamma}(E_1) = \sum_{\lambda,f}\sum_{i}\frac{\Gamma_{\lambda i}}{\Gamma_\lambda}\frac{\Gamma_{if}}{\Gamma_i} = \sum_{\lambda,f}\sum_{j}\frac{\Gamma_{\lambda j}}{<\Gamma_{\lambda j}>M_{\lambda j}}n_j\frac{\Gamma_{jf}}{<\Gamma_{jf}>m_{jf}}. \qquad (1)$$

In interval ΔE_j there are n_j intermediate levels i, to which $M_{\lambda j}=\rho\Delta E_j$ transitions go from initial level λ, and m_{jf} secondary transitions go to final level f ($n_j=\rho\Delta E_j$ and $m_{jf}=\rho\Delta E_j$ at all intermediate-levels energies). At the excitation energy $E_{\text{ex}}< E_d$ (E_d is maximal excitation energy of "discrete" level area) the system (1) contains only experimental data on energies and quantum numbers of known to date levels and their decay modes.

In spite of the nonlinearity inevitably leads to false likelihood maxima, the system of non-linear equations (1) could have a definite solution (hypothetical limit) if the experimental

$I_{\gamma\gamma}(E_1)$-intensities would be known in each energy point. But as there are no high-aperture spectrometers of gammas with an electron-volt resolution, solving of the system of the equations (1) is impossible without using model representations of the nuclear level density and the strength functions $k(E_\gamma)=\Gamma/(A^{2/3}\cdot E_\gamma^3\cdot D_\lambda)$, where A – nuclear mass number, D_λ – average distance between nuclear levels. However, available in RIPL-file [3] models of the required nuclear parameters (based at the representation of a nucleus by a pure fermion system) don't allow a description of real experimental spectra. So the problem of a choice of the most realistic model representations for the $\rho(E_{ex})=\varphi(p_1, p_2, ...)$ and $\Gamma(E_1)=\psi(q_1, q_2, ...)$ functions of some fitted parameters p and q, is as great as ever.

It is important that deformed at every iteration fitted parameters would lead to the best experimental-spectra description. That is guaranteed by the Dubna method, as the model representations of the nuclear-physical parameters are tested and modified in the course of the analysis. Average amplitudes of changing of correction-vector components (no more than 1% of current values of the set of fitted parameters) decrease at each iteration to guarantee χ^2 minimum:

$$\chi^2 = \sum_{n_j} \frac{(I^{cal}_{\gamma\gamma}(E_1) - I^{\exp}_{\gamma\gamma}(E_1))^2}{\sigma^2}, \tag{2}$$

where $I^{cal}_{\gamma\gamma}(E_1)$ and $I^{\exp}_{\gamma\gamma}(E_1)$ are model-parametrized and experimental intensities, and σ^2 is a dispersion of their difference. With all this going on there is no need to use any hypothesis untested experimentally.

A systematical uncertainty of the obtained nuclear parameters is mainly determined by inexactness of model-phenomenological representations about energy dependences of the $\varphi(p_1, p_2, ...)$ and $\psi(q_1, q_2, ...)$ functions.

4. The nuclear-parameters representations in the Dubna empirical method

At given $\rho(E_{ex})=\varphi(p_1, p_2, ...)$ and $\Gamma(E_1)=\psi(q_1, q_2, ...)$ functions parametrized according to definite models there is only one solution of the system of equations (1).

Now for representation of the $\rho(E_{ex})$ function in the Dubna empirical analysis a modern Strutinsky model [4] (which is able to describe successfully pre-equilibrium nuclear reactions) as well as a balance between changes of entropy and energy of quasi-particles' states [5] are being applied.

In a framework of the model [4] an expression for density ρ_l of levels of fermion type is written as:

$$\rho_l = \frac{(2J+1)\exp(-(J+1/2)^2/2\sigma^2)}{2\sqrt{(2\pi)}\sigma^3}\Omega_n(E_{ex}), \qquad \Omega_n(E_{ex}) = \frac{g^n(E_{ex}-U_l)^{n-1}}{((n/2)!)^2(n-1)!}. \tag{3}$$

Here Ω_n is of n-quasi-particle states, a cut-off factor σ of spin J of excited state of compound-nucleus above the energy E_d was taken from back-shifted Fermi-gas model [6], U_l is the energy of l-th Cooper pair breaking threshold, and density $g=6a/\pi^2$ of single-particle states near Fermi-surface was also taken from the [6] model). An influence of the shell inhomogeneities of a single-particle spectrum was taken into account by a definition of the level-density dependence on excitation energy in a value:

$$a(A, E_{ex}) = \tilde{a}\,(1+((1-\exp(\gamma E_{ex}))\,\delta E/E_{ex})). \tag{4}$$

An asymptotic value $\tilde{a} = 0.114A + 0.162A^{2/3}$ and coefficient $\gamma = 0.054$ were taken from [5]. A shell correction δE calculated from the data of mass defect in a liquid-drop nuclear model [3] is lightly changed to keep an average distance D_λ between resonances of an investigated nucleus.

Generally accepted now phenomenological coefficient C_{col} of enhancement of collective level density imitates well an increase in vibrational level density and for given excitation energy E_{ex} on the basis of a theoretical description of [5] is written as:

$$C_{col} = A_l \exp(\sqrt{(E_{\mathrm{ex}} - U_l)/E_\nu} - (E_{\mathrm{ex}} - U_l)/E_\mu) + \beta. \tag{5}$$

Here A_l are fitted independently parameters of densities of vibrational levels above the breaking point of each l-th Cooper pair, E_μ is a change in the nuclear entropy, E_ν is a change of quasi-particles excitation energies, parameter $\beta \geq 1$ can differ from 1 for deformed nuclei.

The smooth parts of the energy dependences of the strength functions, $k(E1,E_\gamma)$ and $k(M1,E_\gamma)$, of dipole electrical and magnet γ-transitions are expressed similarly as in [7]:

$$\begin{aligned} k(E1,E_\gamma) &= w_E \frac{1}{3\pi^2\hbar^2c^2A^{2/3}} \frac{\sigma_{GE}\Gamma_{GE}^2(E_\gamma^2 + \kappa_E 4\pi^2 T_E^2)}{(E_\gamma^2 - E_{GE}^2)^2 + E_{GE}^2\Gamma_{GE}^2}, \\ k(M1,E_\gamma) &= w_M \frac{1}{3\pi^2\hbar^2c^2A^{2/3}} \frac{\sigma_{GM}\Gamma_{GM}^2(E_\gamma^2 + \kappa_M 4\pi^2 T_M^2)}{(E_\gamma^2 - E_{GM}^2)^2 + E_{GM}^2\Gamma_{GM}^2}, \end{aligned} \tag{6}$$

where parameters T_{E} (or T_{M}) are varied thermodynamic parameters, and w_{E} (or w_{M}) and κ_{E} (or κ_{M}) are added parameters of weight and of a change of derivatives of the strength function, correspondingly (indices E and M refer to E1- or M1-transitions). In equations (6) E_{G}, Γ_{G} and σ_{G} are location of the center of giant dipole resonance, its width and cross section in maximum.

If $E_1 \approx B_{\mathrm{n}}$ (B_{n} is the nucleon binding energy), fitted ratios $\Gamma_{\mathrm{M1}}/\Gamma_{E1}$ of $E1$- and $M1$-strength functions are normalized to known experimental values, and their sum Γ_λ is normalized to the full radiation width of the resonance.

5. Analysis of the data from ^{238}U(n,2γ)^{239}U reaction

All multistep γ-cascade spectra measured in [1] were analyzed using DICEBOX-code [8]. DICEBOX algorithm, taking into account the levels from ENSDF-file up to critical energy (830 keV for ^{239}U), above this energy generates levels according to increase in of their number in strict correspondence to statistical theory of a nucleus. Probabilities of individual transitions between each pair of levels are simulated using partial-widths formulae, which includes both the level density and a random number taken from a normal Porter-Thomas distribution. As it is mentioned by the experimenters themselves, in their analysis an extremely large number of different artificial "nuclear realizations" appeared due to Porter-Thomas fluctuations. In those calculations several forward-modelling approaches for the E1 and M1 photon strength functions as well as for the nuclear level density were used. However, the practical-applied Strutinsky model of the nuclear-level density was absent among the most available models used by the experimenters of [1]. By the way, modern theory about dynamics of intra-nuclear processes at the excitation-energy increase (see [9], for example) points to existence of different wave-function structure of the excited levels which excludes smoothness of the energy dependences both the level density and radiative strength functions. It is reasonable also to note that testing of the different types of the strength functions makes sense only with simultaneous testing of the models of the nuclear level density.

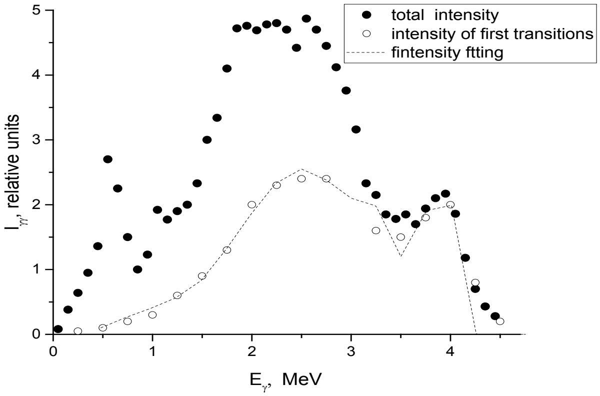

Fig.1. The dependence of intensities of the two-step γ-cascades (relative to their total area) on γ-quanta energies at the decay of compound-state in ^{239}U nucleus (36 eV): close points are the total $I_{\gamma\gamma}(E_\gamma)$-intensities of the two-step cascades; open points are $I_{\gamma\gamma}(E_1)$-intensities of first transitions only; dashed line is the best fit of $I_{\gamma\gamma}(E_1)$-intensity in a framework of the Dubna empirical method.

Unfortunately, the experimental spectrum of the intensities of the two-step γ-cascades in ^{239}U nucleus is shown in [1] by plotted points only. Nevertheless, we separated primary γ-transitions spectrum (open points in Fig.1), as it is necessary for our subsequent analysis. We used a valid assumption that, as a rule, primary transition in the two-step γ-cascade has more energy than secondary one, and removed secondary transitions from the total spectrum, taking into account mirror-symmetry of energy distributions of primary and secondary transitions relative to a central point of the $I_{\gamma\gamma}(E_\gamma)$-intensity spectrum (at a half of total energy of the cascades). Experimental points of the total-intensity of the two-step γ-cascades are shown in Fig.1 as close ones.

In spite of impossibility to get a shape of $I_{\gamma\gamma}(E_1)$-distribution accurately from examinee experimental data, at least, a qualitative evaluation of the energy dependences of the level density and strength functions for ^{239}U nucleus has been accomplished.

The authors of [1] have explained an unsatisfactory description of measured $I_{\gamma\gamma}(E_\gamma)$-intensities by impossibility of taking into account of all parameters of the γ-decay in the used models. We agree with their reasonable assertion completely, but our calculations showed that experimental spectrum of $I_{\gamma\gamma}(E_1)$-intensities cannot be described successfully by any smooth dependence of the nuclear level density on excitation energy.

If a nucleus is imagined as a system of non-interactive nucleons, an assumption about consecutive breaks of Cooper pairs of nucleons in decayed nucleus at an increase in its excitation energy is soundly enough. The step-wise dependence of the level density of nucleus on its excitation energy can be well founded by existence of energy gaps in the spectrum of excited nucleus at discontinuity of a number of pair of excited nucleons.

The dependence of the level density of ^{239}U nucleus on its excitation energy (see Fig.2) obtained from the best $I_{\gamma\gamma}(E_1)$-intensity fits in a framework of the Dubna empirical method, have an evident step-wise behavior. Approximation of the experimental data using a smooth $\rho(E_{ex})$ function postulated by the authors of [1] results in appreciable increase in χ^2.

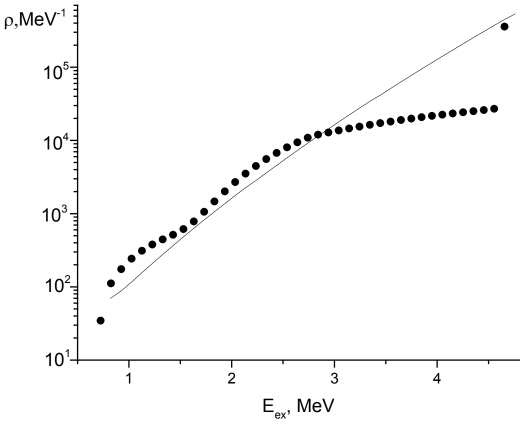

Fig.2. The expected level density of ^{239}U nucleus: close points is our calculation (using fitted parameters from the best $I_{\gamma\gamma}(E_1)$-distribution fit); line is calculation according to the back-shifted Fermi-gas model predictions.

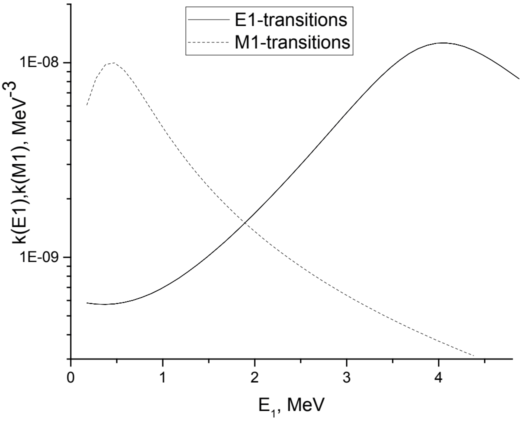

Fig.3. The radiative strength functions for ^{239}U nucleus (our calculations for the $I_{\gamma\gamma}(E_1)$-distribution best fit): solid line is our calculation of k(E1) for E1-transitions in the cascades; dashed line is k(M1)-calculation for M1-transitions.

And a rate of the level-density rise essentially differs from that predicted by the back-shifted Fermi-gas model.

It must be noted that in all nuclei analyzed earlier by the Dubna empirical method (see, for example, [10–12]), the experimental γ-spectra of which were far better suitable for analysis than spectrum from ^{239}U nucleus, the breaks in nuclear level-density dependences on the excitation energy are positioned with a step ≈$2\Delta_0$ (Δ_0 is the pairing energy of the last nuclear nucleon). Our fittings of $I_{\gamma\gamma}(E_1)$-intensities of the cascades in ^{239}U nucleus also do not exclude for this nucleus a possibility of nucleons' pairing and consecutive breaking of these pairs.

The expected behavior of energy dependences of the radiative strength functions for E1- and M1-transitions in the two-step cascades of ^{239}U nucleus obtained from our calculations on a base of fitted parameters at the $I_{\gamma\gamma}(E_1)$-intensities description are presented in Fig.3.

6. Conclusion

An experimental obtaining of the parameters of γ-decay of any compound-state is exclusively important to understand processes which take place in an excited nucleus.

In spite of insufficient energy-resolving power of scintillator detectors of DANCE calorimeter, in the absence of individual cascade peaks in measured γ-spectrum, we have been successful in description of the experimental spectrum of intensities of primary transitions of the two-step γ-cascades in ^{239}U nucleus with subsequent simultaneous obtaining of its, at least, evaluative $\rho(E_{ex})$ and $\Gamma(E_1)$ functions.

Unfortunately, an absence of experimental individual energy-resolved cascades in total γγ-spectra from 4π-experiment doesn't allow a clarification of the intra-nuclear processes in ^{239}U nucleus. A process of breaking of Cooper pairs is not been experimentally investigated until now. Nevertheless, our calculations visually demonstrate that successful description of the experimental intensities of the two-step γ-cascades in ^{239}U nucleus is possible if only the nuclear-level density has not smooth dependence on the excitation energy.

Only high-transmission spectrometers of gammas and testing of suitable model representations of required strong-correlated nuclear parameters can provide their reliability.

References

1. J.L. Ullmann, T. Kawano, B. Baramsai, *et al.*, Phys.Rev. C **96**, 024627 (2017).
2. A.M. Sukhovoj, L.V. Mitsyna, D.C. Vu, N.N. Anh, N.X. Hai, P.D. Khang, H.H. Thang, in *Proceedings of the XXV International Seminar on Interaction of Neutrons with Nuclei,* Dubna, Russia, 2017, p. 175.
3. *Reference Input Parameter Library RIPL-2, Handbook for calculations of nuclear reaction data*, IAEA-TECDOC (2002).
4. V.M. Strutinsky, in *Proceedings of the International Congress on Nuclear Physics, Paris, France, 1958*, p. 617.
5. A.V. Ignatyuk, Report INDC-233(L), IAEA (Vienna, 1985).
6. W. Dilg, W. Schantl, H. Vonach, and M. Uhl, Nucl. Phys. A **217**, 269 (1973).
7. S.G. Kadmensky, V.P. Markushev, V.I. Furman, Sov. J. Nucl. Phys. **37**, 165 (1983).
8. F. Becvar, NIM A **417**, 434 (1998).
9. L.A. Malov, V.G. Solovjev, Sov. J. Nucl. Phys., **26**, 384(1977).
10. D.C. Vu, A.M. Sukhovoj, L.V. Mitsyna, Sh. Zeinalov, N. Jovancevic, D. Knezevic, M. Krmar, A. Dragic, Phys. Atom. Nucl. **80**, N2, 237 (2017).
11. N.A. Nguyen, X.N. Nguyen, D.K. Pham, D.C. Vu, A.M. Sukhovoj, L.V. Mitsyna, Phys. Atom. Nucl. **81**, N3, 296 (2018).
12. N. Jovancevic, L.V. Mitsyna, A.M. Sukhovoj, D. Knezevic, M. Krmar, J. Petrovic, S. Oberstedt, A. Dragic, F.-J. Hambsch, V.D. Cong, Journal of the Korean Physical Society, **75**, Issue 2, 100 (2019).

Научное издание

FUNDAMENTAL INTERACTIONS & NEUTRONS, NUCLEAR STRUCTURE, ULTRACOLD NEUTRONS, RELATED TOPICS

XXVIII International Seminar on Interaction of Neutrons with Nuclei

Proceedings of the Seminar

ФУНДАМЕНТАЛЬНЫЕ ВЗАИМОДЕЙСТВИЯ И НЕЙТРОНЫ, СТРУКТУРА ЯДРА, УЛЬТРАХОЛОДНЫЕ НЕЙТРОНЫ, СВЯЗАННЫЕ ТЕМЫ

XXVIII Международный семинар по взаимодействию нейтронов с ядрами

Труды семинара

Ответственная за подготовку сборника к печати *Л. В. Мицына*.

Сборник отпечатан методом прямого репродуцирования с оригиналов,
предоставленных оргкомитетом.

Е3-2021-48

Подписано в печать 26.11.2021
Формат 60×90/16. Бумага офсетная. Печать цифровая
Усл. печ. л. 17,38. Уч.-изд. л. 30,27. Тираж 75 экз. Заказ № 60303

Издательский отдел Объединенного института ядерных исследований
141980, г. Дубна, Московская обл., ул. Жолио-Кюри, 6.
E-mail: publish@jinr.ru
www.jinr.ru/publish/